AN INSILICO DESIGN OF NANOCLAY BASED NANOCOMPOSITES AND SCAFFOLDS IN BONE TISSUE ENGINEERING

A Dissertation
Submitted to the Graduate Faculty
of the
North Dakota State University
of Agriculture and Applied Science

By

Anurag Sharma

In Partial Fulfillment of the Requirements
for the Degree of
DOCTOR OF PHILOSOPHY

Major Program:
Materials and Nanotechnology

July 2016

Fargo, North Dakota

North Dakota State University
Graduate School

Title

INSILICO DESIGN OF NANOCLAY BASED NANOCOMPOSITES AND SCAFFOLDS IN BONE TISSUE ENGINEERING

By

Anurag Sharma

The Supervisory Committee certifies that this ***disquisition*** complies with North Dakota State University's regulations and meets the accepted standards for the degree of

DOCTOR OF PHILOSOPHY

SUPERVISORY COMMITTEE:

Dr. Dinesh R. Katti (Chair)

Dr. Kalpana S. Katti (Co-Chair)

Dr. Achintya N. Bezbaruah

Dr. Lawrence P. Reynolds

Approved:

November 18th, 2016 — Date

Dr. Erik K. Hobbie — Department Chair

ABSTRACT

A multiscale *in silico* approach to design polymer nanocomposites and scaffolds for bone tissue engineering applications is described in this study. This study focuses on the role of biomaterials design and selection, structural integrity and mechanical properties evolution during degradation and tissue regeneration in the successful design of polymer nanocomposite scaffolds. Polymer nanocomposite scaffolds are synthesized using aminoacid modified montmorillonite nanoclay with biomineralized hydroxyapatite and polycaprolactone (PCL/in situ HAPclay). Representative molecular models of polymer nanocomposite system are systematically developed using molecular dynamics (MD) technique and successfully validated using material characterization techniques. The constant force steered molecular dynamics (fSMD) simulation results indicate a two-phase nanomechanical behavior of the polymer nanocomposite. The MD and fSMD simulations results provide quantitative contributions of molecular interactions between different constituents of representative models and their effect on nanomechanical responses of nanoclay based polymer nanocomposite system. A finite element (FE) model of PCL/in situ HAPclay scaffold is built using micro-computed tomography images and bridging the nanomechanical properties obtained from fSMD simulations into the FE model. A new reduction factor, K is introduced into modeling results to consider the effect of wall porosity of the polymer scaffold. The effect of accelerated degradation under alkaline conditions and human osteoblast cells culture on the evolution of mechanical properties of scaffolds are studied and the damage mechanics based analytical models are developed. Finally, the novel multiscale models are developed that incorporate the complex molecular and microstructural properties, mechanical properties at nanoscale and structural levels and mechanical properties evolution during degradation and tissue formation in the polymer nanocomposite scaffold. Overall, this study

provides a leap into methodologies for *in silico* design of biomaterials for bone tissue engineering applications.

Furthermore, as a part of this work, a molecular dynamics study of rice DNA in the presence of single walled carbon nanotube is carried out to understand the role played by molecular interactions in the conformation changes of rice DNA. The simulations results showed wrapping of DNA onto SWCNT, breaking and forming of hydrogen bonds due to unzipping of Watson–Crick (WC) nucleobase pairs and forming of new non-WC nucleobase pairs in DNA.

ACKNOWLEDGEMENTS

I would like to begin by thanking my advisor Dr. Dinesh Katti and co-advisor Dr. Kalpana Katti for their invaluable guidance and encouragement throughout my doctorate degree. Without their intellectual efforts, patience and constant motivation, I would not have reached this stage of getting my Ph.D. degree and this work would not have been possible without their support and inspiration.

I acknowledge NDSU Center for Computationally Assisted Science and Technology (CCAST) for providing computational resources, which was crucial for carrying out my simulations work. I also acknowledge National Science Foundation MRI instrumentation grant (NSF MRI: #1229316, #0320657 and #0821655) and National Institute of Food and Agriculture (US Department of Agriculture) under USDA-NIFA-AFRI agreement number 2012-67018-30186. I highly appreciate Mr. Scott Payne from NDSU EM Center for his assistance in electron microscopy and computed tomography experiments.

I am grateful to my advisory committee members: Dr. Achintya N. Bezbaruah and Dr. Lawrence Reynolds for their invaluable suggestions, helpful discussions and feedback. My past and present group members and friends whom I shared many joyful experiences and valuable thoughts, I thank you all for your help, cooperation, and constructive advices throughout my study.

Finally, and most importantly, I owe special gratitude to all my proud family members, specially my brother (Abhishek Sharma), sister-in-law (Parul Sharma) and two nephews (Abhigyan and Abeer), for their continuous and unconditional love and support, immeasurable sacrifices, and patience throughout my career.

DEDICATION

This Dissertation is dedicated to

My beloved late father Mr. Amar Chand Sharma (1948-2014) and

Loving mother, Mrs. Prem Sharma.

TABLE OF CONTENTS

ABSTRACT…..... iii

ACKNOWLEDGEMENTS..... v

DEDICATION..... vi

LIST OF TABLES..... xiii

LIST OF FIGURES..... xiv

LIST OF ABBREVIATIONS..... xviii

CHAPTER 1. INTRODUCTION..... 1

1.1. Bone Tissue Engineering.....1

1.2. Nanoparticles in Plants ……..……..2

1.3. Objectives of the Research……....……..3

1.4. Dissertation Organization ……..……..4

1.5. References……..……..5

CHAPTER 2. REVIEW OF LITERATURE..... 7

2.1. Introduction……....……..7

2.1.1. Bio and Synthetic Polymers and Nanoscale Additives……..……..9

2.1.2. Polymer Scaffold Manufacturing Methods in Laboratory and Manufacturing Technologies ……...…..……12

2.2. *In Vitro* Mechanical Properties of Scaffolds and Nanocomposites: Computational Methods……....……16

2.2.1. Ab Initio……....……16

2.2.2. Molecular Modeling..... ……....…...18

2.2.3. Finite Element Methods…….……21

2.3. Design of Nanocomposites and Scaffolds: Computational Approaches …..……24

2.3.1. Material Design of PCN using Molecular Modeling……....……24

2.3.2. Use of Finite Element Methods for Predictive Capabilities of Scaffold Properties.. ……..…..26

2.4. Degradxation of Polymers Scaffolds ……....…..29

2.4.1. Degradation of Scaffolds in Accelerated Degradation Conditions……..…..29

2.4.2. Degradation of Scaffolds in Cell Culture Media ……...…..31

2.4.3. Modeling Degradation of Scaffolds....…….....32

2.5. Multiscale *In Silico* Strategies for Scaffolds Design …….……..33

2.6. References……..…..36

CHAPTER 3. MOLECULAR INTERACTIONS IN BIOMINERALIZED HYDROXYAPATITE AMINO ACID MODIFIED NANOCLAY: INSILICO DESIGN OF BONE BIOMATERIALS……..48

3.1. Introduction.. ……..48

3.2. Materials and Methods……...…..51

3.2.1. Materials ……...…..51

3.2.2. Synthesis of Organically Modified Montmorillonite (OMMT) Clay……...…..51

3.2.3. Preparation of *In situ* Hydroxyapatite (HAP) Clay……...…..52

3.2.4. X-Ray Diffraction ……..…..52

3.2.5. Transmission Electron Microscopy ……...…..52

3.3. Model Construction ……...…..53

3.3.1. Model of Na-Montmorillonite and Organically Modified Montmorillonite Clay……...53

3.3.2. Model of Organically Modified Montmorillonite Clay - Hydroxyapatite…….....60

3.4. Simulation Details……...…….67

3.4.1. Organically Modified Montmorillonite Clay…….…..67

3.4.2. Organically Modified Montmorillonite Clay – Hydroxyapatite……..68

3.4.3. Interaction Energy Calculations……..68

3.5. Results and Discussion ……..…..69

3.5.1. X-ray Diffraction Results ……..…..69

3.5.2. Interactions in Organically Modified MMT clay……...…..69

3.5.3. Results from OMMT-HAP Simulations……...…..72

3.5.4. Interactions of OMMT Perpendicular to HAP……...…..74

3.5.5. Interactions of OMMT Parallel to HAP……....…..77

3.6. Conclusions……...……...83

3.7. References……...……84

CHAPTER 4. EVALUATING MOLECULAR INTERACTIONS IN POLYCAPROLACTONE-BIOMINERALIZED HYDROXYAPATITE NANOCOMPOSITES USING STEERED MOLECULAR DYNAMICS…….90

4.1. Introduction……...……...90

4.2. Materials and Methods…….94

4.2.1. Materials……...…….94

4.2.2. Preparation of Polycaprolactone (PCL)/*In situ* Hydroxyapatite (OMMT-HAP) Clay……..95

4.2.3. X-Ray Diffraction……..95

4.2.4. Transmission Electron Microscopy……...95

4.3. Model Construction……...…...95

4.3.1. Computational Methodology……...95

4.3.2. Model of Organically Modified Montmorillonite Clay - Hydroxyapatite - Polycaprolactone……..96

4.3.3. Steered Molecular Dynamics Model of Organically Modified Montmorillonite Clay - Hydroxyapatite - Polycaprolactone ……....…102

4.4. Simulation Details……...…...102

4.5. Results and Discussion……...106

4.5.1. OMMT-HAP-PCL Simulations……106

4.5.2. Interactions in OMMT-HAP-PCL……106

4.5.3. Evaluation of Mechanical Response of OMMT-HAP-PCL at Molecular Level……113

4.6. Conclusions……..……118

4.7. References……..……...119

CHAPTER 5. MULTISCALE MODELS OF DEGRADATION AND HEALING OF BONE TISSUE ENGINEERING NANOCOMPOSITE SCAFFOLDS……...123

5.1. Introduction……123

5.2. Materials and Methods……...131

5.2.1. Materials……..……..131

5.2.2. Preparation of Polycaprolactone (PCL)/*In situ* Hydroxyapatite (HAP) clay Scaffolds……131

5.2.3. Scanning Electron Microscopy (SEM) Characterization……..…132

5.2.4. Steered Molecular Dynamics Simulation ……..…132

5.2.5. Micro Computed Tomography (μCT) of PCL/*In situ* HAPclay Scaffolds……..……..133

5.2.6. Finite Element Modeling of PCL/*In situ* HAPclay Scaffolds……...…134

5.2.7. Accelerated Degradation Studies in 0.1M NaOH……..…135

5.2.8. Mechanical Degradation of Scaffolds in 0.1 M NaOH……..…135

5.2.9. Human Osteoblast (hOB) Cell Culture Experiments……....…136

5.2.10. Cell Proliferation Study using WST-1 Assay.... ……...…136

5.2.11. Mechanical Properties of Scaffolds Seeded with hOB Cell ……..…137

5.2.12. Integrative Finite Element Modeling of PCL/*In situ* HAPclay Scaffold of 'Critical Size.'……..138

5.2.13. Statistical Analysis..... ..…139

5.3. Results……..……139

5.3.1. Initial Morphology and Mechanical Properties……. 139

5.3.2. Finite Element Analysis of PCL/*In situ* HAPclay Scaffolds……...…140

5.3.3. Accelerated Degradation in PCL/*In situ* HAPclay Scaffolds……...…142

5.3.4. Human Osteoblast Cells Seeded PCL/*In situ* HAPclay Scaffolds……...……..150

5.3.5. Integrative Multiscale Model……154

5.4. Discussion……...……...162

5.4.1. Finite Element Analysis of PCL/*In situ* HAPclay Scaffolds .. ……..…162

5.4.2. Effect of Accelerated Degradation on PCL/*In situ* HAPclay Scaffolds……...……..164

5.4.3. Effect of Human Osteoblast Cells on PCL/*In situ* HAPclay Scaffolds……...……..164

5.4.4. Analytical Modeling of PCl/*In situ* HAPclay Scaffolds Degradation……...….165

5.4.5. Finite Element Modeling of Implant scale PCL/*In situ* HAPclay Scaffold in Critical Size Bone Defects……...166

5.5. Conclusions……...……166

5.6. References……...……...168

CHAPTER 6. CARBON NANOTUBE PROXIMITY INFLUENCES RICE DNA…….174

6.1. Introduction……...……174

6.2. Computational Methods……178

6.2.1. Model Construction……178

6.2.2. Simulation Details……..182

6.3. Results and Discussion……...182

6.4. Conclusions……...……190

6.5. References……...……...191

CHAPTER 7. SUMMARY AND CONCLUSIONS……..197

CHAPTER 8. FUTURE WORKS……...205

LIST OF TABLES

Table		Page
3.1.	Non-bonded interactions between MMT clay and different constituents of aminovaleric in modified MMT clay	70
3.2.	Non-bonded interaction energies between different constituents of MMTclay, aminovaleric and HAP in OMMT-HAP perpendicular	75
3.3.	Non-bonded interaction energies between different constituents of MMTclay, aminovaleric and HAP in OMMT-HAP parallel	80
4.1.	The non-bonded interaction energies between MMT clay and different constituents of HAP, aminovaleric acid and PCL in OMMT–HAP–PCL	109
4.2.	The non-bonded interaction energies between HAP and different constituents of aminovaleric acid and PCL in OMMT–HAP–PCL	110
4.3.	The non-bonded interaction energies between different constituents of aminovaleric acid molecules and PCL in OMMT–HAP–PCL	112
4.4.	The average values of elastic modulus calculated at 1000 μN and 5000 μN applied forces in nanoindentation tests [46] and modulus calculated from the region-1 and region-2 of the SMD simulations of OMMT-HAP-PCL system	116
5.1.	Verification of Degradation function (D). Comparison of strain energy between predicted and experiment data at 14 days	148
5.2.	Verification of Degradation function (D). Comparison of strain energy between predicted and experiment data at 7 days	156
6.1.	Number of hydrogen bonds between DNA Watson-Crick base pairs	186
6.2.	Non-bonded interaction energies between different bases of DNA and water	187

LIST OF FIGURES

Figure Page

2.1. Multiscale and multi-process schematic of PCL/in situ HAPclay scaffold…..……..34

3.1. Chemical structure of protonated 5-aminovaleric acid……..54

3.2. Initial orientations of protonated aminovaleric acid molecules placed in four different ways: (a) parallel to the MMT clay surface, (b) inclined at angle of 45^0 to the MMT clay surface, (c) NH_3^+ functional group closer to MMTclay surface and (d) COOH functional group to MMTclay surface……..55

3.3. Final orientations of protonated aminovaleric acid molecules placed in four different ways: (a) parallel to the MMT clay surface, (b) inclined at angle of 45^0 to the MMT clay surface, (c) NH_3^+ functional group closer to MMTclay surface and (d) COOH functional group close to MMTclay surface…….……56

3.4. Variation of final d-spacing with no. of protonated aminovaleric acid in OMMT models at 300 K and 1 atm……57

3.5. X-ray diffraction of montmorillonite (MMT), modified MMTclay and in situ HAPclay…….…58

3.6. Structure of final representative model of organically modified MMTclay at a temperature of 300 K and 1 atm pressure (d-spacing = 14.08 Å)……..59

3.7. TEM image of in situ HAPclay. Clay sheets appear to have both parallel and perpendicular orientations with HAP crystals……..61

3.8. Structure of OMMT-HAP perpendicular before minimization (initial d-spacing = 14.08 Å)…….……..63

3.9. Structure of OMMT-HAP perpendicular at 300 K and 1 atm (final d-spacing = 13.92 Å)…….……..64

3.10. Structure of OMMT-HAP perpendicular before minimization (initial d-spacing = 14.08 Å)…….……..65

3.11. Structure of OMMT-HAP parallel at 300 K and 1 atm (final d-spacing = 13.08 Å)…66

3.12. Total non-bonded interaction energies between MMTclay, HAP and aminovaleric acid in OMMT-HAP perpendicular…….....73

3.13. Map of total non-bonded interactions between different constituents of HAP, aminovaleric acid and MMTclay in OMMT-HAP perpendicular…….....76

3.14. Total non-bonded interaction energies between MMTclay, HAP and aminovaleric acid in OMMT-HAP parallel……78

3.15. Map of total non-bonded interactions between different constituents of HAP, aminovaleric acid and MMTclay in OMMT-HAP parallel…….....79

4.1. (a. b) TEM image of PCL/in situ HAPclay……..…….98

4.2. Initial structure of organically modified MMTclay–Hydroxyapatite (OMMT-HAP)……..……..99

4.3. Structure of annealed polycaprolactone (PCL) chain containing 14 monomers…….100

4.4. Structure of organically modified MMT clay–Hydroxyapatite–Polycaprolactone (OMMT-HAP-PCL) before minimization……...101

4.5. Structure of final representative model of OMMT-HAP-PCL at a temperature of 300 K and 1 atm pressure after 50 ns……..103

4.6. Compressive point loads are applied in the z direction on the top surface atoms of the OMMT-HAP-PCL……104

4.7. Total non-bonded interaction energies between MMTclay, HAP, aminovaleric acid and PCL in OMMT-HAP-PCL……105

4.8. Different constituents of HAP, aminovaleric acid modifier, MMTclay and PCL in OMMT-HAP-PCL……...107

4.9. Map of total non-bonded interactions between different constituents of MMTclay, aminovaleric acid modifier, HAP and PCL in OMMT-HAP-PCL…….108

4.10. Stress-strain characteristics in the OMMT-HAP-PCL at molecular level……..113

4.11. Stress–strain plot of the OMMT-HAP-PCL molecular model in the region-1……...114

4.12. Stress–strain plot of the OMMT-HAP-PCL molecular model in the region-2……...115

5.1. (a) 3D reconstruction of the PCL/in situ HAPclay scaffold in Mimics, (b) Mechanical response of PCL/in situ HAPclay at molecular scale obtained from steered molecular dynamics (SMD) simulations, (c) The loading conditions for the scaffold in the FE model……..…..134

5.2. SEM micrograph of PCL/in situ HAPclay scaffold. Macropores ranging between 100-300μm sizes……..137

5.3. SEM micrograph of PCL/in situ HAPclay scaffold. Micropores (<10 μm and 10–30 μm range) in the walls of PCL/in situ HAPclay scaffold microstructure…….138

5.4. Wall porosity correction (Reduction factor) applied to finite element analysis stress due to wall porosity = K = total wall length/material length = x/y =8……....140

5.5. Comparison of mechanical behavior obtained from experiments and finite element analysis. Results show good agreement after wall porosity correction…….141

5.6. Compressive mechanical properties of undegraded (control) and degraded (day 1, 5, 7, 14 and 18) PCL/in situ HAPclay scaffolds in alkaline condition (0.1M NaOH). The compressive mechanical properties of PCL/in situ HAPclay scaffold decreases with degradation time…….....143

5.7. Mechanical property degradation (D) of PCL/in situ HAPclay scaffolds in alkaline condition (0.1M NaOH)…...……..145

5.8. Plot for calculation of parameters for degradation function (D) of PCL/in situ HAPclay scaffolds in alkaline condition (0.1M NaOH)……..146

5.9. Model verification: Experimental compressive stress–strain curve of PCL/in situ HAPclay scaffolds degraded in alkaline conditions (0.1M NaOH) at 14 days and compared to the model predicted compressive stress-strain curve...……...148

5.10. WST-1 cell proliferation study of hOB cells cultured on PCL/in situ HAPclay scaffolds. The data were obtained after 4, 7, 18 and 28 days of cell culture and presented as mean ± standard deviations…….149

5.11. (a, b) SEM micrographs of hOB cells cultured on PCL/in situ HAPclay after 28 days……..151

5.12. Compressive mechanical properties of PCL/in situ HAPclay scaffolds seeded with hOB cells (day 4, 7, 18 and 28)……...152

5.13. Mechanical property degradation (D) of PCL/in situ HAPclay scaffolds seeded with hOB cells…….153

5.14. Calculation of critical parameters for degradation function (D) of PCL/in situ HAPclay scaffolds seeded with hOB cells……..155

5.15. Model verification: Experimental compressive stress–strain curve of PCL/in situ HAPclay scaffolds seeded with hOB cells at 7 days and compared to the model predicted compressive stress-strain curve……...156

5.16. Finite element model of PCL/in situ HAPclay implant scaffold in critical size bone defects…….157

5.17. Mechanical behavior evolution of integrative finite element analysis of PCL/in situ HAPclay implant scaffold in critical size bone defects for undegraded (control) and degraded (day 1, 5, 7, 14 and 18) in alkaline condition (0.1M NaOH)…… ...158

5.18. Time-dependent deformation profiles of integrative FE model of PCL/in situ HAPclay implant scaffold in alkaline condition (0.1M NaOH)……..…159

5.19. Mechanical behavior evolution of integrative finite element analysis of PCL/in situ HAPclay implant scaffold in critical size bone defects for hOB cells seeded (day 4, 7, 18 and 28)……160

5.20. Time-dependent deformation profiles of integrative FE model of hOB cells seeded (day 4, 7, 18 and 28) PCL/in situ HAPclay implant scaffolds.....161

6.1. (a) Initial conformation of rice DNA, (b) final conformation of rice DNA after 10ns in model-1 shows no changes in base pairing……..180

6.2. (a) Initial conformation of rice DNA-SWCNT and (b) final conformation of rice DNA-SWCNT after 10ns in model-2……..181

6.3. Snapshots of rice DNA-SWCNT at different simulation times (a) DNA wrapping onto SWCNT starts at 1ns, (b) more number of the WC bases pairs have unzipped at 5ns and (c) wrapping process of DNA onto SWCNT appears more visible at 10ns in model-2……...184

6.4. Hydrogen bonding between water molecules and different nucleobases of DNA in model-2…….....185

6.5. Non-bonded interaction energies plot between different bases of DNA and CNT in model-2……..…….188

LIST OF ABBREVIATIONS

CNT's	Carbon Nanotubes
DNA	Deoxyribose Nucleic Acid
ELE	Electrostatic Energy
FEM	Finite Element Method
FTIR	Fourier Transform Infrared
hMSCs	Human Mesenchymal Stem Cells
hOB	Human Osteoblast Cells
HAP	Hydroxyapatite
MD	Molecular Dynamics
Na-MMT	Sodium Montmorillonite
OMMT	Organically Modified Montmorillonite
OMMT-HAP	Organically Modified Montmorillonite-Hydroxyapatite
OMMT-HAP-PCL	Organically Modified Montmorillonite-Hydroxyapatite-Polycaprolactone
PCL	Polycaprolactone
PCNs	Polymer Clay Nanocomposites
SEM	Scanning Electron Microscopy
SMD	Steered Molecular Dynamics
TEM	Transmission Electron Microscopy
VDW	Vander Waals Energy
XRD	X-ray Diffraction

CHAPTER 1. INTRODUCTION

1.1. Bone Tissue Engineering

The increasing number of bone related injuries and diseases over the years have significantly increased the importance of bone grafting. According to American Academy of Orthopaedic Surgeons, in US alone more than 500,000 cases require bone grafting every year [1]. It is estimated that the bone grafts and substitutes global market would expand to USD 3.48 billion in 2023 from USD 2.35 billion in 2014 [2]. In a recently published report, the number of fracture incidences are expected to rise by 310% in men and 240% in women by 2050 [3]. Osteoporosis, a common bone disease alone causes 8.9 million fractures annually and affects 1 in 2 women over the age of 50 in the world [4, 5]. These studies indicate the great need of bone graft substitutes that can act as alternatives for damaged bone and regenerate natural body tissues.

Bone tissue engineering is a promising interdisciplinary field that provides an alternative approach to develop biological substitutes for damaged or diseased bone tissues. Bone tissue engineering techniques mainly require a porous three dimensional scaffold that supports cell initiation, attachment and subsequently bone tissue regenerations using the growth factors. The bone tissue engineered scaffolds must possesses excellent biocompatibility, biodegradability, microstructure that can attach and promote cell growth and adequate mechanical properties. However, bone tissue regeneration is a highly complex process that involves the interactions and regulations of different biochemical, biophysical and mechanical factors at multiple length and time scale. Several computational and experimental methodologies have been developed to design the tissue engineered scaffolds, which attempt to mimic the material and mechanical behavior of bone at multiscale level. The *in vitro* experimental models have shown a great control over the design of scaffolds. However, they lack the complexities present inside the human body during the

different biological processes. On the other hand, *in vivo* studies are often carried out on animal models and therefore, their results for the human body are not completely reliable. In this context, computational modeling or *in silico* modeling can be used as a potential tool in designing scaffolds for bone tissue engineering. The computational *in silico* methodologies not only improve the understanding of mechanisms involved in the complex multiscale biological system but also help in predicting the various properties of the system under different environmental conditions. The predictive *in silico* models can be used in developing *in vitro* scaffolds that can also withstand in the *in vivo* like conditions.

The complexity of material systems in bone tissue engineering applications necessitate the use of advanced modeling techniques to accurately predict the scaffold and regenerated tissue behavior. This thesis a new multiscale modeling technique for *in silico* design of polymer composite scaffolds for bone tissue engineering applications. The representative molecular models are constructed to understand the role of molecular interactions on the mechanical properties of clay-based polymer nanocomposite. A micro computed tomography image based finite element modeling approach is presented for scaffold-tissue mechanical behavior prediction. Degradation experiments are carried out for a specific material system and incorporated into general purpose degradation modeling theories using damage mechanics. Essentially, this procedure may be easily implemented for other biomaterial systems including degradable metals and ceramics.

1.2. Nanoparticles in Plants

Recent development of engineered nanoparticles (ENPs) have offered innovative discoveries in areas such as cosmetics, electronics, drugs and other biomedical applications [6-9]. With rapidly growing demand and their commercial production, ENPs are finding their way into the environment. Due to their small size, nanoparticles such as carbon nanotubes are able to

penetrate into plant cells and have a potential to interact with DNA that may lead to significant changes to the plants. The phytotoxicity studies of carbon nanotubes have shown that their interactions with plants are complex. Some studies have revealed that the presence of carbon nanotubes may activate the hypersensitive responses in the plant cells and thus, retard the growth of plant [10, 11]. Other phytotoxicity studies have found that the carbon nanotubes affect the gene expression and aid water uptake, translocations, cell division and root elongation in the plants [12, 13]. Therefore, it is important to study the carbon nanotubes with plant DNA at molecular level to understand their interaction mechanism. Rice happens to be the most consumed food in the world. 1/3rd of the population depends on rice for more than 50% of caloric intake. That makes it most important plant to study the advantages and disadvantages of nanoparticles in plants. However, despite the number of experimental studies, no computational modeling study has been done to fully understand the molecular interaction mechanism between carbon nanotubes and rice plants. Here, as part of my Ph.D. work, I have studied the effect of single walled carbon nanotubes on the rice plant DNA using molecular dynamics simulation technique. This work provides a detailed insight into the conformation changes and molecular interaction mechanism in rice DNA due to the presence of carbon nanotubes.

1.3. Objectives of the Research

The summary of the objectives of this doctoral research are as follows:

- To guide a design of materials and scaffolds for bone tissue engineering applications using an In-silico approach.
- To systematically develop representative molecular model of polymer nanocomposite for bone tissue engineering.

- To understand the molecular interactions mechanism and mechanical response in the polymer nanocomposites using molecular dynamics and material characterization techniques.
- To systematically develop a multiscale representative design of the polymer scaffold by bridging molecular scale to macroscale.
- To develop analytical model for evolution of mechanical degradation of polymer scaffolds under different degradation conditions.
- To understand the molecular interaction mechanism between carbon nanotube and rice plant DNA.

1.4. Dissertation Organization

This dissertation is organized into following chapters:

1) Chapter 1: Introduction

2) Chapter 2: This chapter presents review of literature on the common materials and methods used in the fabricating the scaffolds and computational methods used to understand the *in vitro* mechanical properties of scaffolds. It further describes the use of FE methods for predicting scaffold properties and degradation of polymer scaffolds in different degradation conditions. This chapter also discusses the methodologies used for multiscale *in silico* design of polymer scaffolds.

3) Chapter 3: A simulations driven approach to design of a novel biomaterial nanocomposite system for bone tissue engineering is described in this chapter.

4) Chapter 4: The molecular interactions and mechanical response in a complex polycaprolactone-biomineralized hydroxyapatite nanocomposite system is presented in this chapter.

5) Chapter 5: This chapter presents a new multiscale mechanics based *in silico* approach to design polymer scaffolds for bone tissue engineering applications.

6) Chapter 6: The role of carbon nanotube on the conformation changes in rice DNA is discussed in this chapter.

7) Chapter 7: This chapter presents summary and major conclusions of the research presented in this dissertation.

8) Chapter 8: The future directions for the research in this field are discussed in this chapter.

1.5. References

[1] American academy of orthopedic surgeons (AAOS), http://www.aaos.org/, (2006).

[2] Bone Grafts and Substitutes Market-Global Industry Analysis, Size, Share, Growth, Trends and Forecast 2015 - 2023, http://www.transparencymarketresearch.com/bone-grafts-substitutes-market.html, (2015).

[3] B. Gullberg, O. Johnell, J. Kanis, Osteoporosis international 7 (1997) 407-413.

[4] O. Johnell, J. Kanis, Osteoporosis international 17 (2006) 1726-1733.

[5] R. Keen, Best Practice & Research Clinical Rheumatology 21 (2007) 109-122.

[6] A. Bianco, K. Kostarelos, M. Prato, Current opinion in chemical biology 9 (2005) 674-679.

[7] L. Lacerda, A. Bianco, M. Prato, K. Kostarelos, Advanced drug delivery reviews 58 (2006) 1460-1470.

[8] C. Lorenz, N. Von Goetz, M. Scheringer, M. Wormuth, K. Hungerbühler, Nanotoxicology 5 (2011) 12-29.

[9] L. Dykman, N. Khlebtsov, Chemical Society Reviews 41 (2012) 2256-2282.

[10] F. Aslani, S. Bagheri, N. Muhd Julkapli, A.S. Juraimi, F.S.G. Hashemi, A. Baghdadi, The Scientific World Journal 2014 (2014).

[11] X.-m. Tan, C. Lin, B. Fugetsu, Carbon 47 (2009) 3479-3487.

[12] R. Nair, M.S. Mohamed, W. Gao, T. Maekawa, Y. Yoshida, P.M. Ajayan, D.S. Kumar, Journal of Nanoscience and Nanotechnology 12 (2012) 2212-2220.

[13] M.V. Khodakovskaya, K. de Silva, D.A. Nedosekin, E. Dervishi, A.S. Biris, E.V. Shashkov, E.I. Galanzha, V.P. Zharov, Proceedings of the National Academy of Sciences 108 (2011) 1028-1033.

CHAPTER 2. REVIEW OF LITERATURE[1]

This chapter presents a background about the common materials and methods used in the fabricating the scaffolds. It also discusses different modeling methods used to understand the *in vitro* mechanical properties of scaffolds. Further, this chapter reviews the use of molecular modeling in understanding the role of molecular interactions on the mechanical properties of clay-based polymer nanocomposite and use of FE methods for predicting scaffold properties. Also, this chapter reviews the degradation of scaffolds in accelerated degradation conditions and cell culture media and discuses mathematical degradation modeling of polymer scaffold. Finally, the state of the art in multiscale *in silico* modeling strategies for scaffolds design are presented in this chapter. The contents of this chapter have been submitted as a book chapter by Dinesh R. Katti, Anurag Sharma, Kalpana S. Katti, Predictive methodologies for design of bone tissue engineering scaffolds.

2.1. Introduction

Tissue engineering combines the fields of life sciences and engineering with a purpose of developing biological substitutes that can repair/replace damaged tissues and organs of the human body. Over the years, significant progress has been made in designing implants/scaffolds for bone tissue regenerations. In general, tissue engineered scaffolds should have (i) suitable porosity for cell migration, nutrients delivery, and removal of biodegraded materials; (ii) adequate mechanical properties that can support and stimulate the tissue formation; and (iii) controllable biodegradation rate. However, designing a hierarchical tissue engineered polymer scaffold is a complex process

[1] The material in this chapter was co-authored by Anurag Sharma and Dinesh Katti. Anurag Sharma had primary responsibility for collecting samples in the field and for interviewing users of the test system. Anurag Sharma was the primary developer of the conclusions that are advanced here. Anurag Sharma also drafted and revised all versions of this chapter. Dinesh Katti served as proof reader and checked the math in the statistical analysis conducted by Anurag Sharma.

and requires to consideration of factors such as biomaterial selection and design, structural integrity and mechanical properties evolution during degradation and tissue regeneration. These parameters if not properly optimized in the synthesis process may result in a final product with the mismatched mechanical properties which eventually lead to severe wear and in even damage of implants inside the body. Therefore, it is important to investigate the role of these parameters in the successful design of a polymer scaffold for bone tissue regeneration.

Many of the scaffold designs for bone tissue engineering applications in literature are investigated *in vitro*. These models are often studied for specific scale and process and thus, fail to capture complex multiscale processes involved in the bone tissue formation. Also, these models are inadequate to predict the scaffold behavior in *in vivo* conditions. Likewise, *in vivo* models are tested with animal models and therefore, lack translatability to human. In this context, *in silico* modeling technique has emerged as a powerful tool for simulations and prediction of highly complex multiscale processes of scaffold design. An '*in silico*' approach implies any biological experiment performed on the computer or via computer simulations. This approach is based on linking modeling with experiments in a multiscale regime. This technique can bridge the gap between *in vitro* and *in vivo* modeling by simulating the model using *in vitro* parameters in *in vivo* conditions.

In silico approaches are limited and few in literature. The deformation, perfusion, and revascularization of human mesenchymal cells seeded porous β-tricalcium phosphate scaffold was investigated using the *in silico* approach. The deformation and perfusion processes were combined into the computational model, and mechanical forces that acted on the cells due to scaffold-cells interactions, nutrient supply, and cellular glucose consumption were modeled. Additionally, the model was pre-loaded with pro-angiogenic factors such as VEGF-A to induce angiogenesis. The

computational model integrated mechanical, fluid, nutrient, glucose consumption and vascular growth situations in the bone tissue regeneration [1]. A numerical micro-macro model was proposed that predicted the effect of bone regeneration on the evolution of mechanical properties and scaffold microstructure [2]. Similar, multiscale computational techniques were applied to design nonlinear elastic model for soft tissue [3], bone microstructure for scaffold design [4] and scaffold microstructure for tissue engineering [5]. A new atomic-scale finite element method (AFEM) was proposed that combines MD and FE techniques. In this method, the interatomic potential energy functions in MD was represented by the finite elements and computational demands were significantly reduced compared to MD method [6]. In a separate study, they used AFEM to calculate the effect of polymer chain scission on the Young's modulus of the amorphous poly(lactide) structure at the atomic level [7]. The computational models provide a framework for an in-depth understanding of underlying mechanism during complex scaffold design.

2.1.1. Bio and Synthetic Polymers and Nanoscale Additives

Materials selection is the initial and most important step in the fabrication of a bone tissue-engineered scaffold. Hydroxyapatite (HAP) is the main mineral phase in the human bone and thus, widely used for fabrication of tissue-engineered scaffolds. HAP is known for its good osteoconductivity, biocompatibility and high biological affinity to proteins [8-10]. HAP has been used to control the pH in the vicinity of biodegrading PLA-PGA implants [11]. Nano-HAP is also used due its improve cell adhesive properties [12]. The mechanical strength, stoichiometry, and size of HAP can be controlled by changing the synthesis methods of HAP [13-16]. Due to all these properties, HAP is also used as a nanofiller to enhance the properties of nanocomposites [17, 18]. In an earlier study, we have used in situ biomineralized HAP using the amino acid modified nanoclays to enhance the mechanical properties and bone regeneration [19].

Montmorillonite (MMT) is the most commonly used clay mineral, and it demonstrates good biocompatibility and biodegradability I combination with good mechanical properties. Na-MMTclay unit cell consists of two silica tetrahedral layers with a sandwiched alumina octahedral layer. The negative charge is created in the clay sheets due to the isomorphous substitution of Al^{3+} by Mg^{2+} or Fe^{2+} in the octahedral layer. The negatively charged clay sheets are stacked in the crystalline phase by the positive counter cations such as Na^{+} placed between the clay sheets. The MMTclay sheets are up to 1µm in lateral dimension and 1nm in thickness. Nanocomposites using the nano MMT has been The mechanical strength of Gel/MMT-CS nanocomposite scaffold increased with the increase of MMT % in nano-composite from 0% to near 11%. Also, nanocomposite showed highly porous surface within this range [20]. It has been reported that the small amount of MMTclay enhanced the nanomechanical properties of polymer nanocomposites [21]. MMTclay based nanocomposite system was first introduced by the Katti et al. for the bone tissue engineering applications [22]. Further studies have demonstrated the use of nanoclay as a good viable system for bone tissue engineering [23].

Carbon nanotubes showed a wide range of practical applications due to their good mechanical, sensor and medical properties [24]. Biocompatibility studies have enhanced their potential use in biomaterials application [25]. Although lacking superior mechanical properties of synthetic polymers natural polymers are used in tissue engineering due to their improved biological properties. Collagen is widely used as a natural polymer in the fabrication of tissue engineering scaffold because it is a component of extracellular matrices. It shows good biocompatibility. Results of *in vitro* studies as well as in vivo studies showed that addition of collagen in scaffolds supports the regeneration of the articular cartilage tissues [24], cardiovascular tissues [26] as well as other tissues [27]. Naturally derived polymers like collagen are also added to synthetic

biodegradable polymers like PLGA, PGAfor fabricating 3D scaffolds with high mechanical strength, high porosity, and improved biocompatibility. Such hybrid scaffolds also provide suitable surface properties for cell growth, cell proliferation, and cell distribution. A common biopolymer investigated is chitosan. Chitosan (Chi) and polygalactouronic acid (Pga) was used in a polyelectrolyte formulation to produce ChiPga scaffold Polyelectrolyte complex formed due to strong electrostatic interactions between chitosan and PGA. Effects of initial concentration of ChiPga on freeze dried tissue engineer scaffolds were studied. Negative charge ChiPga does not support osteoblasts adhesion. Similar results were also shown in our previous work [28]. Some other natural polymers used in the fabrication of tissue engineering scaffold are gelatin, silk fibroin, and starch.

Synthetic polymers such as poly(lactic acid) (PLA), polycaprolactone (PCL), poly (glycolic acid) and poly(lactic-co-glycolic acid) (PLGA) belong to the class of aliphatic polyesters. Due to the good biodegradability and high molecular weight, these polymers are extensively investigated for bone tissue engineering applications. PLA exists in two optical isomers; D-lactide also referred as PLLA is a semi-crystalline polymer and L-lactide as PLDA is an amorphous polymer [29]. Among two, PLLA is a transparent polymer and have high modulus. On the other hand, PLA has poor thermal stability and is brittle. The PLLA is often used in biodegradation due to its hydrolysis degradation product, which also found in the human body [30, 31]. The addition of MMT nano-sized platelets in PLLA polymer exhibited improvement in mechanical strength and structural integrity of nanocomposite scaffold during biodegradation compared to pristine polymer scaffold [32]. Modified PLLA surface by incorporating HAP particles has been used for tissue engineering applications [33]. PGA is a highly crystalline polymer and has good mechanical properties but exhibits poor solubility in organic solvents due to high crystallinity. Although PGA

has improved hydrolysis based degradation rate compared to PLA, the degradation product of PGA is acidic and therefore, its use in scaffold fabrication is limited [29, 31]. Nanoparticulate HAP/PLGA composite material have also been designed to enhance the natural bone regeneration and sustained drug release [34]. Highly porous and interconnected PGA/β-TCP composite 3D scaffolds were fabricated that improved the osteogenesis, mineralization, and biodegradation during the bone replacement process [35]. PCL is the most extensively used and studied biopolymer in tissue engineering applications. It has low melting point, good solubility, blending, viscoelastic properties, rheological properties and lower degradation rate compared to PLA and PGA [36, 37]. These numerous advantages over other biopolymers make PCL a suitable candidate for bone tissue engineering applications [36, 38-40]. Various techniques to improve the hydrophilicity and biological properties of PCL nanofibrous scaffolds have been applied. An alkaline hydrolysis method has been used to investigate *in vitro* cell adhesion and proliferation study on nerve precursor cells [41].

2.1.2. Polymer Scaffold Manufacturing Methods in Laboratory and Manufacturing Technologies

2.1.2.1. Particulate Leaching

Particulate leaching method was introduced for the fabrication of highly porous scaffolds for tissue engineering applications [42]. Using this technique amount of pores can be controlled, and a highly porous membrane scaffolds can be achieved [43]. Some of the major disadvantages of this method are the use of toxic solvents, poor pore interconnectivity and long processing time (evaporation can take longer time). Over the years, many similar shaping methods which involve compression molding were tested [44-46]. This technique provides high porous scaffolds and higher productivity, but thermal properties of scaffolds degrade due to a high processing

temperature. A novel room temperature injection molding (RTIM/PL) was developed to fabricate three-dimensional PLGA and PCL-based tissue engineered composite scaffolds with high porosity and interconnectivity [47].

2.1.2.2. Freeze Drying

Freeze drying method is widely used to fabricate polymer scaffolds with high porosity and pores interconnectivity. This method is a very inexpensive and only requires basic laboratory equipment. Here, a solution of desired concentration of polymer and solvent (usually organic) is prepared. After that, the solvent is removed by freezing the solution at very low temperature leaving a highly porous scaffold. The pore size of the polymer scaffold can be controlled by adjusting the freezing rate and pH. Freeze drying method also depends on freezing temperature, time period and initial solution concentration [48]. In other studies, very high porosity nanoclay based composite scaffolds with different polymers were fabricated via freeze drying technique [23, 28].

2.1.2.3. Electrospinning

Electrospinning technique is used for fabricating high nanofibrous scaffolds [49, 50]. Some of the advantages of electrospinning are the achievement of high mechanical properties, high surface area to mass ratio and reduction in the use of toxic components in the process. Many studies in the literature have reported improvement in cells adhesion and cell growth due to the large surface area in electrospun nanofiber scaffolds [51-54]. However, due to the size of fibers, it is difficult to achieve large pore sizes in the scaffold. Also, use of polar solvents with high dielectric constant may limit their use as biological material. A novel hybrid electrospinning process to fabricate 3D scaffolds with millimeter scale thickness has been developed. These nano-

/microfibrous scaffolds exhibited very high cell adhesion and cell growth compared to microfibrous scaffolds without nanofibers [55].

2.1.2.4. Textiles Techniques

Textile technologies have a great potential to be used in highly porous fabrics. Fibers have a naturally large surface area to volume ratio which enhances the properties of scaffold materials. Non-woven textiles composed of polymer fibers lack in structural stability that is important to withstand the biomechanical loading. Even though biomechanical loading is a problem with textile based techniques, some of the major techniques used in tissue engineering in bone, cartilage, heart valves, bladder and liver have used non-woven composed textiles. These techniques include but are not limited to PGA, PGA/PDLA, and PGA/PLLA. Since biomechanical loading proves to be quite a bit of challenge, some techniques have been developed to overcome this issue. Fiber bonding techniques were developed to prepare interconnecting fiber networks with different shapes [56]. Alternative methods involve coating a non-bonded mesh of PGA fiber with solutions of PLLA or PLGA [57].

2.1.2.5. Solid free-form (SFF) fabrication

In recent times, there have been a lot of advances in manufacturing technologies. Advanced manufacturing technologies also known as rapid prototyping (RP) or solid freeform fabrication (SFF) technologies are now being explored [58, 59]. With rapid prototyping, one can create a 3D object through repeatedly depositing and processing the material layer by layer. This technology has a wide use in research where we quickly need to see the actual prototype from a computer aided design. This technique has gained importance in the medical domain where patient data from MRI and CT scans is often converted to 3D models and then prototyped. There are several RP methods available such as selective laser sintering, laminated object manufacturing, etc.[60-63].

RP finds extensive use in early verification of product design. Tissue engineering applications require greater control over pore interconnections, microstructure and reproducible morphology which is the subject of current studies using rapid prototyping techniques.

2.1.2.6. Three-dimensional printing

Three-dimensional (3D) printing technology involves making free-form solids by using ink-jet printing a binder into sequential powder layers [64]. The technique involves first obtaining a thin layer of powder on the surface. A computer algorithm then computes the slicing information for the model. A binder is then ejected using ink-jet technology on to the powder where the object is to be formed. This step is repeated until the entire product is fabricated. The packing density of the powder particles plays a very crucial role in the entire process. The aggregation of binder and powder is governed by the mechanical properties of the powder which in turn is effected by the packing density of the powder. These agglomerates of powder and binder can spread to multiple layers, and if such effect is undesirable, the product quality will get reduced. Several studies have been done on the mechanical properties of biomaterials components made using 3D printing. For example, in one study, mechanical properties of PLLA made using 3D printing are reported [65]. The tensile strength for the low molecular weight PLLA (53000) was reported as 17.40±0.71 MPa and for a molecular weight PLLA (312000) as 15.94± 0.71 MPa. Various methods such as cold isostatic printing, variations in binder strength, etc. were used to increase the overall mechanical properties of the product. An indirect three-dimensional printing method is also investigated in which molds were printed with three-dimensional printing and then this mold use for casting the final desired product [66]. PLGA solution was cast into a mold to fabricate tissue engineered scaffolds with uniform and high inter-connected pores [67].

2.1.2.7. Fused deposition modeling

Fused deposition modeling (FDM) is another of the latest advances in manufacturing technology [68, 69]. Similar to three-dimensional printing, this technology also involves layer-by-layer concept of manufacturing. The process takes in data from a CAD model and virtually draws layer-by-layer. The source of the CAD data could be a geometric conceptual model that may be derived from MRI/CT data [70]. The FDM extrusion head moves in X, Y axes while the platform is lowered in the Z-direction. The FDM extrusion head feeds on the thermoplastic polymer filaments which are fed in a temperature controlled fashion. The layer deposition is done ultrathin and direction of heat in very critical for placing the material directly into place. After a layer is completed, the platform is lowered, and another layer is constructed. In this manner, layer-by-layer the entire 3D model is generated. The materials used for FDM have increased in number over the last few years. Biocompatible products with good mechanical properties and interconnectivity of pores with high porosity can be achieved.

2.2. *In Vitro* Mechanical Properties of Scaffolds and Nanocomposites: Computational Methods

2.2.1. Ab Initio

Ab initio calculations also known as first principles method is used to solve Schrödinger equation. This method allows to investigate the structure and materials properties of different materials at the atomistic level [71-73]. Hartree-Fock (HF) and density functional theory (DFT) methods are often used for ab initio calculations to obtain the energy levels. With an appropriate wavefunction, ab initio calculations can be used to investigate various polymers, large macromolecules and minerals including hydroxyapatite (HAP) structure. Hydroxyapatite is a main mineral phase of the bone and critical for the mechanical strength of bone. Thus, it is important to

calculate the electronic structure and lattice parameters of HAP. Also, molecular dynamics (MD) methods that are used for solving complex biological phenomenon such as apatite growth on surface, interactions between protein and HAP, surface ion exchange in simulated body fluid and nucleation of HAP strongly depend on the reliable interatomic potential. In an earlier study, ab initio calculations to derive partial charges, lattice constants, interatomic distances, vibrational spectra and bond parameters of different surfaces of HAP structure have been reported [74]. Similarly, the interatomic potential of the hexagonal structure of HAP was also reported where the geometric parameters such as unit cell size, bond lengths, lattice dynamics and internal coordinates were derived with excellent agreement with the experimental results [75]. Depending on the nature of interacting atoms/molecules, many different force fields have been developed over the years. The derived HAP structures enable further studies of complex biological phenomenon in design of polymer scaffolds for tissue engineering applications.

Similar studies have also been done on natural bone. Human bone is a composite of water, an organic/protein phase and a mineral phase. Ab initio methods have been applied to study the interactions between these phases of the bone. DFT calculations of adsorption of monosaccharides onto HAP showed that the adsorption process depends on crystallographic faces of HAP [76]. Conversely, binding of peptides to HAP also affected by the orientations of the HAP surfaces [77]. In both studies, organic phases preferred (0110) compared to (0001) for the adsorption process, indicating the role of HAP surface in the bone formation. Ab initio modeling of surface interactions between HAP and protein have revealed that the polar proteins (basic and/or acidic side chains) strongly adsorb to the HAP surfaces and the adsorption strength is affected by the type of side chains and the crystal face of HAP surface. The calculations showed hydrogen bonding between

surface oxygen atoms of HAP and strong electrostatic interactions between NH_3^+ protons and strong electrostatic interactions between calcium ions of HAP and COO^- [78-80].

2.2.2. Molecular Modeling

Molecular dynamics (MD) simulation is a useful methodology to determine the molecular structure, dynamics and thermodynamic properties of the system. It allows evaluation of the interactions/relationship between molecular structure and biological function at nanoscale length and time. In this method, classical mechanics is used to predict the trajectory of atoms in terms of positions and velocities over time. MD technique is a step-by-step, numerical solution of the Newton's second law of motion for a set of 'N' number of atoms. The Newton's equation of motion for the system of N atoms can be written as:

$$F_i = m_i a_i = m_i \frac{d^2x}{dt^2} \quad (2.1.)$$

where, m_i is mass, a_i is the acceleration, x_i is a position and F_i is a force exerted on an atom i in the direction of x_i. The force, F_i acting on an atom is obtained from the potential energy function of the system, E(x) as follows:

$$F_i = \frac{dE}{dx_i} \quad (2.2.)$$

Therefore, from equations 2.1. and 2.2., we obtain:

$$\frac{dE}{dx_i} = m_i \frac{d^2x}{dt^2} \quad (2.3.)$$

Further, the potential energy function of the system can be represented in the form of a 'force field'. The force field is set of parameters needed to define the behavior of the atoms and bonds. These parameters are divided into two energy sets (equation 2.1): (a) bonded energy: comprises of the bond, angle, dihedral and torsional energy and (b) non-bonded energy, includes electrostatic and van der Waals energy.

$$E = E_{Bond} + E_{Angle} + E_{Dihedral} + E_{Torsional} + E_{Electrostatic} + E_{van\ der\ Waals} \quad (2.4.)$$

Depending on the nature of interacting atoms/molecules, many different force fields have been developed over the years. One of the widely used force field for protein, large macromolecules, and organic molecules is CHARMm (Chemistry at Harvard Macromolecular Mechanics) [81]. The potential equation of CHARMm force field is as follows:

$$E = \sum_{bond} K_b(b - b_0)^2 + \sum_{angle} K_a(\theta - \theta_0)^2 + \sum_{dihedral} K_\Phi[1 + \cos(n\Phi + \delta)] +$$

$$\sum_{electrostatic} \sum_{i \neq j} \frac{q_i q_j}{r_{ij}} + \sum_{van\ der\ Waals} \sum_{i \neq j} 4\varepsilon_{ij} \left[\left(\frac{\sigma_{ij}}{r_{ij}} \right)^{12} - \left(\frac{\sigma_{ij}}{r_{ij}} \right)^{6} \right] \quad (2.5.)$$

where, K_b is force constant of bonds, K_a is force constant of angles, and K_Φ is force constant of dihedrals and b_0 and θ_0 are equilibrium bond length and bond angle, respectively. The terms n, Φ and δ are the dihedral angles, a multiplicity of dihedral angle and phase angle of the dihedral cosine function. The Lenard-Jones potential parameters are represented as σ_{ij} and ε_{ij}. The distance between atoms is represented by r_{ij} and the partial charges of atoms are denoted as q_i and q_j.

Steered molecular dynamics (SMD) simulation approach is used to determine the binding/unbinding mechanisms of biomaterials and mechanical properties of different molecules [82]. There are two type of SMD techniques: (i) constant force method, where a constant force of the order of picoNewtons (pN) is applied to selected atoms in a given direction and (ii) constant velocity method, in which one end or center of mass of a virtual spring is attached to the molecule, and the other end of the spring is pulled with a constant velocity. The force exerted on the pulling atoms can be calculated from the constant velocity:

$$F = K(x_0 + vt - x) \quad (2.6.)$$

where, K is force constant, v is pulling velocity, x_0 is the initial position and x is the position at time t of the end attached to pulled atom.

MD and SMD simulations have been widely used for investigating the molecular level mechanics in bone. The role of hierarchy [83], mineralization [84], crosslinks densities [85], mineral proximity [86], water [87] and direction of mineral-collagen interactions [88] in the nanomechanics of collagen fibrils were evaluated using SMD simulations. Recently, a MD model of a full length (~300 nm) collagen molecule was built and revealed that the mechanics of collagen is controlled by the three-level helical hierarchy of collagen [89]. In other MD modeling approach, for biomaterials applications, the interactions between HAP surface and biopolymers such a polyacrylic acid, collagen and polycaprolactone in the nanocomposite biomaterials were investigated in detail by Katti's research group [74, 86, 90-93]. The modeling results showed the biomineralization process through the unidentate calcium-bridge between calcium atoms at the bulk HAP surface and carbonyl atoms of the polymer. Further, the effect of HAP mineral-polymer molecular interactions on the mechanical properties of the nanocomposite was analyzed using SMD simulations. The load-deformation behavior of polymer indicated high stiffness in the close proximity of the mineral compared to in the absence of mineral due to the high molecular interactions between the polymer and mineral surface.

MD simulations were also used in evaluating the mechanical properties during the degradation process of the polymers. It was shown that a change in Young's modulus of semi-crystalline biopolymer (similar to poly(glycolic acid) and polyethylene) caused by polymer chain scission using MD [94]. The modeling results indicated two different mechanisms of Young's modulus degradation during the polymer scissions. Below the glass transition temperature, the Young's modulus of the polymer was reduced simultaneously with chain scissions and controlled by the van der Waals interactions between polymer chains. On the other hand, above the glass transition temperature, there was a significant lag between chain scissions and a decrease in

Young's modulus. This delay was attributed to the insufficient scissions of polymer chains and consequently, insignificant entropy change during the deformation of the polymer [95].

2.2.3. Finite Element Methods

The finite element (FE) method is a numerical technique that can be used for finding solutions for complex engineering problems such as structural mechanics, fluid mechanics, electromagnetics and thermal analysis. The complex engineering problem is considered as a continuum mathematical model which consists of differential equations. The differential equations have an infinite number of degrees of freedom, and thus, the analytical solution of the model may not be available. The concept of discretization is employed to limit the number of degrees of freedom and solve the field variables such as pressure, velocity, temperature, and displacement. In the FE method, a model is represented as a collection of a smaller finite number of elements also knows as 'finite elements.' These elements are interconnected with each other at specified finite number of points called 'Nodes' or 'Nodal points.' Since the variation of field variable within the finite element is unknown, an interpolation or shape function is defined in terms of the value of the field variables at the nodes to approximate the variation over the continuum model. The shape function is described as follows:

$$u_i(x) = N_i(x)\tilde{u_i} \qquad (2.7.)$$

where, $u_i(x)$ and $\tilde{u}_i$ are values of field variable at the x and nodes, respectively, and $N_i(x)$ is a shape function. For the FE models with general continuum and structural elements such as truss, plane stress, axisymmetric elements and hexahedral element, the procedure for FE method is as follows:

Step (1) The first step involves dividing the structure or body into the FE with the suitable type, size and a number of elements. The selection of these parameters for FE analysis primarily

depends on the engineering/analyst judgment and how closely the FE model can describe the actual physical behavior of the structure.

Step (2) Next step is to define displacement function within the element in terms of nodal values of the finite element. Then, the displacement function within an element is described as nodal unknowns. This function should satisfy certain requirements so that obtained numerical solution can converge to correct results. For deformation problems, the function is strain and expressed as:

$$\{\varepsilon(x) = [B]\{q\}\} \tag{2.8.}$$

where, [B] is a strain-displacement transformation matrix, ε and {q} are nodal displacement vector and strain vector, respectively. After that, the constitutive relations of a material and geometrical properties is used to relate the stress and strain within the element,

$$\{\sigma(x)\} = [C]\{\varepsilon(x)\} \tag{2.9.}$$

where [C] is the material and geometric properties (elastic) matrix and {σ(x)} is the stress vector.

Step (3) For an element, the displacements of the nodal points are linked to the applied nodal forces and stiffness matrix of element using force equilibrium conditions and is given by:

$$\{f\} = [k]\{q\} \tag{2.10.}$$

where, {f} is a nodal load (force) vector, [k] is an element property (stiffness) matrix and {q} is a nodal displacement vector. The element stiffness matrix can be calculated as:

$$[k] = \int_v [B]^T [\mathrm{C}][\mathrm{B}]\, d\mathrm{V} \tag{2.11.}$$

Then, the nodal equilibrium equation of complete structure is calculated by assembling the element nodal equilibrium equations of each element. The global nodal equilibrium equation can be written as:

$$\{F\} = [K]\{q\} \tag{2.12.}$$

where, {F} is the global nodal force matrix, [K] is the global stiffness matrix of complete structure and {q} is the generalized global nodal displacement matrix.

Step (4) Finally, the boundary conditions are imposed to global equilibrium equations and then are solved for any unknown using numerical methods.

FE modeling is by far the most widely used technique to study the mechanical behavior of all structures and is also used for biomaterial scaffolds. Several FE models have been developed to understand and predict the degradation mechanism in polymer scaffolds under different conditions. Han *in vitro* degradation kinetics model of poly(DL-lactide-*co*-glycolide) scaffolds has been reported [96]. The effect of scaffold porosity under static and fluid flow conditions on degradation rate were predicted from the model and successfully validated by using experimental results. Others have used FE modeling approach to study the hydrolytic degradation and time-dependent behavior of biodegradable polymers [97-99]. The hyperelastic constitutive models as a function of time were proposed, and mechanical properties evolution during the *in vitro* degradation of biodegradable polymers were described. In another study, the time-dependent mechanical behavior of PLA-PCL fiber was simulated by adapting Bergstrom-Boyce viscoplastic model [99]. The success of a scaffold is significantly depended on the compatibility of mechanical properties of the scaffold with its surrounding tissues inside the body. A mismatch between the load bearing strength of replaced scaffold/implant and surrounding tissues during the degradation and tissue formation process will lead to implant failure. Therefore, it is critical to capture the evolution of the biomechanical properties of bone tissue around the replaced scaffold. The Young's modulus and crystallinity of PCL/HA scaffolds were predicted over time during the degradation process using representative volumes (RVs) FE modeling approach. The FEM predicted results showed reasonably good agreement with experimental results [100].

2.3. Design of Nanocomposites and Scaffolds: Computational Approaches

2.3.1. Material Design of PCN using Molecular Modeling

Polymer clay nanocomposite (PCN) is synthesized by adding/dispersing nanoclay particles in polymers. The Toyota research group in 1990's first time used MMT clay with nylone-6 to synthesize nylone-6-clay nanocomposite [106]. Since then, PCN is widely studied to significantly increase the properties of polymers. It has been observed that the addition of small amount of modified clay nanoparticles in polymer matrix improves the thermal, mechanical, liquid/gas barrier properties, biodegradability, and biocompatibility of PCN [22, 107-111]. These modified clay nanoparticles act as reinforcement and polymer as a matrix in the PCN. Based on type of polymers, modifiers and clay minerals; the PCNs are basically of two types: (a) exfoliated PCN in which clay structure is delaminated in the polymer matrix due to individual dispersion of clay layers, and (b) intercalated PCN in which clay interlayer spacing maintains its periodicity and structure of clay expand due to the insertion of polymer into the clay interlayer. Computational methodologies such as molecular modeling have been used to investigate the structure, dynamics and interactions of PCN. This technique allows evaluation of the role of clay, organic modifier and polymer in the enhancement of physical properties of PCN at the molecular level. Tanaka et al. predicted the binding energies for the PCN comprising nylon6,6 resin (polymer) and exfoliated clay layers treated with 12 different ammonium salts (organic modifiers) using molecular dynamics (MD) simulations [112]. The MD results revealed a significant role of the organic modifier volume on the binding energies of the PCN. The binding energy between clay and polymer linearly decreases with increasing volume of the organic modifiers. On the other hand, binding energy between organic modifier and clay, and organic modifier and polymer increases with increasing volume. In separate studies, a similar effect on the binding energies between

polymer, clay and organic modifier due to increasing concentration of organic modifier in PCN [113, 114] was also observed. MD simulations were used to calculate the modulus of PCN indicating good agreement between experimental and predicted results [115]. MD was also used for the ε-caprolactone based PCN to understand the intercalation process of caprolactone into sodium montmorillonite (Na-MMT) clay [116]. The MD simulations of nylon-6 based PCN showed that the length of the polymer chains has no significant effect on the bulk modulus, density and basal spacing of PCN [117]. Using MD simulations, realistic models of organically modified MMT (OMMT) and PCN containing MMT clay, polyamide-6 polymer and organic modifiers was developed [105, 118, 119]. The constructed models were then successfully validated by using minimum energy conformation of the models, XRD and FTIR results of OMMT and PCN. The non-bonded interactions between different constituents of PCN were quantitatively calculated in terms of electrostatic and van der Waals energies, and consequently, the intercalation mechanism, nature and contribution of specific molecular interaction in the molecular system were investigated. The simulations revealed significant attractive non-bonded interactions among clay, polymer and organic modifiers in PCN. It was observed that the final orientation of organic modifiers does not depend on their initial orientation and is flat and parallel with respect to the interlayer clay surface.

The effect of organic modifiers on the crystallinity and nanomechanical properties of PCN was studied by evaluating molecular non-bonded interactions between different constituents. It was found that the backbone and functional groups of the polymer and organic modifiers interact differently in the PCN system, and these molecular interactions control the mechanical properties of PCN. The molecular interactions between functional groups of modifiers and polymer were attractive in nature. On the other hand, interactions between modifiers and polymer backbone were

repulsive. These strong attractive and repulsive interactions resulted in the disruption of polymer conformation in the clay gallery of PCN and appeared to create a “ripple action” in the polymer. Higher the level of “ripple action”, higher the disruption of crystallinity of the polymer. This leads to lower crystallinity and consequently, the higher elastic modulus in PCNs. Furthermore, MD simulations of PCNs indicated that the molecular interactions between intercalated nanoclay and polymer create a localized zone of influence surrounding the clay gallery, and the crystallinity of the polymer is significantly altered inside the zone of influence compared to outside. The AFM phase imaging showed that this influence zone in the PCN exists up to 200-300 Å from the clay surface. Based on these results, the concept of ‘altered phase theory’ in the PCN system was developed. Further, nanoindentation tests and SMD simulations results revealed that the elastic modulus of the polymer in ‘altered phase’ is significantly higher than the bulk unaltered polymer. Further, the molecular structure and interactions between different constituents can be controlled or tailored for the different applications of PCN by using this new molecular modeling approach.

2.3.2. Use of Finite Element Methods for Predictive Capabilities of Scaffold Properties

One of the major challenges in the optimized design of scaffold is to maintain a strength-porosity relationship comparable to the damaged tissue/organ. The high porosity facilitates the cell migration and increases the permeability, however, this also leads to decrease in mechanical strength of scaffolds. Similarly, increase in mechanical strength at the expense of porosity might inhibit the tissue growth and biological performance of the scaffolds. Therefore, it is important to optimize these material parameters in scaffolds for successful tissue engineering applications.

The concept of combined use of micro-computed tomography (μCT) and FE modeling also known as μCT-FE modeling has emerged as a powerful tool for design optimization and mechanical behavior prediction of scaffolds [121]. This technique has been used to optimize the

design of porous scaffolds for tissue engineering applications[122]. It was concluded that the non-regular porosity distribution within the scaffolds significantly affects the mechanical stimuli experienced by seeded cells. The μCT-FE modeling technique applied by Lacroix et al. to study the relationship between mechanical properties and porosity of highly porous scaffolds of calcium phosphate (CaP)-based bone cement and glass ceramic materials. The FE simulations predict a linear relationship between effective Young's modulus and scaffold porosity. The strain distributions in scaffolds showed tension in many parts of struts linking pores during the FE compressive loading of scaffolds. The areas of stress concentrations were observed owing to the non-uniformity of the scaffolds architecture[122]. In another study, the μCT-FE modeling approach was used to predict the mechanical stimuli behavior in the CaP based scaffolds [123]. The 3D mesh models were developed for fluid flow distribution analysis within the pores of the scaffolds. The FE simulation results showed that wide range of pore size has influenced the fluid pressure, fluid shear stress and fluid velocity in the scaffolds. The mechanical stimuli caused by interstitial fluid flow within the internal walls of scaffolds sensed by the cells during the migration process and thus affected the cell attachment, cell differentiation and subsequently, bone formation in the scaffolds [123]**.** Similarly, micro-CT images were employed to create 3D high-resolution FE models of implanted interconnected porous hydroxyapatite (IPHA) and time-dependent changes of mechanical properties of IPHA was estimated. The FE analysis revealed that the in vivo biomechanical changes in IPHA are strongly influenced by the bone ingrowth. The increase in predicted elastic modulus with bone mineral density and evolution of strain energy density (SED) distribution over the period of time provided the insight into the mechanobiological mechanisms of porous ceramic scaffolds [124].

Computer-aided fabrications methods such as solid free-form (SFF) techniques allow a detailed control over the microstructure, porosity, pore interconnectivity and pore size in the design of tissue engineering scaffolds [58, 59, 125]. The high degree of control and layer-by-layer additive process in SFF technique also enables the design of anisotropic and heterogeneous scaffolds that can match the mechanical properties of bone defects. These factors significantly influence the internal and external architecture of scaffolds and subsequently, the cell proliferation, flow of nutrients, tissue growth and mechanical properties of scaffolds. Therefore, it is critical to understand and predict the mechanical behavior in designing a complex multilayer structure and highly porous scaffold for tissue engineering applications. In recent years, FE methods have been employed to investigate and predict the mechanical behavior and optimization of scaffolds. The FE method was used to predict the fracture modes of robocast hydroxyapatite and β-tricalcium phosphate (TCP) 3D scaffolds [126]. The prototype structures of the 3D tetragonal lattice of interpenetrating rods of HAP or β-TCP were subjected to different loading conditions for compression, tension and shear testing. The fracture strength of scaffolds was evaluated and successfully validated with experimental compression tests. The predicted FE modeling results showed the critical locations of stresses acting on the scaffolds and thereby further optimization of design and mechanical performance of scaffolds [126]. The potential use of FE methods to analyze the mechanical performance of SLS fabricated PA and PCL scaffolds was also shown [127]. The FE predicted, and experimental results showed that the micro defects such as micropores and surface roughness present within the scaffold struts can have a significant effect on the mechanical properties of scaffolds. Thus, these features should be taken into account to design scaffolds with suitable and desirable pore size and strut thickness [127]. Recently, geometrical parameters of an open-porous titanium scaffold were systematically optimized using FE modeling to match the

mechanical properties of cortical bone [128]. In another FE analysis study, the micromechanical model was developed to predict the reinforcement effect of HAP loading on the mechanical properties of PCL-HAP composite scaffolds. The FE predicted, and experimental compressive tests results showed good agreement [129].

2.4. Degradation of Polymers Scaffolds

2.4.1. Degradation of Scaffolds in Accelerated Degradation Conditions

Synthetic linear polyesters such as polyglycolic acid (PGA), polycaprolactone (PCL), polylactic acid (PLA) and their copolymers have been commonly used in tissue engineering applications due to their wide range of mechanical properties and biodegradation rates. Their degradation in aqueous and accelerated conditions involve cleavage of chain bonds of polymers and result in degradation products that are present in metabolic pathways of the body. Degradation studies of polymer and nanocomposite biomaterials are usually performed in *in vitro* or in vivo conditions [39]. The *in vitro* experiments are generally carried out under aqueous, accelerated (basic medium), different physiological conditions or with different kinds of cell lines. In the case of PCL, it degrades in two phases; initially, the ester groups in the PCL chains undergo hydrolytic cleavage for a long time, followed by loss of polymer due to its low molecular weight and high crystallinity, thus, loss of molecular weight and mechanical strength of the polymers [101].

Further, modified MMTclay nanoparticles with quaternary ammonium salts and nanoparticles of fumed silica enhance the degradation rate via aminolysis and hydrolysis of the polymer. On the other hand, unmodified MMTclay nanoparticles and carbon nanotubes reduce the thermal degradation of polymers due to shielding effect [102]. The rate of hydrolytic degradation in polymer composite scaffolds can be accelerated by using alkaline conditions during degradation studies. In a recent hydrolytic degradation study of PCL/in situ HAPclay composite scaffolds

under alkaline conditions (0.1M NaOH), a significant increase in weight loss from 7 (<2%) to 18 (>12%) days of degradation was observed. However, the overall structure of composite scaffolds remained intact during the degradation period, indicating the surface degradation pathway in the scaffolds [23]. The degradation of porous PLGA based scaffold in distilled water (dH_2O), phosphate buffered saline (PBS) solution, and human promyelocytic leukemia cells (HL-60) was investigated [103]. In this study, under the wet condition, the porosity and pore size of the scaffolds decreased in all degradation medium. However, the mechanical properties of scaffolds were affected differently with different degradation medium. It was observed that the Young's modulus of scaffold increased in HL-60 cells and decreased in dH_2O and PBS medium. Other studies have compared the *in vitro* degradation of PCL-based scaffolds under alkaline accelerated and simulated physiological conditions [104]. The results revealed that under accelerated conditions scaffolds degrade via surface degradation pathway and bulk degradation pathway under long-term physiological conditions.

Thus, although the *in vitro* degradation studies of polymers are performed to mimic the clinical situation of the body; however, it is observed that the in vivo degradation exhibits faster degradation process compared to *in vitro* conditions. This may be owing to the complex dynamic processes such as enzymatic degradation, the autocatalytic effect due to the accumulation of acidic products near implants, phagocytosis, reactive species generated by inflammatory cells during in vivo degradation compared to *in vitro* degradation. Collectively, the *in vitro* and in vivo degradation studies of polymer based composite scaffolds demonstrate that the degradation mechanisms depend significantly on the degradation medium and thus, the medium selection is critical while replicating actual environment that would be experienced by scaffolds.

2.4.2. Degradation of Scaffolds in Cell Culture Media

Generally, the mechanical properties of degraded scaffolds are measured in the dry state and room temperature, however, such conditions are different than the actual body conditions where scaffolds are to be implanted. Hence, it is important to understand the degradation mechanical properties under "wet-state" (tissue fluid and 37 ^{0}C). The compressive modulus and compressive strength at 10% strain decrease by 10-35% and 10-25%, respectively under the simulated "wet" physiological environment as compared with the usual "dry/25°C" condition [130]. In addition to material degradation, one must also consider the effect of cell culture media and cell viability on the *in vitro* biodegradability of scaffolds. Scaffolds materials such as calcium alginate hydrogel have shown different degradation behavior in the cell culture media as compared to water. This is attributed to the exposure of phosphate ions and monovalent cations (present in cell culture media) dissipating the cross-linked calcium ions in alginate hydrogels. Hunt at al. investigated the effect of cell encapsulation on the alginate hydrogel degradation (28 days). The mechanical properties of degraded encapsulating hydrogels significantly decreased in first seven days due to the high release of calcium ions in the early stages of culture. The rate of degradation of alginate slowed down after seven days, and this was attributed to the proliferation of cells and secretion of ECM due to the release of encapsulated cells with the alginate degradation [131]. In another study, cell seeded PCL based scaffolds showed lower degradation and thus, no significant change in mechanical properties compared to scaffolds without cells. This may be due to the deposition of cell-secreted ECM molecules in the cell-seeded scaffolds, which was not present in the acellular scaffolds. The new tissue regeneration initiated by seeded cells may have compensated the reduction in mechanical properties owing to the degradation [132]. Similar improvement in mechanical properties of cell-seeded polymer scaffolds due to the deposition of

new ECM molecules was reported recently [133]. The hOB cells are known to play an important role in the initiation of mineralization and ECM synthesis. The ECM matrix in turn aid the bone nodule formation. A 28 days study of hOB cells viability on the PCL/in situ HAPclay scaffolds in culture media showed significant growth in cells proliferation. The increase in mechanical properties of seeded scaffolds over cell culture time is found to be similar to the increase in cell proliferation. This indicated the possible contribution of the hOB cells growth in the mechanical properties of HOB seeded PCL/in situ HAPclay scaffolds.

2.4.3. Modeling Degradation of Scaffolds

Considerable efforts have been made recent years use computational modeling techniques to predict the mechanical behavior of polymer composite scaffolds during degradation over the period of time. Hydrolysis process is the most common degradation mechanism in polymer biomaterials [134]. During the degradation of the polymer via hydrolysis process, long chains in the bulk of polymer react with water molecules and subsequently break into shorter chains (oligomers). The cleaving of chains into smaller chains decreases the molecular weight of a polymer and successively its mechanical properties. Several mathematical models of scissions of polymer chains due to hydrolysis reaction have been reported to predict the evolution in molecular weight and mechanical properties of biodegradable polymers. Comprehensive coverage on degradation modeling of biodegradable polymers and composites is presented in a recent new book [135]. The authors have summarized mathematical degradation models incorporating rate of chain scission in the amorphous and semi-crystalline phase of the polymer. The numerical equations were further extended by considering crystallinity and diffusion of short chains during the degradation process. Molecular scale models of bioresorbable polymer were simulated to understand the changes in mechanical properties during degradation due to polymer chain scission.

In another study, FE method was used to demonstrate the use of mathematical equations for polymer chain scission during hydrolysis degradation of the amorphous polymer. The results revealed the effect of pore size and porosity of scaffolds on the degradation rate [136].

2.5. Multiscale *In Silico* Strategies for Scaffolds Design

Human bone is a hierarchical composite that consists of mineral and organic phases linked to each other at different length of the scale. The structural hierarchy promotes and controls biological functions and biomechanical properties of bone at each scale. The hierarchical design allows the bone to sustain different mechanical loads by distributing stresses to different levels of bone structure. However, designing a hierarchical tissue engineered polymer scaffold with desirable mechanical properties is a complex process. In this context, multiscale modeling strategies are used to understand and predict the scaffolds mechanics at the different level of the hierarchy. Significant improvement in computational resources and modeling software in last two decades have allowed simulation of complex and large scaffold structures for bone tissue engineering applications. Several different multiscale techniques were studied.

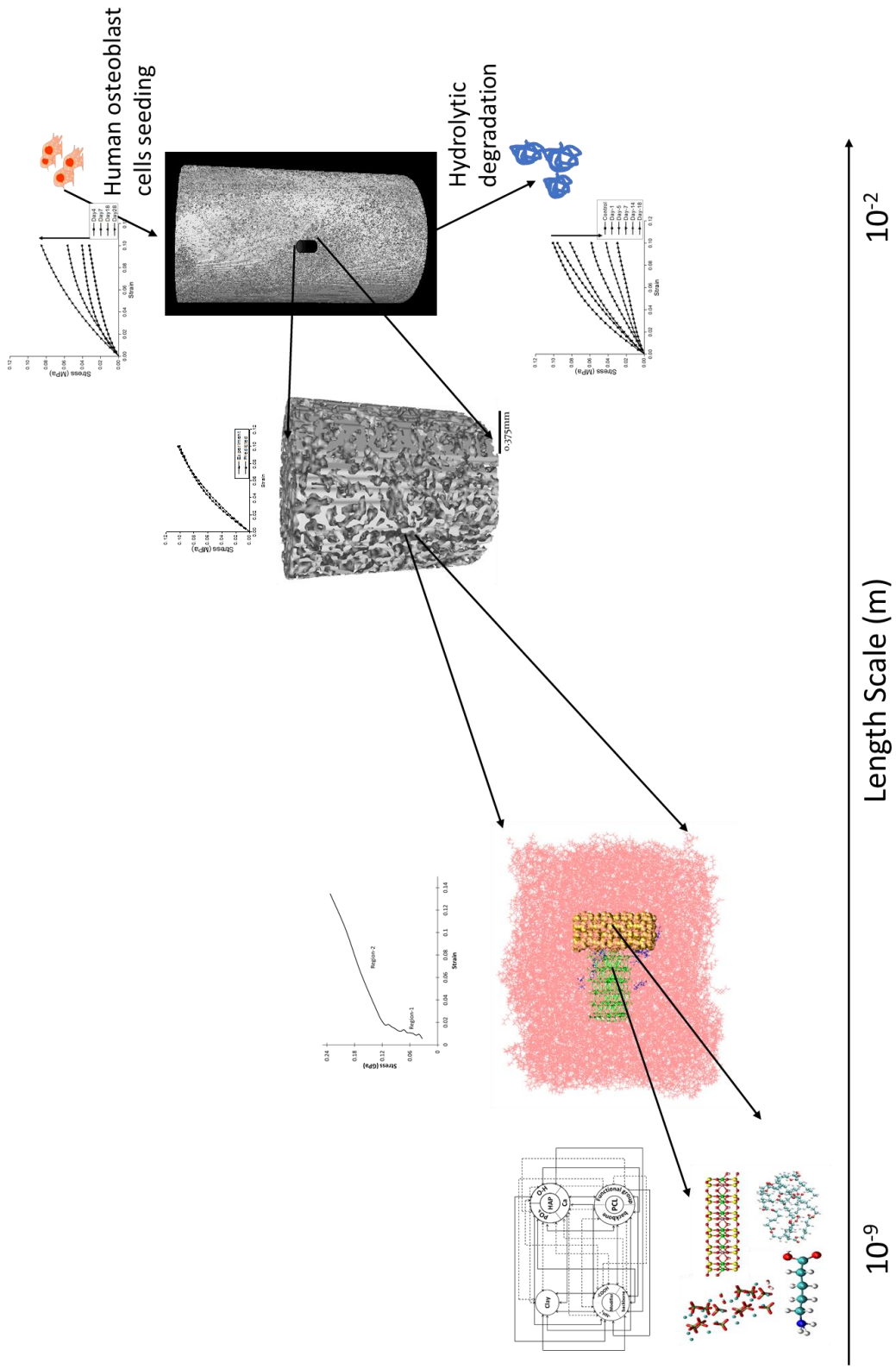

Figure 2.1. Multiscale and multi-process schematic of PCL/in situ HAPclay scaffold.

Most of the multiscale mechanics models use specific mechanical properties such as Young's modulus to capture mechanical behavior evolution of biological materials and biomaterials. However, these models are often failed to simulate the hierarchically organized and highly complex structure of these materials system and therefore, need the entire stress-strain material response [137]. In this work, a truly multiscale biomechanics methodology is presented to predict the evolution of mechanical properties of biomaterials. The mechanical properties at molecular scale are used as material parameters for multiscale modeling of polymer scaffolds. Here, a multiscale model of PCl/in situ HAPclay scaffold is developed for bone tissue engineering and summarized in Fig 2.1.

Several attempts have been made to use *in silico* methods for designing the scaffolds and predicting the biomechanical and biochemical properties for bone tissue engineering applications. Recently a multiscale *in silico* perfusion bioreactor to investigate the influence of stresses and flow properties in the pores of the porous polymer scaffold has been developed. The proposed model incorporated the dynamics of the different species involved during the growth of bone tissues in the scaffold [138]. An integrative model approach was developed to investigate the biological processes of in vivo bone formation in the CaP scaffolds. The multiscale modeling results were further used to design the optimal cell-customized CaP scaffold for enhancing the bone tissue regeneration [139]. Recently, an integrative *in silico* approach to predict the mechanical properties evolution in PCL/in situ HAPclay scaffold during degradation and tissue regeneration for critical size bone defects is also developed. The developed multiscale mechanics model captured the microstructure and time-dependent mechanical behavior of scaffold at multiscale level [133].

In silico modeling techniques combine mathematics with biology and offer potential solutions for designing scaffolds with desirable properties for bone tissue engineering applications.

However, the complexity of the processes and limitations of computational resources only allow addressing the problems in separation (length-time scale, biological-mechanical-physical-chemical process) and not fully coupled as true biological processes are. This makes it extremely challenging to model the tissue formation and its impact on the design of scaffolds in its entirety. Therefore, there is a tremendous opportunity for designing biomaterials using efficient and reliable multiscale methodologies, which can provide reliable predictions and an in-depth understanding of materials structure/ property relationship in scaffolds for bone tissue engineering applications. There is also interest and need to develop multiscale physics of the biological processes. Synergy between the physical and biological sciences with advanced engineering and computational technologies could overcome the current limitations in modeling coupled biological phenomena. Another goal of *in silico* modeling is to provide solutions for patient specific problems in tissue engineering. In the future, this technique has tremendous potential to replace *in vitro* techniques by reducing the laboratory testing cost and time, reducing animal testing, and enable further improvement of biological substitutions for regenerative medicine. Availability of massively parallel computing capabilities makes the multiscale *in silico* approach a real possibility for advancing biomaterials design in tissue engineering for various regenerative medicine applications.

2.6. References

[1] A. Kalig, J. Hansmann, F. Groeber, Curr Anal Chem 9 (2013) 16-28.

[2] J.A. Sanz-Herrera, J.M. García-Aznar, M. Doblaré, Computer Methods in Applied Mechanics and Engineering 197 (2008) 3092-3107.

[3] S.J. Hollister, C.G. Jeong, J.J. Schwiedrzik, A.G. Mitsak, H. Kang, F. Migneco, Nonlinear Elastic Scaffold Design, Modeling and Fabrication for Soft Tissue Engineering, Advances on Modeling in Tissue Engineering, Springer, (2011), pp. 35-53.

[4] Y. Holdstein, L. Podshivalov, A. Fischer, Geometric modeling and analysis of bone micro–structures as a base for scaffold design, Advances on Modeling in Tissue Engineering, Springer, (2011), pp. 91-109.

[5] H.C. Rodrigues, P.G. Coelho, P.R. Fernandes, Multiscale Modelling of Bone Tissue–Remodelling and Application to Scaffold Design, Advances on Modeling in Tissue Engineering, Springer, (2011), pp. 15-33.

[6] A. Gleadall, J. Pan, L. Ding, M.-A. Kruft, D. Curcó, Journal of the mechanical behavior of biomedical materials 51 (2015) 409-420.

[7] A. Gleadall, J. Pan, M.-A. Kruft, Journal of the mechanical behavior of biomedical materials 51 (2015) 237-247.

[8] H. Wang, Y. Li, Y. Zuo, J. Li, S. Ma, L. Cheng, Biomaterials 28 (2007) 3338-3348.

[9] X. Li, L. Wang, Y. Fan, Q. Feng, F.Z. Cui, F. Watari, Journal of Biomedical Materials Research Part A 101 (2013) 2424-2435.

[10] J. Ong, M. Appleford, S. Oh, Y. Yang, W.-H. Chen, J. Bumgardner, W. Haggard, Jom 58 (2006) 67-69.

[11] C.M. Agrawal, K.A. Athanasiou, Journal of biomedical materials research 38 (1997) 105-114.

[12] H.J. Lee, S.E. Kim, H.W. Choi, C.W. Kim, K.J. Kim, S.C. Lee, European polymer journal 43 (2007) 1602-1608.

[13] D.-M. Liu, Ceramics International 23 (1997) 135-139.

[14] S. Pramanik, A.K. Agarwal, K. Rai, A. Garg, Ceramics International 33 (2007) 419-426.

[15] E. Charriere, J. Lemaitre, P. Zysset, Biomaterials 24 (2003) 809-817.

[16] Y. Daniels, S.D. Alexandratos, Waste and Biomass Valorization 1 (2010) 157-162.

[17] F.G. Lyons, J.P. Gleeson, S. Partap, K. Coghlan, F.J. O'Brien, Clinical Orthopaedics and Related Research® 472 (2014) 1318-1328.

[18] R. Khanna, K.S. Katti, D.R. Katti, Journal of engineering mechanics 135 (2009) 468-478.

[19] A. Ambre, K.S. Katti, D.R. Katti, Materials Science and Engineering: C 31 (2011) 1017-1029.

[20] F. Zhao, Y. Yin, W.W. Lu, J.C. Leong, W. Zhang, J. Zhang, M. Zhang, K. Yao, Biomaterials 23 (2002) 3227-3234.

[21] D. Sikdar, D. Katti, K. Katti, B. Mohanty, Journal of applied polymer science 105 (2007) 790-802.

[22] S.K.a.D.R.K.a.R.D. Kalpana, Biomedical Materials 3 (2008) 034122.

[23] A.H. Ambre, D.R. Katti, K.S. Katti, Journal of Biomedical Materials Research Part A 103 (2015) 2077-2101.

[24] S. Balaji, R. Kumar, R. Sripriya, U. Rao, A. Mandal, P. Kakkar, P.N. Reddy, P.K. Sehgal, Polymers for Advanced Technologies 23 (2012) 500-507.

[25] S.K. Smart, A.I. Cassady, G.Q. Lu, D.J. Martin, Carbon 44 (2006) 1034-1047.

[26] C. Shi, Q. Li, Y. Zhao, W. Chen, B. Chen, Z. Xiao, H. Lin, L. Nie, D. Wang, J. Dai, Biomaterials 32 (2011) 2508-2515.

[27] W. Dai, N. Kawazoe, X. Lin, J. Dong, G. Chen, Biomaterials 31 (2010) 2141-2152.

[28] A.H. Ambre, K.S. Katti, D.R. Katti, Journal of Nanotechnology in Engineering and Medicine 1 (2010) 031013.

[29] I. Vroman, L. Tighzert, Materials 2 (2009) 307-344.

[30] C. Agrawal, R.B. Ray, Journal of biomedical materials research 55 (2001) 141-150.

[31] B.D. Ulery, L.S. Nair, C.T. Laurencin, Journal of polymer science Part B: polymer physics 49 (2011) 832-864.

[32] Y.H. Lee, J.H. Lee, I.-G. An, C. Kim, D.S. Lee, Y.K. Lee, J.-D. Nam, Biomaterials 26 (2005) 3165-3172.

[33] N.D. Luong, I.-S. Moon, D.S. Lee, Y.-K. Lee, J.-D. Nam, Materials Science and Engineering: C 28 (2008) 1242-1249.

[34] N. Ignjatović, V. Uskoković, Z. Ajduković, D. Uskoković, Materials Science and Engineering: C 33 (2013) 943-950.

[35] H. Cao, N. Kuboyama, Bone 46 (2010) 386-395.

[36] T.K. Dash, V.B. Konkimalla, Journal of Controlled Release 158 (2012) 15-33.

[37] M.A. Woodruff, D.W. Hutmacher, Progress in Polymer Science 35 (2010) 1217-1256.

[38] G. Nitya, G.T. Nair, U. Mony, K.P. Chennazhi, S.V. Nair, Journal of Materials Science: Materials in Medicine 23 (2012) 1749-1761.

[39] A. Yeo, B. Rai, E. Sju, J. Cheong, S. Teoh, Journal of Biomedical Materials Research Part A 84 (2008) 208-218.

[40] F. Yahiaoui, F. Benhacine, H. Ferfera-Harrar, A. Habi, A. Hadj-Hamou, Y. Grohens, Polymer Bulletin (2014) 1-20.

[41] L. Ghasemi-Mobarakeh, M.P. Prabhakaran, M. Morshed, M.H. Nasr-Esfahani, S. Ramakrishna, Materials Science and Engineering: C 30 (2010) 1129-1136.

[42] A.G. Mikos, A.J. Thorsen, L.A. Czerwonka, Y. Bao, R. Langer, D.N. Winslow, J.P. Vacanti, Polymer 35 (1994) 1068-1077.

[43] I. Engelberg, J. Kohn, Biomaterials 12 (1991) 292-304.

[44] R.C. Thomson, M.J. Yaszemski, J.M. Powers, A.G. Mikos, Journal of Biomaterials Science, Polymer Edition 7 (1996) 23-38.

[45] R.C. Thomson, M.J. Yaszemski, J.M. Powers, A.G. Mikos, Biomaterials 19 (1998) 1935-1943.

[46] L. Wu, H. Zhang, J. Zhang, J. Ding, Tissue engineering 11 (2005) 1105-1114.

[47] L. Wu, D. Jing, J. Ding, Biomaterials 27 (2006) 185-191.

[48] D. Verma, K.S. Katti, D.R. Katti, Materials Science and Engineering: C 29 (2009) 2079-2084.

[49] M. Ngiam, S. Liao, A.J. Patil, Z. Cheng, C.K. Chan, S. Ramakrishna, Bone 45 (2009) 4-16.

[50] J. Venugopal, S. Ramakrishna, Applied biochemistry and biotechnology 125 (2005) 147-157.

[51] Z. Zhou, X.-F. Wu, H. Fong, Applied Physics Letters 100 (2012) 023115.

[52] A.K. Gaharwar, S. Mukundan, E. Karaca, A. Dolatshahi-Pirouz, A. Patel, K. Rangarajan, S.M. Mihaila, G. Iviglia, H. Zhang, A. Khademhosseini, Tissue Engineering Part A 20 (2014) 2088-2101.

[53] W.J. Li, C.T. Laurencin, E.J. Caterson, R.S. Tuan, F.K. Ko, Journal of biomedical materials research 60 (2002) 613-621.

[54] T.J. Sill, H.A. von Recum, Biomaterials 29 (2008) 1989-2006.

[55] A.G. Mikos, G. Sarakinos, S.M. Leite, J.P. Vacant, R. Langer, Biomaterials 14 (1993) 323-330.

[57] D.J. Mooney, D.F. Baldwin, N.P. Suh, J.P. Vacanti, R. Langer, Biomaterials 17 (1996) 1417-1422.

[58] K. Leong, C. Cheah, C. Chua, Biomaterials 24 (2003) 2363-2378.

[59] E. Sachlos, J. Czernuszka, Eur Cell Mater 5 (2003) 39-40.

[60] S. Lohfeld, S. Cahill, H. Doyle, P. McHugh, Journal of Materials Science: Materials in Medicine 26 (2015) 1-12.

[61] J.M. Williams, A. Adewunmi, R.M. Schek, C.L. Flanagan, P.H. Krebsbach, S.E. Feinberg, S.J. Hollister, S. Das, Biomaterials 26 (2005) 4817-4827.

[62] L.G. Cima, M.J. Cima, Computer aided design; stereolithography, selective laser sintering, three-dimensional printing, Google Patents, 1996.

[63] K. Tan, C. Chua, K. Leong, C. Cheah, P. Cheang, M.A. Bakar, S. Cha, Biomaterials 24 (2003) 3115-3123.

[64] B.M. Wu, S.W. Borland, R.A. Giordano, L.G. Cima, E.M. Sachs, M.J. Cima, Journal of Controlled Release 40 (1996) 77-87.

[65] R.A. Giordano, B.M. Wu, S.W. Borland, L.G. Cima, E.M. Sachs, M.J. Cima, Journal of Biomaterials Science, Polymer Edition 8 (1997) 63-75.

[66] M. Lee, J.C. Dunn, B.M. Wu, Biomaterials 26 (2005) 4281-4289.

[67] S.S. Kim, H. Utsunomiya, J.A. Koski, B.M. Wu, M.J. Cima, J. Sohn, K. Mukai, L.G. Griffith, J.P. Vacanti, Annals of surgery 228 (1998) 8.

[68] I. Zein, D.W. Hutmacher, K.C. Tan, S.H. Teoh, Biomaterials 23 (2002) 1169-1185.

[69] D.W. Hutmacher, T. Schantz, I. Zein, K.W. Ng, S.H. Teoh, K.C. Tan, Journal of biomedical materials research 55 (2001) 203-216.

[70] B. Tellis, J. Szivek, C. Bliss, D. Margolis, R. Vaidyanathan, P. Calvert, Materials Science and Engineering: C 28 (2008) 171-178.

[71] J.K. Christie, R.I. Ainsworth, N.H. de Leeuw, Biomaterials 35 (2014) 6164-6171.

[72] D.K. Dubey, V. Tomar, Journal of Engineering Materials and Technology 135 (2013) 021015.

[73] F. Ren, Y. Leng, R. Xin, X. Ge, Acta Biomaterialia 6 (2010) 2787-2796.

[74] R. Bhowmik, K.S. Katti, D. Katti, Polymer 48 (2007) 664-674.

[75] A. Pedone, M. Corno, B. Civalleri, G. Malavasi, M.C. Menziani, U. Segre, P. Ugliengo, Journal of Materials Chemistry 17 (2007) 2061-2068.

[76] I. Streeter, N.H. de Leeuw, Binding of glycosaminoglycan saccharides to hydroxyapatite surfaces: a density functional theory study, Proceedings of the Royal Society of London A: Mathematical, Physical and Engineering Sciences, The Royal Society, 2011, p. rspa20100559.

[77] N. Almora-Barrios, N.H. de Leeuw, Langmuir 26 (2010) 14535-14542.

[78] A. Rimola, M. Corno, C.M. Zicovich-Wilson, P. Ugliengo, Journal of the American Chemical Society 130 (2008) 16181-16183.

[79] A. Rimola, M. Corno, C.M. Zicovich-Wilson, P. Ugliengo, Physical Chemistry Chemical Physics 11 (2009) 9005-9007.

[80] A. Rimola, M. Corno, J. Garza, P. Ugliengo, Phil. Trans. R. Soc. A 370 (2012) 1478-1498.

[81] B.R. Brooks, R.E. Bruccoleri, B.D. Olafson, D.J. States, S. Swaminathan, M. Karplus, Journal of Computational Chemistry 4 (1983) 187-217.

[82] B. Israelewitz, M. Gao, K. Schulten, Current opinion in structural biology 11 (2001) 224-230.

[83] A. Gautieri, S. Vesentini, A. Redaelli, M.J. Buehler, Nano letters 11 (2011) 757-766.

[84] M.J. Buehler, Nanotechnology 18 (2007) 295102.

[85] M.J. Buehler, Journal of the mechanical behavior of biomedical materials 1 (2008) 59-67.

[86] R. Bhowmik, K.S. Katti, D.R. Katti, Journal of engineering mechanics 135 (2009) 413-421.

[87] R. Bhowmik, K.S. Katti, D.R. Katti, Journal of Materials Science 42 (2007) 8795-8803.

[88] D.R. Katti, S.M. Pradhan, K.S. Katti, Journal of Biomechanics 43 (2010) 1723-1730.

[89] S.M. Pradhan, K.S. Katti, D.R. Katti, Biomacromolecules 13 (2012) 2562-2569.

[90] P. Ghosh, D.R. Katti, K.S. Katti, Biomacromolecules 8 (2007) 851-856.

[91] R. Bhowmik, K.S. Katti, D. Verma, D.R. Katti, Materials Science and Engineering: C 27 (2007) 352-371.

[92] R. Bhowmik, K.S. Katti, D.R. Katti, International Journal of Nanotechnology 6 (2009) 511-529.

[93] P. Ghosh, D.R. Katti, K.S. Katti, Journal of Nanomaterials 2008 (2008).

[94] L. Ding, R.L. Davidchack, J. Pan, Journal of the mechanical behavior of biomedical materials 5 (2012) 224-230.

[95] Y. Wang, X. Han, J. Pan, C. Sinka, Journal of the mechanical behavior of biomedical materials 3 (2010) 14-21.

[96] M.K. Heljak, W. Swieszkowski, K.J. Kurzydlowski, Journal of Applied Polymer Science 131 (2014).

[97] A.C. Vieira, J.C. Vieira, J.M. Ferra, F.D. Magalhães, R.M. Guedes, A.T. Marques, Journal of the Mechanical Behavior of Biomedical Materials 4 (2011) 451-460.

[98] A. Vieira, A. Marques, R. Guedes, V. Tita, Procedia Engineering 10 (2011) 1597-1602.

[99] A.C. Vieira, R.M. Guedes, V. Tita, International Journal of Solids and Structures 51 (2014) 1164-1174.

[100] N. Bawolin, M. Li, X. Chen, W. Zhang, Journal of biomechanical engineering 132 (2010) 111001.

[101] Woodward SC, Brewer P, Moatamed F, Schindler A, Pitt C. Journal of biomedical materials research (1985);19:437.

[102] Chrissafis K, Antoniadis G, Paraskevopoulos K, Vassiliou A, Bikiaris D. Composites science and technology (2007);67:2165.

[103] Perron JK, Naguib HE, Daka J, Chawla A, Wilkins R. Journal of Biomedical Materials Research Part B: Applied Biomaterials (2009);91B:876.

[104] Lam CX, Savalani MM, Teoh S-H, Hutmacher DW. Biomedical materials 2008;3:034108.

[105] Sikdar D, Katti DR, Katti KS, Bhowmik R. Polymer (2006);47:5196.

[106] Okada A, Kawasumi M, Usuki A, Kojima Y, Kurauchi T, Kamigaito O, Schaefer D, Mark J. Polymer based molecular composites. MRS symposium proceedings, vol. 171, 1990. p.45.

[107] Gupta N, Lin TC, Shapiro M. JOM (2007);59:61.

[108] Picard E, Vermogen A, Gérard JF, Espuche E. Journal of Membrane Science (2007);292:133.

[109] Mieszawska AJ, Llamas JG, Vaiana CA, Kadakia MP, Naik RR, Kaplan DL. Acta Biomaterialia (2011);7:3036.

[110] Maiti P, Batt CA, Giannelis EP. Biomacromolecules (2007);8:3393.

[111] Yano K, Usuki A, Okada A, Kurauchi T, Kamigaito O. Journal of Polymer Science Part A: Polymer Chemistry (1993);31:2493.

[112] Tanaka G, Goettler LA. Polymer (2002);43:541.

[113] Fermeglia M, Ferrone M, Pricl S. Fluid Phase Equilibria (2003);212:315.

[114] Fermeglia M, Ferrone M, Pricl S. Molecular Simulation (2004);30:289.

[115] Luo J-J, Daniel IM. Composites science and technology (2003);63:1607.

[116] Gaudel-Siri A, Brocorens P, Siri D, Gardebien F, Brédas J-L, Lazzaroni R. Langmuir (2003);19:8287.

[117] Anoukou K, Zaoui A, Zaïri F, Naït-Abdelaziz M, Gloaguen JM. Computational Materials Science (2013);77:417.

[118] Katti KS, Sikdar D, Katti DR, Ghosh P, Verma D. Polymer (2006);47:403.

[119] Sikdar D, Katti DR, Katti KS. Langmuir (2006);22:7738.

[120] Sikdar D, Pradhan SM, Katti DR, Katti KS, Mohanty B. Langmuir (2008);24:5599.

[121] Jaecques SVN, Van Oosterwyck H, Muraru L, Van Cleynenbreugel T, De Smet E, Wevers M, Naert I, Vander Sloten J. Biomaterials (2004);25:1683.

[122] Lacroix D, Chateau A, Ginebra M-P, Planell JA. Biomaterials (2006);27:5326.

[123] Sandino C, Planell J, Lacroix D. Journal of biomechanics (2008);41:1005.

[124] Ren L-M, Arahira T, Todo M, Yoshikawa H, Myoui A. Journal of Materials Science: Materials in Medicine (2012);23:463.

[125] Danforth SC, Agarwala M, Bandyopadghyay A, Langrana N, Jamalabad VR, Safari A, Van Weeren R. Solid freeform fabrication methods. Google Patents,(1998).

[126] Miranda P, Pajares A, Guiberteau F. Acta biomaterialia (2008);4:1715.

[127] Cahill S, Lohfeld S, McHugh P. Journal of Materials Science: Materials in Medicine (2009);20:1255.

[128] Wieding J, Wolf A, Bader R. Journal of the mechanical behavior of biomedical materials (2014);37:56.

[129] Eshraghi S, Das S. Acta biomaterialia (2012);8:3138.

[130] Wu L, Zhang J, Jing D, Ding J. Journal of Biomedical Materials Research Part A (2006);76:264.

[131] Hunt NC, Smith AM, Gbureck U, Shelton RM, Grover LM. Acta Biomaterialia (2010);6:3649.

[132] Sant S, Iyer D, Gaharwar AK, Patel A, Khademhosseini A. Acta biomaterialia (2013);9:5963.

[133] Anurag S, Shahjahan MM, Kalpana K, Dinesh K. Multiscale Model of Degradation and Healing of Bone Tissue Engineering Nanocomposite Scaffolds. J. Nanomech. Micromech (2017); In print.

[134] Göpferich A. Biomaterials (1996);17:103.

[135] Pan J. Modelling degradation of bioresorbable polymeric medical devices: Elsevier, 2014.

[136] Han X, Pan J. OA Biotechnology (2013);2:10.

[137] Hellmich C, Katti D. MRS Bulletin (2015);40:309.

[138] Spencer T, Hidalgo-Bastida L, Cartmell S, Halliday I, Care C. Biotechnology and bioengineering (2013);110:1221.

[139] Carlier A, Chai YC, Moesen M, Theys T, Schrooten J, Van Oosterwyck H, Geris L. Acta Biomaterialia (2011);7:3573.

CHAPTER 3. MOLECULAR INTERACTIONS IN BIOMINERALIZED HYDROXYAPATITE AMINO ACID MODIFIED NANOCLAY: INSILICO DESIGN OF BONE BIOMATERIALS[2]

This chapter describes a simulation driven design of novel nanoclay based biomaterial nanocomposite system for bone tissue engineering applications. The contents of this chapter have been published in D. R. Katti, A. Sharma, A. H. Ambre, K. S. Katti; "Molecular interactions in biomineralized hydroxyapatite amino acid modified nanoclay: *In silico* design of bone biomaterials", Materials Science and Engineering C. 46 (2015) 207–217.

3.1. Introduction

Although cellular biochemical response of biomolecules has been extensively investigated using modeling, [1-3] biomaterials design using a multiscale simulations-based-design is a methodology that has been investigated only recently [4-6]. Particularly promising, are the potential large implications of a simulations-based-methodology on the field of tissue engineering. Tissue engineering is an interdisciplinary field pioneered by Langer and Vacanti with a goal of developing biological substitutes for damaged tissues and organs [7]. Tissue engineering uses three dimensional porous scaffolds that are suitable for cell growth and function that are seeded with cells. These scaffolds are degradable and result in the formation of new tissues as scaffolds degrade

[2] The material in this chapter was co-authored by Anurag Sharma and Dinesh Katti. Anurag Sharma had primary responsibility for collecting samples in the field and for interviewing users of the test system. Anurag Sharma was the primary developer of the conclusions that are advanced here. Anurag Sharma also drafted and revised all versions of this chapter. Dinesh Katti served as proof reader and checked the math in the statistical analysis conducted by Anurag Sharma.

and cells develop appropriate tissues. Scaffolds are expected to exhibit adequate mechanical strength, appropriate pore size, biocompatibility, pore size distribution, pore volume, pore interconnectivity, and porosity. In addition, the degradation rate of scaffolds needs to match the tissue regeneration rate [8-12]. Biodegradable biopolymer-based scaffolds have been widely used due to their biocompatibility and non-toxic degradability. The major limitations of biopolymer based scaffolds are their poor mechanical strength and uncontrolled degradation rate. Scaffolds based on synthetic polymers offer improved mechanical and degradation properties with poor biological properties.

Hydroxyapatite ($Ca_{10}(PO_4)_6(OH)_2$) (HAP) is the primary inorganic constituent of bone and teeth. HAP exhibits excellent biocompatibility, osteoconductitvity and high biological affinity towards proteins [13-15]. Due to these unique properties, HAP has been extensively used in biologically active system [16-18]. However, poor mechanical strength of HAP limits its applications in scaffolds.

Polymer clay nanocomposites first proposed by the Toyota research group [19] in 1990, introduced a new concept of polymer nanocomposites (PCN) by using montmorillonite (MMT) clay mineral in the synthesis of nylon-6-clay nanocomposite. Addition of nanosized clay to polymers resulted in many fold increase in properties of the polymers. Thus clay based polymer nanocomposites have been considered as an effective method to improve mechanical, [19-21] liquid/gas barrier [22, 23], thermal properties [24, 25], biocompatibility [26] and biodegradability [27] of conventional polymer composites. The Altered Phase Theory of the PCNs was developed [28] that described that molecular interactions result in causing a ripple effect with influence on long range order of polymers and thus impact mechanical properties of PCNs. Based on the proposed model efforts were made to use nanoclays in design of biomaterials for bone [29-33].

We have used unique mineralization routes to mineralize hydroxyapatite inside nanoclays galleries for use in nanocomposites for bone tissue engineering [32, 33]. Experimental characterization techniques were used to evaluate molecular interactions between constituents of intercalated amino acid modified clay [33].

Many computational studies have been conducted on several biomaterial systems using ab initio, molecular dynamics and density functional theory [34-38]. Interactions of hydroxyapatite in natural bone with collagen have also been investigated. [39-46]. The hydroxyapatite system itself has been investigated computationally using ab initio, molecular dynamics and density functional theory [37, 44, 46-48]. Also, ab initio methods have been applied to study the adsorption of glycine on hydroxyapatite surfaces indicating that adsorption in this case has strong electrostatic affinity between COO^- and Ca^{2+} ions and hydrogen bonding between NH_3^+ protons and surface oxygen atoms of hydroxyapatite [49]. Adsorption processes of different amino acids with COOH-CH-NH_2 as common moiety with hydroxyapatite surfaces suggests that hydrogen bonds, and electrostatic interactions at HAP surface stabilizes amino acids in zwitterionic or deprotonated forms and these strong interactions arrange amino acids in α-helix conformation in the adsorption process [50]. The initial stage of the nucleation process of HAP at collagen molecule in an aqueous medium was also recently investigated by the de Leeuw group [47].

Material selection is an important step in designing scaffolds with optimal characteristics/properties. Many experimental methods are investigated to improve elastic modulus, stiffness and other mechanical properties of scaffolds such as use of coatings [51], crystal shape [52] and use of novel nanomaterials including carbon nanotubes [53, 54]. In this study, we describe a simulations driven approach to a novel biomaterial nanocomposite system. We investigate molecular interactions between constituents of a nanocomposite scaffold system for

developing a methodology of materials selection and use. In this work, molecular dynamic simulations were carried out along with transmission FTIR spectroscopy to study the specific nature of interactions in OMMT-HAP. Hydroxyapatite is mineralized using montmorillonite nanoclay modified with aminovaleric acid (OMMT). We have constructed representative models of OMMT and OMMT with HAP using molecular dynamics approach. XRD, TEM and FTIR techniques were used to validate these models. The molecular interaction energies between different constituents of the system were obtained to understand the mechanism of HAP mineralization, conformation and orientation changes in aminovaleric acid molecules, functions of functional groups and backbone of aminovaleric acid and hydrogen bonding in the system.

3.2. Materials and Methods

3.2.1. Materials

Na-montmorillonite (SWy-2, Crook County, Wyoming, USA) was purchased from the Clay Minerals Repository at the University of Missouri, Columbia, MO, USA. The cationic exchange capacity of Na-montmorillonite is 76.4 mequiv per 100 g. 5-aminovaleric acid, used as a modifier, was obtained from Sigma Aldrich. To prepare *in situ* HAPclay, sodium phosphate (Na_2HPO_4) from J.T.Baker and calcium chloride ($CaCl_2$) from EM sciences were used.

3.2.2. Synthesis of Organically Modified Montmorillonite (OMMT) Clay

Detailed procedure of OMMT clay synthesis is described in our previous work [31]. Briefly, first, 5 g fine Na-montmorillonite (Na-MMT) powder was dispersed into 400 mL of deionized water pre-heated at 60^0 C. Further, 1.9 g of aminovaleric acid was added to the MMT clay suspension. The pH of the solution was maintained at 1.8 by adding hydrochloric acid (HCl). The solution was vigorously stirred for about 60 minutes. This solution was further centrifuged and then washed several times with DI water to remove Cl^- ions. The resulting modified MMT

clay mixture was dried in an oven maintained at 70^0 C for 24 hours. Finally, a fine powder of OMMT clay was obtained by grinding and passing the mixture through a no.325 sieve (45 μm).

3.2.3. Preparation of *In situ* Hydroxyapatite (HAP) Clay

This procedure consists of synthsis of HAP inside nanoclay galleries modified by unnatural amino acids. This is a multistep procedure and details are provided elsewhere [33]. To summarize, the fine powder of organically modified montmorillonite (described in the section 3.2.2.) was dispersed in Na_2HPO_4 solution and the mixture was stirred for 2 hours. In OMMT clay-Na_2HPO_4 suspension, $CaCl_2$ solution was added, and the resulting mixture was maintained at pH 7.4. This was followed by further stirring for eight hours, settling of precipitate for 24 hours, removal of water over settled precipitate by centrifuging, drying at 70^0 C, grinding and sieving to obtain fine powder of *in situ* HAPclay.

3.2.4. X-Ray Diffraction

In order to obtain d-spacing of Na-MMT, OMMT and *in situ* HAPclay, X-ray diffraction analysis was performed on a Philips X'pert, Almelo, Netherlands, X-ray diffractometer. The X-ray diffractometer was equipped with secondary monochromator and Cu tube using CuKα radiation of wavelength 1.54056 Å. XRD experiments were performed at scan rate of 2^0/min, and the scan range was from $2\theta = 2\text{-}30^0$.

3.2.5. Transmission Electron Microscopy

For performing TEM imaging experiments, *in situ* HAPclay (powdered form) was dispersed on a copper grid with lacey carbon film. JEOL JEM-2100 analytical transmission electron microscope operated at 200kV was used for obtaining the images.

3.3. Model Construction

3.3.1. Model of Na-Montmorillonite and Organically Modified Montmorillonite Clay

Amino acid molecules contain carboxyl acid group (COOH) and amine (NH_2) as functional groups. These two functional groups are connected with each other through a carbon backbone (CH_2) chain. The aminovaleric acid used as the modifier has four carbon and eight hydrogen atoms in the backbone chain (Fig 3.1.). The module 'Builder' of InsightII^{TM} 2005 of Accelrys, Inc., San Diego, CA, USA was used for constructing aminovaleric acid molecular model. Partial charge and force field parameters for aminovaleric acid atoms were obtained from the library of CHARMm27 [55]. The organic modifier structures were minimized by InsightII^{TM} 2005 before being incorporated in the OMMT model. The montmorillonite unit cell has a tetrahedral-octahedral-tetrahedral (T-O-T) structure. For this study, two layers of montmorillonite (MMT)clay sheets each comprising of 18 unit cells were used [56]. The initial dimensions of Na- MMT 6X3 model used in this study were x = 31.68 Å, y = 27.44 Å and z = 24.16 Å [56]. The coordinates for montmorillonite unit cell are based on the parameters from the pyrophyllite model proposed by Skipper et al.[57, 58] and the partial charges of each atom of unit cell are based on those developed by Teppen et al.[59]. The CHARMm force field parameters used here are found in our earlier work.[60-62]. In the intercalated OMMT model, the structure of Na-MMT [$NaSi_{16}(Al_6FeMg)O_{20}(OH)_4$] was obtained by isomorphic ion substitution of pyrophyllite. In isomorphic substitution, one of every four Aluminum (Al^{3+}) ions in each unit cell of Na-MMT was alternately replaced by magnesium (Mg^{2+}) and iron (Fe^{2+}) ions. Partial charge on Al^{3+} and Fe^{2+} was 1.68 each and Mg^{2+} was 0.68. Thus, each layer has -9e charge due to isomorphic ion substitution and this charge is balanced by positively charged Na^+ ions in the interlayer.

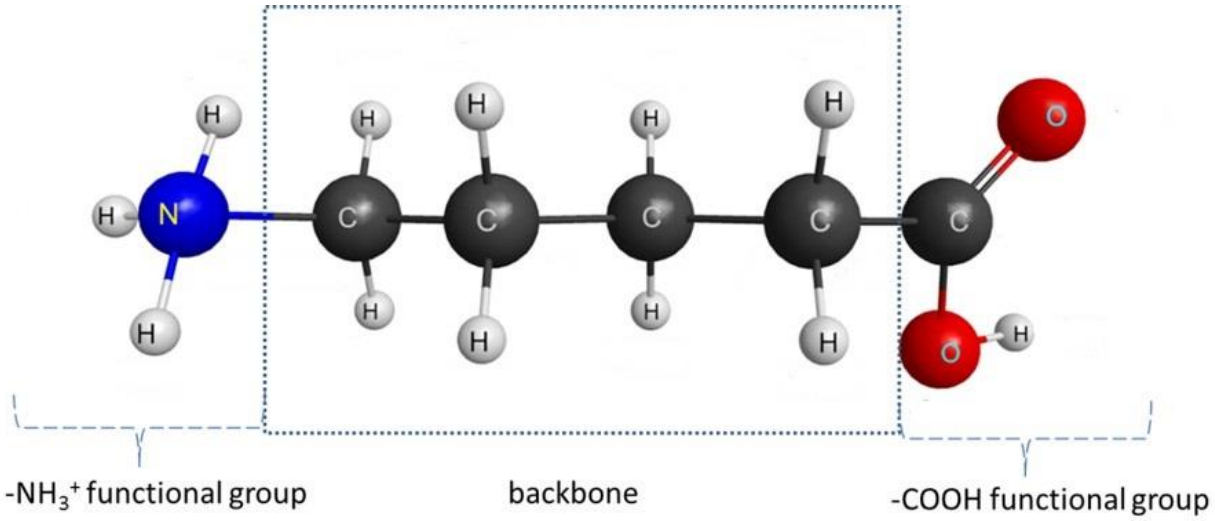

Figure 3.1. Chemical structure of protonated 5-aminovaleric acid

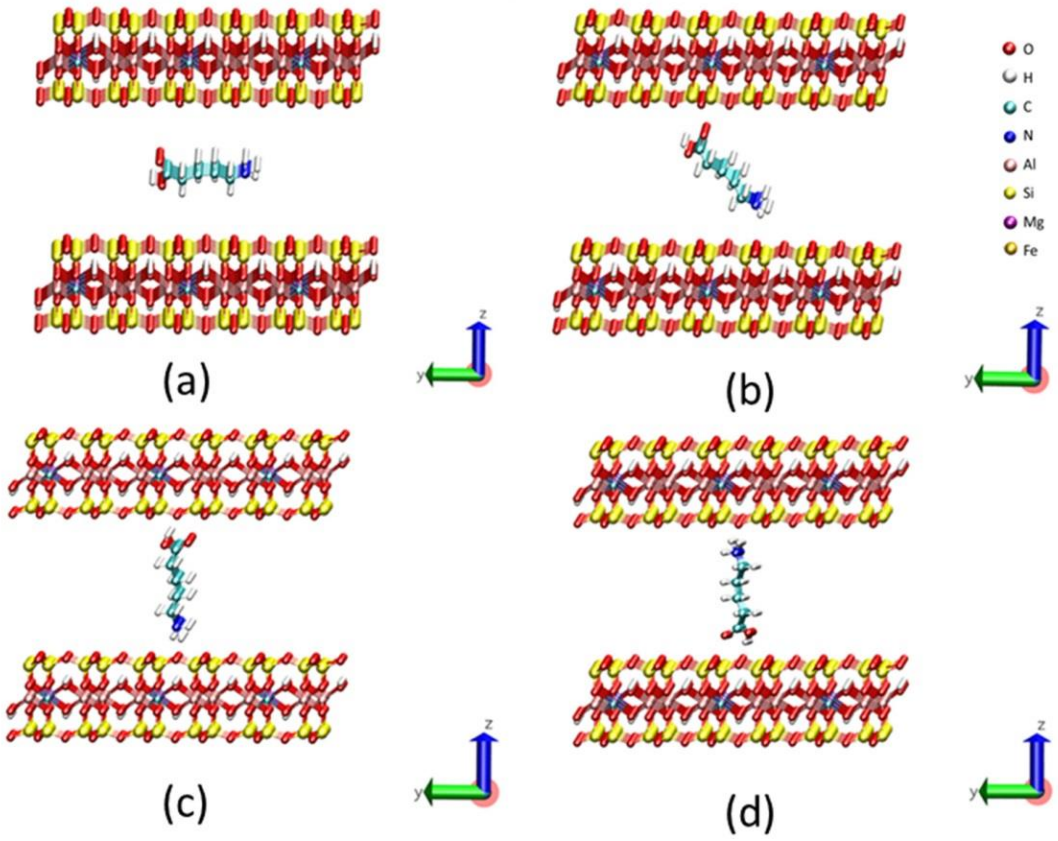

Figure 3.2. Initial orientations of protonated aminovaleric acid molecules placed in four different ways: (a) parallel to the MMT clay surface, (b) inclined at angle of 45^0 to the MMT clay surface, (c) NH_3^+ functional group closer to MMT clay surface and (d) COOH functional group to MMT clay surface.

In modified MMT clay synthesis, HCl was added in sufficient amount to protonate aminovaleric acid. Towards the end of the preparation, OMMT solution was washed rigorously with ionized water to remove Na^+ and Cl^- ions. Cation exchange capacity experiments were performed on Na-MMT and organic modified MMT clay to estimate Na^+ ions in the clay before and after OMMT preparation. It was found that the Na-MMT had a Na exchange capacity of 40.54 meq/100, and the OMMT had a Na exchange capacity of 0.96 meq/100g. This result indicates that

sodium ions of clay are replaced by protonated aminovaleric acid in modified MMT clay. Hence, in order to render a neutral charge to OMMT model, nine molecules of protonated aminovaleric acid were inserted in each MMT clay interlayer.

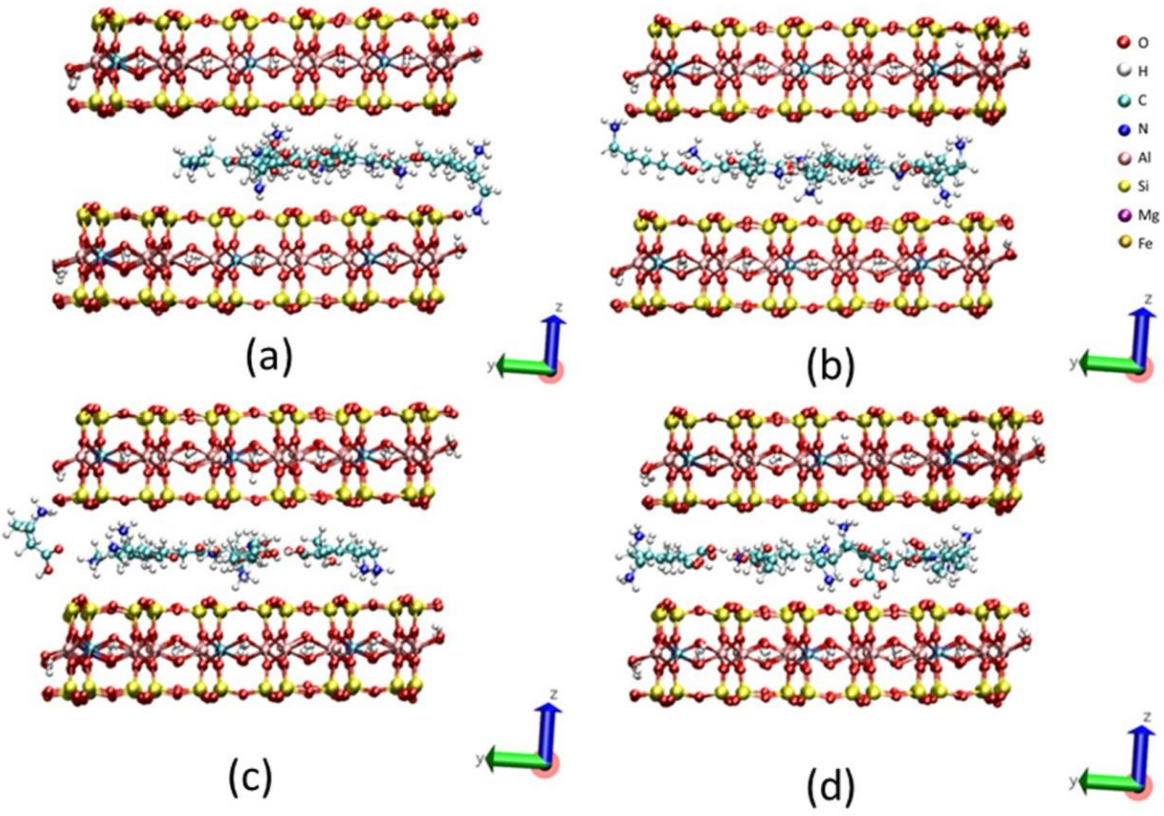

Figure 3.3. Final orientations of protonated aminovaleric acid molecules placed in four different ways: (a) parallel to the MMT clay surface, (b) inclined at angle of 45^0 to the MMT clay surface, (c) NH_3^+ functional group closer to MMT clay surface and (d) COOH functional group close to MMT clay surface.

In this work, montmorillonite (MMT) and aminovaleric acid structures have been used to build organically modified MMT clay models. We investigate the role of initial orientation of

organic modifier on final orientation of modifier in intercalated modified MMT. For this purpose, aminovaleric acid molecules were placed in four orientations as shown in Fig 3.2.: (a) parallel to the clay surface, (b) inclined at an angle of 45^0 to the clay surface, (c) NH_3^+ functional group closer to the clay surface and (d) COOH functional group closer to clay surface. Final orientations of modifier in these OMMT models are shown in in Figs 3.3.a-d. It was observed that, in all cases, the final orientation of modifiers was parallel to the clay surface.

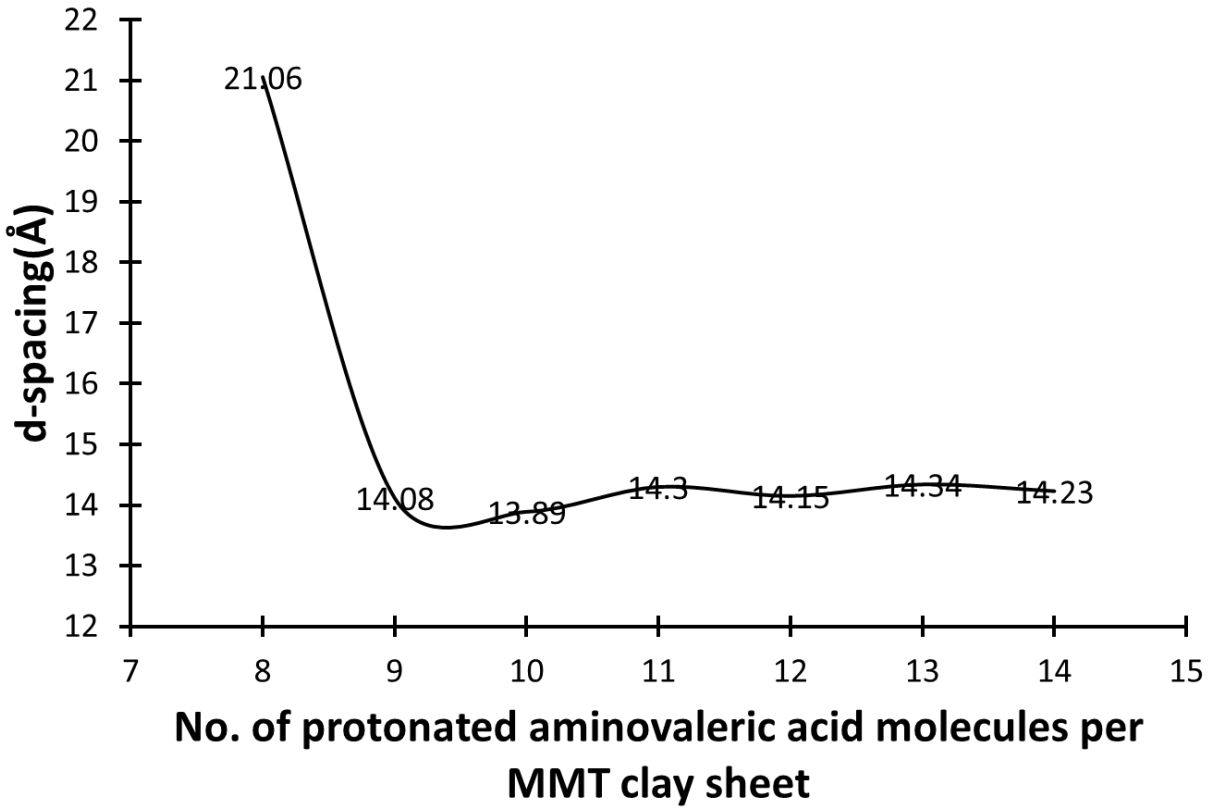

Figure 3.4. Variation of final d-spacing with no. of protonated aminovaleric acid in OMMT models at 300 K and 1 atm

Some aminovaleric acid molecules appear at the edge of MMT clay with their NH_3^+ functional groups pointed towards clay surface. These results are in good agreement with our

previous studies with different organic modifiers [56, 60]. The final d_{001} spacing in the case of parallel and inclined modifier models was 14.08 Å and 14.55 Å, respectively. The final d-spacing, when NH_3^+ and COOH were placed closer to MMT surface are 14.18 Å and 14.23 Å, respectively.

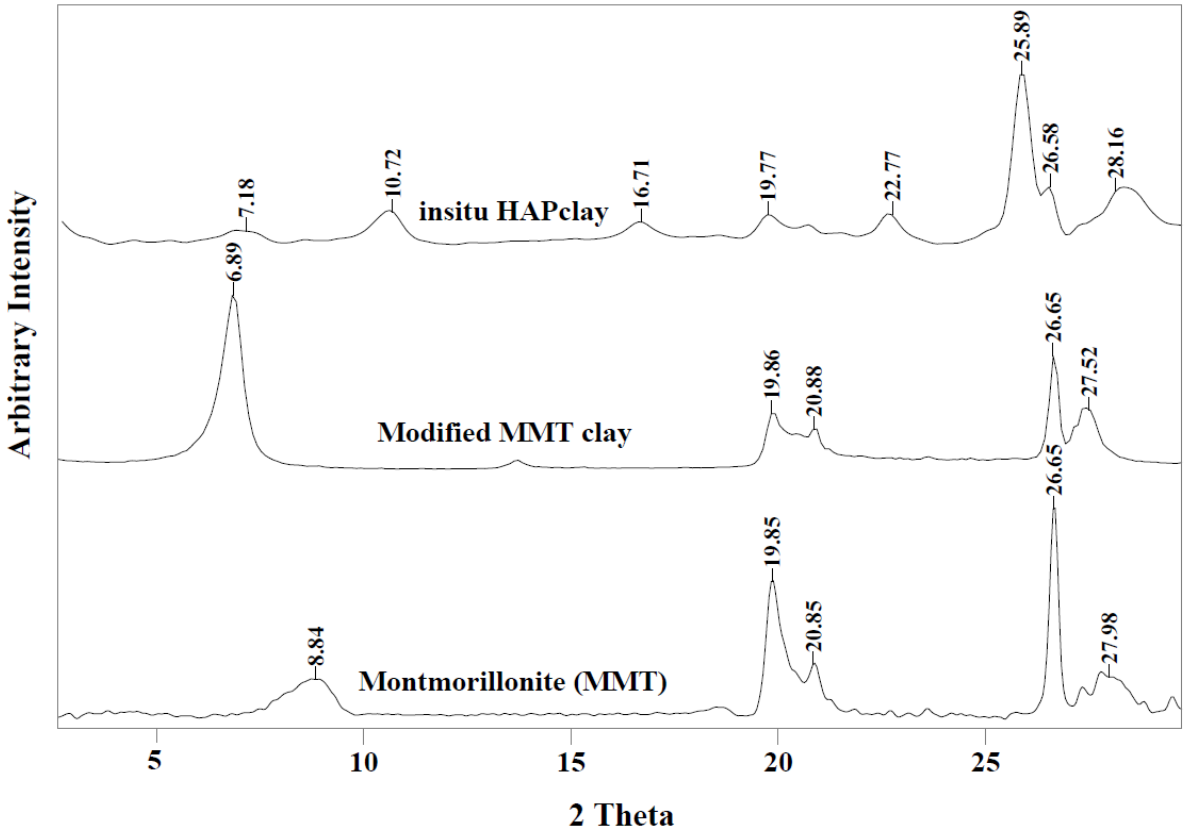

Figure 3.5. X-ray diffraction of montmorillonite (MMT), modified MMT clay and in situ HAPclay

Further, the role of number of protonated aminovaleric molecules in the interlayer on final d-spacing of OMMT was studied. Variation of final d-spacing with number of protonated amino acid molecules was shown in Fig 3.4. Modified MMT clay models were constructed with 8, 9, 10, 11, 12, 13 and 14 modifiers placed between MMT clay sheets. The final d-spacing values calculated from these models are found to be 21.06 Å, 14.08 Å, 13.89 Å, 14.30 Å, 14.15 Å, 14.34 Å and 14.23 Å, respectively. Variation in the number of protonated amino acids in MMT clay

interlayer has not shown significant effect on final d-spacing of OMMT models. It was observed that, in each case, nine protonated aminovaleric acid molecules remain inside the clay interface. Using procedure developed earlier for development of clay–modifier representative models for polymer clay nanocomposites [56], in this work, the following conditions were applied to select the final representative model of organically modified MMT

1. The final d-spacing of the molecular model of OMMT closely matches with the d-spacing of organically modified MMT, obtained from XRD experiment (Fig 3.5.).
2. Minimum energy conformation was satisfied in the OMMT model.

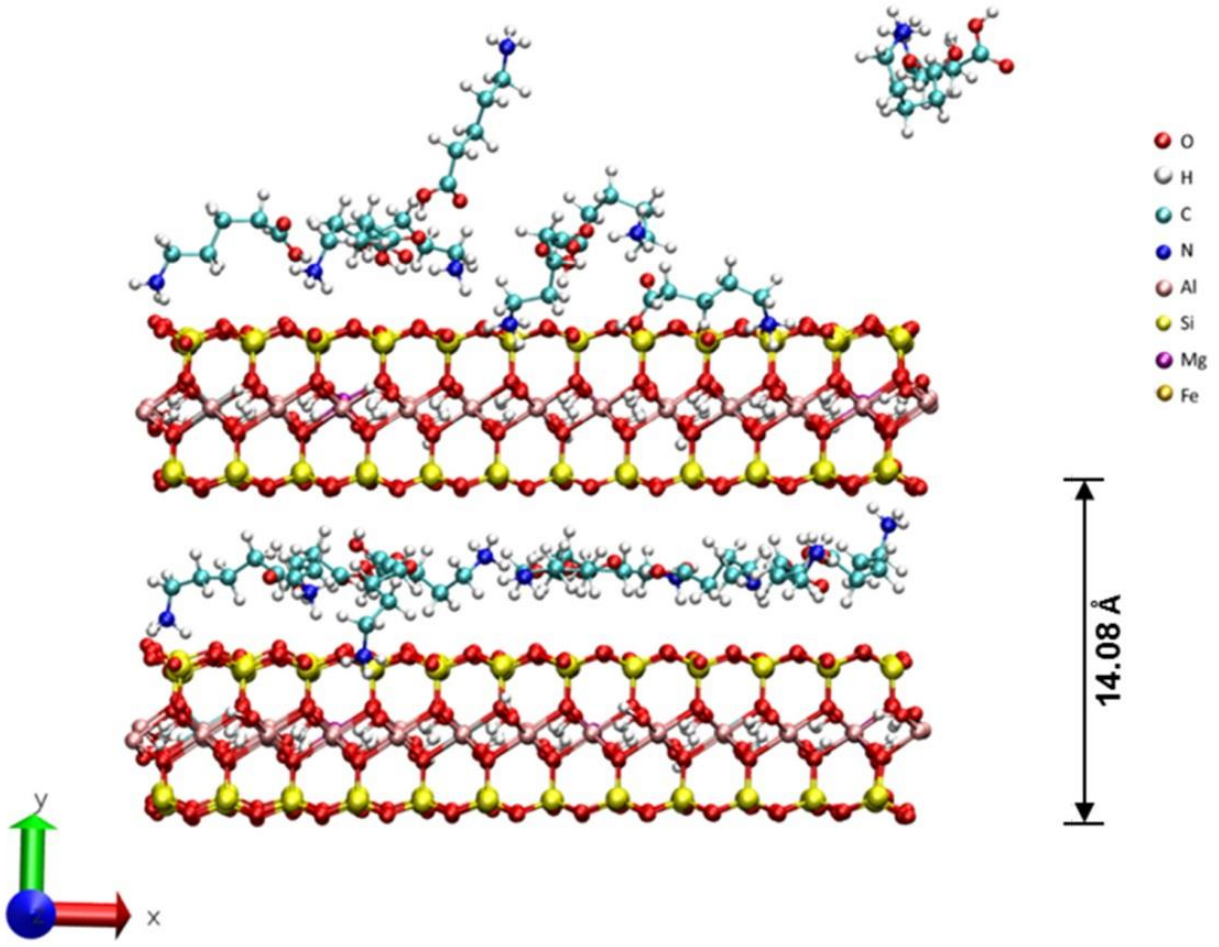

Figure 3.6. Structure of final representative model of organically modified MMT clay at a temperature of 300 K and 1 atm pressure (d-spacing = 14.08 Å).

On the basis of XRD experiments, Molecular Dynamics (MD) simulation studies and applying above two conditions, representative models of organic modified MMT clay were built. Further, four different initial d-spacing (12.6 Å, 14.6 Å, 17.6 Å and 18.6 Å) of organic modifier MMT model were used for obtaining final d-spacing of OMMT. It has found that, model with 17.6 Å as initial d-spacing has closest final d-spacing of 14.08 Å that matches with experimental XRD results. The initial representative OMMT model has 17.6 Å initial d-spacing, and nine protonated aminovaleric acid molecules, placed in parallel to the MMT clay interlayer. The final representative OMMT model after MD simulations is shown in Fig 3.6. The final d_{001} spacing of OMMT model after simulation was found to be 14.08 Å.

3.3.2. Model of Organically Modified Montmorillonite Clay - Hydroxyapatite

Transmission electron microscopy (TEM) image of in situ HAPclay (as shown in Fig 3.7.) shows HAP formation in modified MMT clay. Detailed analysis of the HAP lattice fringes in high resolution transmission electron micrographs indicates HAP mineralization occurs in both parallel and perpendicular directions with respect to clay sheets. The clay sheets themselves are consistently flat on the TEM foil samples and rarely in the [001] direction due to sample placement on TEM holey carbon grids. Based on these experimental results, two OMMT-HAP models were constructed; in the first model (Fig 3.8.) final OMMT model (built in section 3.3.1.) was placed in the perpendicular direction to HAP surface. In the second case (Fig 3.10.), the final OMMT model was placed in the parallel direction to HAP surface. Details of the construction of the [0001] HAP surface are described earlier [38].

The HAP structural parameters are: a = 33.836 Å, b = 33.836 Å, c = 14.093 Å and $\alpha = 90^0$, $\beta = 90^0$, $\gamma = 120^0$. The HAP model size used in OMMT-HAP construction was similar to the size

of final OMMT model. The modified MMT clay model is placed close to [0001] surface of HAP in initial OMMT-HAP models.

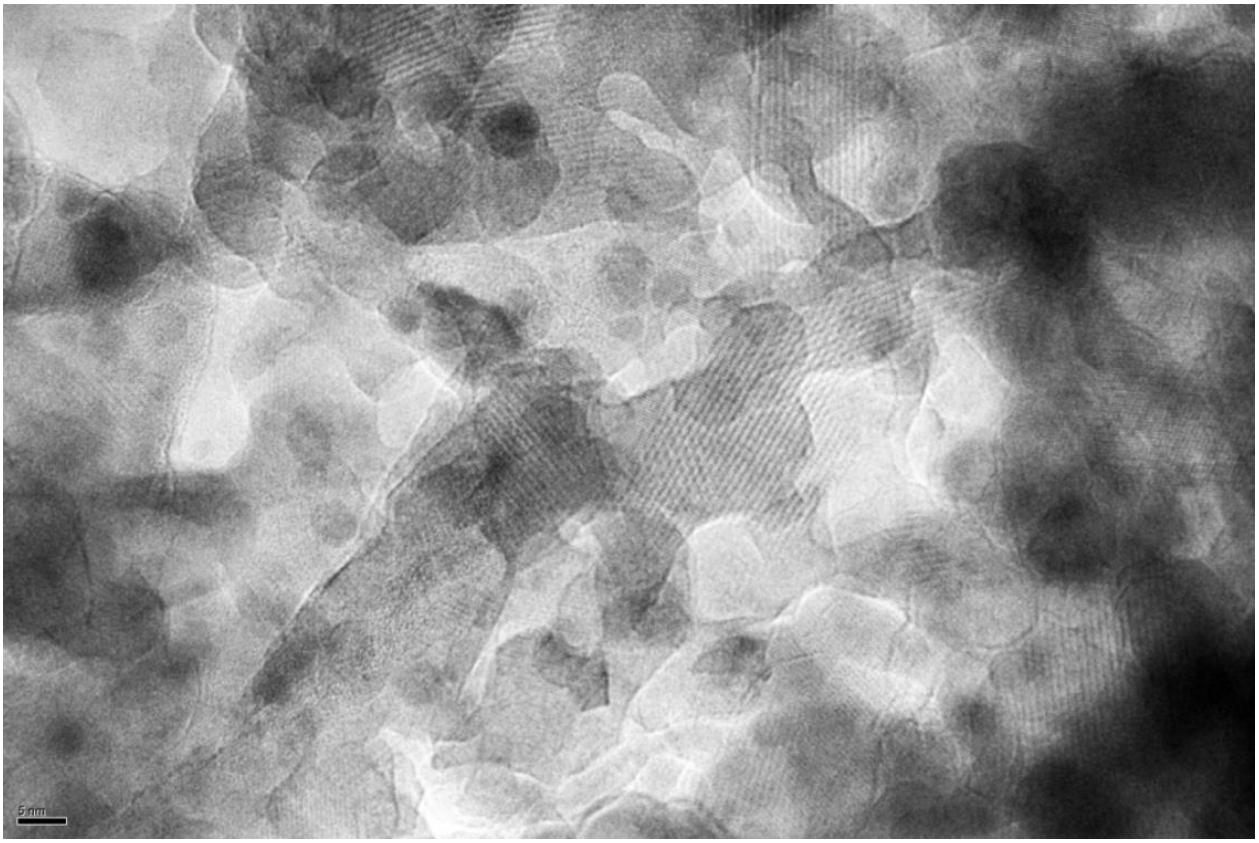

Figure 3.7. TEM image of in situ HAPclay. Clay sheets appear to have both parallel and perpendicular orientations with HAP crystals.

Further, HAP was mineralized on the organically modified nanoclays. FTIR spectroscopy study indicates that bonded interactions between OMMT and HAP are not present in the OMMT-HAP[31]. In the model, all OMMT and HAP interactions are non-bonded. The FTIR study of OMMT-HAP also indicated the formation of chelate (unidentate structure or Calcium Bridge) between carboxylate groups of aminovaleric acid and Ca^{2+} ions present in the OMMT-HAP. Also, XRD analysis of OMMT-HAP showed decrease in d-spacing of modified MMT clay by 0.50 Å (Fig 3.5.).

Hence, the representative OMMT-HAP model was constructed by following these three conditions.

1. Decrease in d-spacing of modified MMT clay in the OMMT-HAP model compared to the OMMT model**.**
2. Formation of Calcium Bridge between Ca^{2+} ions of hydroxyapatite and carbonyl oxygen atoms of COOH group of aminovaleric acid as observed earlier in experiments [38, 63].
3. The OMMT-HAP model satisfies the minimum energy conformation.

Figs 3.9. and 3.11. show the final representative models of OMMT-HAP, which satisfy the above three conditions. The overall dimensions of initial OMMT-HAP perpendicular model are x = 51.281 Å, y = 36.614 Å and z = 48.007 Å. The periodic boundary conditions in x, y and z direction, are applied to minimize boundary effects in the OMMT-HAP model. The overall dimensions of initial OMMT-HAP parallel model are x = 51.281 Å, y = 37.102 Å and z = 50.102 Å.

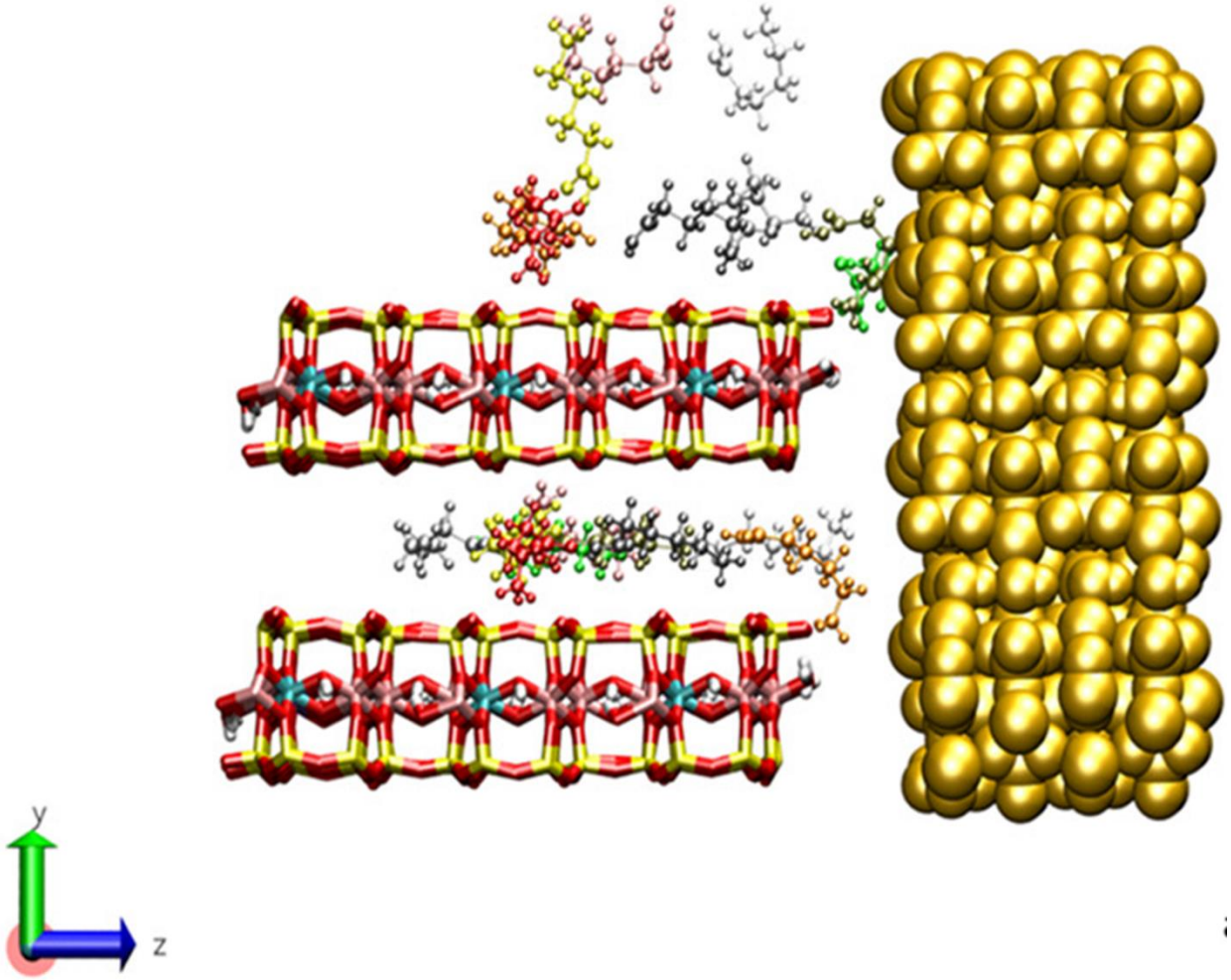

Figure 3.8. Structure of OMMT-HAP perpendicular before minimization (initial d-spacing = 14.08 Å). HAP represented as ball model, aminovaleric molecules as ball and stick model, and MMT clay as stick model.

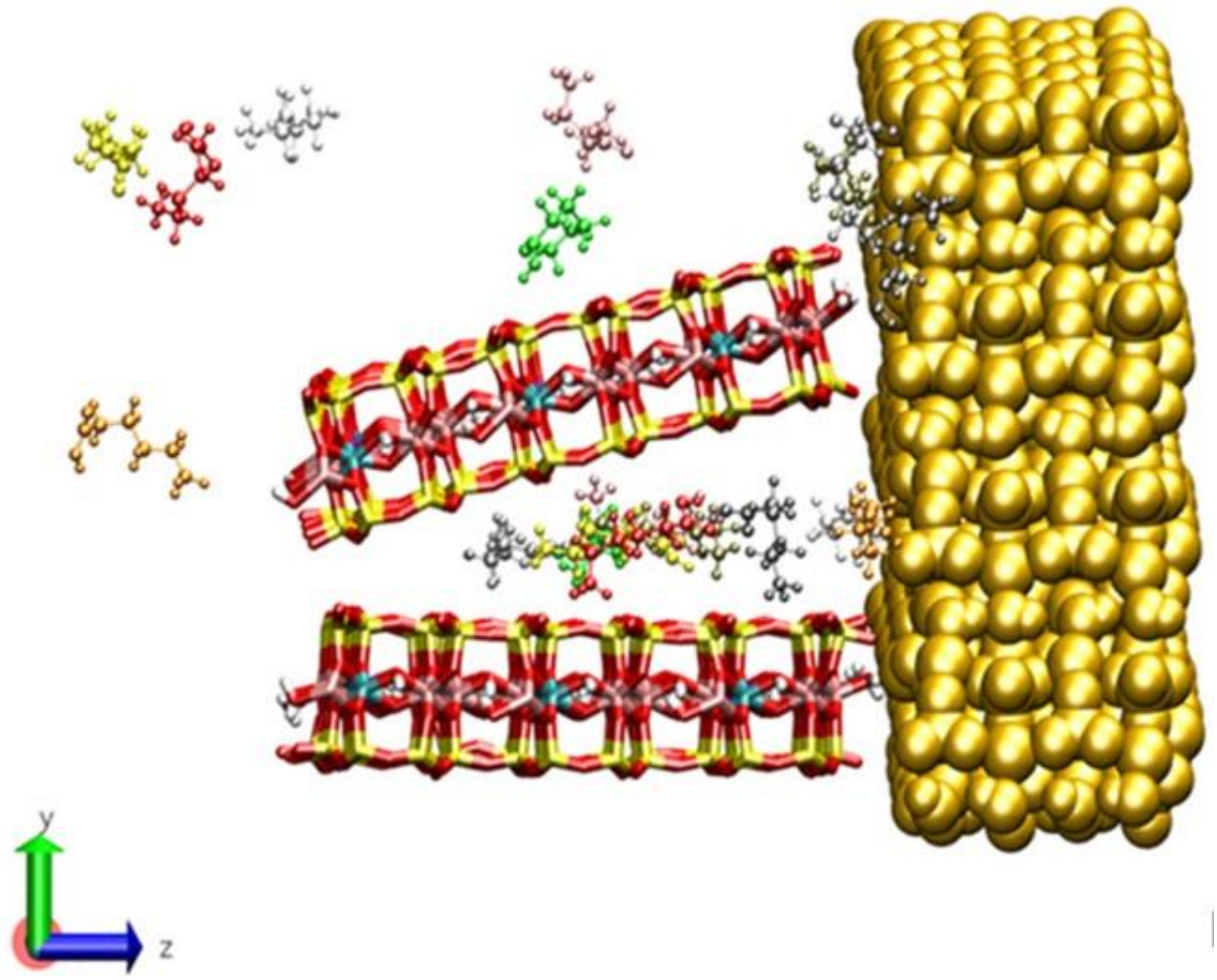

Figure 3.9. Structure of OMMT-HAP perpendicular at 300 K and 1 atm (final d-spacing = 13.92 Å). HAP represented as ball model, aminovaleric molecules as ball and stick model, and MMT clay as stick model.

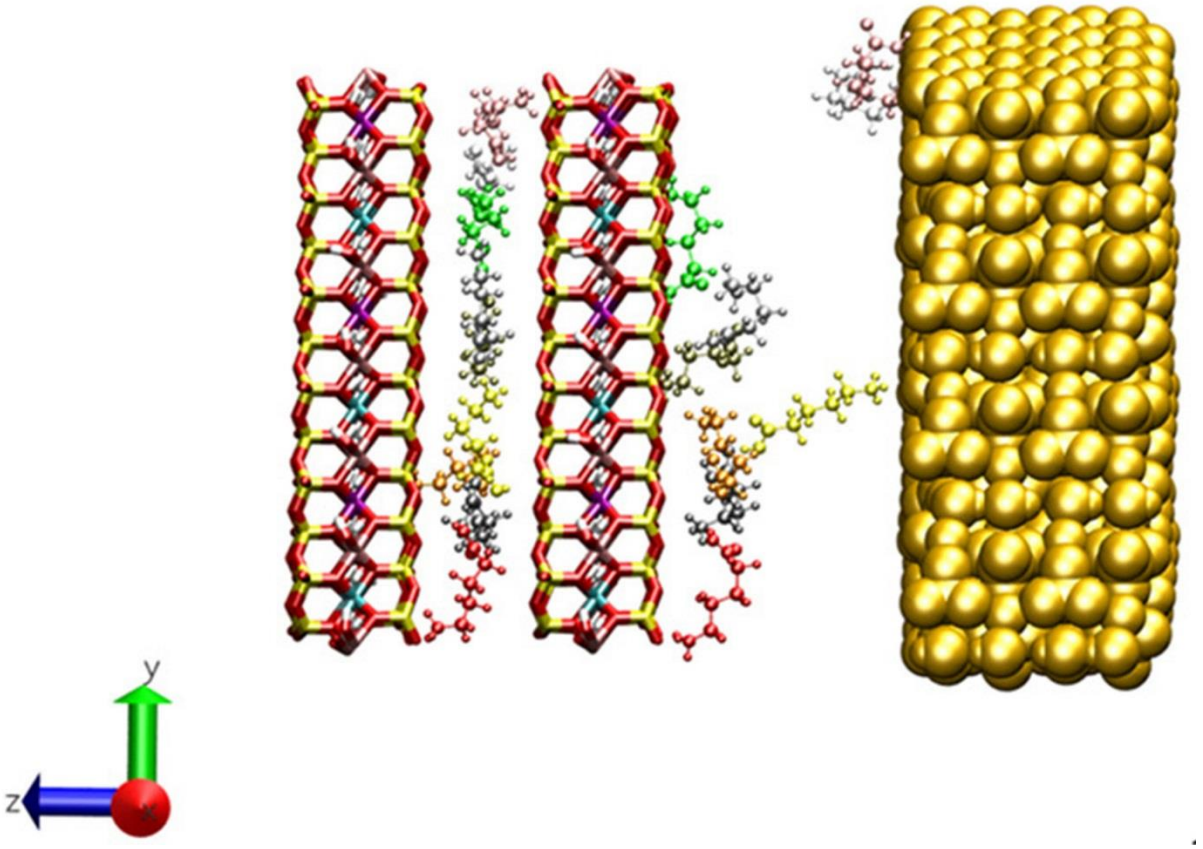

Figure 3.10. Structure of OMMT-HAP perpendicular before minimization (initial d-spacing = 14.08 Å). HAP represented as ball model, aminovaleric molecules as ball and stick model, and MMT clay as stick model.

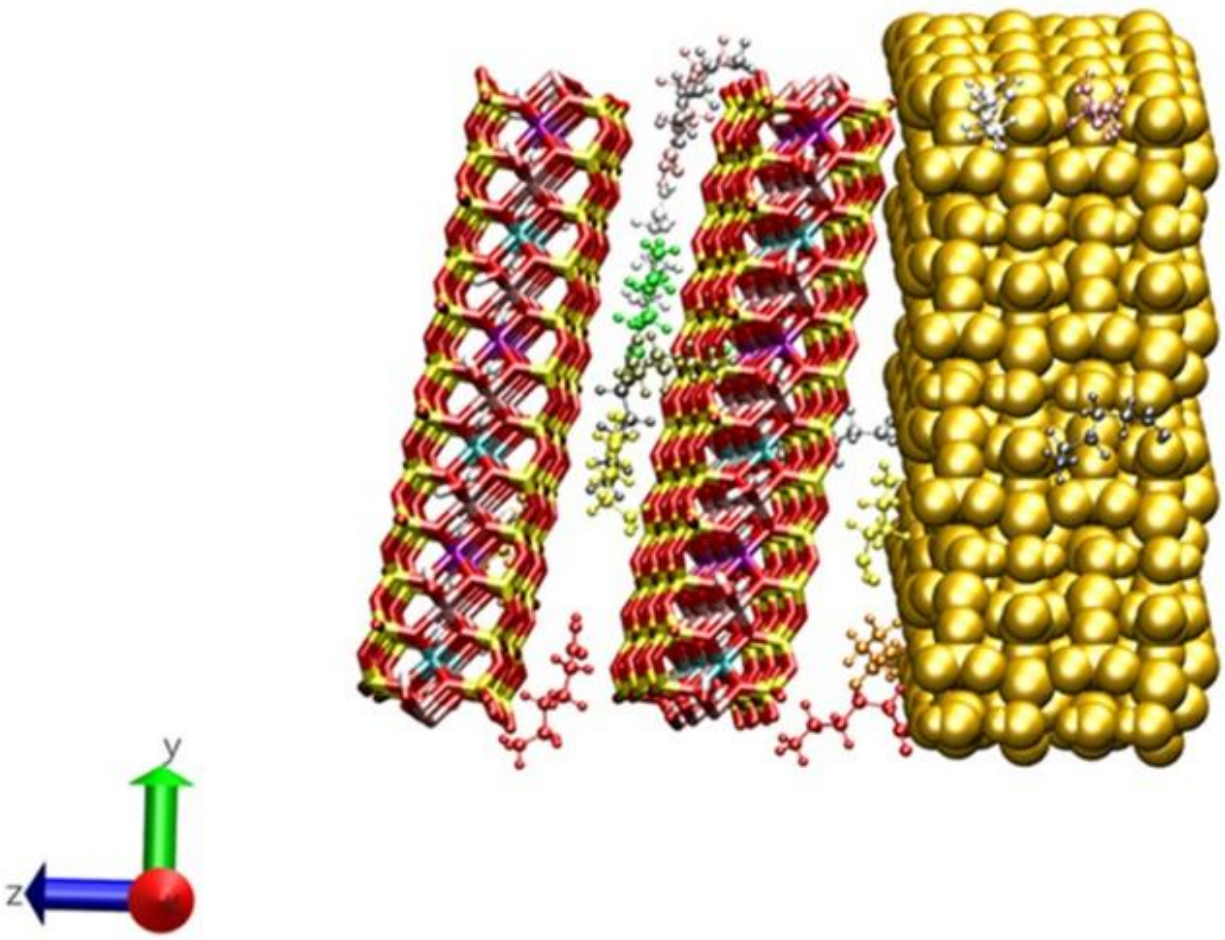

Figure 3.11. Structure of OMMT-HAP parallel at 300 K and 1 atm (final d-spacing = 13.08 Å). HAP represented as ball model, aminovaleric molecules as ball and stick model, and MMT clay as stick model.

3.4. Simulation Details

3.4.1. Organically Modified Montmorillonite Clay

Molecular dynamics (MD) simulations were conducted using NAMD2.7b1 [64] and VMD1.9 [65]. All initial OMMT models were first run at 0 K and 0 atm pressure to bring the models to their minimum energy level. The temperature of the OMMT models was further increased to 300 K in three steps, each of 100 K at 0 atm pressure by using Langevin dynamics control. The pressure of the system was increased from 0 to 0.25, 0.25 to 0.5, 0.5 to 0.75 and 0.75 to 1 atm in four steps at 300 K by using Nose Hoover Langevin piston control. The experimental synthesis of OMMT involved increase in temperature of the system to 333 K followed by reducing the temperature to 300 K (room temperature). Hence, in our simulation we increased the temperature of OMMT models to 333 K from 300 K at 1 atm pressure followed by decreasing to room temperature at 1 atm. Each simulation was run for 50 ps at time step of 0.5 fs. Next, for attaining equilibrium condition, OMMT models were run for another 200 ps at room temperature and pressure. The total energy vs. simulation time plots show that the 200 ps duration was adequate for complete convergence of energy of our OMMT system. The constant number of particles, pressure, and temperature (NPT) condition was applied, and Verlet leapfrog algorithm was used for running all OMMT simulations. In this study, MMT clay sheets were constrained in x and y direction but allowed to move in z direction. Further, the aminovaleric acid molecules were allowed to move in all directions. The periodic boundary condition was maintained in all OMMT models using the cell basis vectors; x = 37 Å, y = 32 Å and z = 37 Å. The switch and cut off distance used for van der Waals and electrostatic force calculations were 16 Å and 18 Å respectively.

3.4.2. Organically Modified Montmorillonite Clay – Hydroxyapatite

The OMMT-HAP model simulations were also performed using NAMD2.7b1 [64] and VMD1.9 [65]. HAP structure was separately minimized to attain minimum energy. OMMT-HAP models were first minimized in vacuum at 0 K. Next; temperature was increased using Langevin dynamics to 300 K in three steps of 100 K each. At 300 K, pressure was increased to 1 atm from 0 atm in four equal steps using Langevin piston control method. MD simulations were run for 50 ps with time step of 0.5 fs. At room temperature and pressure, all OMMT-HAP models were run for another 200 ps. The total energy vs. simulation time plot confirms that 200 ps duration was sufficient to attain equilibrium energy condition for the OMMT-HAP models. HAP structure was constrained in all directions, and no constraint was placed on MMT clay sheets and modifier molecules. The switch and cut off distance used in all OMMT-HAP models were 16 Å and 18 Å, respectively. The Verlet leapfrog algorithm was used for integrating Newton's equation of motions, and NPT condition is applied during all OMMT-HAP model simulations. All MD simulations were conducted at the Center for Computationally Assisted Science and Technology (CCAST) using eight processors on one DakTech node at the North Dakota State University in Fargo, ND.

3.4.3. Interaction Energy Calculations

The trajectory files obtained from MD simulation were used to obtain interaction energies between different constituents of OMMT and OMMT-HAP. MDEnergy^{TM} module in NAMD was used as energy evaluation tool for calculating these energies.[64] The bonded and non-bonded energies were calculated using their specific cutoff and switch distance, interaction parameters and structural information. Average values from last 25 ps were used for all interaction energy calculations.

3.5. Results and Discussion

3.5.1. X-ray Diffraction Results

X-ray diffraction plots of MMT clay, MMT clay modified with aminovaleric acid and *in situ* HAPclay are shown in Fig 3.5. The XRD spectra of MMT clay shows a distinct peak of the d_{001} = 9.992 Å) plane at $2\theta = 8.842^0$. This peak was found to shift to 6.896^0 in modified MMT clay corresponding to d_{001} = 12.81 Å. An increase in d-spacing indicates the intercalation of MMT clay. The length of the backbone chain and the functional group position of amino acids play a significant role in the increase of OMMT d-spacing.

The X-ray diffraction plot of *in situ* HAPclay shows a decrease in d_{001} spacing of the OMMT clay from 12.81 Å to 12.3 Å ($2\theta = 7.182$). In *in situ* HAPclay synthesis, the carboxylic functional group of the aminovaleric acid dissociates into the carboxylate due to the addition of a basic Na_2PO_4 solution. The negatively charged carboxylate group forms a complex with the calcium ions of $CaCl_2$ solution and acts as a nucleating site of hydroxyapatite. This fact was observed in synthetic mineralization of HAP in supersaturated solutions [66]. The formation of hydroxyapatite possibly affects the interactions between MMT clay and aminovaleric acid, and this may be attributed to a change in d-spacing of modified MMT clay.

3.5.2. Interactions in Organically Modified MMT clay

Detailed vibrational spectroscpic studies are reported in our previous studies using transmission FTIR [33]. The results indicate observed shifts in C=O stretching band in pure aminovaleric acid and Si-O bands in pure MMT clay with respect to modified MMT clay. The band corresponding to ν_1 P-O stretching appears at 951 cm^{-1} in HAP. These shifts in phosphate vibrations in *in situ* HAPclay with respect to HAP may be attributed to the change in chemical environment and molecular interactions during the hydroxyapatite formation process. These shifts

suggest the interaction between surface oxygen of MMT clay and functional groups of aminovaleric acid. The N-H deformation band observed in modified MMT clay was absent in pure MMT clay. FTIR study results suggest chelate formation in the *in situ* HAPclay. The interactions between COOH functional group and Ca atoms are attractive in nature in both OMMT-HAP models. It was observed that the oxygen atoms of C=O group of aminovaleric form calcium chelate with the Ca^{2+} ions of HAP. No change in NH_3^+ deformation band position was observed in our FTIR experiments [33]. This may be attributed to the similar interaction energy between NH_3^+–MMT clay and NH_3^+–HAP in OMMT-HAP.

Table 3.1. Non-bonded interactions between MMT clay and different constituents of aminovaleric in modified MMT clay. Attractive interactions are represented by negative value, and repulsive interactions are indicated by positive values.

Non-bonded interactions between	Electrostatic (ELE) Energy (kcal/mol)	Van der Waals (VDW) Energy (kcal/mol)	Total (VDW+ELE) Energy (kcal/mol)
MMTclay – backbone	-619	-106	-725
MMTclay – functional groups	-1038	-99	-1137
MMTclay – COOH	+216	-87	+128
MMTclay – NH_3^+	-1254	-12	-1266
MMTclay – backbone H	-1096	-6	-1102
MMTclay – backbone C	+477	-100	+377
MMTclay – functional N	+517	-6	+511
MMTclay – functional C	-1060	-27	-1087
MMTclay – functional O	+2018	-60	+1958
MMTclay – COOH functional H	-799	-2	-801
MMTclay – NH_3^+ functional H	-1771	-6	-1777

In the current simulation work, modified MMT clay was studied using MDEnergy^{TM} of NAMD to investigate the molecular interactions of MMT clay with aminovaleric modifier. Non-bonded interactions were measured by calculating electrostatic (ELE), van der Waals (VDW) and hydrogen bond energies between different constituents of OMMT. Hydrogen bond energy is included in van der Waals energy term as NAMD calculates them collectively. The electrostatic energy term strongly depends on the charge for two given sets of atoms and distances between them. On the other hand, van der Waals and hydrogen bond energy terms depend only on the distance between the two atoms. Table 1 shows the non-bonded interactions between different constituents of modified MMT clay. Attractive interactions are represented by negative values of energy, and repulsive interactions are indicated by positive values of energy in the Table 3.1.

As mentioned in model construction section 3.3., the aminovaleric acid molecule was divided in two major entities: the backbone and the functional group. It can be seen in Table 3.1., that clay functional group and backbone both have strong attractive interaction with MMT clay and these interactions were largely electrostatic in nature. Although the van der Waals interactions between clay-functional group and clay-backbone were similar, the electrostatic interactions of clay-functional groups were higher than clay–backbone in the OMMT model. Since partial charges of functional group atoms were higher than values for carbon and hydrogen atoms of the backbone, this results in higher electrostatic interactions between clay and functional groups. High values of van der Waals attractive interaction energy between clay and backbone was largely due to backbone carbon atoms. Attractive interaction was observed to be highest between clay and functional hydrogen atoms, and highest repulsive interaction was observed between clay and functional group oxygen atoms. Electrostatic interaction energy of clay with backbone carbon atoms was found to be repulsive in nature but attractive with the functional groups. This attributed

to the fact that the partial charges of backbone carbon atoms are negative, while that of functional carbon atoms are positive. High attractive interaction energy was observed between clay and functional group hydrogen in modified MMT clay model.

As seen in Fig 3.6., COOH and NH_3^+ functional groups of aminovaleric acid have tilted towards the interlayer MMT clay sheets. This indicates strong interactions between modifier functional group and clay sheets. Oxygen atoms on the surface of the MMT clay exhibited non-bonded interaction with these functional groups. The distance between functional hydrogen atoms and surface oxygen atoms was calculated to estimate hydrogen bond interactions. Functional hydrogen atoms of seven out of eighteen aminovaleric modifier molecules satisfied the criteria of hydrogen bond interactions [56, 67]. Hydrogen bonding between functional hydrogen atoms and surface oxygen also confirmed strong interaction between modifier functional group and clay sheets. Further, it was observed in the final OMMT model that some hydrogen atoms of NH_3^+ were within the range of hydrogen bond interactions with oxygen atoms of COOH functional group of the modifier.

3.5.3. Results from OMMT-HAP Simulations

In the initial OMMT-HAP models, both the clay sheets were parallel to each other, and [0001] HAP surface was placed closer to the aminovaleric acid molecules. Figs 3.9. and 3.11., indicate that in the final OMMT-HAP model, MMT clay sheets were no longer parallel to each other and tilted near the HAP surface. Some of the aminovaleric molecules were moved outside of the clay galleries in the direction of HAP and appeared to be interacting with the surface atoms of HAP. It was observed that, between the clay sheets, functional groups of aminovaleric molecules point towards MMT. These observations indicate that the conformation of modifiers in OMMT-HAP models have changed and no longer similar to the conformation of modifiers in OMMT

model. The decrease in distance between clay sheets and HAP surface in the final OMMT-HAP models indicated the interactions between MMT clay and HAP surface. Figs 3.9. and 3.11. also show that COOH and NH_3^+ functional groups of modifier have tilted towards the HAP surface. The carbonyl oxygen atoms of aminovaleric molecules present near the HAP appeared to have potential sites for the formation of Ca^{2+} bridge (chelation) with calcium atoms of HAP surface. The detailed analysis of the formation of chelation (unidentate) between amino acid and HAP was described in earlier works of our group [38, 63].

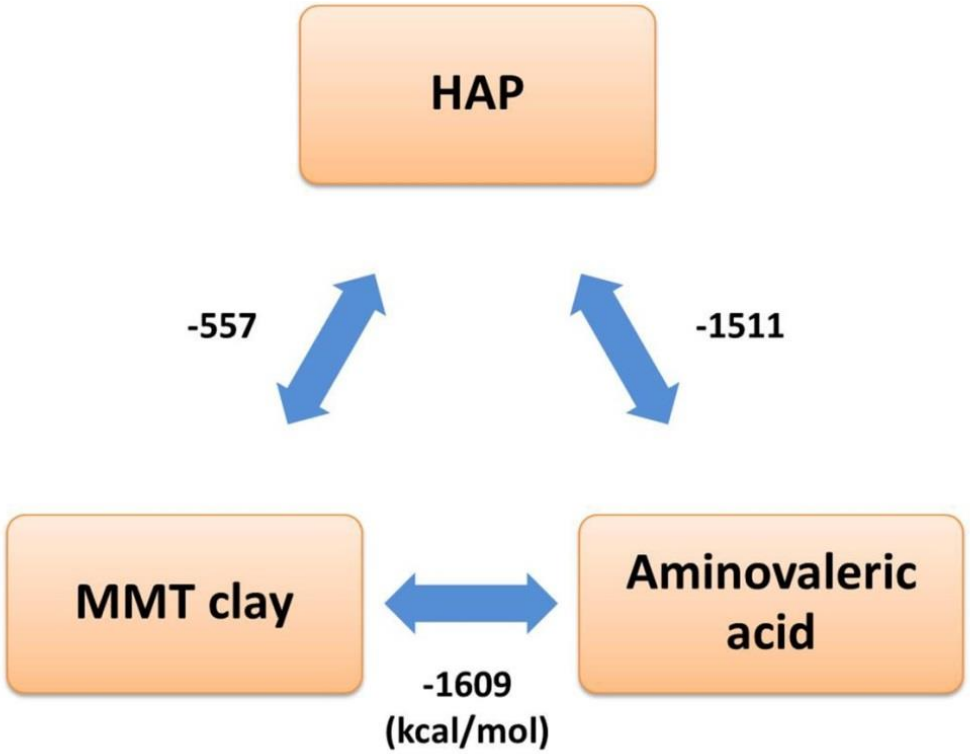

Figure 3.12. Total non-bonded interaction energies between MMT clay, HAP and aminovaleric acid in OMMT-HAP perpendicular.

The d-spacing of the representative models of OMMT-HAP perpendicular and OMMT-HAP parallel orientations were observed to be 13.92 Å and 13.08 Å. The final d_{001} spacing was

obtained by taking the average of 25 different values of d-spacing calculated between surface atoms and also between center atoms of two clay sheets. The d-spacing of OMMT in OMMT-HAP model was found to be lower than the OMMT model d-spacing (14.08 Å). The decrease in d-spacing of OMMT was also observed in x-ray diffraction (figure 3) plot of OMMT-HAP. Both the representative OMMT-HAP models shown in figures 6b and 7b were at lowest total energy conformation.

3.5.4. Interactions of OMMT Perpendicular to HAP

Considering both the XRD results and the TEM images of *in situ* HAPclay system, it appears that HAP may be oriented perpendicular or parallel to MMT clay sheets. Hence, it is important to study the molecular interactions between MMT clay, modifier and HAP, for both conditions. The total non-bonded interaction energies between MMT clay, HAP and aminovaleric acid in OMMT-HAP perpendicular are presented in Fig 3.12.

High attractive interactions are observed between HAP and aminovaleric acid (-1511 kcal/mol), MMT clay and aminovaleric acid (-1609 kcal/mol) and MMT clay and HAP (-557 kcal/mol). The HAP–aminovaleric acid and MMT clay–aminovaleric acid entities exhibit higher electrostatic interactions than van der Waals interactions, whereas, in HAP–MMT clay interactions, both non-bonded interactions contribute almost equally. The electrostatic interaction energy and van der Waals interaction energy among different constituents of MMT clay, aminovaleric acid and HAP in OMMT-HAP perpendicular are presented in Table 3.2.

Table 3.2. Non-bonded interaction energies between different constituents of MMT clay, aminovaleric and HAP in OMMT-HAP perpendicular. Attractive interactions are represented by negative values, and repulsive interactions are indicated by positive values.

Non-bonded interactions between	Electrostatic (ELE) Energy (kcal/mol)	Van der Waals (VDW) Energy (kcal/mol)	Total (VDW+ELE) Energy (kcal/mol)
MMTclay – backbone	-561	-76	-637
MMTclay – COOH	+133	-58	+75
MMTclay – NH_3^+	-1040	-7	-1047
MMTclay – PO_4	+9406	-219	+9187
MMTclay – OH	+979	-6	+973
MMTclay – Ca	-10707	-10	-10717
PO_4–backbone	-3996	-19	-4015
PO_4 – COOH	+446	-8	+438
PO_4 – NH_3^+	-10614	+58	-10556
OH – backbone	-497	-1	-498
OH – COOH	+50	-1	+49
OH – NH_3^+	-1325	+8	-1317
Ca – backbone	+4154	-3	+4151
Ca – COOH	-682	+11	-671
Ca – NH_3^+	+10910	-2	+10908

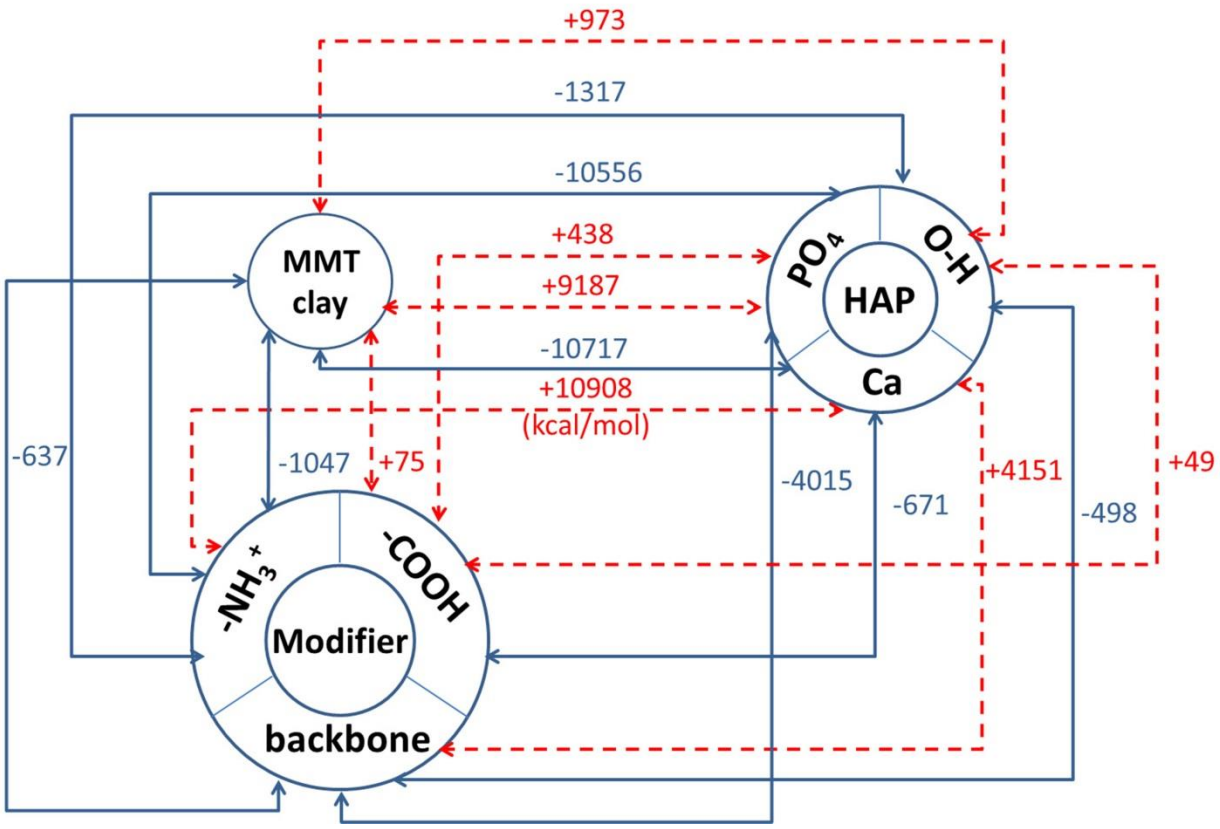

Figure 3.13. Map of total non-bonded interactions between different constituents of HAP, aminovaleric acid and MMT clay in OMMT-HAP perpendicular. Negative values indicate attractive interactions and positive values indicate repulsive interactions.

The evaluate in further detail, HAP was analyzed further by probing individual atoms/atom groups Ca, PO_4 and OH, whereas the modifier was analyzed by probing backbone and functional groups (NH_3^+ and COOH). The total non-bonded interaction energies between different constituents of HAP, aminovaleric acid modifier and MMT clay in OMMT-HAP perpendicular are presented in Fig 3.13. The dotted lines denote the repulsive interactions, and solid lines denote the attractive interaction in OMMT-HAP. Large attractive interactions were observed between Ca of HAP and MMT clay sheets (-10717 kcal/mol) and PO_4 of HAP and NH_3^+ (-10566 kcal/mol). High repulsive interactions were observed between Ca and NH_3^+ of aminovaleric acid (-10908 kcal/mol) and PO_4 and clay sheets (-9187 kcal/mol). The relative partial atomic charges of different

atoms of HAP[68] are higher, and this results in strong electrostatic non-bonded interactions between different constituents of HAP and aminovaleric acid and MMT clay sheets as shown in Fig 3.13. Attractive interactions were observed between COOH functional group of aminovaleric acid and Ca of HAP (-671 kcal/mol). The backbone of modifier has attractive interactions with PO_4 and OH, groups of HAP.

3.5.5. Interactions of OMMT Parallel to HAP

The total non-bonded interaction energies between MMT clay, HAP and aminovaleric acid in OMMT-HAP parallel are presented in Fig 3.14. Strong attractive interactions were observed in between all three constituents (HAP and aminovaleric acid (-1746 kcal/mol), MMT clay and aminovaleric acid (-1937 kcal/mol) and MMT clay and HAP (-202 kcal/mol)) of OMMT-HAP parallel. In parallel OMMT-HAP, high electrostatic interactions have found between HAP and aminovaleric acid and MMT clay and aminovaleric acid and low electrostatic interactions observed between HAP and MMT clay as compared to van der Waals interactions. In parallel OMMT-HAP, MMT clay sheets were placed parallel to HAP surface.

The total non-bonded interaction energies between different constituents of HAP, aminovaleric acid and MMT clay in OMMT-HAP parallel are presented in Fig 3.15. Again, HAP was analyzed for atoms/atom groups Ca, PO_4 and OH and modifier for the backbone, NH_3^+ and COOH. It was observed that OMMT-HAP parallel model has similar nature of non-bonded interactions as the OMMT-HAP perpendicular model. Strong attractive interactions were observed between MMT clay and Ca atoms of HAP (-6185 kcal/mol). Between aminovaleric acid and HAP, attractive interactions were observed between modifier backbone and PO_4 (-4417 kcal/mol), NH_3^+

and PO_4 (-10729 kcal/mol) and COOH and Ca (-328 kcal/mol). High repulsive interactions were found between NH_3^+ and Ca (+10894 kcal/mol) and backbone and Ca of HAP (+4523 kcal/mol).

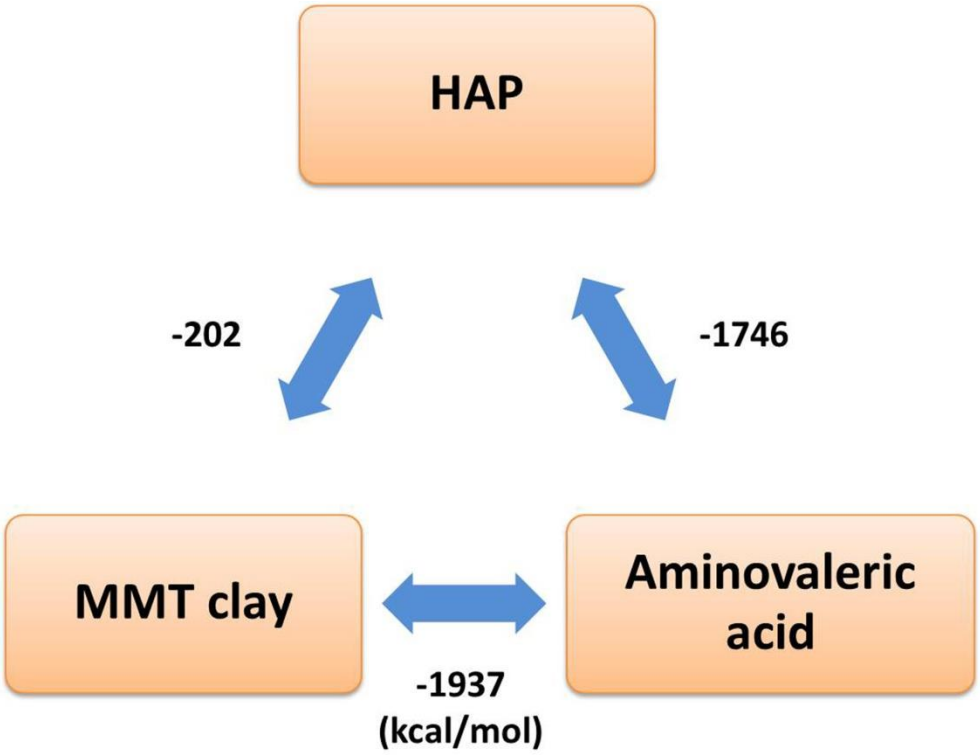

Figure 3.14. Total non-bonded interaction energies between MMT clay, HAP and aminovaleric acid in OMMT-HAP parallel.

Attractive interactions are denoted by solid lines, and repulsive interactions are denoted in dashed lines in non-bonded energy map (Fig 3.15.) of OMMT-HAP parallel. The electrostatic interaction energy and van der Waals interaction energy among different constituents of MMT clay, aminovaleric acid and HAP in OMMT-HAP parallel are presented in Table 3.3. A comparison of non-bonded interaction energies in Tables 3.2. and 3.3. indicate that higher interactions of aminovaleric acid molecules with HAP and MMT clay in parallel OMMT-HAP result from the electrostatic energy. On the other hand, both van der Waals and electrostatic

energies contribute to higher attractive interaction between MMT clay–HAP in perpendicular OMMT-HAP compared to parallel OMMT-HAP. High attractive interactions between HAP-aminovaleric acid and MMT clay–aminovaleric acid than MMT clay–HAP suggest that MMT clay interacts with HAP primarily through aminovaleric acid.

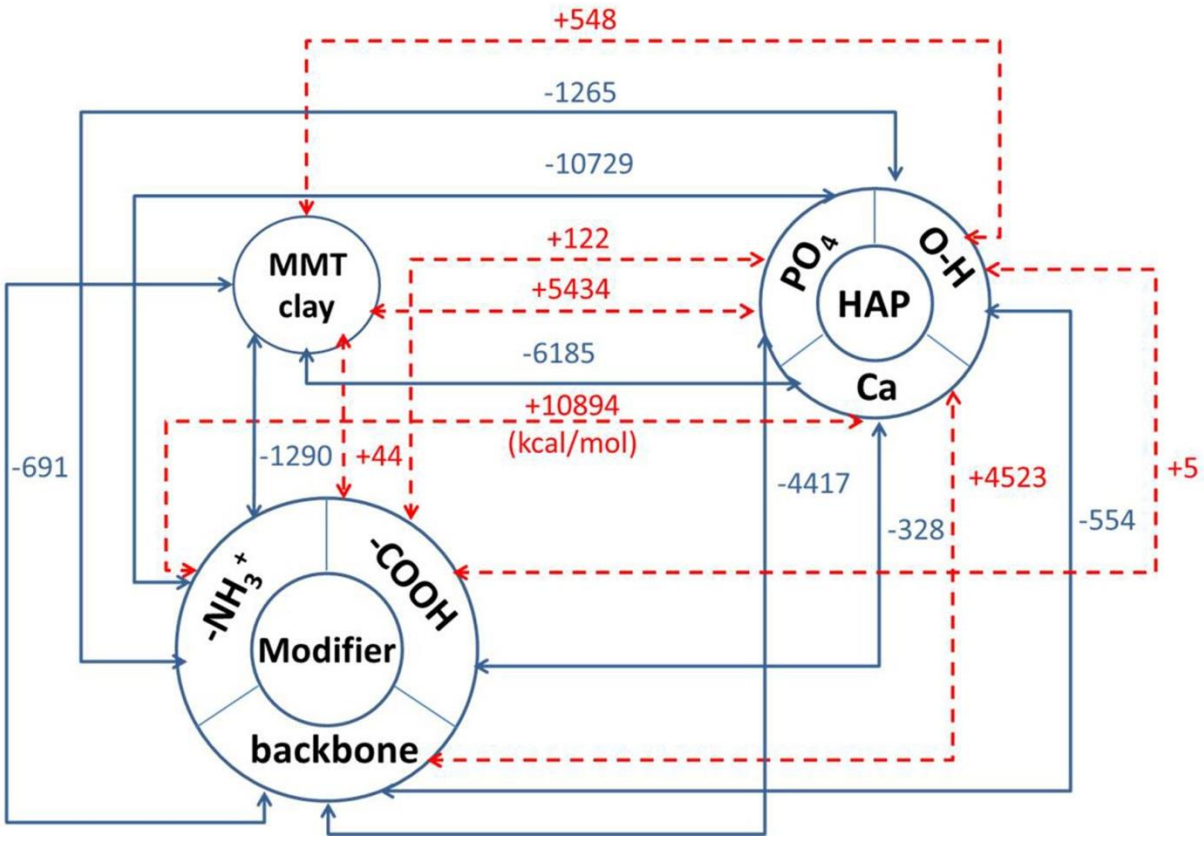

Figure 3.15. Map of total non-bonded interactions between different constituents of HAP, aminovaleric acid and MMT clay in OMMT-HAP parallel. Negative values indicate attractive interactions and positive values indicate repulsive interactions.

The results of Tables 3.2. and 3.3. were compared, and it was observed that the nature of non-bonded interaction energies similar in parallel OMMT-HAP and perpendicular OMMT-HAP. The molecular interactions between different components in both models were found to be largely electrostatic. Again, from Tables 3.2. and 3.3., it was observed that perpendicular OMMT-HAP

has significantly higher repulsive interactions between MMT clay–PO4 and MMT clay–OH than parallel OMMT-HAP, and higher attractive interaction between MMT clay–Ca than parallel OMMT-HAP.

Table 3.3. Non-bonded interaction energies between different constituents of MMT clay, aminovaleric and HAP in OMMT-HAP parallel. Attractive interactions are represented by negative value, and repulsive interactions are indicated by positive values.

Non-bonded interactions between	Electrostatic (ELE) Energy (kcal/mol)	Van der Waals (VDW) Energy (kcal/mol)	Total (VDW+ELE) Energy (kcal/mol)
MMTclay – backbone	-616	-75	-691
MMTclay – COOH	+118	-74	+44
MMTclay – NH_3^+	-1297	+7	-1290
MMTclay – PO_4	+5558	-124	+5434
MMTclay – OH	+552	-4	+548
MMTclay – Ca	-6170	-15	-6185
PO_4–backbone	-4393	-24	-4417
PO_4 – COOH	+130	-8	+122
PO_4 – NH_3^+	-10790	+61	-10729
OH – backbone	-553	-1	-554
OH – COOH	+6	-1	+5
OH – NH_3^+	-1264	-1	-1265
Ca – backbone	+4526	-3	+4523
Ca – COOH	-337	+9	-328
Ca – NH_3^+	+10896	-2	+10894

This fact is attributed to the close proximity of the large number of MMT clay atoms to HAP surface in perpendicular OMMT-HAP. This results in low values of van der Waals interactions, which depend only on the distance between two atoms. The difference in final MMT clay orientations in Figs 3.9. and 3.11. also indicate a difference in nature of interactions between MMT clay and different components of HAP. It is also seen in Tables 3.2. and 3.3. that although there is no significant change in interactions between MMT clay with modifier backbone and COOH functional group, the attractive interaction between MMT clay–NH_3^+ increases in parallel OMMT-HAP. It appears that the hydrogen atoms of NH_3^+ functional group are in close proximity of surface oxygen atoms of MMT clay and form hydrogen bonds between them. Strong attractive interactions were observed between surface oxygen atoms of MMT clay and aminovaleric acid modifier in both OMMT-HAP models. These strong electrostatic interactions result from high partial atomic charge of surface oxygen as well as of functional group atoms of aminovaleric acid and different atoms of HAP. It is also observed in the Figs 3.9. and 3.11. that hydrogen bonds have been formed between functional hydrogen atoms of NH_3^+ and oxygen atoms of PO_4 and OH groups of HAP. From Tables 3.2. and 3.3., it appears that amine group of modifier has high attractive interactions with PO_4 of HAP. This indicates that amino groups interact significantly with HAP surface equally in both directions.

Further, FTIR spectroscopy results from prior work [33] were compared with the molecular interactions among the different constituents of aminovaleric acid and MMT clay using molecular dynamic simulations. The C=O stretching band at 1702 cm^{-1} in modified MMT clay was found to shift to 1541 cm^{-1} in *in situ* HAPclay. This shift is attributed to the dissociation of COOH group of aminovaleric acid into COO^-. COOH is used as the functional group of aminovaleric acid in the MD simulation of OMMT. Hence, in this work, we have used COOH functional group in MD

simulations of OMMT-HAP to evaluate unidentate formation between oxygen atoms in C=O and Ca ions of HAP. As seen, the interactions between COOH functional group and Ca atoms are attractive in nature. The distances between oxygen atoms and Ca atoms were measured, and it was observed that C=O groups were in close vicinity of Ca atoms. Based on the above observations and also other studies[63], it is evident that chelation occurs in OMMT-HAP.

Further, NH_3^+ deformation band at 1499 cm^{-1} was observed in *in situ* HAPclay and modified MMT clay. This indicates that there is no change in position of NH_3^+ vibrations. In modified MMT clay, NH_3^+ exhibits attractive interactions with clay alone and after the introduction of HAP, NH_3^+ functional groups exhibit attractive interactions with both MMT clay as well as HAP. It is clear from the Tables 3.2. and 3.3. that non-bonded interactions between NH_3^+ and MMT clay are similar to the non-bonded interactions between NH_3^+ and HAP. These results can elucidate that no change in NH_3^+ deformation band position was observed. The band in the 1465-1407 cm^{-1} region in modified MMT clay corresponds to $–CH_2–$ deformation of aminovaleric acid molecules. These bands were observed to shift to 1458-1417 cm^{-1} region in case of *in situ* HAPclay. In Tables 3.2. and 3.3., it is observed that the backbone of aminovaleric acid interacts with HAP and MMT clay. Although interactions between backbone and Ca atoms are repulsive, the interactions between backbone–PO_4 and backbone–OH are largely attractive. Thus, the overall non-bonded interactions between HAP and modifier backbone are attractive. We have also seen the change in conformation of backbone chains of modifiers in our OMMT-HAP models compared to OMMT model.

The PO_4 groups of HAP have high negative partial charge of -3.0. As seen in the Tables 3.2. and 3.3., this results in the strong non-bonded interactions between PO_4 and different constituents of aminovaleric acid and MMT clay. Shifts in ν_6 and ν_3 band positions of phosphate

ions in HAP compared to OMMT-HAP [33], may be attributed to the high attractive and repulsive interactions of PO_4 group with its neighboring atoms in OMMT-HAP as seen in Tables 3.2. and 3.3.. The band corresponding to Si-O stretching vibrations shifts to 1119 cm^{-1} in *in situ* HAPclay from 1130 cm^{-1} in case of modified MMT clay. It has seen in Figs 3.9. and 3.11. that functional group hydrogen atoms of COOH and NH_3^+ form hydrogen bonds with surface oxygen atoms of MMT clay. The number of hydrogen bonds increases significantly in OMMT-HAP models compared to OMMT model.

3.6. Conclusions

- In this study, we have constructed representative models of MMT clay with aminovaleric acid and organically modified MMT clay with HAP. The molecular model with d-spacing closest to experimental d-spacing (12.85 Å) and balanced charge system was selected as representative OMMT model. This model has nine protonated aminovaleric molecules per MMT clay sheet and d-spacing = 14.08 Å.
- In the OMMT model, we have observed that functional group hydrogen atoms of seven out of eighteen aminovaleric modifier molecules satisfy the criteria of hydrogen bond interactions with surface oxygen atoms of MMT clay. This indicates that functional groups of aminovaleric acid are strongly interacting with interlayer MMT clay sheets.
- XRD results show 0.5 Å decrease in d_{001}-spacing in *in situ* HAPclay. The d-spacing of OMMT in OMMT-HAP perpendicular (13.92 Å) and parallel (13.08 Å) models are found to be smaller than the OMMT model d-spacing.
- High attractive non-bonded interactions are observed in between backbone of modifier molecules and HAP. These new interactions between backbone and HAP in OMMT-HAP compared to OMMT change the $–CH_2–$ deformation of aminovaleric acid molecules.

- High attractive and repulsive interactions are found between PO_4^{3-} and MMT clay, as well as aminovaleric molecules in OMMT-HAP perpendicular and parallel models. Large values of non-bonded interactions in OMMT-HAP indicate the influence of neighboring environment on phosphate ions in *in situ* HAPclay.
- A large numbers of hydrogen bonds formed between functional group hydrogen atoms of modifier and MMT clay in OMMT-HAP as compared to OMMT indicate that HAP interacts with clay through the aminovaleric acid. It appears that aminovaleric acid plays an important role in enhancing the interactions between OMMT clay-HAP systems.
- The complementary modeling and experimental approach described in this work provides detailed molecular scale insight into complex nanoscale materials systems.

3.7. References

[1] M. Sotomayor, K. Schulten, Science 316 (2007) 1144-1148.

[2] A.R. Sedaghat, A. Sherman, M.J. Quon, American Journal of Physiology-Endocrinology and Metabolism 283 (2002) E1084-E1101.

[3] Y. Li, X. Chen, N. Gu, Journal of Physical Chemistry B 112 (2008) 16647-16653.

[4] D. Raabe, B. Sander, M. Friak, D. Ma, J. Neugebauer, Acta Materialia 55 (2007) 4475-4487.

[5] D. Lacroix, J.A. Planell, P.J. Prendergast, Philosophical Transactions of the Royal Society a-Mathematical Physical and Engineering Sciences 367 (2009) 1993-2009.

[6] E. Jabbarzadeh, C.F. Abrams, Tissue Engineering 13 (2007) 2073-2086.

[7] R. Langer, J. Vacanti, Science 260 (1993) 920-926.

[8] D.W. Hutmacher, Biomaterials 21 (2000) 2529-2543.

[9] V. Karageorgiou, D. Kaplan, Biomaterials 26 (2005) 5474-5491.

[10] S.J. Hollister, Nature materials 4 (2005) 518-524.

[11] K. Hing, S. Best, W. Bonfield, Journal of Materials Science: Materials in Medicine 10 (1999) 135-145.

[12] K. Rezwan, Q.Z. Chen, J.J. Blaker, A.R. Boccaccini, Biomaterials 27 (2006) 3413-3431.

[13] H. Wang, Y. Li, Y. Zuo, J. Li, S. Ma, L. Cheng, Biomaterials 28 (2007) 3338-3348.

[14] C.M. Botelho, R.A. Brooks, S.M. Best, M.A. Lopes, J.D. Santos, N. Rushton, W. Bonfield, Journal of Biomedical Materials Research Part A 79A (2006) 723-730.

[15] N. Olmo, Martı, amp, x, A.I. n, A.J. Salinas, J. Turnay, R. Vallet, Marı, M.A. Lizarbe, Biomaterials 24 (2003) 3383-3393.

[16] T. Iwatsubo, K. Sumaru, T. Kanamori, T. Shinbo, T. Yamaguchi, Biomacromolecules 7 (2005) 95-100.

[17] S.P. Nukavarapu, S.G. Kumbar, J.L. Brown, N.R. Krogman, A.L. Weikel, M.D. Hindenlang, L.S. Nair, H.R. Allcock, C.T. Laurencin, Biomacromolecules 9 (2008) 1818-1825.

[18] D. Verma, K.S. Katti, D.R. Katti, B. Mohanty, Materials Science and Engineering: C 28 (2008) 399-405.

[19] A. Okada, M. Kawasumi, A. Usuki, Y. Kojima, T. Kurauchi, O. Kamigaito, D. Schaefer, J. Mark, Polymer based molecular composites, MRS symposium proceedings, vol 171, 1990, p. 45.

[20] E.P. Giannelis, Advanced Materials 8 (1996) 29-35.

[21] M. Pramanik, S.K. Srivastava, B.K. Samantaray, A.K. Bhowmick, Journal of Applied Polymer Science 87 (2003) 2216-2220.

[22] R.K. Bharadwaj, Macromolecules 34 (2001) 9189-9192.

[23] E. Picard, A. Vermogen, J.F. Gérard, E. Espuche, Journal of Membrane Science 292 (2007) 133-144.

[24] A. Leszczyńska, J. Njuguna, K. Pielichowski, J. Banerjee, Thermochimica Acta 453 (2007) 75-96.

[25] M.A. Paul, M. Alexandre, P. Degée, C. Henrist, A. Rulmont, P. Dubois, Polymer 44 (2003) 443-450.

[26] A.J. Mieszawska, J.G. Llamas, C.A. Vaiana, M.P. Kadakia, R.R. Naik, D.L. Kaplan, Acta Biomaterialia 7 (2011) 3036-3041.

[27] P. Maiti, C.A. Batt, E.P. Giannelis, Biomacromolecules 8 (2007) 3393-3400.

[28] D. Sikdar, S.M. Pradhan, D.R. Katti, K.S. Katti, B. Mohanty, Langmuir 24 (2008) 5599-5607.

[29] K.S. Katti, D.R. Katti, R. Dash, Biomedical Materials 3 (2008) 12.

[30] A.H. Ambre, Nanoclay Based Composite Scaffolds For Bone Tissue Engineering Applications, Journal of Nanotechnology for Engineering and Medicine, vol 1, ASME, 2010, p. 031013.

[31] K.S. Katti, A.H. Ambre, N. Peterka, D.R. Katti, Philosophical Transactions of the Royal Society a-Mathematical Physical and Engineering Sciences 368 (2010) 1963-1980.

[32] A.H. Ambre, D.R. Katti, K.S. Katti, Journal of Biomedical Materials Research Part A 101 (2013) 2644-2660.

[33] A. Ambre, K.S. Katti, D.R. Katti, Materials Science & Engineering C-Materials for Biological Applications 31 (2011) 1017-1029.

[34] A. Redondo, R. LeSar, Annual Review of Materials Research 34 (2004) 279-314.

[35] R.A. Latour, Current Opinion in Solid State & Materials Science 4 (1999) 413-417.

[36] N. Almora-Barrios, N.H. de Leeuw, Langmuir 26 (2010) 14535-14542.

[37] N. Almora-Barrios, K.F. Austen, N.H. de Leeuw, Langmuir 25 (2009) 5018-5025.

[38] R. Bhowmik, K.S. Katti, D. Katti, Polymer 48 (2007) 664-674.

[39] R. Bhowmik, K.S. Katti, D.R. Katti, Journal of Engineering Mechanics-Asce 135 (2009) 413-421.

[40] R. Bhowmik, K.S. Katti, D.R. Katti, Journal of Materials Science 42 (2007) 8795-8803.

[41] S.M. Pradhan, K.S. Katti, D.R. Katti, Biomacromolecules 13 (2012) 8.

[42] Katti D. R., Pradhan S. M., Katti K. S., J Biomech 43 (2010) 1723-1730.

[43] A. Gautieri, S. Vesentini, A. Redaelli, M.J. Buehler, Nano Letters 11 (2011) 757-766.

[44] D.K. Dubey, V. Tomar, Journal of Materials Science-Materials in Medicine 21 (2010) 161-171.

[45] D.K. Dubey, V. Tomar, Journal of Computational and Theoretical Nanoscience 7 (2010) 1306-1316.

[46] D.K. Dubey, V. Tomar, Materials Science & Engineering C-Materials for Biological Applications 29 (2009) 2133-2140.

[47] N. Almora-Barrios, N.H. De Leeuw, Crystal Growth & Design 12 (2011) 756-763.

[48] N.H. de Leeuw, Geochimica Et Cosmochimica Acta 74 (2010) A220-A220.

[49] A. Rimola, M. Corno, C.M. Zicovich-Wilson, P. Ugliengo, Journal of the American Chemical Society 130 (2008) 16181-16183.

[50] M. Corno, A. Rimola, V. Bolis, P. Ugliengo, Physical Chemistry Chemical Physics 12 (2010) 6309-6329.

[51] J. Hum, K.W. Luczynski, P. Nooeaid, P. Newby, O. Lahayne, C. Hellmich, A.R. Boccaccini, Strain 49 (2013) 431-439.

[52] A. Fritsch, C. Hellmich, L. Dormieux, Philosophical Transactions of the Royal Society a-Mathematical Physical and Engineering Sciences 368 (2010) 1913-1935.

[53] B.S. Harrison, A. Atala, Biomaterials 28 (2007) 344-353.

[54] R. Shenhar, V.M. Rotello, Accounts of Chemical Research 36 (2003) 549-561.

[55] B.R. Brooks, R.E. Bruccoleri, B.D. Olafson, D.J. States, S. Swaminathan, M. Karplus, Journal of Computational Chemistry 4 (1983) 187-217.

[56] D. Sikdar, D.R. Katti, K.S. Katti, Langmuir 22 (2006) 7738-7747.

[57] N. Skipper, F.R.C. Chang, G. Sposito, Clays and Clay Minerals 43 (1995) 285-293.

[58] N. Skipper, G. Sposito, F.R.C. Chang, Clays and Clay minerals 43 (1995) 294-303.

[59] B.J. Teppen, K. Rasmussen, P.M. Bertsch, D.M. Miller, L. Schäfer, The Journal of Physical Chemistry B 101 (1997) 1579-1587.

[60] D.R. Katti, P. Ghosh, S. Schmidt, K.S. Katti, Biomacromolecules 6 (2005) 3276-3282.

[61] D.R. Katti, S.R. Schmidt, P. Ghosh, K.S. Katti, Clays and Clay Minerals 53 (2005) 171-178.

[62] S.R. Schmidt, D.R. Katti, P. Ghosh, K.S. Katti, Langmuir 21 (2005) 8069-8076.

[63] R. Bhowmik, K.S. Katti, D. Verma, D.R. Katti, Materials Science and Engineering: C 27 (2007) 352-371.

[64] J. Phillips, R. Braun, W. Wang, J. Gumbart, E. Tajkhorshid, E. Villa, C. Chipot, R. Skeel, L. Kalé, K. Schulten, Journal of Computational Chemistry 26 (2005) 1781-1802.

[65] W. Humphrey, A. Dalke, K. Schulten, Journal of Molecular Graphics 14 (1996) 33-38.

[66] D. Verma, K. Katti, D. Katti, Journal of Biomedical Materials Research Part A 78A (2006) 772-780.

[67] G.A. Jeffrey, W. Saenger, Hydrogen bonding in biological structures, Springer-Verlag Berlin, 1994.

[68] S. Hauptmann, H. Dufner, J. Brickmann, S.M. Kast, R.S. Berry, Physical Chemistry Chemical Physics 5 (2003) 635-639.

CHAPTER 4. EVALUATING MOLECULAR INTERACTIONS IN POLYCAPROLACTONE - BIOMINERALIZED HYDROXYAPATITE NANOCOMPOSITES USING STEERED MOLECULAR DYNAMICS[3]

This chapter presents the molecular interactions and mechanical response in a complex polycaprolactone-biomineralized hydroxyapatite nanocomposite system. The contents of the chapter have been published in A. Sharma, S. Payne, K.S. Katti, D.R. Katti; "Evaluating molecular interactions in polycaprolactone-biomineralized hydroxyapatite nanocomposites using steered molecular dynamics", JOM 67, 4 (2015).

4.1. Introduction

Recent developments in multiscale simulation based design of biomaterials have improved our understanding towards the functioning of complex biological processes [1-4]. Multiscale design based models provides a unique opportunity to investigate different parameters and variables of biomaterials that are difficult to determine experimentally. Scaffolds with tailored chemical, physical, mechanical and geometrical properties can be developed using multiscale design models for bone tissue engineering applications [5]. The increasing number of bone grafts done every year results in an increased need for advanced biomaterials that can heal/replace damaged tissues and organs inside the body. Since early 1990s tissue engineering has evolved as

[3] The material in this chapter was co-authored by Anurag Sharma and Dinesh Katti. Anurag Sharma had primary responsibility for collecting samples in the field and for interviewing users of the test system. Anurag Sharma was the primary developer of the conclusions that are advanced here. Anurag Sharma also drafted and revised all versions of this chapter. Dinesh Katti served as proof reader and checked the math in the statistical analysis conducted by Anurag Sharma.

a multidisciplinary field aiming to improve human health by providing a biological alternative which can support, maintain and regenerate damaged tissues [6]. Tissue engineering scaffolds are three dimensional matrices used for initial cell attachment and tissue formation and subsequently degrade inside the body. Polymer based composites are widely used as tissue engineering scaffolds. They can be easily tailored at the nanoscale to macro scale level depending on their biological applications. Nano-scale polymer composites show enhanced physical and chemical properties due to their large surface to volume ratios and role of molecular interactions. However, lower mechanical properties of the replaced implant materials as compared to the natural bone/organs result in inadequate performance and limit their use. Studies have shown that over a period of time this mechanical property mismatch can lead to severe wear and in some cases broken implants inside the body [7]. Designing polymeric scaffolds with good biological properties, suitable porosity for tissue formation and adequate mechanical properties are some of the significant challenges in bone tissue engineering applications.

Nanoclays such as Na-montmorillonite [$NaSi_{16}(Al_6FeMg)O_{20}(OH)_4$] have been used to enhance antibacterial properties, thermal properties, and mechanical properties of polymer clay nanocomposites (PCN) [8-13]. Nanoindentation experiments have shown that small amount of modified nanoclay can significantly improve the mechanical properties of PCN [14]. Molecular interactions studies of PCN performed in our group revealed that the backbone and functional groups of polymer and modifier behave differently in the PCN system and these molecular interactions control the mechanical properties of PCN [15]. It was found that molecular interactions between intercalated nanoclay and polymer create a zone of influence outside the clay gallery. High attractive and repulsive interactions between polymer and modifier disturb the polymer near the clay gallery creating a ripple effect in polymer. Crystallinity of polymer in the

disturbed zone was found to be different than bulk undisturbed polymer. AFM analysis showed that this disturbance in the polymer exists for a distance of about 200-300 A [16]. Based on these studies [16] the concept of 'altered phase polymer' in PCN was introduced. Indentation studies showed that elastic modulus of the altered polymer is significantly higher than the unaltered polymer. Hydroxyapatite is widely used as synthetic biomaterials due to its high biological affinity towards proteins, good osteoconductivity and biocompatibility [17-19]. Hydroxyapatite along with other minerals such as sodium, silicon, carbonate, etc. influences the mineralization process in the bone.[20] It is used as inorganic bioactive filler in biocompatible polymers to make polymeric scaffolds with a bone like mechanical properties [21-23]. One such biopolymer is polycaprolactone (PCL). PCL is a biodegradable and biocompatible polymer, which has shown potential applications for bone repair [24]. Prior work [25] has also shown good bioactivity and mechanical properties of HAP/PCL composite. Our modeling studies also indicate that HAP strongly influences PCL when the two phases are in close proximity of each other [26]. In another study, organoclays were added into PCL to enhance its antibacterial, mechanical and barrier properties. These PCL/organoclay nanocomposites showed 36% increase in modulus compared to pristine PCL [27].

Both experimental and theoretical approaches have been used to investigate the mechanical properties of nanobiocomposites [28]. Computational methods such as density functional theory, ab initio and molecular dynamics were carried out to understand the interactions between HAP and collagen in natural bone, PCL and HAP in nanocomposites, adsorption mechanism of aminoacids on HAP surfaces [29-32]. Chiatti et al. [33] used quantum mechanical modeling to study CO adsorption on HAP surface for recognition of surface termination of HAP nanoparticles. It was observed that the adsorption between Ca^{2+} at HAP surface and C=O is largely driven by

dispersive and electrostatic interactions. Recently, experimental and simulations models were proposed, which suggest the mechanism of amorphous calcium phosphate formation at the early stage of HAP mineralization [34-36].

Steered molecular dynamics (SMD) method is a modeling tool, which is used to analyze the mechanical response of biomolecular systems at molecular level [37]. In SMD, mechanical responses and conformational changes in the biomolecules are calculated by applying external point forces on the desired atoms. Extensive research has been done to study the deformation of proteins, minerals, collagen, DNA, etc. using SMD [30, 31, 38-40]. Recently, we have carried out SMD simulation on the full length collagen and revealed multilevel structural hierarchy in the collagen structure [41]. Deformation mechanisms of extended collagen were found to be depended on helical conformations at three different levels in collagen. In another study for bone biomaterials, a single tropocollagen molecule was sandwiched between two HAP crystals and mechanical properties were calculated by applying shear loading on the HAP crystals. It was suggested that formation and breaking of inter-molecular H-bonds play an important role in mechanical performance of the composite [42]. Prior studies in our group have used constant-force steered molecular dynamics simulations to evaluate the nanomechanical properties of clay nanocompostie (PCN) [16]. In this procedure, compressive point loads were applied on the surface oxygen atoms of the intercalated MMT clay sheet and deformation response of interlayer was calculated [43-45]. Elastic moduli and Poisson's ratio of PCN system were evaluated by varying point loads. Further, the responses of SMD simulations of PCN were compared to the nanoindentation and AFM experimental results. It was found that elastic modulus values estimated from constant-force SMD simulations have the same order of magnitude as the elastic modulus values obtained from the 'modulus mapping' of PCN system.

Considering desirable mechanical and biological properties of modified nanoclay, HAP and PCL, we have designed a PCL based polymeric scaffolds by adding PCL biopolymer into the modified nanoclay-HAP hybrid (in situ HAPclay) [46]. We found that this system is conducive to mesenchymal stem cells (MSC), allow cell differentiation and form mineralized extracellular matrix (ECM) similar to the human bone. Nanomechanical tests on PCL/in situ HAPclay have showed more than 400% increase in elastic modulus. Mechanical properties at structure level also showed jump of nearly 200%.

In this work, we designed a representative molecular model of PCL/in situ HAPclay (OMMT-HAP-PCL) system using molecular dynamics simulation approach. The representative model was validated by experimentally observed material density, XRD, FTIR results and minimum energy conformation. Molecular interactions between different constituents of OMMT-HAP-PCL model were studied to understand the role of MMT clay, modifier, HAP and PCL in the system. Further, SMD simulations were conducted to evaluate the nanomechanical properties of OMMT-HAP-PCL. Elastic properties of representative model calculated from SMD were then compared to the nanoindentation results of the PCL/in situ HAPclay system.

4.2. Materials and Methods

4.2.1. Materials

Na-montmorillonite (SWy-2, Crook County, Wyoming, USA) was obtained from the Clay Minerals Repository at the University of Missouri, Columbia, 5-aminovaleric acid, polycaprolactone (PCL) (average Mn580,000) and 1,4 dioxane (anhydrous,99.8 %) were obtained from Sigma Aldrich, Na_2HPO_4 from J.T.Baker and $CaCl_2$ was obtained from EM sciences.

4.2.2. Preparation of Polycaprolactone (PCL)/*In situ* Hydroxyapatite (OMMT-HAP) Clay

PCL/in situ HAPclay films were prepared according to the method described in our previous studies [46]. In summary, 0.4 g of in situ HAPclay (preparation procedure described here [47]) was sonicated in 16 mL of 1.4 dioxane. The sonicated solution was then added to the PCL solution (3.6 g of PCL dissolved in 40 mL of 1,4 dioxane) at room temperature. The composite solution was stirred for another 2 h. The final solution was then transferred to glass slide and dried for 8 hours to obtained composite films for TEM analysis.

4.2.3. X-Ray Diffraction

X-ray diffraction analysis of PCL/in situ HAPclay was done on diffractometer (Philips X'pert, Almelo, Netherlands) equipped with secondary monochromator and Cu tube using CuKα radiation of wavelength 1.54056 Å. The scan rate of 2^0/min and scan range of $2\theta = 2\text{-}30^0$ were used.

4.2.4. Transmission Electron Microscopy

The PCL/*in situ* HAPclay film sample was embedded in Epon/Araldite and thin sectioned using an RMC MT-XL ultramicrotome equipped with a diamond knife. The images were taken using a JEOL JEM-2100 LaB6 transmission electron microscope operating at 200 kV.

4.3. Model Construction

4.3.1. Computational Methodology

In this work, molecular dynamics technique was used to build a representative model of polycaprolactone/in situ HAPclay (OMMT-HAP-PCL) to investigate the interactions between montmorillonite (MMT) clay, 5-aminovaleric acid molecules, hydroxyapatite (HAP) and polycaprolactone (PCL) chains in the OMMT-HAP-PCL model. The module 'Builder' of InsightII™ 2005 of Accelrys, Inc., San Diego, CA, USA was used for constructing MMT, HAP,

PCL and aminovaleric acid molecular models. In our previous work [1], representative model of organically modified montmorillonite (OMMT) was built by comparing the results from XRD and transmission Fourier transform infrared spectroscopy and MD simulation (d-spacing and minimum energy conformation) results. Two layers of MMT sheets were used to construct the representative model of intercalated OMMT. Each MMT layer contains 6 and 3 unit cells in x and y direction, respectively [48]. In MMT clay sheets, aluminum octahedral layer was sandwiched between two layers of silica tetrahedral. An isomorphous substitution created negative nine charges for each clay sheet which was balanced by protonated aminovaleric acid molecules. Therefore, molecular model with 9 protonated aminovaleric acid molecules per MMT clay sheet and have d-spacing closer to experimental d-spacing was selected as representative OMMT model. Similarly, the intercalated in situ HAPclay (OMMT-HAP) model was constructed by placing final representative OMMT model perpendicular to HAP surface. The final representative OMMT-HAP model was selected by comparing MD (d-spacing, molecular interactions and formation of calcium bridge) results with experimental results (XRD, TEM and transmission Fourier transform infrared spectroscopy) results [1].

4.3.2. Model of Organically Modified Montmorillonite Clay - Hydroxyapatite - Polycaprolactone

X-ray diffraction results of PCL/in situ HAPclay indicate exfoliated system. Fig 4.1. shows transmission electron microscopy photograph of polycaprolactone/in situ HAPclay film. As seen clay sheets are well dispersed in the PCL polymer matrix. Hence, in the OMMT-HAP-PCL model we have used one MMTclay sheet and 9 protonated aminovaleric acid with (001) HAP surface. As seen in Fig 4.2. MMT clay sheet is sandwiched between nine protonated aminovaleric molecules and HAP surface is placed perpendicular to the sheet. The dimensions of MMT clay

sheet are x = 31.68 Å, y = 27.44 Å and z = 6.99 Å and HAP surface parameters are $\alpha = 90^0$, $\beta = 90^0$, $\gamma = 120^0$ and a = 33.836 Å, b = 33.836 Å, c = 14.093 Å. Additional details about the MMT clay sheet and HAP surface construction and MD simulations procedure can be found in our earlier studies [29, 44, 48].

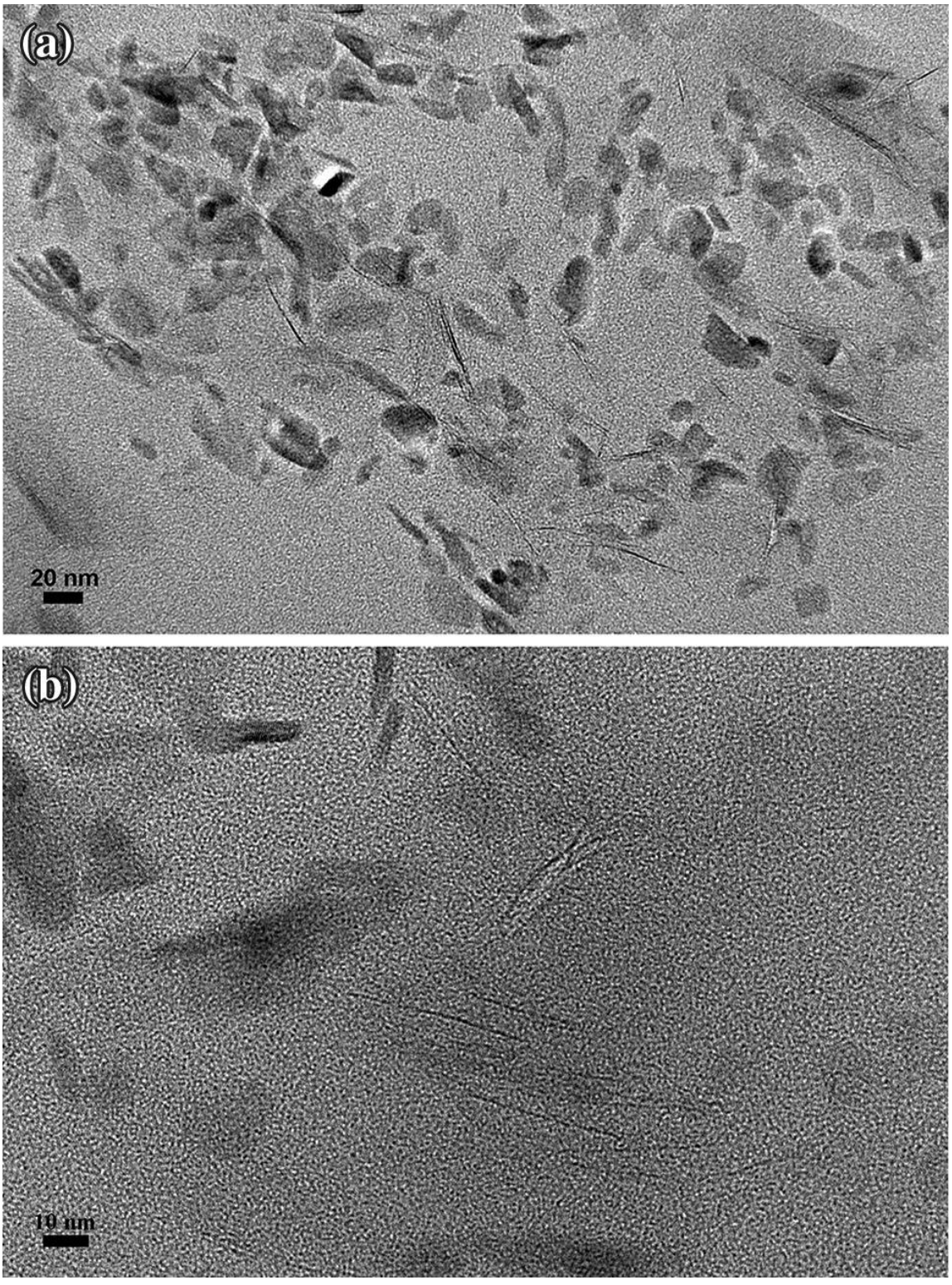

Figure 4.1.(a. b) TEM image of PCL/in situ HAPclay. Clay sheets appear to have dispersed in PCL polymer matrix. The clay sheets can been observed in both parallel and perpendicular orientations.

The MD simulation methodology for annealing the PCL polymer to obtain globally minimized conformation was described previously [26]. Each PCL chain used in this study consists of fourteen monomers. Partial charges on each atoms and CHARMm force field parameters were obtained from Rahul et al.[26]. PCL model was first minimized using MD technique at 0 bar pressure and 0 K temperature. Further, temperature was increased to 300 K at 0 bar. Then, pressure was increased to 1 atm in four equal steps. This was followed by heating from 300 K to 500 K in four steps, each of 50 K. Thereafter, temperature was again reduced to room temperature in same no. of steps. The final optimized geometry of a PCL model with lowest energy is shown in Fig 4.3.

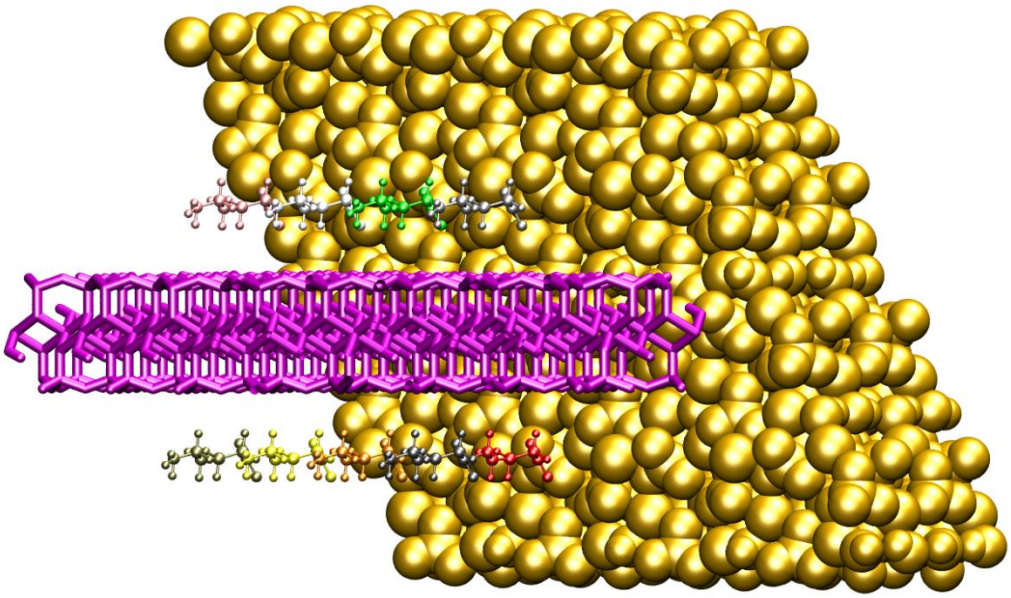

Figure 4.2. Initial structure of organically modified MMT clay –Hydroxyapatite (OMMT-HAP). HAP represented as ball model, aminovaleric molecules as ball and stick model, and MMT clay as stick model.

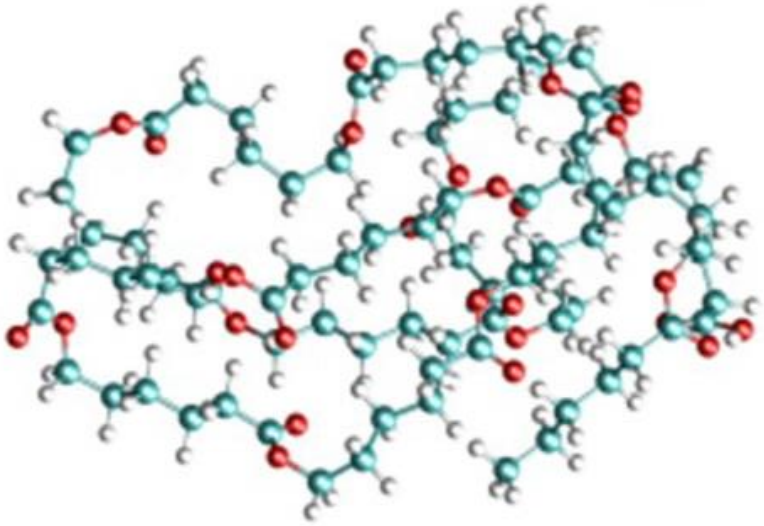

Figure 4.3. Structure of annealed polycaprolactone (PCL) chain containing 14 monomers.

For PCL/in situ HAPclay synthesis, 90 wt % of PCL were added in 10 wt % of in situ HAPclay. Therefore, in our MD model no. of PCL chains (261) were selected according to the weight percentage of PCL used in experiments. In initial structure of OMMT-HAP-PCL as shown in Fig 4.4., OMMT-HAP was surrounded by 261 PCL chains. The overall dimensions of initial OMMT-HAP-PCL model are x = 183.202 Å, y = 115.598 Å and z = 178.691 Å.

As reported earlier, in situ HAPclay mineralization indicated the chelate formation (calcium bridge) between Ca^{2+} ions and carboxylate ions of amiovaleric acid [47]. FTIR spectroscopy results showed no bonded interactions between OMMT, HAP and PCL. Experimental material density of our OMMT-HAP-PCL system was found to be 1.159 g/cc. Hence, following the procedure proposed earlier in our group for development of representative models [1, 48], we applied following three conditions to select the final representative model of OMMT-HAP-PCL:

1. The final density of the molecular model of OMMT-HAP-PCL closely matches with the experimental materials system density.
2. Formation of chelate formation between carbonyl oxygen atoms of COOH group of aminovaleric acid and Ca^{2+} ions of hydroxyapatite as seen during in situ HAPclay mineralization [1, 29, 49].
3. The final model should satisfy minimum energy conformation of the OMMT-HAP-PCL.

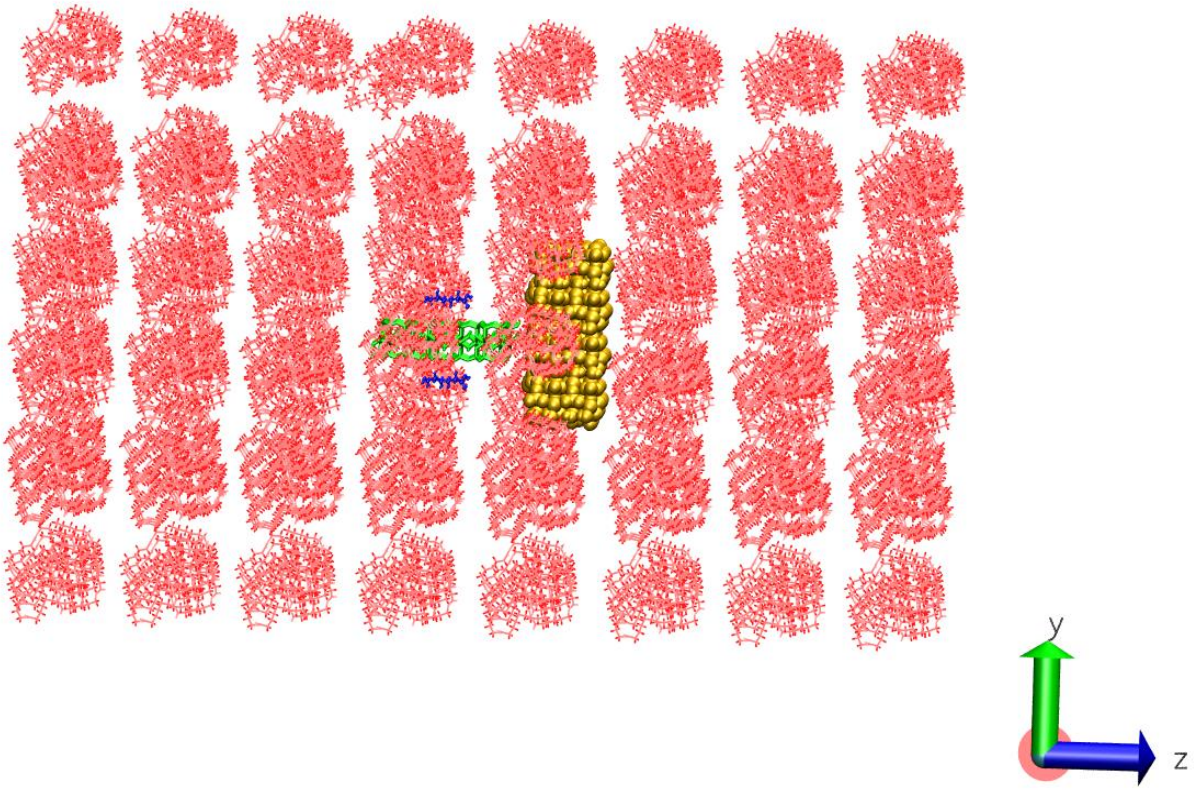

Figure 4.4. Structure of organically modified MMT clay–Hydroxyapatite–Polycaprolactone (OMMT-HAP-PCL) before minimization. HAP represented as ball model, aminovaleric molecules as ball and stick model, and MMT clay as stick model.

The final representative OMMT-HAP-PCL model obtained after satisfying above conditions and applying XRD and FTIR results is shown in Fig 4.5. The final density of OMMT-

HAP-PCL model (1.025 g/cc) that matches to experimental material density was reached after 50 ns of MD simulations. To minimize boundary effects in x, y and z directions we applied periodic boundary conditions in our OMMT-HAP-PCL model.

4.3.3. Steered Molecular Dynamics Model of Organically Modified Montmorillonite Clay - Hydroxyapatite - Polycaprolactone

Constant-force steered molecular dynamics (SMD) were carried out to study stress-strain response in representative molecular model of organically modified montmorillonite-hydroxyapatite-polycaprolactone (OMMT-HAP-PCL). We identified total of 512 (carbon and oxygen) atoms of PCL chains on the top surface and 536 (carbon and oxygen) atoms of PCL chains on the bottom surface of the OMMT-HAP-PCL system for our SMD simulations. Compressive point load was applied in the z direction on each atom of the top surface of the OMMT-HAP-PCL system (Fig 4.6.). Here, bottom surface atoms of OMMT-HAP-PCL were fixed.

4.4. Simulation Details

All molecular dynamics (MD) and steered molecular dynamics (SMD simulations in this study were performed on NAMD2.9 software [37]. VMD1.9 was used for visualization purpose and interaction energy calculation [50]. We applied isothermal-isobaric ensemble (NPT) conditions and Verlet leapfrog algorithm for running the MD simulations. The OMMT-HAP-PCL model was initially minimized at 0 atm and 0 K to attain minimum energy level. Next, temperature of the model was increased from 0 to 100, 100 to 200 and 200 to 300 K in three steps at 0 atm pressure using Langevin dynamics control method [51]. Then, the pressure was raised from 0 atm to 1 atm in four equal steps at 300 K temperature using Nose-Hoover Langevin piston control method [52]. The OMMT-HAP-PCL model was run for another 50 ns (10^{-9} s) at 300 K temperature and 1 atm pressure to achieve material system density. Montmorillonite clay sheet, aminovaleric

acid molecules and PCL chains were unconstrained in all directions. However, on HAP surface constrained were applied in all direction during the MD simulation. Total walltime used during the MD simulations was 600 hours.

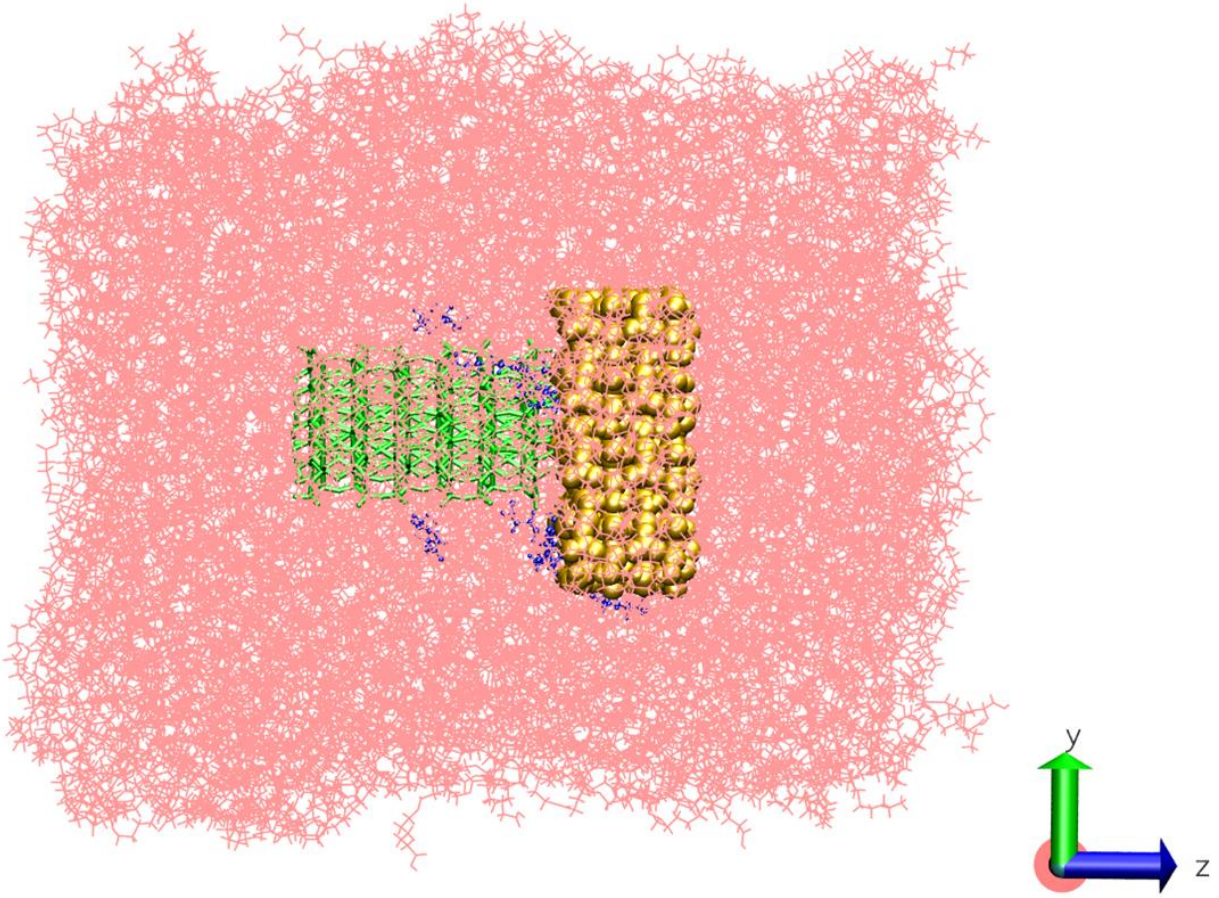

Figure 4.5. Structure of final representative model of OMMT-HAP-PCL at a temperature of 300 K and 1 atm pressure after 50 ns. HAP represented as ball model, aminovaleric molecules as ball and stick model, and MMT clay as stick model.

SMD simulations were conducted on the aforementioned representative model of OMMT-HAP-PCL system obtained from our MD simulations. The different compressive point loads applied on the each atom of top surface were 5, 6, 7, 8, 9, 10, 11, 12, 13, 14, 15, 16, 17, 18, 19, 20, 25, 30 and 35 pN. The average load bearing area in x-y plane and average initial length in z

direction of OMMT-HAP-PCL system are 7692 $Å^2$ and 93.74 Å, respectively. Each SMD simulation was carried out for 5 ns. The average deformation in each top surface atom was calculated from the final 0.25 ns of every simulation.

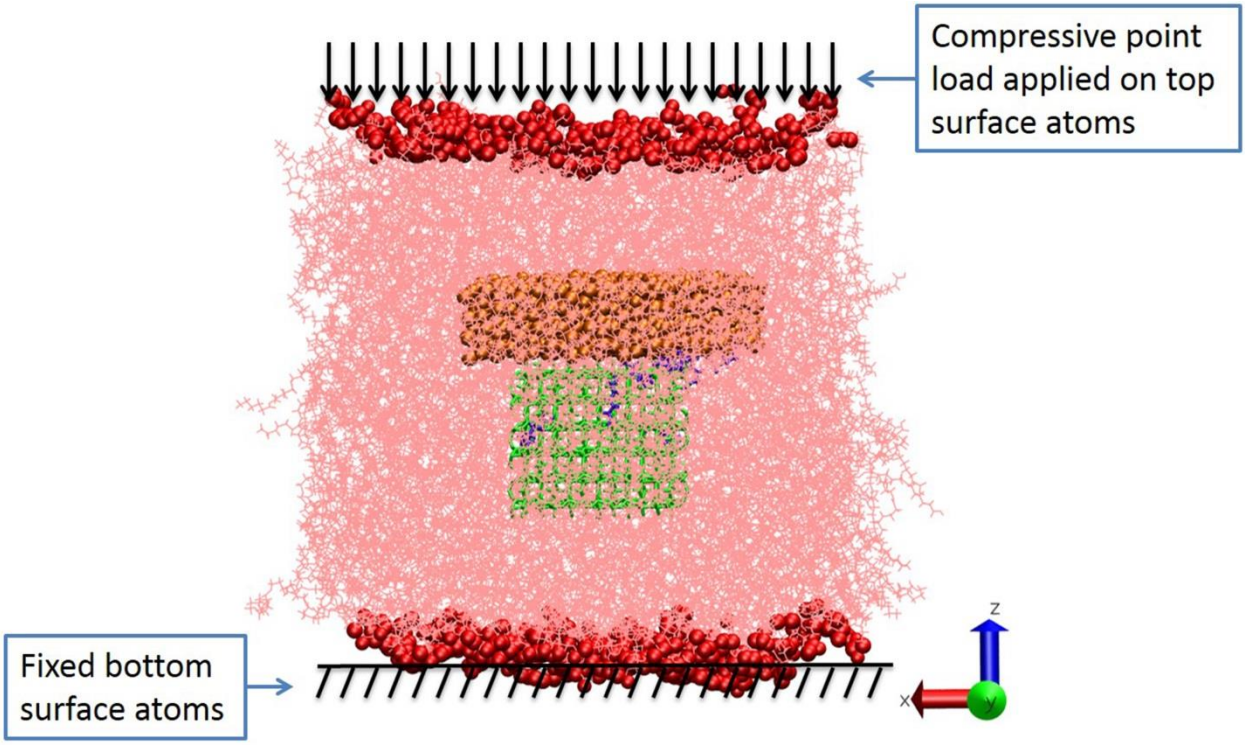

Figure 4.6. Compressive point loads are applied in the z direction on the top surface atoms of the OMMT-HAP-PCL. The bottom surface atoms of OMMT-HAP-PCL are fixed. MMT clay represents in green, aminovaleric acid in purple, HAP in orange and PCL in red. Top and bottom atoms are highlighted in dark red.

We have used 16 Å as switch and 18 Å as cut off distance for calculating van der Waals and electrostatic energy in our MD and SMD simulations. The non-bonded molecular interaction energy between different constituents of MMT clay, aminovaleric acid molecules, HAP and PCL in OMMT-HAP-PCL were calculated using MDEnergy^{TM} module of VMD. Interaction energy values of last 25 ps were averaged for final calculations. All MD and SMD simulations were run

on 256 processors (32 nodes and 8 processors) at Center for Computationally Assisted Science & Technology (CCAST) clusters at North Dakota State University.

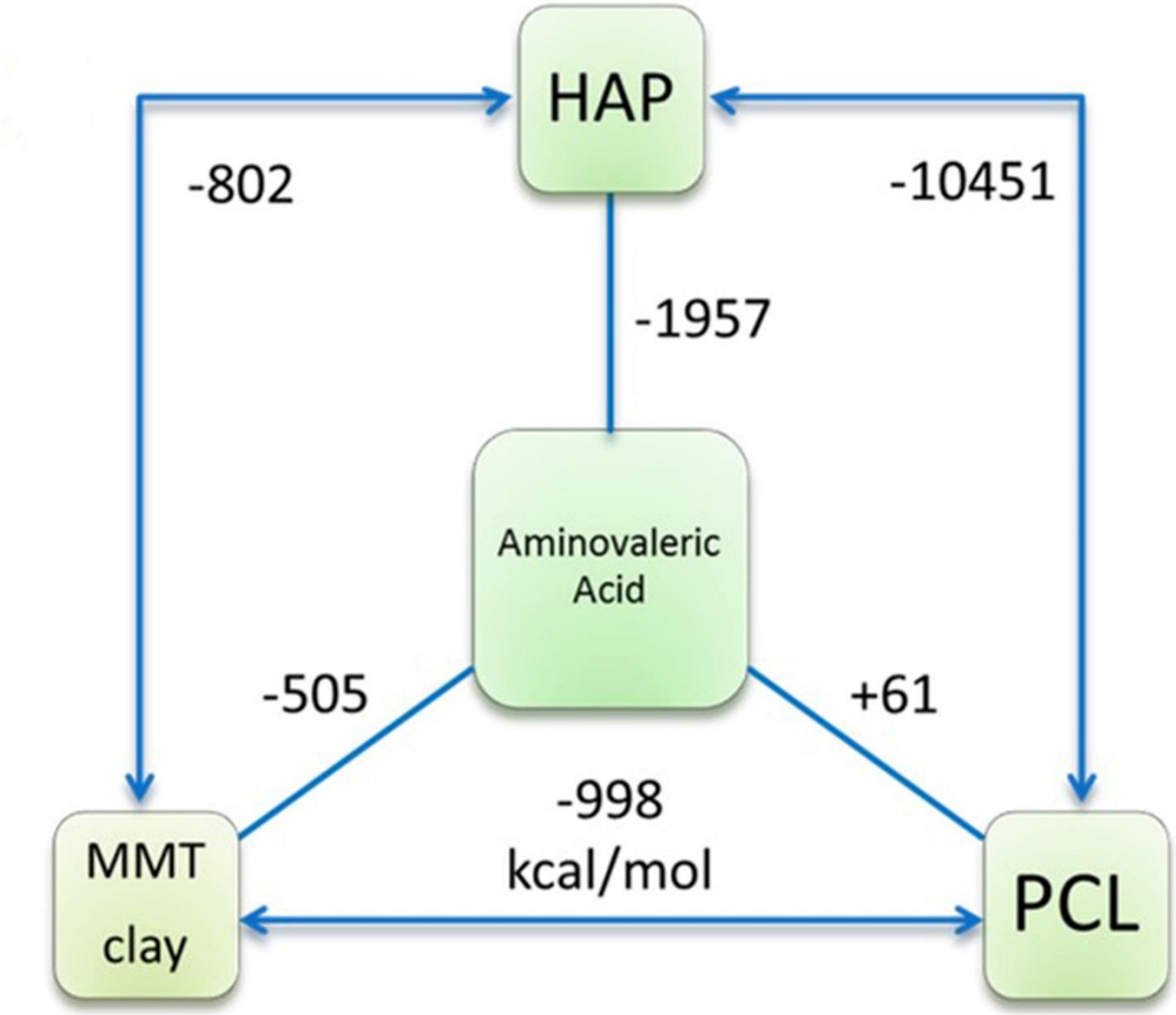

Figure 4.7. Total non-bonded interaction energies between MMT clay, HAP, aminovaleric acid and PCL in OMMT-HAP-PCL.

4.5. Results and Discussion

4.5.1. OMMT-HAP-PCL Simulations

It was observed from XRD and TEM analysis that OMMT-HAP-PCL is an exfoliated system. As seen in Fig 4.2., we placed HAP surface perpendicular to MMT clay sheet and aminovaleric molecules. Further, 261 PCL chains of 14 monomers each were placed around MMT, aminovaleric acid molecules and HAP as per wt % calculation used in OMMT-HAP-PCL synthesis. MD simulation was run for 50 ns at NPT to reach density of the model close to experimentally calculated material system density. Fig 4.5. shows the final OMMT-HAP-PCL model after 50 ns. The aminovaleric molecules were moved towards HAP surface and showed interaction with surface calcium atoms. It should be noted here that these aminovaleric molecules have carbonyl oxygen atoms that provide potential sites for chelate formation (Calcium Bridge) with calcium atoms at HAP surface. The formation of chelation indicates the mineralization of in situ HAP clay in the system. MMT clay sheet was also moved towards HAP surface and changed its orientation. Similar change in MMT clay sheet was also observed in our previous study of OMMT-HAP representative model [1].

4.5.2. Interactions in OMMT-HAP-PCL

The non-bonded interaction energies between MMT clay, aminovaleric acid molecules, HAP and PCL chains in OMMT-HAP-PCL are presented in Fig 4.7. The total non-bonded interaction energy between the two constituents includes electrostatic energy (ELE) and van der Waals energy (VDW). In NAMD, van der Waals energy term is the summation of van der Waals energy and hydrogen bond energy. The positive values of energy indicate repulsive interaction and negative values represent attractive interaction between the two constituents of the system. Fig 4.7. shows strong attractive interactions between HAP and PCL (-10451 kcal/mol), HAP and

aminovaleric acid (-1957 kcal/mol), HAP and MMT clay (-802 kcal/mol), MMT clay and PCL (-998 kcal/mol) and MMT clay and aminovaleric acid (-505 kcal/mol). Repulsive interaction between PCL and aminovaleric acid molecules (+61 kcal/mol) is mainly due to high electrostatic energy between these constituents. Our OMMT-HAP-PCL system consists of four different materials. Therefore, to understand the molecular interactions of the system we divided OMMT-HAP-PCL system in different constituents. As shown in Fig 4.8., the HAP has categorized into Ca, OH and PO_4 constituents, aminovaleric acid modifier into COOH, NH_3^+ and backbone constituents and PCL into functional group and backbone constituents.

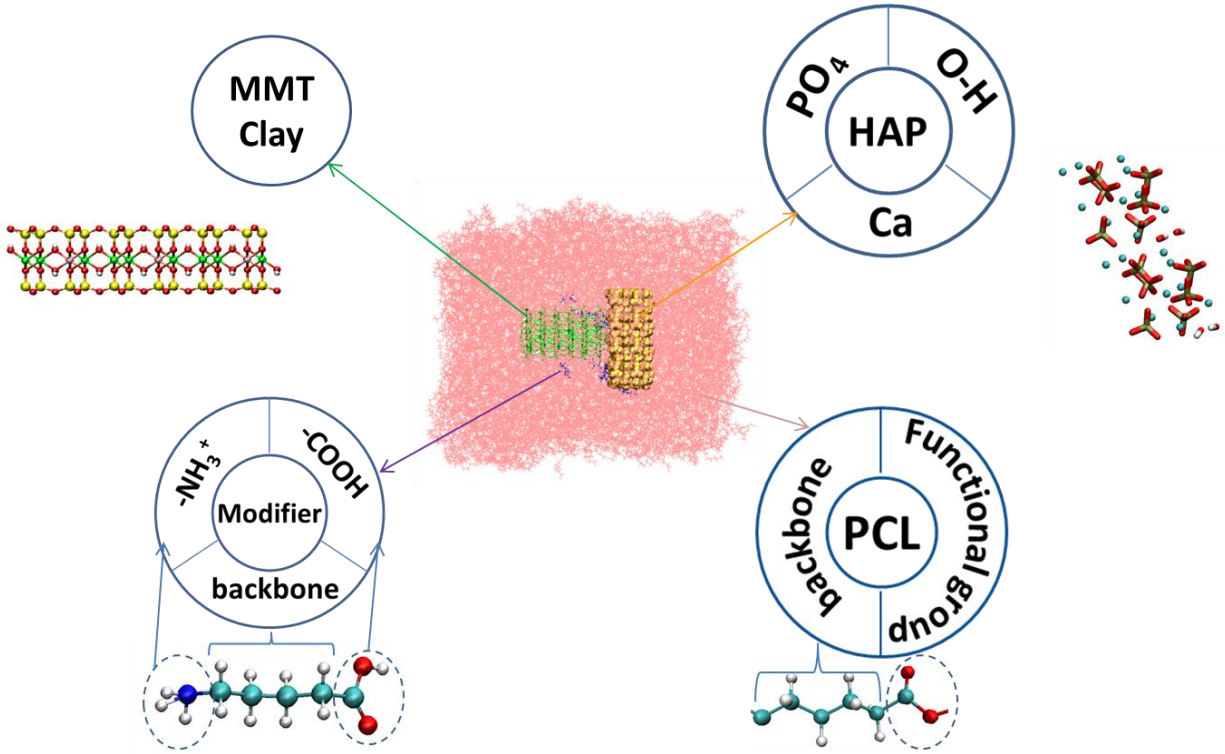

Figure 4.8. Different constituents of HAP, aminovaleric acid modifier, MMTclay and PCL in OMMT-HAP-PCL.

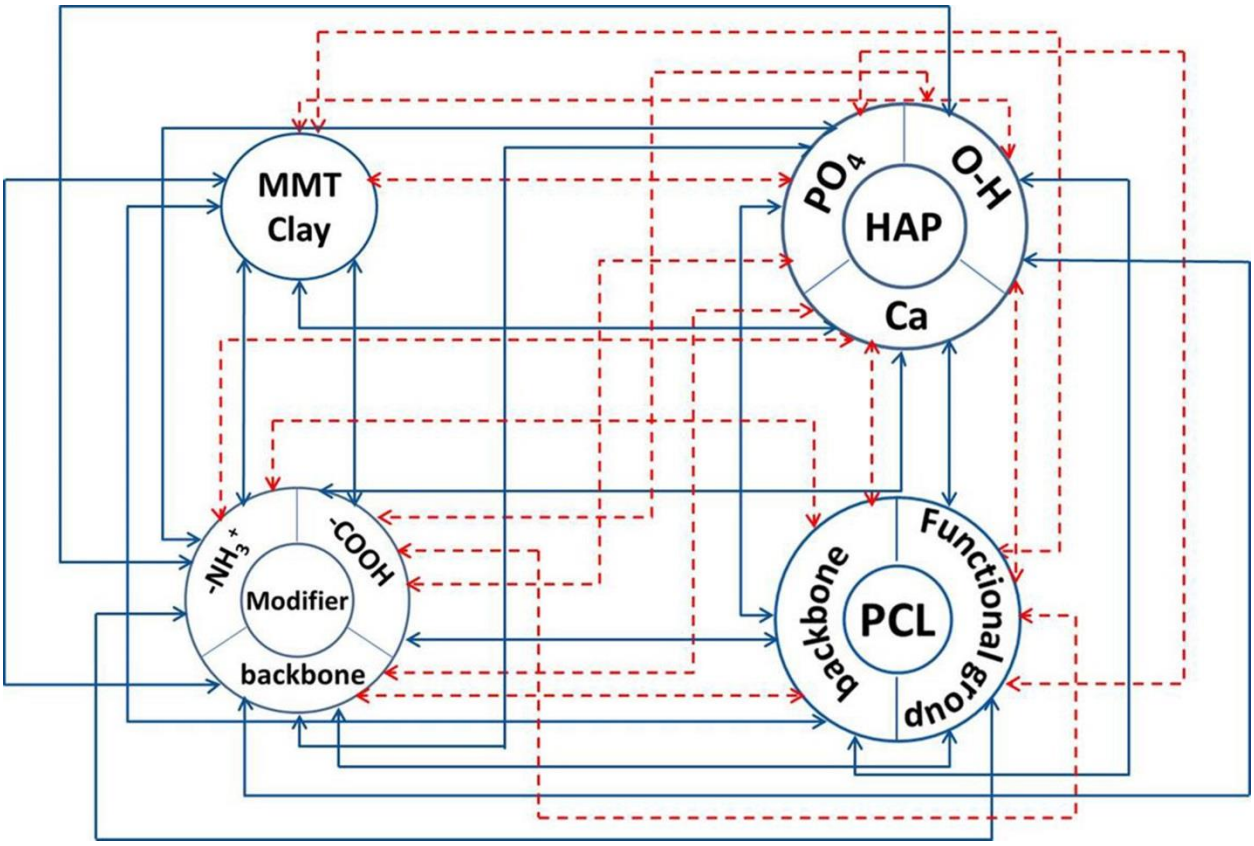

Figure 4.9. Map of total non-bonded interactions between different constituents of MMT clay, aminovaleric acid modifier, HAP and PCL in OMMT-HAP-PCL. Solid blue lines indicate attractive interactions and dotted red lines indicate repulsive interactions.

Fig 4.9. shows the map of total non-bonded interaction energy between different constituents in OMMT-HAP-PCL. It can be seen that it is a very complex system and the detail analysis of molecular interaction will be helpful in further tailoring of the material system. The solid blue lines represent attractive interactions and dotted red lines represent repulsive interactions between two constituents in the OMMT-HAP-PCL model. Molecular interactions between different constituents were further examined separately to understand the mechanism in details. Table 4.1. shows the non-bonded interaction energies between MMT clay and different constituents of HAP, aminovaleric acid and PCL in OMMT-HAP-PCL. Large repulsive interactions were found between MMT clay and PO_4 of HAP (+8,446 kcal/mol) and high attractive

interactions were found between MMT clay and Ca of HAP (-10,118 kcal/mol). High attractive and repulsive interactions between MMT clay and different constituents of HAP were mainly electrostatic in nature. The effect of these strong interactions can be seen in Fig 4.5., which shows shift of MMT clay sheet in the close proximity of HAP and change in its orientation in the final OMM-HAP-PCL model. Molecular interactions between MMT clay and aminovaleric acid have also shown high contribution of electrostatic energy. However, van der Waals energy has played significant role in the interactions between MMT clay and PCL constituents (-714 kcal/mol). Similar molecular interactions between MMT clay, HAP and aminovaleric acid modifier were observed in our previous study of OMMT-HAP [1].

Table 4.1. The non-bonded interaction energies between MMT clay and different constituents of HAP, aminovaleric acid and PCL in OMMT-HAP-PCL. Attractive interactions are represented by negative value, and repulsive interactions are indicated by positive values.

Non-bonded interactions between	Electrostatic (ELE) Energy (kcal/mol)	Van der Waals (VDW) Energy (kcal/mol)	Total (VDW+ELE) Energy (kcal/mol)
MMTclay – modifier backbone	-158	-27	-185
MMTclay – COOH	+18	-15	+3
MMTclay – NH_3^+	-325	+2	-323
MMTclay – PO_4	+8615	-169	+8446
MMTclay – OH	+876	-6	+870
MMTclay – Ca	-10124	+6	-10118
MMTclay – PCL backbone	-1016	-528	-1544
MMTclay – PCL functional group	+710	-186	+524

Table 4.2. The non-bonded interaction energies between HAP and different constituents of aminovaleric acid and PCL in OMMT-HAP-PCL. Attractive interactions are represented by negative value, and repulsive interactions are indicated by positive values.

Non-bonded interactions between	Electrostatic (ELE) Energy (kcal/mol)	Van der Waals (VDW) Energy (kcal/mol)	Total (VDW+ELE) Energy (kcal/mol)
PO_4– modifier backbone	-4324	-29	-4353
PO_4 – COOH	+765	+8	+773
PO_4 – NH_3^+	-10780	+69	-10711
PO_4 – PCL backbone	-42936	-623	-43559
PO_4 – PCL functional group	+58350	-304	+58046
OH – modifier backbone	-617	-1	-618
OH – COOH	+100	-1	+99
OH – NH_3^+	-1526	+5	-1521
OH – PCL backbone	-5807	-18	-5825
OH – PCL functional group	+4628	-7	+4621
Ca – modifier backbone	+4431	-4	+4427
Ca – COOH	-973	+7	-966
Ca – NH_3^+	+10914	-3	+10911
Ca – PCL backbone	+45488	-107	+45381
Ca – PCL functional group	-69433	+319	-69114

The Non-bonded interaction energies between HAP and different constituents of aminovaleric acid and PCL in OMMT-HAP-PCL are shown in Table 4.2. It was observed that the HAP constituents and PCL constituents have very strong interactions with each other. Large attractive molecular interaction between Ca of HAP and PCL functional group (-69,114 kcal/mol) and PO_4 of HAP and PCL backbone (-43,559 kcal/mol) and repulsive molecular interactions between Ca and PCL backbone (+45,381 kcal/mol) and PO_4 of HAP and PCL functional group (+58,046 kcal/mol) are the result of electrostatic energy which depends on high partial atomic charges of Ca and PO_4 constituents of HAP. Strong molecular interactions of phosphate group with different constituents of MMT clay and modifier in OMMT-HAP-PCL were of the same nature as observed in our modeling work of OMMT-HAP [1].

Table 4.3. shows the non-bonded interaction energies between different constituents of aminovaleric acid molecules and PCL in OMMT-HAP-PCL. The total repulsive interaction between aminovaleric acid and PCL chains was due to the PCL backbone interactions with NH_3^+ and backbone of modifier. It appears from the molecular interactions calculation between modifier and other constituents of the OMMT-HAP-PCL in Tables 4.1., 4.2. and 4.3. that the contribution of electrostatic term was much higher compared to van der Waals. Attractive interaction between Ca and COOH (-966 kcal/mol) was attributed to the formation of unidentate (chelation) between surface calcium atoms and oxygen atoms of C=O group of aminovaleric acid molecules. Significant no. of hydrogen bonds were observed between oxygen atoms of PO_4 and OH constituents of HAP and hydrogen atoms of NH_3^+ of aminovaleric. Hydrogen atoms of NH3+ functional group of some of the aminovaleric acid molecules were also formed hydrogen bonding with oxygen atoms of Si-O of MMT clay sheet. As reported earlier, these results suggest that aminovaleric acid molecules play significant role in the interaction between MMT clay and HAP.

Table 4. 3. The non-bonded interaction energies between different constituents of aminovaleric acid molecules and PCL in OMMT-HAP-PCL. Attractive interactions are represented by negative value, and repulsive interactions are indicated by positive values

Non-bonded interactions between	Electrostatic (ELE) Energy (kcal/mol)	Van der Waals (VDW) Energy (kcal/mol)	Total (VDW+ELE) Energy (kcal/mol)
NH_3^+ – PCL backbone	+697	-9	+688
NH_3^+ – PCL function	-614	+9	-605
COOH – PCL backbone	-116	-21	-137
COOH – PCL function	+91	-5	+86
Modifier backbone – PCL backbone	+477	-45	+432
Modifier backbone – PCL functional group	-390	-15	-405

We compared MD simulation results of OMMT-HAP-PCL model with photoacoustic FTIR spectroscopy (PA-FTIR) results of PCL/in situ HAP clay obtained from our previous work. PA-FTIR results showed change in C=O stretching of amorphous region of PCL at 1741 cm^{-1} in PCL to 1739 cm^{-1} in PCL/in situ HAPclay. The band corresponding to hydrogen bonded carbonyl groups of PCL appeared at 1707 cm^{-1} in PCL. This band shifted to 1710 cm^{-1} in PCL/in situ HAPclay. Similar shift of bands correspond to C-O and C-C stretching in crystalline phase and OC-O stretching have been observed in PCL/in situ HAP clay. These shifts in the PCL vibrations were the result of interaction of in situ HAPclay with the PCL polymer in PCL/in situ HAPclay. From Tables 4.1., 4.2. and 4.3., it was observed that PCL functional group and PCL backbone were strongly interacting with different constituents of OMMT-HAP-PCL. Significantly high attractive interactions were observed between HAP and PCL. Our previous modeling work of HAP

and PCL also showed that HAP strongly influences the PCL when they are in proximity of each other [26]. We also found in our current study that high attractive interaction between MMTclay and PCL and repulsive interaction between modifier and PCL were mainly due to the PCL backbone.

4.5.3. Evaluation of Mechanical Response of OMMT-HAP-PCL at Molecular Level

The mechanical response of OMMT-HAP-PCL at molecular level was simulated using the constant force steered molecular dynamics (SMD). As seen in Fig 4.6., we applied compressive point loads on the top surface of OMMT-HAP-PCL representative model obtained from our MD simulations.

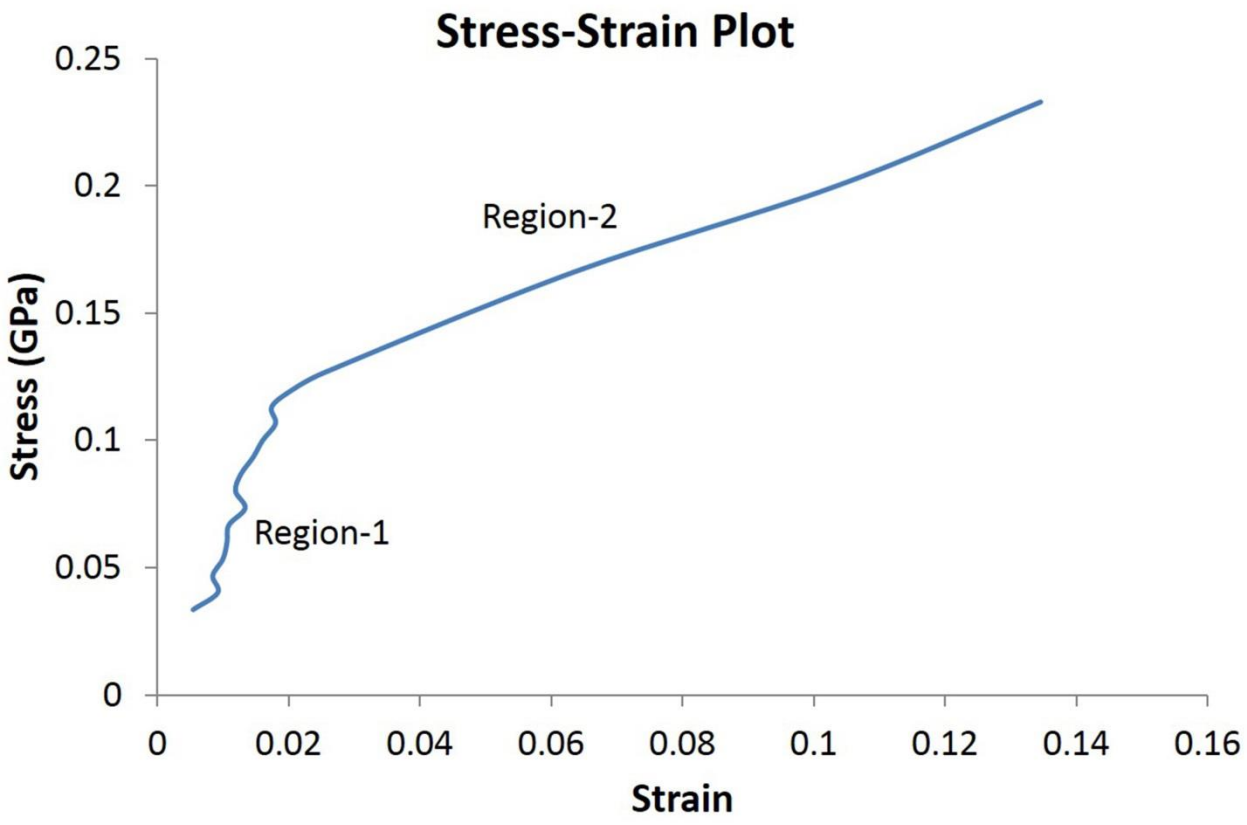

Figure 4.10. Stress-strain characteristics in the OMMT-HAP-PCL at molecular level.

The bottom surface of the model was kept fixed. The different compressive point loads applied in the SMD simulations were ranging from 5 pN to 35 pN. Equivalent compressive stresses were calculated from total 512 numbers of atoms and total top surface area of 76.92 nm^2, to which compressive loads have been applied. The compressive stresses applied were ranging from 0.033 GPa to 0.233 GPa. Fig 4.10. shows the stress-strain characteristics in the OMMT-HAP-PCL system at molecular level obtained from the SMD simulations by applying different constant forces per atoms.

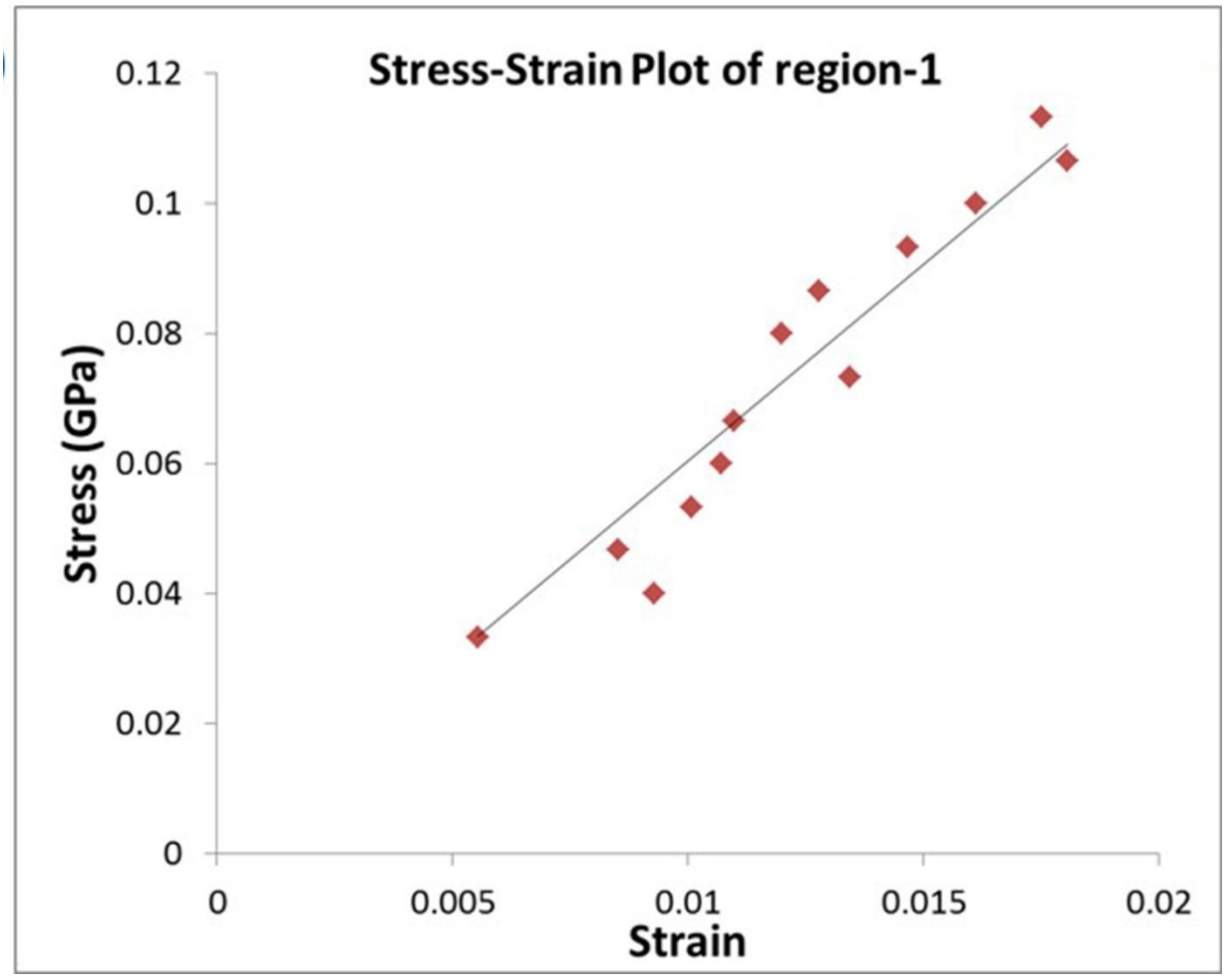

Figure 4.11. Stress–strain plot of the OMMT-HAP-PCL molecular model in the region-1.

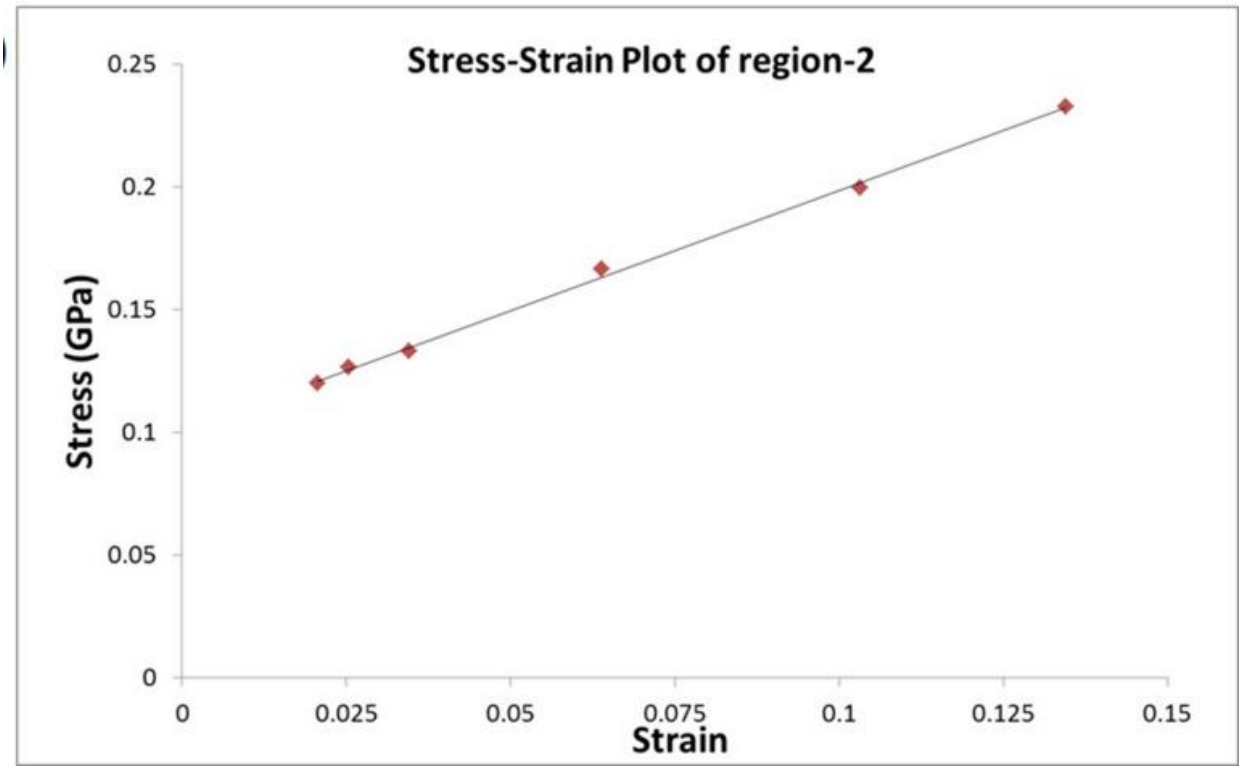

Figure 4.12. Stress–strain plot of the OMMT-HAP-PCL molecular model in the region-2.

It can be seen that stress-strain behavior of the OMMT-HAP-PCL is nonlinear. We observed two distinct stress-strain responses in the Fig 4.10. In the region-1, point loads vary from 5 pN to 17 pN and from 18 pN to 35 pN in region-2. It was observed that the non-bonded interaction energies between aminovaleric modifier and HAP, MMT clay and HAP and PCL and HAP changed during the SMD simulations of OMMT-HAP-PCL system. This suggests the contribution of MMT clay, modifier, PCL and HAP in mechanical response of OMMT-HAP-PCL system. Stress-strain responses in region-1 and region-2 were separately analyzed in Figs 4.11. and 4.12., respectively. In attempt to evaluate the modulus of the OMMT-HAP-PCL system, a trend line was added in each region. The slope of the trend line was assumed to represent the modulus of the OMMT-HAP-PCL system in that region. The modulus calculated from the stress-

strain responses in the region-1 was estimated to be about 6.03 GPa. In this range of stress, the strain in the OMMT-HAP-PCL system increases to 0.018. Our previous SMD simulations have shown very small deformations in the MMT clay sheet in this range of stresses. The compressive stress-strain studies of the Na-MMT interlayer intercalated with amino acids and Na-MMT intercalated with water were showed that clay sheets remain nearly rigid in this range of stresses and the noticeable change in can only be seen at very high applied stresses [43, 44]. In other SMD study of PCN, which composed of MMT clay, 12-aminovaleric acid modifier and PA6 polymer was calculated very small strain (<0.004) at very high stresses (~2.2GPa) [16]. In our current work, we also observed very small deformation in the MMT clay of the OMMT-HAP-PCL system. Fig. 8b gives the stress-strain characteristics of OMMT-HAP-PCL system for stresses between 0.12 GPa and 0.233 GPa. In this range of applied stresses, the system strain increases from 0.02 to 0.135. As seen in Fig 4.12., stress-strain relationship in region-2 is nearly linear. The modulus calculated in the region-2 was estimated to be about 0.98 GPa.

Table 4.4. The average values of elastic modulus calculated at 1000 μN and 5000 μN applied forces in nanoindentation tests[46] and modulus calculated from the region-1 and region-2 of the SMD simulations of OMMT-HAP-PCL system.

	Elastic Modulus (GPa)
Nanoindentation test (1000μN)	2.8
Nanoindentation test (5000μN)	1.7
Steered molecular dynamics (Region-1)	6.03
Steered molecular dynamics (Region-2)	0.98

Further, the results of constant-force steered molecular dynamics of OMMT-HAP-PCL model were compared with nanoindentation results obtained from our prior work [46]. Table 4.4.

shows the average values of elastic modulus calculated at 1000 μN and 5000 μN applied forces in nanoindentation tests and modulus calculated from the region-1 and region-2 of the SMD simulations of OMMT-HAP-PCL system. It can be seen that the magnitude of the modulus values obtained from the computational and experimental results are of the same order. It has been reported that the elastic modulus of nanoscale in situ mineralized HAP decreases with increase in applied loads in nanoindentation tests. This was attributed to the fact that at low load nanoindentation, majority of indentation responses come from the surface/interface of the sample. Whereas, at higher load, nanomechanical responses mainly come from bulk deformation of the sample [53]. As seen in Table 4.4., average elastic modulus of OMMT-HAP-PCL obtained from nanoindentation tests have decreased from 2.8 GPa to 1.7 GPa when applied load increased from 1000 μN to 5000 μN. It was observed that the nanomechanical properties were influenced by the size and distribution of in situ HAPclay particles and interfacial interactions between PCL and in situ HAPclay. In our SMD simulation, we also observed similar responses in the OMMT-HAP-PCL system. At low applied stresses in region-1, we observed high modulus of 6.03 GPa compared to low modulus of 0.98 GPa at high applied stresses in region-2. At a stress of 0.113 GPa, the interaction energy between HAP and PCL was significantly reduced to -10,137 kcal/mol from -10,451 kcal/mol. However, interaction energy between HAP and aminovaleric modifier and HAP and MMT clay was increased by 81 and 45 kcal/mol, respectively. This indicates that HAP interactions play an important role in the mechanical properties of OMMT-HAP-PCL system.

4.6. Conclusions

- In this work, a representative model of organically modified MMT clay with hydroxyapatite and polycaprolactone has been constructed using molecular dynamics simulation. This exfoliated OMMT-HAP-PCL representative model was validated by experimentally observed TEM, XRD and material density results.
- Molecular interactions study of OMMT-HAP-PCL model showed a complex four component system. Evaluation of non-bonded interaction energies between MMT clay, aminovaleric modifier, HAP and PCL indicated strong interactions between them.
- Fairly high attractive and repulsive interactions are found between different constituents of HAP and PCL. Strong molecular interactions were also observed between MMT clay, aminovaleric modifier and PCL functional group and PCL backbone. These molecular interactions elucidate the change in C=O vibrations of PCL in OMMT-HAP-PCL compared to pristine PCL.
- Steered molecular dynamics simulations of the representative model were conducted to quantitatively evaluate the stress-strain response of the OMMT-HAP-PCL system. Our results indicated two distinct stress-strain regions in the system.
- The modulus of the OMMT-HAP-PCL system in region-1 and region-2 were found to be 6.03 GPa and 0.98 GPa, respectively. The molecular interactions study of our SMD simulations suggested the significant role of HAP in stress-strain response of OMMT-HAP-PCL system.
- Our MD and SMD simulations study provide a detailed quantitative view of the molecular interactions and stress-strain response of complex OMMT-HAP-PCL system. These studies provide a framework for a simulation driven design of bone biomaterials.

4.7. References

[1] D.R. Katti, A. Sharma, A.H. Ambre, K.S. Katti, Materials Science and Engineering: C (2014).

[2] D. Raabe, B. Sander, M. Friák, D. Ma, J. Neugebauer, Acta Materialia 55 (2007) 4475-4487.

[3] D. Lacroix, J.A. Planell, P.J. Prendergast, Philosophical Transactions of the Royal Society A: 367 (2009) 1993-2009.

[4] X. Sun, Y. Kang, J. Bao, Y. Zhang, Y. Yang, X. Zhou, Biomaterials 34 (2013) 4971-4981.

[5] F.T. Wu, M.O. Stefanini, F. Mac Gabhann, C.D. Kontos, B.H. Annex, A.S. Popel, American Journal of Physiology-Heart and Circulatory Physiology 298 (2010) H2174-H2191.

[6] R. Langer, J. Vacanti, Science 260 (1993) 920-926.

[7] M. Niinomi, Journal of the Mechanical Behavior of Biomedical Materials 1 (2008) 30-42.

[8] A. Okada, M. Kawasumi, A. Usuki, Y. Kojima, T. Kurauchi, O. Kamigaito, D. Schaefer, J. Mark, Polymer based molecular composites, MRS symposium proceedings, vol 171, 1990, p. 45.

[9] E. Picard, A. Vermogen, J.F. Gérard, E. Espuche, Journal of Membrane Science 292 (2007) 133-144.

[10] K.S. Katti, D.R. Katti, R. Dash, Biomedical Materials 3 (2008) 034122.

[11] A.J. Mieszawska, J.G. Llamas, C.A. Vaiana, M.P. Kadakia, R.R. Naik, D.L. Kaplan, Acta Biomaterialia 7 (2011) 3036-3041.

[12] P. Maiti, C.A. Batt, E.P. Giannelis, Biomacromolecules 8 (2007) 3393-3400.

[13] N. Gupta, T.C. Lin, M. Shapiro, JOM 59 (2007) 61-65.

[14] D. Sikdar, D. Katti, K. Katti, B. Mohanty, Journal of applied polymer science 105 (2007) 790-802.

[15] D. Sikdar, D.R. Katti, K.S. Katti, Journal of applied polymer science 107 (2008) 3137-3148.

[16] D. Sikdar, S.M. Pradhan, D.R. Katti, K.S. Katti, B. Mohanty, Langmuir 24 (2008) 5599-5607.

[17] H. Wang, Y. Li, Y. Zuo, J. Li, S. Ma, L. Cheng, Biomaterials 28 (2007) 3338-3348.

[18] X. Li, L. Wang, Y. Fan, Q. Feng, F.Z. Cui, F. Watari, Journal of Biomedical Materials Research Part A 101 (2013) 2424-2435.

[19] J. Ong, M. Appleford, S. Oh, Y. Yang, W.-H. Chen, J. Bumgardner, W. Haggard, Jom 58 (2006) 67-69.

[20] A. Porter, N. Patel, J. Skepper, S. Best, W. Bonfield, Biomaterials 24 (2003) 4609-4620.

[21] R.K. Roeder, G.L. Converse, R.J. Kane, W. Yue, Jom 60 (2008) 38-45.

[22] F.G. Lyons, J.P. Gleeson, S. Partap, K. Coghlan, F.J. O'Brien, Clinical Orthopaedics and Related Research® 472 (2014) 1318-1328.

[23] H. Liu, W. Jiang, A. Malshe, Jom 61 (2009) 67-69.

[24] J.-W. Rhim, S.-I. Hong, C.-S. Ha, LWT-Food Science and Technology 42 (2009) 612-617.

[25] D. Verma, K. Katti, D. Katti, Journal of Biomedical Materials Research Part A 77 (2006) 59-66.

[26] R. Bhowmik, K.S. Katti, D.R. Katti, International Journal of Nanotechnology 6 (2009) 511-529.

[27] F. Yahiaoui, F. Benhacine, H. Ferfera-Harrar, A. Habi, A. Hadj-Hamou, Y. Grohens, Polymer Bulletin (2014) 1-20.

[28] C. Jeong, S.-C. Lee, H. Rhee, K. Park, S.-H. Choi, Metals and Materials International 20 (2014) 593-600.

[29] R. Bhowmik, K.S. Katti, D. Katti, Polymer 48 (2007) 664-674.

[30] S. Pradhan, D. Katti, K. Katti, Journal of Nanomechanics and Micromechanics 1 (2011) 104-110.

[31] D.R. Katti, S.M. Pradhan, K.S. Katti, Journal of Biomechanics 43 (2010) 1723-1730.

[32] M. Corno, A. Rimola, V. Bolis, P. Ugliengo, Physical Chemistry Chemical Physics 12 (2010) 6309-6329.

[33] F. Chiatti, M. Corno, Y. Sakhno, G. Martra, P. Ugliengo, The Journal of Physical Chemistry C 117 (2013) 25526-25534.

[34] J. Ma, Journal of Materials Science 49 (2014) 3099-3106.

[35] L.-W. Du, S. Bian, B.-D. Gou, Y. Jiang, J. Huang, Y.-X. Gao, Y.-D. Zhao, W. Wen, T.-L. Zhang, K. Wang, Crystal Growth & Design 13 (2013) 3103-3109.

[36] N. Almora-Barrios, N.H. De Leeuw, Crystal Growth & Design 12 (2011) 756-763.

[37] J.C. Phillips, R. Braun, W. Wang, J. Gumbart, E. Tajkhorshid, E. Villa, C. Chipot, R.D. Skeel, L. Kale, K. Schulten, Journal of computational chemistry 26 (2005) 1781-1802.

[38] R. Bhowmik, K.S. Katti, D.R. Katti, Journal of Materials Science 42 (2007) 8795-8803.

[39] R. Bhowmik, K. Katti, D. Katti, Journal of Engineering Mechanics 135 (2009) 413-421.

[40] B. Israelewitz, M. Gao, K. Schulten, Current opinion in structural biology 11 (2001) 224-230.

[41] S.M. Pradhan, K.S. Katti, D.R. Katti, Biomacromolecules 13 (2012) 2562-2569.

[42] F. Libonati, A.K. Nair, L. Vergani, M.J. Buehler, Mechanics Research Communications 58 (2014) 17-23.

[43] S.R. Schmidt, D.R. Katti, P. Ghosh, K.S. Katti, Langmuir 21 (2005) 8069-8076.

[44] D.R. Katti, S.R. Schmidt, P. Ghosh, K.S. Katti, Clays and Clay Minerals 53 (2005) 171-178.

[45] D.R. Katti, P. Ghosh, S. Schmidt, K.S. Katti, Biomacromolecules 6 (2005) 3276-3282.

[46] A.H. Ambre, D.R. Katti, K.S. Katti, Journal of Biomedical Materials Research Part A (2014).

[47] A. Ambre, K.S. Katti, D.R. Katti, Materials Science and Engineering: C 31 (2011) 1017-1029.

[48] D. Sikdar, D.R. Katti, K.S. Katti, Langmuir 22 (2006) 7738-7747.

[49] R. Bhowmik, K.S. Katti, D. Verma, D.R. Katti, Materials Science and Engineering: C 27 (2007) 352-371.

[50] W. Humphrey, A. Dalke, K. Schulten, Journal of Molecular Graphics 14 (1996) 33-38.

[51] S.E. Feller, Y. Zhang, R.W. Pastor, B.R. Brooks, Journal of Chemical Physics 103 (1995) 4613-4621.

[52] G.J. Martyna, D.J. Tobias, M.L. Klein, The Journal of Chemical Physics 101 (1994) 4177.

[53] R. Khanna, K.S. Katti, D.R. Katti, Journal of engineering mechanics 135 (2009) 468-478.

CHAPTER 5. MULTISCALE MODELS OF DEGRADATION AND HEALING OF BONE TISSUE ENGINEERING NANOCOMPOSITE SCAFFOLDS[4]

This chapter presents studies related to a new multiscale mechanics based *in silico* approach to design polymer scaffolds for bone tissue engineering applications. The contents of this chapter have been published in A. Sharma, MD. S. Molla, K.S. Katti, D.R. Katti; "Multiscale model of degradation and healing of bone tissue engineering nanocomposite scaffolds", J. Nanomech. Micromech. (2017).

5.1. Introduction

Bone tissue regeneration is intrinsically a complex multiscale process where the evolution of tissues depends on the different biochemical, physical, geometrical and mechanical factors. These factors mutually influence the biophysical response of other factors at different spatial and time scales [1]. The mechanical properties of hard tissues such as bone arise from the complex hierarchical structure [2]. Hence, it is important to consider the hierarchy of bone while designing biomaterials that can heal/replace damaged tissues or substitute as an implant in critical size bone defects in the body. The critical size bone defect is considered a large defect that cannot be bridged/healed naturally. Although, biological grafts have been traditionally used in bridging the critical size defects in bone, the risk of donor site morbidity, long healing time, persistent pain in

[4] The material in this chapter was co-authored by Anurag Sharma and Dinesh Katti. Anurag Sharma had primary responsibility for collecting samples in the field and for interviewing users of the test system. Anurag Sharma was the primary developer of the conclusions that are advanced here. Anurag Sharma also drafted and revised all versions of this chapter. Dinesh Katti served as proof reader and checked the math in the statistical analysis conducted by Anurag Sharma.

autografts [3-5] and associated concerns of graft rejection and transmission of diseases in allografts [6, 7] affect the desirable defect healing outcome. To overcome these disadvantages, biomaterials such as tissue engineered polymer scaffold can be considered as a viable candidate for implant in critical size bone defects treatment. Polymer scaffolds are widely used due to their support for tissue formation and controllable degradation properties. However, the material selection, structural integrity, and mechanical properties evolution during degradation and tissue regeneration are still some of the major challenges in designing a complex hierarchical polymer scaffold for bone tissue regeneration. Use of predictive methodologies for the design of biomaterials in general and scaffolds, in particular, is limited and most studies in the literature are testing and experiment based. In recent years, some efforts have been made towards a simulation basis for the design of optimized polymer scaffolds for bone tissue regenerations [8-10]. Multiscale models can intrinsically capture the molecular to macro scale mechanisms of bone regeneration and can be used for the design of polymer scaffolds. Recent studies have indeed elucidated the emergence and importance of multiscale modeling of mechano-biological aspects [11-13] that can also be useful for novel biomaterials design.

Hydroxyapatite (HAP) is a mineral component in the bone and for this reason, it is widely used as a synthetic biomaterial to enhance their osteoconductivity, biocompatibility, and non-immunogenicity [14-16]. However, due to its hard and brittle nature, it is often combined with aliphatic polyesters such as polycaprolactone (PCL) as an inorganic filler to improve the mechanical strength of the polymer based scaffolds [17, 18]. PCL is a hydrophobic, semi-crystalline polymer with excellent blend-compatibility, high rheological and viscoelastic properties [19-21]. Many PCL based drug delivery devices have been approved by FDA because of its good biocompatibility and biodegradability [22-24]. Due to these properties, PCL has

become a potential candidate for fabrication of tissue-engineered scaffolds [25-29]. Experimental and molecular dynamics (MD) simulation studies performed in our group indicate that the mechanical properties of PCL composites are highly influenced by the presence of HAP [30-32]. Montmorillonite (MMT) nanoclay was first used by Toyota research group in 1990's to improve mechanical properties of nylon-6 nanoclay composite [33]. The addition of small amount of modified nanoclay has shown significant improvement in biocompatibility, biodegradability, thermal and mechanical properties of polymer nanocomposites (PCN) [33-35]. Molecular dynamics studies have shown that the interactions between MMTclay and organic modifiers control the mechanical properties of PCN [36]. Previous studies in our group have led to the development of the 'Altered Phase theory' of PCNs [37]. In this theory, high repulsive and attractive interactions between modifiers and MMTclay at molecular level create a ripple action near the clay galleries. The ripple effect influences the crystallinity and nanomechanical properties of polymer and 'altered phase' of the polymer around the clay particles. The 'altered phase model' developed by our group revealed that the altered polymer has higher elastic modulus compared to unaltered polymer in the PCN [37]. We have also used engineered nanoclay to successfully synthesize a biocomposite system for bone tissue engineering applications. The cell culture studies showed good biocompatibility and nanoindentation experiments observed significant improvement in the nanomechanical properties of nanoclay biocomposite [35].

Given the increase in biological and mechanical properties of the biomaterials due to the PCL, HAP, and modified nanoclay, we synthesized a novel PCL/in situ HAP nanoclay biomaterial system for bone tissue engineering applications [38]. The interlayer spacing and biocompatibility of MMT nanoclay were enhanced by modifying it with unnatural aminovaleric acid [39, 40]. The modified MMTclay was then used to prepare a biomineralized HAP (in situ HAPclay) using a

biomimetic strategy[41]. Prior FTIR studies showed that the aminovaleric acid in the modified MMTclay plays an important role through the chelate formation in in situ HAPclay mineralization. Finally, PCL was introduced to synthesize PCL/in situ HAP nanoclay films and scaffolds. The mechanical properties of nanocomposite films and scaffolds were increased compared to pristine PCL because of the presence of the in situ HAP nanoclay [41, 42]. The cell culture study on this system indicated flat and spherical morphology of hMSCs and formation of the mineralized extracellular matrix (ECM) similar to the human bone [38].

To further understand the underlying interaction mechanisms and mechanical properties of our composite system, we developed representative molecular models of organically modified MMTclay (OMMT), OMMT-HAP and OMMT-HAP-PCL [43, 44]. The X-ray Diffraction (XRD), Fourier Transforms Infrared (FTIR) spectroscopy and Transmission Electron Microscopy (TEM) experiments were conducted to validate these representative models. The simulations results showed attractive and repulsive interactions between MMTclay and aminovaleric acid molecules in both OMMT and OMMT-HAP models. The hydrogen bonding between functional groups of modifier and MMTclay was found to increase in OMMT-HAP model compared to OMMT, indicating the interactions between HAP and clay through the aminovaleric modifiers. The chelate formation between carboxylic groups of modifiers and Ca atoms of HAP through high attractive interactions in the in situ HAPclay also confirms the involvement of aminovaleric acid in HAP mineralization. It was observed that the high attractive interactions between modifier backbone and HAP influenced the conformation of modifiers and changed the –CH2- deformation of modifier. The phosphate ions influence the neighboring environment in OMMT-HAP through very strong interactions with the modifier as well as MMTclay. A representative model of a polymeric nanocomposite scaffold system was developed by adding PCL in OMMT-HAP [44]. Strong

interactions between PCL and HAP showed the high influence of HAP on PCL polymer. Further, a steered molecular dynamics (SMD) study was performed to understand the mechanical properties of OMMT-HAP-PCL nanocomposite scaffold. In SMD, force displacement is applied to an atom or a group of atoms to evaluate the mechanical response of the molecule. The mechanical response of OMMT–HAP–PCL at the molecular level showed two distinct regions in the stress-strain curve. At low range of applied stress less than 0.12 GPa, the OMMT-HAP-PCL nanocomposite showed high modulus (6.03 GPa) and at higher applied stresses showed low modulus (0.98 GPa). It was observed that at high applied stresses the interactions between HAP and PCL polymer were significantly reduced compared to low applied stresses. These molecular dynamics simulations results described the molecular interactions contribution between different constituents of HAP, modifier, PCL and MMTclay and provided a detailed insight into a complex biomaterial system for bone tissue engineering applications.

Besides the role of molecular interactions in mechanical properties evaluation, structural integrity also plays an important role in determining the biological responses and performances in bone tissue formation in polymeric scaffolds. Therefore, it is paramount to examine the stress-strain characteristics in polymeric scaffolds at macrostructural level. To this purpose, Finite Element (FE) method is commonly accepted as a numerical tool to predict the mechanical behavior of scaffolds. Among different FE modeling approaches, microcomputed tomography (μCT) based FE method is now widely used to simulate representative three-dimensional (3D) scaffolds microstructure [45-48]. The μCT-FE technique provides an ability to analyze quantitatively the mechanical behavior of highly porous and complex materials such as trabecular bone, polymeric scaffolds, metallic and polymeric foams [49-53]. The mechanical properties are related to the porous architecture of polymer scaffolds with different pores geometries using μCT-FE modeling

[54]. Also, mechanical load transfer and deformation observed by the attached cells in macroporous calcium phosphate bone cement and phosphate glass have been evaluated using the μCT-FE approach [47]. The effect of pore interconnectivity, scaffold porosity, fluid velocity and pressure on the stress-strain distribution in the porous scaffolds [46, 55] has also been described. The local stress concentration and deformation processes in cellular solids (ceramics, metals, polymers) have been calculated [56]. The predicted macroscopic responses of the material show good agreement with experimental results, although with overestimation in elastic properties due to the limitation of tomography resolution. Analysis correlating biomechanical interactions between the porous bioactive HAP ceramics and bone tissue regeneration indicate a strong relationship between bone ingrowth and overall stiffness of scaffolds [57]. Recently, mechanical responses of polycaprolactone/tricalcium phosphate (PCL/TCP) composite scaffolds have been predicted for optimizing scaffold design [58]. The relationship between microporosity and material properties or greyscale values and energy density was proposed to generate more accurate FE models for scaffold design. MD and SMD simulations provide a framework to analyze the mechanical responses in scaffolds material system at the molecular level quantitatively and similarly FE modeling approach allows to simulate the stress-strain behavior in scaffolds at the macroscopic level. However, not many attempts have been made to connect quantitatively the mechanical behavior obtained at the molecular level to macroscopic mechanics for designing the scaffolds for bone tissue engineering applications. This is particularly challenging due to the complex degradation mechanisms in the cell-scaffold system.

Chemical degradation via hydrolysis or enzyme-catalysed hydrolysis is the most common degradation mechanism in polymer scaffolds. It is now well established that hydrolytic degradation of poly (α-hydroxy) esters such as PCL occur through surface or bulk degradation pathways. The

degradation of PCL-based scaffolds under accelerated (alkaline) and simulated physiological conditions indicate that PCL composite scaffolds are degraded via surface degradation and for long periods, the degradation in simulated conditions appears similar to bulk degradation [59]. In a subsequent *in vivo* degradation study, it was revealed that for a short duration (6 months) degradation mechanism is mainly through the surface and for a longer period (2 years), it was bulk degradation [60]. These studies indicate that PCL composites exhibit similar degradation mechanism in *in vivo* and in-vitro conditions. More recently, it was reported that the addition of nanoparticles such as HAP can be used for modulating the degradation rate of PCL composite scaffolds. The higher concentration of HAP nanoparticles showed an increase in water absorption during the initial degradation process, and this leads to accelerated weight loss of the composite scaffolds [61]. The addition of biomineralized HAP-nanoclay into PCL influences the degradation behavior of the scaffold[38]. It has also been reported that young's modulus of composite scaffolds was increased when cells were seeded on the scaffolds[62]. In addition to *in vitro* and *in vivo* studies several mathematical models have been developed, linking the changes in molecular weight and mass loss to the degradation of polymeric scaffolds [63-65]. Several *in vivo* studies are also reported by PCL-nanocomposite scaffold degradation behavior [66, 67] We have also reported that mineralization in the nanoclay-PCL scaffolds mimics biology by the formation of intercellular vesicles in PCL/ *in situ* HAPclay composite films seeded with hMSCs cells[68] similar to that observed in biological systems. The TEM imaging results showed highly crystalline mineral inside the vesicles, indicating that the composite films provide a favorable bone-mimetic environment for new bone formation. Thus, in addition, to understanding the tissue regeneration and polymer degradation for bone tissue engineering applications, it is also important to incorporate and investigate the effect of these processes on the mechanical behavior of polymeric scaffolds.

The main goal of this study is to develop a multiscale mechanics approach to design a three-dimensional polymer scaffold for bone tissue regeneration. To achieve this, (1) a μCT-FE model of PCL/*in situ* HAPclay scaffolds was created using the 3D reconstructed μCT images and materials properties obtained from our previous SMD simulations [44]. The predicted FE model is verified, and mechanical behavior is analyzed against the experimental compression tests results. (2) The effect of accelerated degradation on the mechanical properties of scaffolds was obtained experimentally. (3) The response of hOB cells to scaffolds and their effect on mechanical properties of seeded scaffolds were also found experimentally. (4) Analytical models are developed for mechanical properties prediction in accelerated degraded scaffolds and hOB cells seeded scaffolds. A new scaffold degradation modeling approach based on damage mechanics principles were developed in this work. We have used the mathematical formulation for the Disturbed state Concept (DSC) previously developed for porous materials, solids and interfaces to model mechanical behavior of the scaffolds in this work. The DSC was first introduced by Desai et al. to express the behavior of the disturbed/deformed material through the reference of its undisturbed/undeformed (intact) state [69]. This concept is widely used due to its simple numerical formulation and ability to predict the behavior of a wide range of materials [70-72].

The mechanical compression tests were performed to study the stress-strain responses in the PCL/in situ HAPclay scaffolds. Scanning electron microscopy was used to study the hOB cells behavior and capture scaffold wall porosity. WST-1 assay was performed to assess the viability of hOB cells on scaffolds. (5) Finally, integrative FE model was developed using the predicted FE model and analytical models of PCL/in situ HAPclay scaffolds for critical size bone defects implants.

5.2. Materials and Methods

5.2.1. Materials

Sodium-montmorillonite clay (SWy-2; Crook County, WY, USA) was purchased from the Clay Minerals Repository at the University of Missouri, Columbia. Polycaprolactone (average M_n = 80,000), 1,4 dioxane (anhydrous, 99.8%) and 5-aminovaleric acid were purchased from Sigma-Aldrich. Sodium phosphate (Na_2HPO_4) and calcium chloride ($CaCl_2$) were purchased from J.T. Baker and EM Sciences, respectively. Human osteoblast cells (hFOB 1.19 cell line number: CRL 11372) were obtained from American Type Culture Collection (ATCC). Cell culture medium used in hOB cells culture was made of fetal bovine serum (FBS) from ATCC, G418 antibiotic from JR Scientific and HyQ Dulbecco's modified eagle's medium (DMEM)-12 (1:1) from Hyclone.

5.2.2. Preparation of Polycaprolactone (PCL)/*In situ* Hydroxyapatite (HAP) clay Scaffolds

PCL/in situ HAPclay scaffolds were prepared following the method described in our previous study [38]. In summary, 3.6 g of PCL was added to 40 mL of 1,4 dioxane and stirred in a beaker until all the polymer was dissolved. A 0.4 g of in situ HAPclay (preparation procedure described here Ref. 47) was sonicated in 16 mL of 1.4 dioxane. The sonicated suspension was then added to the PCL solution, and the resulting solution was further stirred for another two h at room temperature. The final solution was transferred into the polypropylene (PP) centrifuge tubes and these tubes were then frozen overnight in isopropyl alcohol bath at -20^0C. Further, these cylindrical shaped frozen PCL composite samples were removed from tubes and transferred into absolute ethanol (-20^0C) for solvent extraction. The absolute ethanol solution was replaced every 24 h. After four days, the frozen PCL composite samples were removed from the solution and dried at room temperature. Finally, these scaffolds were cut into 13 mm length and 13 mm diameter size for all our studies presented in this paper.

5.2.3. Scanning Electron Microscopy (SEM) Characterization

A JEOL JSM-6490LV scanning electron microscope was used to study the microstructure of PCL/in situ HAPclay scaffolds. The SEM imaging of the adhesion of hOB cells on the PCL/in situ HAPclay scaffolds was performed on the same SEM instrument. The seeded scaffolds were washed with phosphate buffer saline to remove the cell culture media. For fixing the live hOB cells, seeded scaffolds were first treated with glutaraldehyde (2.5%), then dehydrated in ethanol series (10% v/v, 30% v/v, 50% v/v, 70% v/v, and 100%). After that, hexamethyldisilazane was used to replace the dried 100% ethanol. Before viewing in SEM, all these samples were sputter coated with gold and mounted on SEM sample stub.

5.2.4. Steered Molecular Dynamics Simulation

Representative molecular models of the nanoclay-amino acid-PCL system were built as reported in our previous studies [10]. The molecular interactions of the OMMT-HAP-PCL model were evaluated and non-bonded interaction energies between MMT clay, aminovaleric modifier, HAP and PCL indicated strong interactions between them. Our results indicated two distinct stress-strain regions in the system. Further, constant-force steered molecular dynamics (SMD) studies were carried out on these models to study stress-strain behavior of the representative models [44]. The simulations indicated an approximately linear stress-strain plot with two significantly different moduli of the OMMT-HAP-PCL system in two regions, designated as region-1 (stress range 0-0.2 GPa) and region-2 (>0.2 GPa). The magnitudes of the moduli were found be 6.03 GPa and 0.98 GPa, respectively[44]. The bilinear stress-strain response of the material was introduced in the finite element models of scaffolds as described in the subsequent section 5.2.6.

5.2.5. Micro Computed Tomography (µCT) of PCL/*In situ* HAPclay Scaffolds

Three samples of PCL/in situ HAPclay scaffolds were scanned using a micro computed tomography technique. The samples were attached to a glass rod using carbon tape and placed inside a GE Phoenix v|tome| x s X-ray computed tomography system (µCT) equipped with an 180 kV high power nanofocus X-ray tube xs|180nf and a high contrast GE DXR250RT flat panel detector. One thousand projections of the sample were acquired at a voltage of 60 kV and a current of 350 mA using a molybdenum target. Detector timing was 1000 ms and the total acquisition time was 1 hour and 6 minutes. Sample magnification was 7.28x with a voxel size of 24.38 µm. The acquired images were reconstructed into a volume data set using GE datos|x 3D computer tomography software version 2.2. A Diconde image series was then acquired from the reconstructed volume. Finally, a commercial image analysis software MIMICS (Materialize) was used for three-dimensional reconstruction of the scaffold (Fig 5.1a.). Cylinders of 1.5 mm height and 1.5 mm diameter from each sample were modeled.

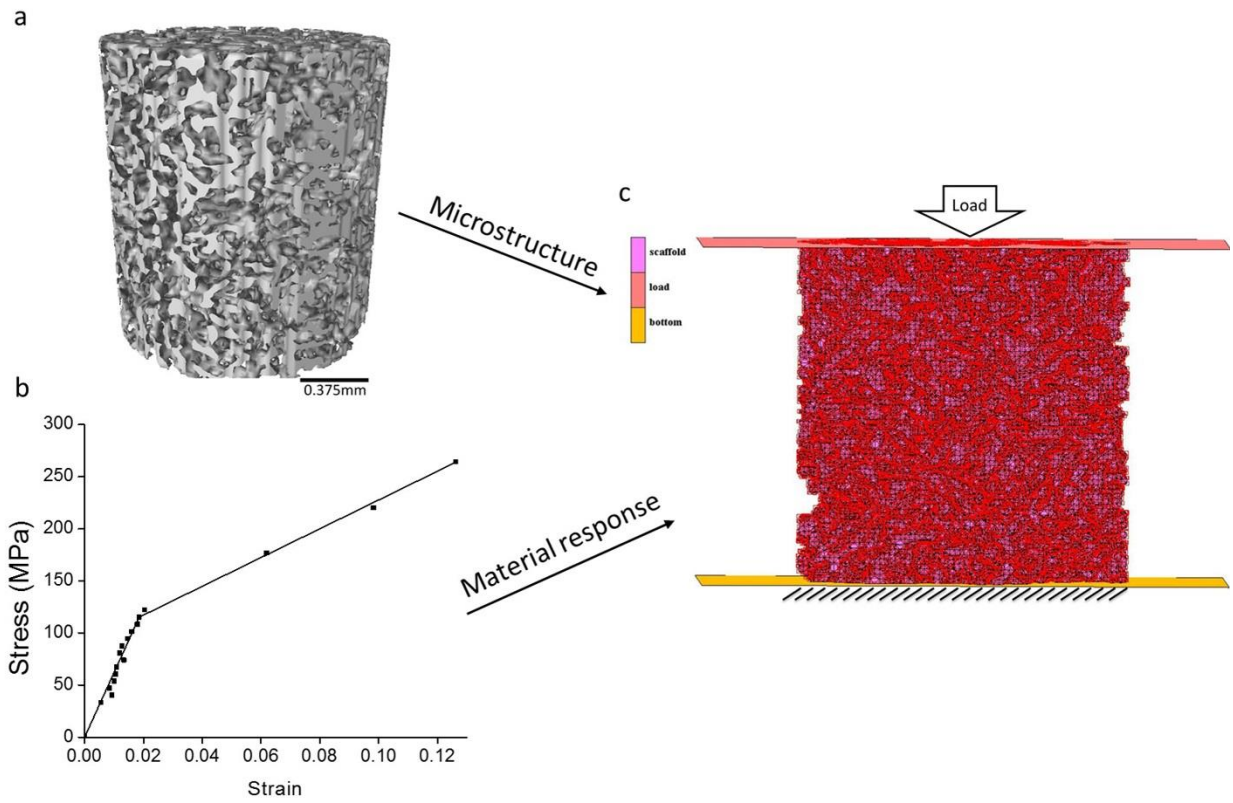

Figure 5.1. (a) 3D reconstruction of the PCL/in situ HAPclay scaffold in Mimics, (b) Mechanical response of PCL/in situ HAPclay at molecular scale obtained from steered molecular dynamics (SMD) simulations, (c) The loading conditions for the scaffold in the FE model.

5.2.6. Finite Element Modeling of PCL/*In situ* HAPclay Scaffolds

To evaluate the mechanical properties of PCL/in situ HAPclay scaffolds, the finite element (FE) models were created from the assembly of 3D STL geometric models of scaffolds. The small cylinders obtained after 3D reconstructions were then converted into a 3D tetrahedral mesh using 3-Matic software (Materialize) and used as FE models. The typical 3D FE model contains 134,929 nodes and 352,316 tetrahedral elements of around 10-25μm length. The scaffold models were then imported into Mentat™ (MSC software) for FE analysis simulations. An unconfined compressive

loading condition was simulated to determine the mechanical properties of scaffolds. Parallel plates were attached to the top and bottom surfaces of the scaffold. For loading condition, the axial load was uniformly applied on the upper plate of the model whereas the lower plate was constrained in all directions. The material parameters used in the FE analysis simulations were obtained from our previous SMD study (Fig 5.1b.) [44]. The loading conditions for the scaffold is shown in Fig 5.1c. Finally, the stress-strain responses in the meshed scaffold were analyzed with Marc™ 13.0 FE analysis software (MSC software). All FE analysis simulations were run on 256 processors (32 nodes; eight processors per node) at the Center for Computationally Assisted Science & Technology (CCAST) clusters at North Dakota State University using MARC™ 13.0 software. SEM images of the scaffolds showing the porosities and also microporosities in the scaffold walls are shown in Figs 5.2. and 5.3.

5.2.7. Accelerated Degradation Studies in 0.1M NaOH

The mechanical degradation of PCL/in situ HAPclay scaffolds was studied in alkaline conditions (0.1M NaOH). For this purpose, scaffold samples were UV sterilized for 45 minutes and then immersed in 70% alcohol overnight. Finally, samples were washed with phosphate buffer saline (PBS) to use them for degradation studies. The PBS washed scaffold samples were transferred to 0.1M NaOH solution in separate glass vials. These scaffolds samples in glass vials were then placed at 37 ^{0}C temperature and 5% CO_2 for degradation. Finally, scaffolds were removed from glass vials after each degradation period (1, 5, 7, 14 and 18 days) and washed with deionized water and dried at room temperature conditions.

5.2.8. Mechanical Degradation of Scaffolds in 0.1 M NaOH

The mechanical properties of scaffolds were obtained after each degradation period using a material testing servo mechanical test frame (MTS 858, Eden Prairie, MN). The compressive

mechanical tests were carried out on undegraded (0 days, control) and degraded (1, 5, 7, 14 and 18 days) PCL/in situ HAPclay composite scaffold samples. A 1 mm/min of constant deformation rate was applied for up to 10% strain to each test sample. The load and corresponding displacement data were recorded. The load-displacement data were used to construct the stress-strain response curves for each sample.

5.2.9. Human Osteoblast (hOB) Cell Culture Experiments

Cell culture experiments for cell viability and mechanical properties studies of PCL/in situ HAPclay scaffolds were carried out using hOB cells. For this purpose, UV sterilized, 70% alcohol-immersed and PBS washed scaffolds samples were used. The PBS washed scaffold samples were first immersed in cell culture medium and kept at 37 ^{0}C and 5% CO_2 in the incubator. After 24 hours, 1 x 10^5 hOB cells were seeded on each sample and 1mL of cell culture medium was then added. This was followed by incubation of cell-seeded scaffolds at 37 ^{0}C and 5% CO_2 for 4 days, 7 days, 18 days and 28 days. Cell culture medium was changed in every 3 days.

5.2.10. Cell Proliferation Study using WST-1 Assay

An investigation of the viability of hOB cells grown in the PCL/in situ HAPclay scaffolds was studied using WST-1 (Roche) assay. The cell viability analysis was performed on hOB cells seeded scaffolds for 4, 7, 18 and 28 days following the manufacturer protocol. In brief, the hOB cells seeded scaffolds were removed from the culture medium and washed with PBS. Then, washed scaffolds were placed in a 96-well plate filled with culture medium and WST-1 reagent and further, incubated at 37 ^{0}C and 5% CO_2. After 4 hours of incubation scaffolds were removed from the solution and the absorbance of formazan formed solution, which is directly related to a number of live cells, was read at 450 nm using a microplate spectrophotometer (Bio-Rad, Benchmark Plus).

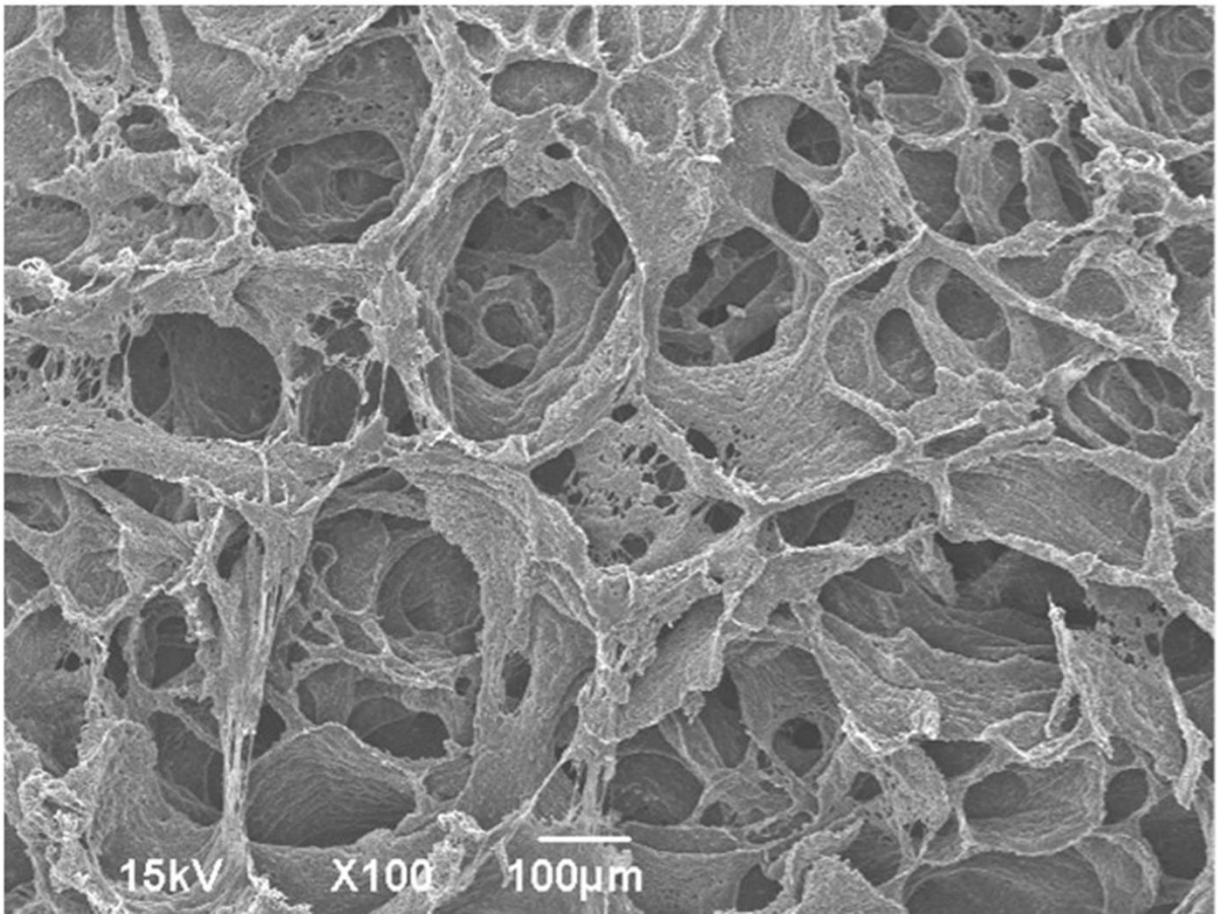

Figure 5.2. SEM micrograph of PCL/in situ HAPclay scaffold. Macropores ranging between 100-300µm sizes.

5.2.11. Mechanical Properties of Scaffolds Seeded with hOB Cell

The compressive mechanical properties were calculated for of PCL/in situ HAPclay scaffolds seeded with hOB cells. All compression tests were performed in wet conditions using compression testing machine (SATEC, model 22 EMF, PA, USA). For wet testing, scaffolds were directly removed from the cell culture medium (at 37 ^{0}C) after 4 days, 7 days, 18 days and 28 days and tested at room temperature. Deformation control loading was applied at a constant rate of 1

mm/min up to 10% strain. The load-displacement results were analyzed using Instron Bluehill® software v. 2.5 and used for stress-strain calculations.

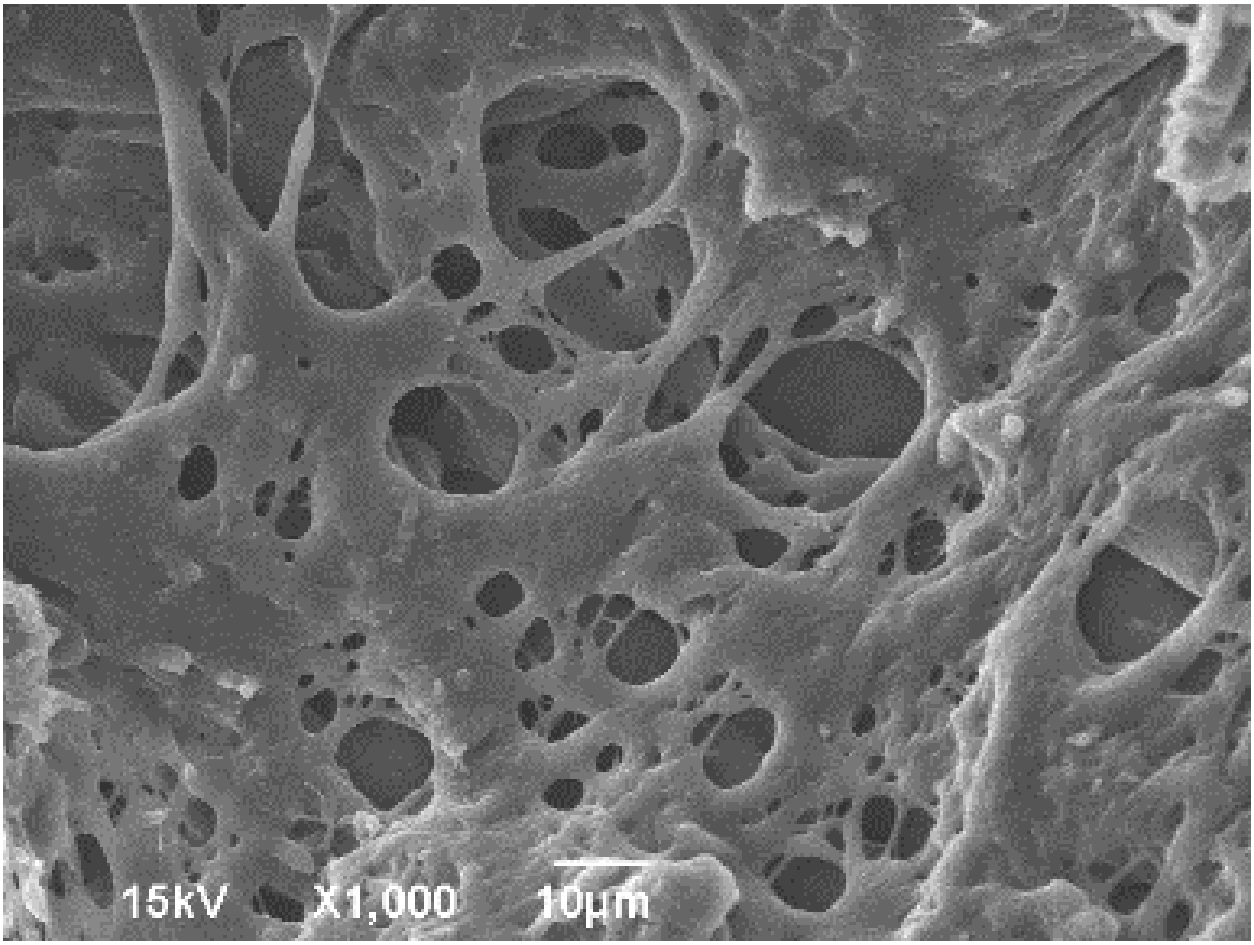

Figure 5.3. SEM micrograph of PCL/in situ HAPclay scaffold. Micropores (<10 µm and 10–30 µm range) in the walls of PCL/in situ HAPclay scaffold microstructure.

5.2.12. Integrative Finite Element Modeling of PCL/*In situ* HAPclay Scaffold of 'Critical Size.'

An integrative FE modeling was performed to analyze the effect of the time-dependent process of accelerated degradation and hOB cell culture on the mechanical behavior of implant PCL/in situ HAPclay scaffold in critical size bone defects. The length and diameter of the FE model were 4cm and 2.82cm, respectively. The FE model was constructed using 1.5mm sized

tetrahedral elements. The element length was same as the size of our FE model of PCL/in situ HAPclay. The total number of nodes and elements of the FE model were 7,133 and 36,037, respectively. The bottom and top surfaces were attached to plates. The bottom plate was constrained in all three directions, and a uniform axial load in z direction was applied on the top plate. The time-dependent material parameters used in FE simulations were obtained from the integration of the stress-strain response of our predicted FE model of PCL/in situ HAPclay scaffolds (section 5.3.2.) and proposed degradation function (sections 5.3.3. and 5.3.4.). Finally, the stress-strain responses were reported for the FE simulations of implant scaffold in critical size bone defects. The FE model was carried out using the Marc Mentat 13.0.

5.2.13. Statistical Analysis

All experimental data were analyzed using Student's t-test and expressed as a mean ± standard deviation. The data between more than two different samples were compared by using one-way ANOVA. The difference between samples was considered significantly if $p < 0.01$.

5.3. Results

5.3.1. Initial Morphology and Mechanical Properties

The SEM images of the PCL/in situ HAPclay scaffold are presented in Figs 5.2. and 5.3. The sizes of pores in the scaffolds are in the range of 100-300 μm. In addition to the larger pores, the PCL/in situ HAPclay scaffolds also have wall porosity of sizes less than 10 μm and 10-30 μm range, Fig 5.3. These porosities reduce the amount of material in the scaffold walls. The compression loading tests were performed (10% strain) to evaluate the mechanical behavior of PCL/in situ HAPclay scaffolds. The stress-strain behavior of the scaffold was obtained from the stress-strain response obtained from the experiments as shown in Fig 5.5.

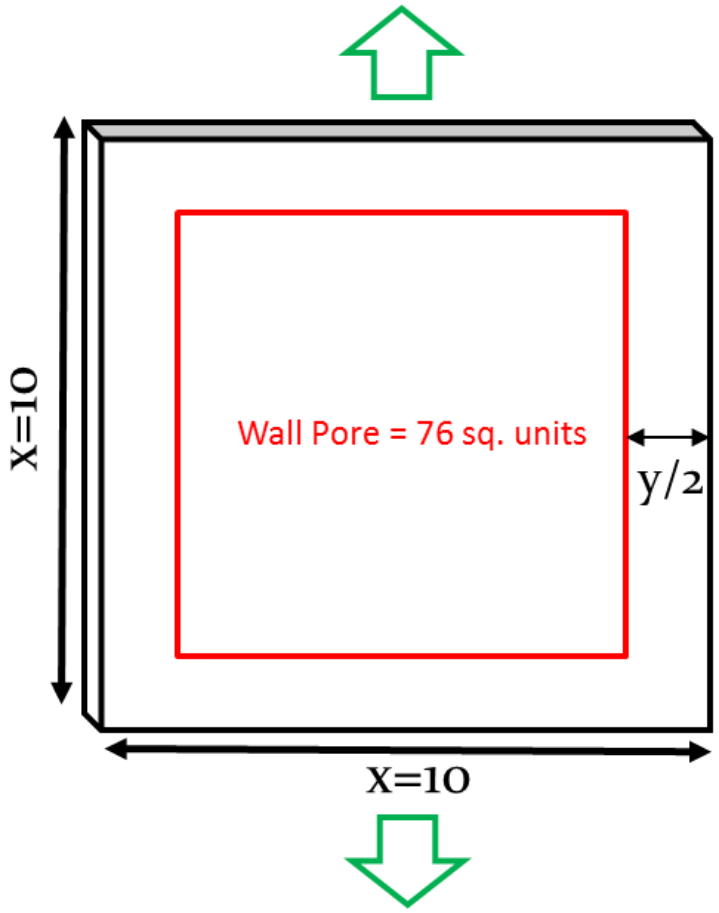

Figure 5.4. Wall porosity correction (Reduction factor) applied to finite element analysis stress due to wall porosity = K = total wall length/material length = x/y =8.

5.3.2. Finite Element Analysis of PCL/*In situ* HAPclay Scaffolds

In this study, a micro-computed tomography aided FE modeling approach is applied to analyze mechanical behavior in the PCL/ in situ HAPclay scaffolds. As shown in Fig 5.1c., a PCL/in situ HAPclay scaffold FE model was designed from the 3D reconstruction of µCT images. A cylindrical region of interest was isolated from the whole 3D scaffold model for the FE analysis calculations. The FE model was subsequently constructed by converting 3D scaffold model into the 3D tetrahedral mesh. To reproduce mechanical compressive test conditions, we have applied similar boundary conditions in our FE model. Therefore, up to a 10% compressive strain was applied on the FE model.

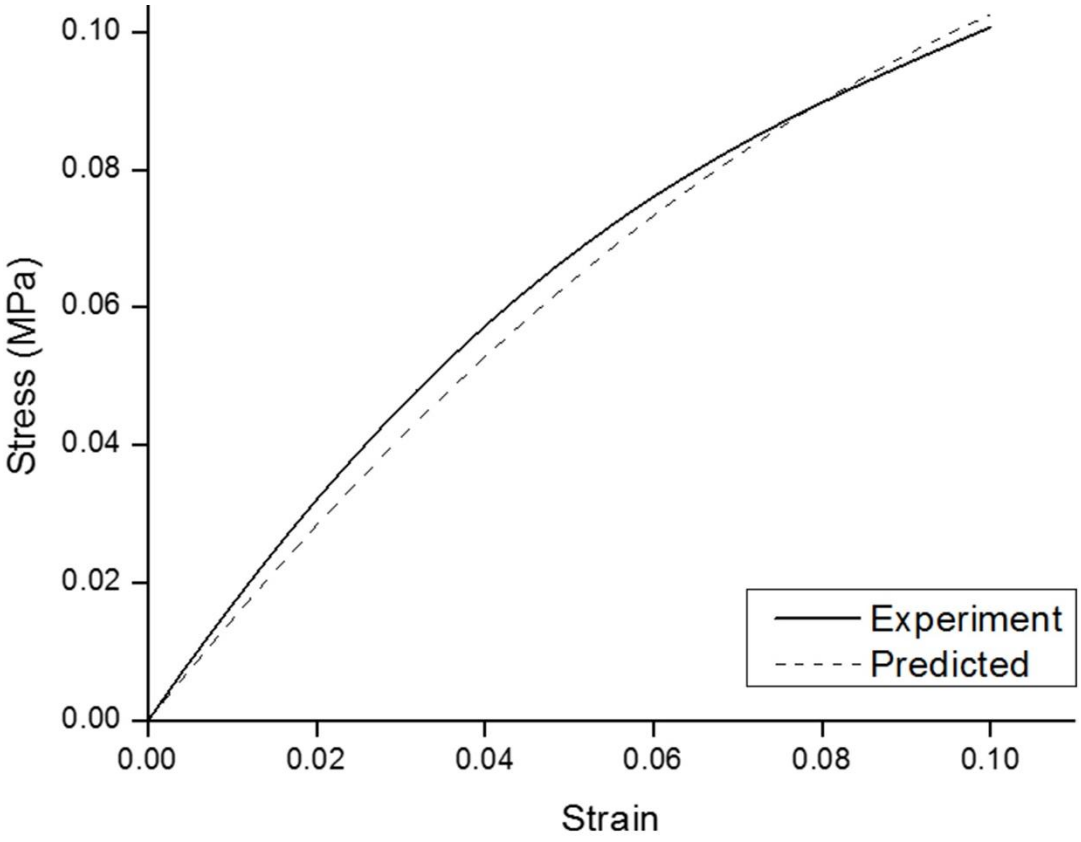

Figure 5.5. Comparison of mechanical behavior obtained from experiments and finite element analysis. Results show good agreement after wall porosity correction.

It is found that the stress calculated from FE analyzes is higher than the experimentally calculated stress because the FE model does not include wall porosity since the μCT is unable to image features less than 20 μm. The size range of wall porosity is 0-20 μm. As a result, the FE model has lower porosity than the actual scaffold and as a consequence, higher predicted stress values. To incorporate the effect of micropores (10-30 μm or less) in the walls on the mechanical properties prediction of PCL/in situ HAPclay scaffold, the porosity of the scaffold walls was calculated using Fig 5.4. SEM images indicate 76% wall porosity in the scaffold walls. To include this wall porosity which is not represented in FE model, we introduced a new reduction factor, K. Reduction factor 'K' is a wall porosity correction and defined as a total wall length divided by

material length (x/y), Fig 5.4. The stress values obtained from FE analysis were then corrected by multiplying them by the reduction factor, K. As shown in Fig 5.4., K for PCL/in situ HAPclay is obtained to be 8. A comparison between stress-strain behavior from experimental compression tests and multiscale model after the incorporation of reduction factor, K is shown in Fig 5.5.

5.3.3. Accelerated Degradation in PCL/*In situ* HAPclay Scaffolds

5.3.3.1. Mechanical Properties of PCL/*In situ* HAPclay Degradation in 0.1M NaOH

The accelerated degradation studies (0.1M NaOH maintained at 37^0C) were carried out on PCL/in situ HAPclay scaffolds. The stress-strain plots of the undegraded and degraded samples are shown in Fig 5.6. As seen, the compressive mechanical properties of the scaffolds decrease with time. The plot shows a gradual decrease in first 5 days followed by a more rapid drop up to 18 days. The significant drop in the mechanical properties can be observed between 5 to 7 days.

5.3.3.2. Analytical Model for Degradation

In the present study, we propose a new analytical mechanical degradation model of PCL/in situ HAPclay scaffolds. The model is developed to predict the mechanical properties of scaffolds with degradation. The proposed analytical modeling approach is inspired by the disturbed state concept (DSC) [72]. The DSC can be utilized to analyze and predict the mechanical degradation behavior of polymer scaffolds.

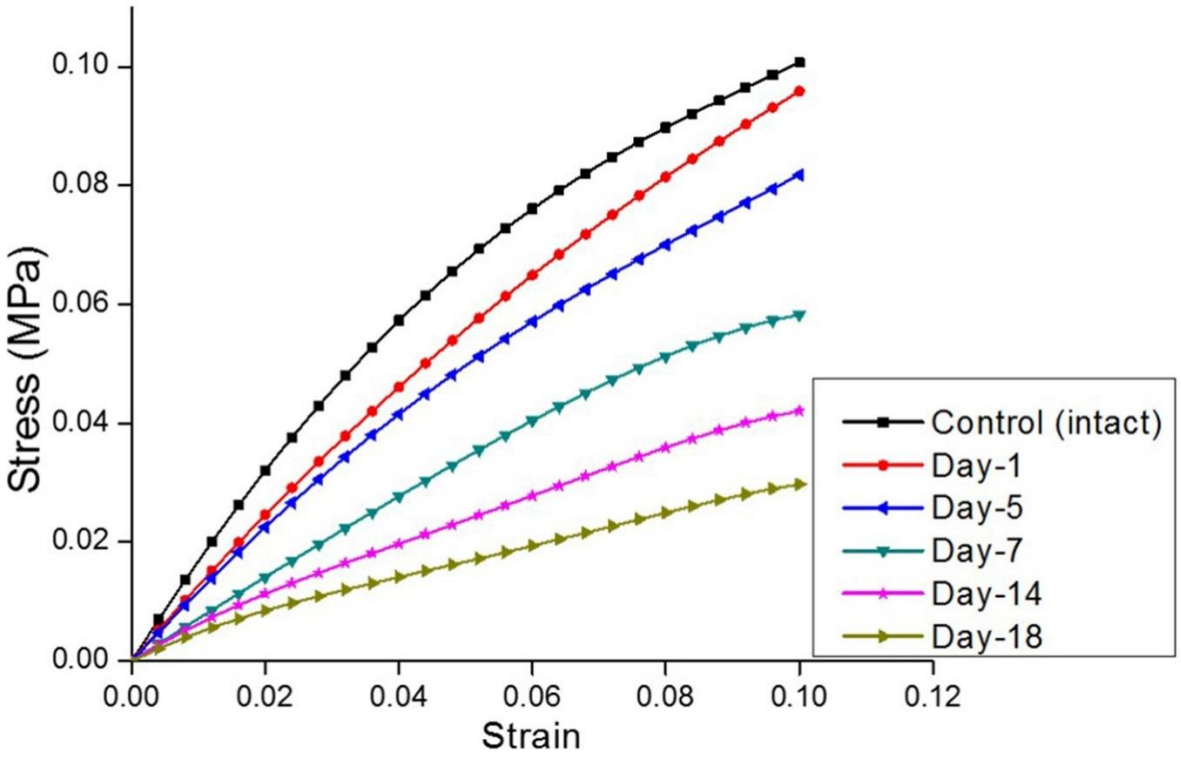

Figure 5.6. Compressive mechanical properties of undegraded (control) and degraded (day 1, 5, 7, 14 and 18) PCL/in situ HAPclay scaffolds in alkaline condition (0.1M NaOH). The compressive mechanical properties of PCL/in situ HAPclay scaffold decreases with degradation time.

The DSC considers material to be completely intact at relative intact (RI) state and completely deformed at fully adjusted (FA) state or vice-versa. For degradation studies, RI is undegraded scaffolds and FA is completely degraded scaffold. In the current work, the degradation is computed as:

$$D=1-\left(\frac{S_t}{S_0}\right) \quad (5.1.)$$

where D is the degradation; S_t is the strain energy of degraded sample at time t; S_0 is the strain energy of the undegraded sample. The strain energies are calculated as,

$$S=\int_0^p \sigma \, d\epsilon \quad (5.2.)$$

where, p is a predetermined strain value used for calculating the strain energy for mechanical experiments on intact samples and samples at various degradation times. Effectively, S is the area under the stress-strain curves up to strain p. In the current study, p used is 10%. The value of D ranges from D=0 for intact (undegraded sample) to D=1 or a residual value for the fully degraded sample. As shown in Fig 5.6., the mechanical response of the scaffolds degrades with increasing time and thus, the strain energy S_t decreases with time of the degradation D increases with time.

A degradation time evolution function is proposed to capture the experimental behavior and is used as a predictive mathematical model. We propose to use a mathematical form used in damage mechanics and also used by the author (D. Katti) earlier [72].

$$D=D_u(1-\exp(-At^z)) \qquad (5.3.)$$

where D is the degradation, D_u is the residual degradation value if degradation does not lead to a complete loss of mechanical properties, t is the time, A and Z are the degradation evolution parameters for the scaffolds obtained from mechanical tests on scaffolds. A and Z parameters could be affected by pressure and fluid flow rate. In the present work, all experiments were conducted at atmospheric pressure and at no flow conditions. Also, D_u=1 in the current work. Consequently, equation 5.3. becomes,

$$D=(1-\exp(-At^z)) \qquad (5.4.)$$

As we will see subsequently, the above function is effective in modeling the degradable behavior of scaffolds used in the study.

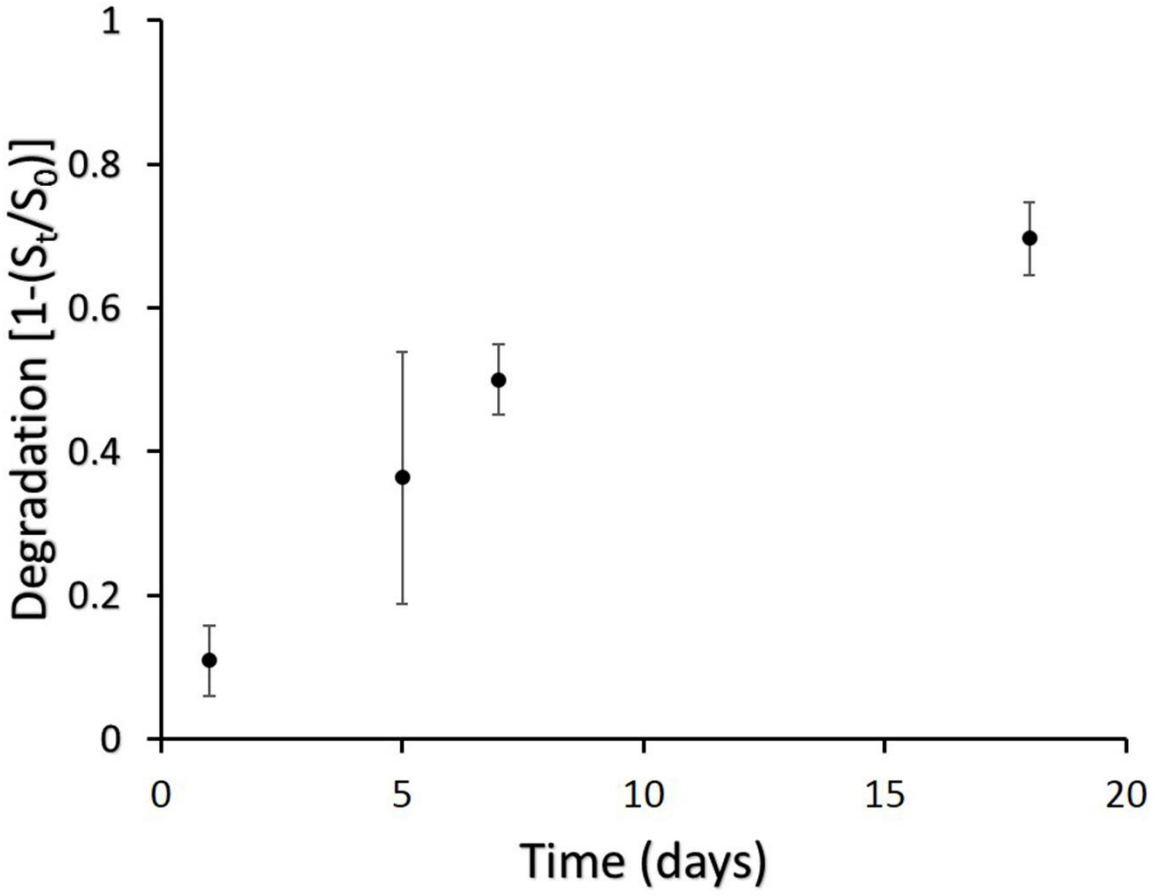

Figure 5.7. Mechanical property degradation (D) of PCL/in situ HAPclay scaffolds in alkaline condition (0.1M NaOH).

5.3.3.3. Parameter Determination

The accelerated degradation, D of PCL/in situ HAPclay scaffolds at day 1, 5, 7 and 18 were obtained from experimental compression tests results presented in Fig. 5.6. The values of D were found from calculating strain energy of the scaffolds at 10% strain using equation 5.1. Further, S was found from the area under the stress-strain curve from compression tests results in Fig 5.6. Fig 5.7. shows the degradation values calculated using equation 5.1. versus time. As seen in Fig 5.7.,

mechanical degradation increases with time. Applying natural log on the left and right-hand side of the equation 5.4. leads to,

$$\ln[-\ln(1-D)] = \ln(A) + z\ln(t) \quad (5.5.)$$

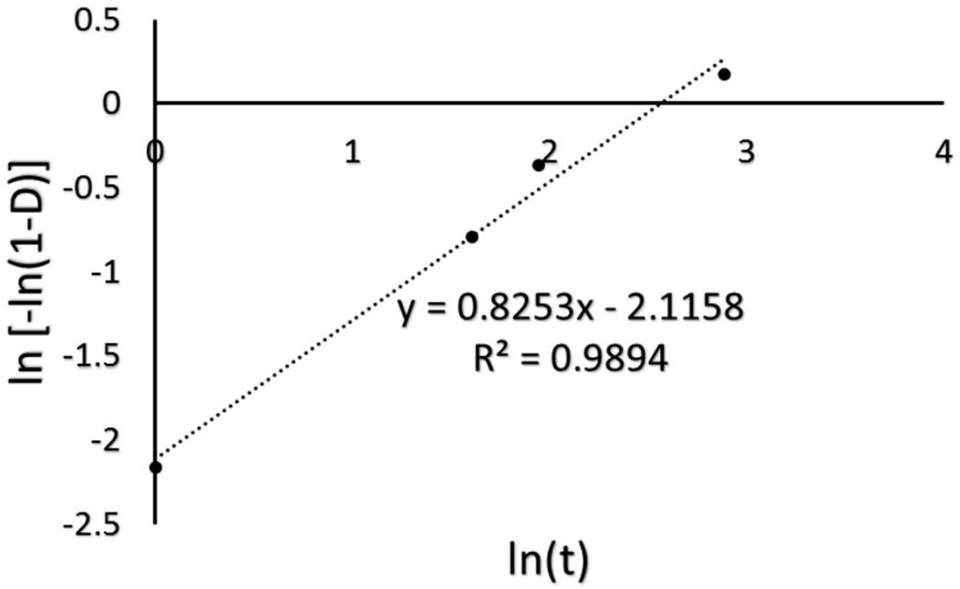

Figure 5.8. Plot for calculation of parameters for degradation function (D) of PCL/in situ HAPclay scaffolds in alkaline condition (0.1M NaOH).

Equation 5.5. is a line in the ln [-ln(1-D)] vs. ln(t) space (Fig. 4b), ln(A) is the intercept and z is the slope of the line. The calculated degradation data at different days is found from Fig 5.7. It should be noted that we have not used the data for day 14 for calculation of parameters, and the data will be subsequently used for validation. By substituting degradation values at different days, A and z were found by using the least-square method. The value of A and z are 0.1205 and 0.8253, respectively (Fig 5.8.). Therefore, for the accelerated degradation of PCL/in situ HAPclay scaffolds, the mechanical degradation function, D in equation 5.4. can be written as:

$$D=1-\exp(-0.1205t^{0.8253}) \quad (5.6.)$$

5.3.3.4. Validation of Model

The accelerated degradation analytical model proposed in equation 5.4. was validated by predicting compression mechanical tests results not used in finding the parameters. The model was validated with respect to the stress-strain response for the degraded PCL/in situ HAPclay scaffold at day 14. The degradation value for degraded PCL/in situ HAPclay scaffold at day 14 was obtained from equation 5.6. Further, the stress values were calculated by using following equation:

$$\sigma = (1 - D)\sigma_0 \quad (5.7.)$$

where σ is the stress of degraded sample; σ_0 is the stress of the undegraded sample at the same strain, and D is the degradation function value at day t.

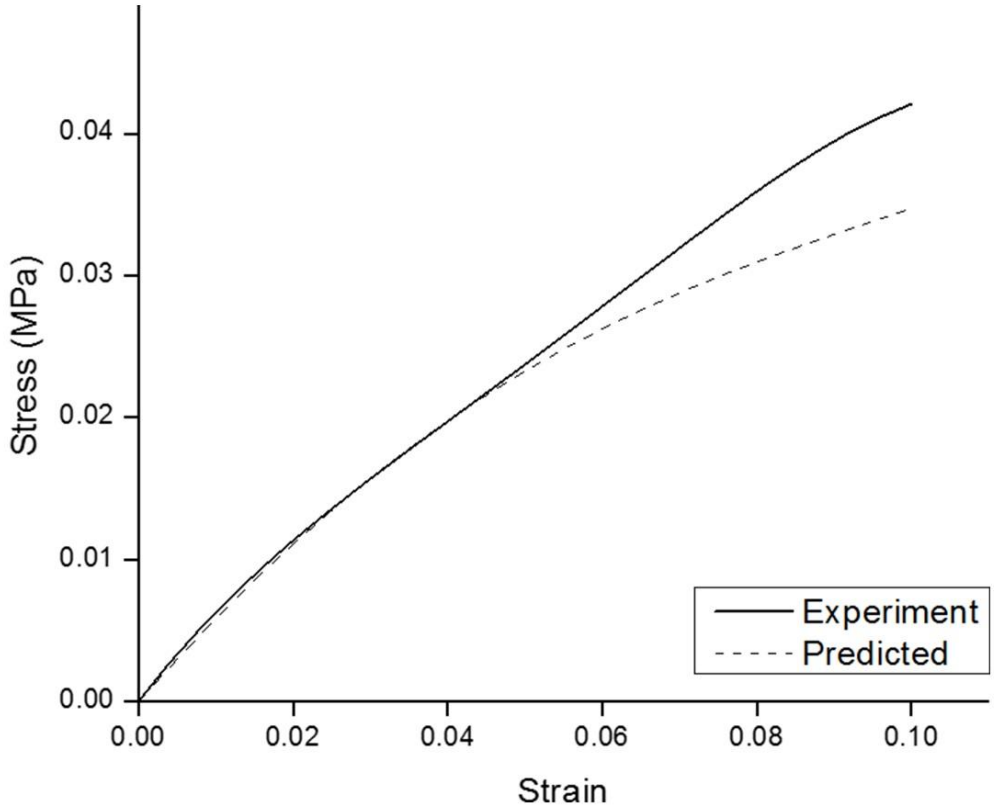

Figure 5.9. Model verification: Experimental compressive stress–strain curve of PCL/in situ HAPclay scaffolds degraded in alkaline conditions (0.1M NaOH) at 14 days and compared to the model predicted compressive stress-strain curve.

Table 5.1. Verification of Degradation function (D). Comparison of strain energy between predicted and experiment data at 14 days.

Strain	Strain Energy (exp) (Pa)	Strain Energy (predicted) (Pa)	Difference
5%	651.82	642.68	1.40%
10%	2334.57	2123.13	9.06%

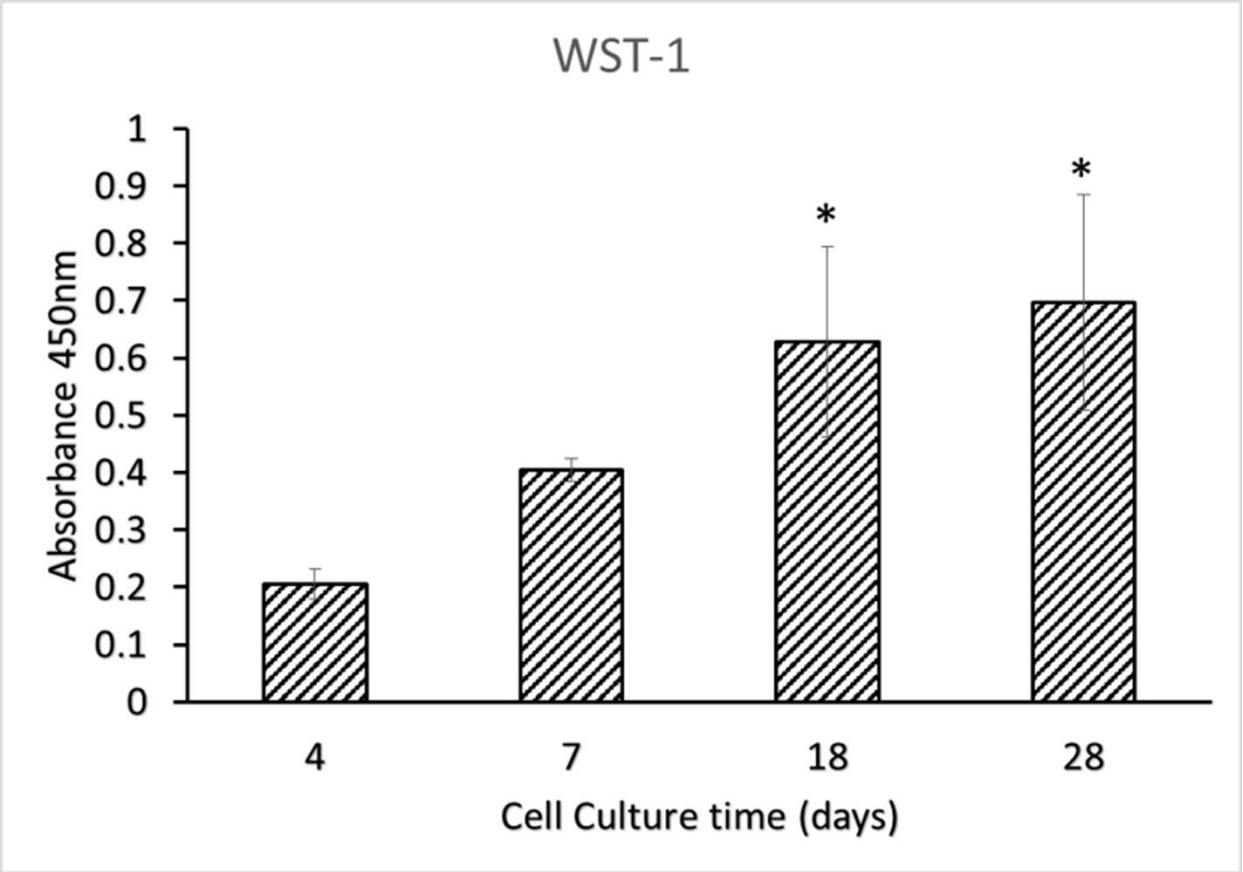

Figure 5.10. WST-1 cell proliferation study of hOB cells cultured on PCL/in situ HAPclay scaffolds. The data were obtained after 4, 7, 18 and 28 days of cell culture and presented as mean ± standard deviations. *Represents significant difference from day-4 with $p < 0.01$.

Fig 5.9. shows the comparison of stress-strain response after 14 days degradation, between the predicted stress response obtained from the analytical model and stress response from the compression tests. The comparison presented shows good agreement between tests results and predicted model for stress-strain responses of the degraded PCL/in situ HAPclay scaffolds. Also, the strain energy of the 14 days degraded sample was also back-predicted using the D value calculated from the analytical model. The comparison of strain energy at 5% and 10% strains, between predicted from model and compression tests results is presented in Table 5.1. The difference of strain energy at 5% and 10% strains, calculated from model and compression tests is

1.40% and 9.06%, respectively. We found good agreement between predicted model and compression tests results, indicating that the proposed model (equation 5.4.) provides a satisfactory prediction of the mechanical behavior of the degradation of PCL/in situ HAPclay scaffolds with time.

5.3.4. Human Osteoblast Cells Seeded PCL/*In situ* HAPclay Scaffolds

5.3.4.1. Cell Proliferation

The viability of hOB cells on PCL/in situ HAPclay scaffolds at 4, 7, 18 and 28 days was quantitatively obtained using WST-1 assay. In WST-1 assay, the metabolic activity of living cells converts WST-1 reagent into colored formazan the number of cells can be estimated by measuring the intensity of formazan, which is proportional to the number of living cells. The results showed a progressive increase in hOB cell proliferation with the number of days (Fig 5.10.).

5.3.4.2. Morphology and Mechanical Properties

SEM micrographs in Fig 5.11 show the behavior of hOB cells on PCL/in situ HAPclay scaffolds for a cell culture period of 28 days. The hOB cells grown on these scaffolds showed attachment, spreading and formation of mineralized ECM. These images indicate that the PCL/in situ HAPclay scaffolds used in this study are biocompatible and have the potential for bone tissue regeneration.

The compressive mechanical properties of PCL/in situ HAPclay scaffolds seeded with hOB cells were carried out in wet condition. During the compression testing, scaffolds were soaked with cell culture medium at room temperature. The stress-strain plot of the seeded scaffolds is shown in Fig 5.12. The compressive mechanical properties of seeded scaffolds increased with time in Fig 5.12. The increase in mechanical properties indicated the progressive (healing) effect of hOB cells on PCL/in situ HAPclay scaffolds.

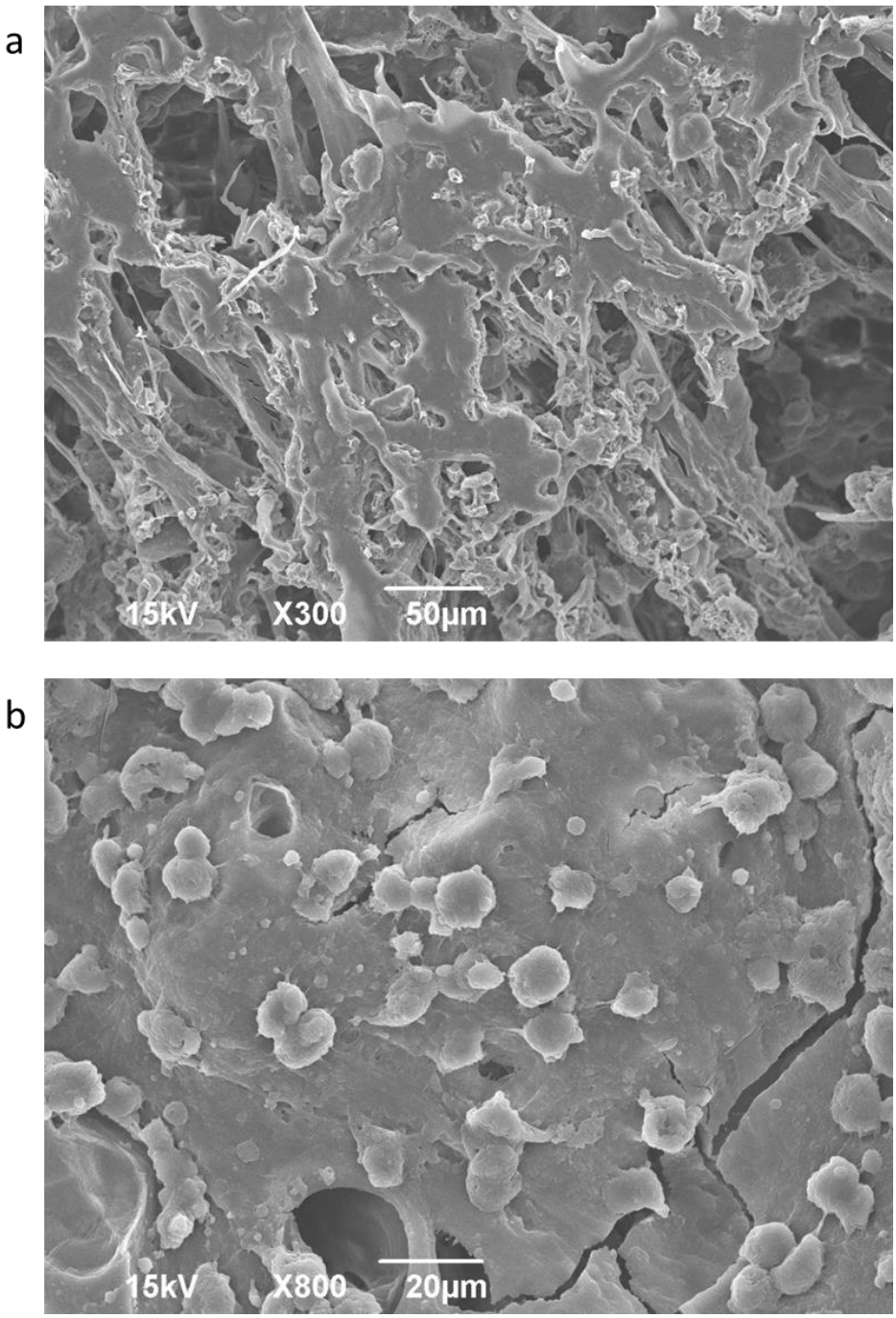

Figure 5.11. (a, b) SEM micrographs of hOB cells cultured on PCL/in situ HAPclay after 28 days. Images show flat and round morphologies indicating cells attachment and ECM formation.

5.3.4.3. Analytical Model Approach and Parameter Determination

Similar to mechanical degradation model of PCL/in situ HAPclay in 0.1M NaOH, we have proposed an analytical model of PCL/in situ HAPclay seeded with hOB cells. For hOB cells culture studies, RI is unseeded scaffolds and FA is completely seeded scaffold. The degradation, D of PCL/in situ HAPclay scaffolds seeded with hOB cells at day 4,18 and 28 were obtained from compression tests results (Fig 5.12.). Note that the day seven data is not used for parameter determination and will be used subsequently for validation. The values of D were calculated using equation 5.1. and shown in Fig 5.13. The D values were found to be decreasing with time indicating improved mechanical properties we refer to as healing.

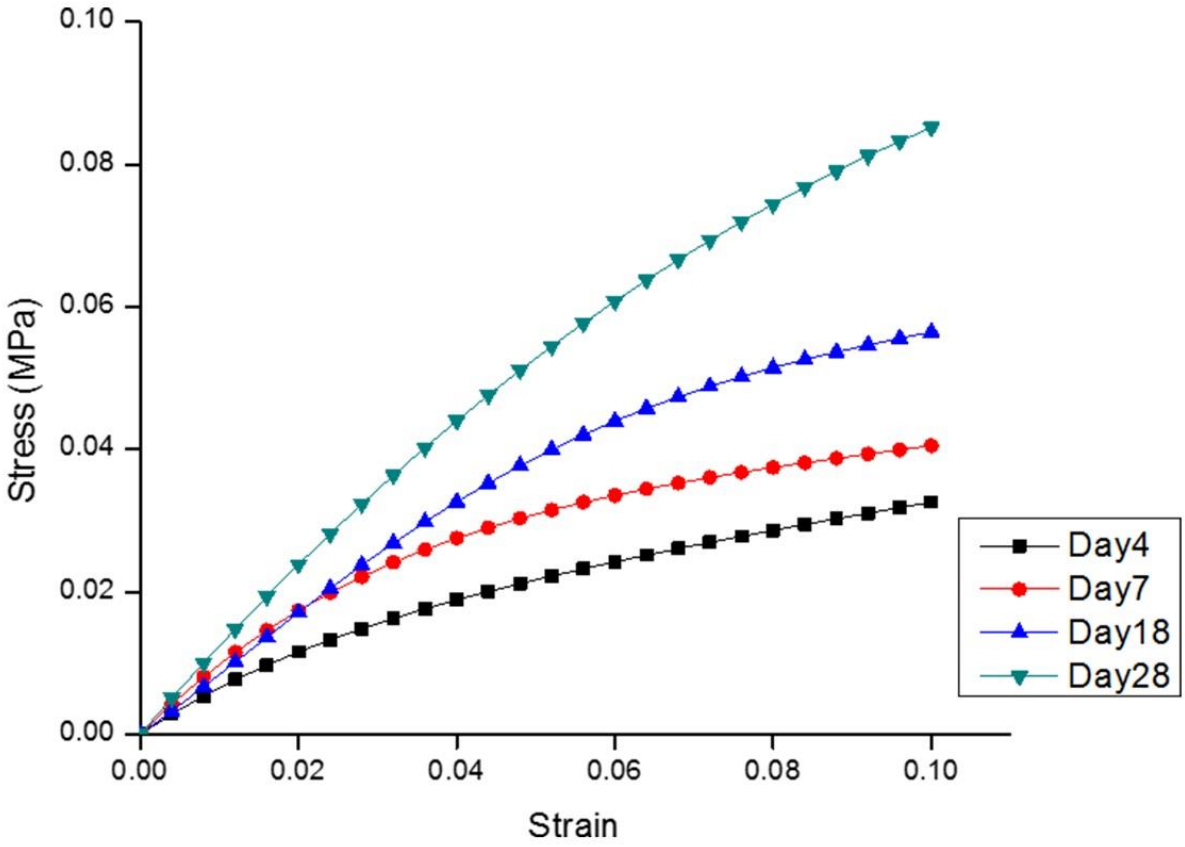

Figure 5.12. Compressive mechanical properties of PCL/in situ HAPclay scaffolds seeded with hOB cells (day 4, 7, 18 and 28). The compressive mechanical properties of PCL/in situ HAPclay scaffold increases with cell culture time.

Further, parameters A and z were obtained from Fig 5.14. using equation 5.5. The value of A is 1.9644 and z is -0.4786 for analytical model of scaffolds seeded with hOB cells. Therefore, for the hOB cells culture studies of PCL/in situ HAPclay scaffolds, the mechanical degradation function, D can be written as:

$$D=1-\exp(-1.9644t^{-0.4786}) \quad (5.8)$$

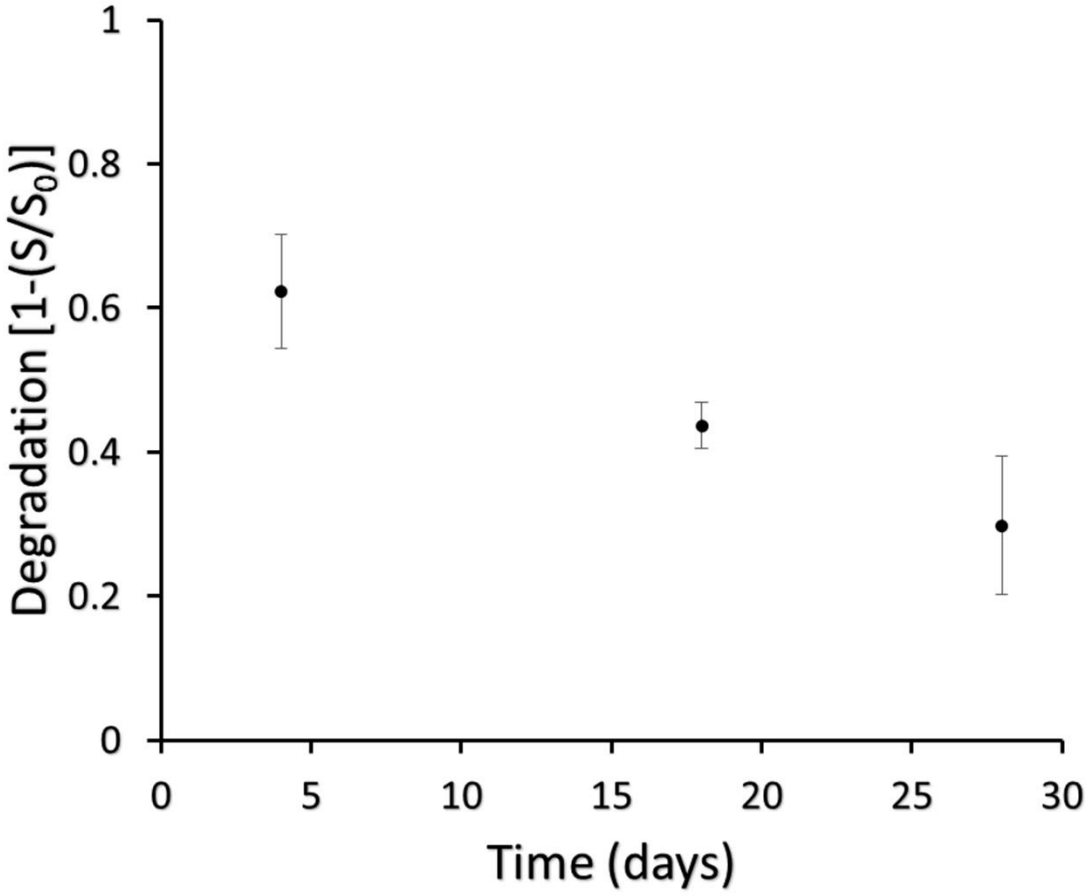

Figure 5.13. Mechanical property degradation (D) of PCL/in situ HAPclay scaffolds seeded with hOB cells. Decreased degradation with time indicates improvement in mechanical properties due to cell growth and tissue formation.

5.3.4.4. Validation of Model

To validate the analytical model of PCL/in situ HAPclay scaffolds seeded with hOB cells, we compared stress-strain response and strain energy (at 5% and 10%) between experimental compression tests obtained at day 7 and predicted stress-strain response calculated using equation 5.8. The stress-strain response comparison is plotted in Fig 5.15. and strain energy is shown in Table 2. The comparison of strain energy at 5% and 10% strains, between predicted from model and compression tests results are presented in Table 5.2. The difference of strain energy at 5% and 10% strains, calculated from model and compression tests is 4.14% and 1.58%, respectively. It is evident from Fig 5.15. and Table 5.2. that our proposed analytical model (equation 5.8.) exhibits good prediction of the mechanical behavior of PCL/in situ HAPclay scaffolds seeded with hOB cells.

5.3.5. Integrative Multiscale Model

The integrative FE analysis simulations were performed to predict the mechanical behavior of PCL/in situ HAPclay scaffold in critical size bone defects with time in accelerated degradation (0.1 M NaOH) and hOB cells seeded conditions. We constructed an FE model of a solid cylinder, 4 cm in diameter and 2.82 cm in height to represent a critical bone defect. Details about the model and simulations are presented in section 5.2.12., and the model is shown in Fig 5.16. Each element of the multiscale integrative model (Fig 5.16. used in this study was considered as a representative model of our PCL/in situ HAPclay scaffold (Fig 5.1c.) and thus, represents the microstructure and material properties of PCL/in situ HAPclay scaffold.

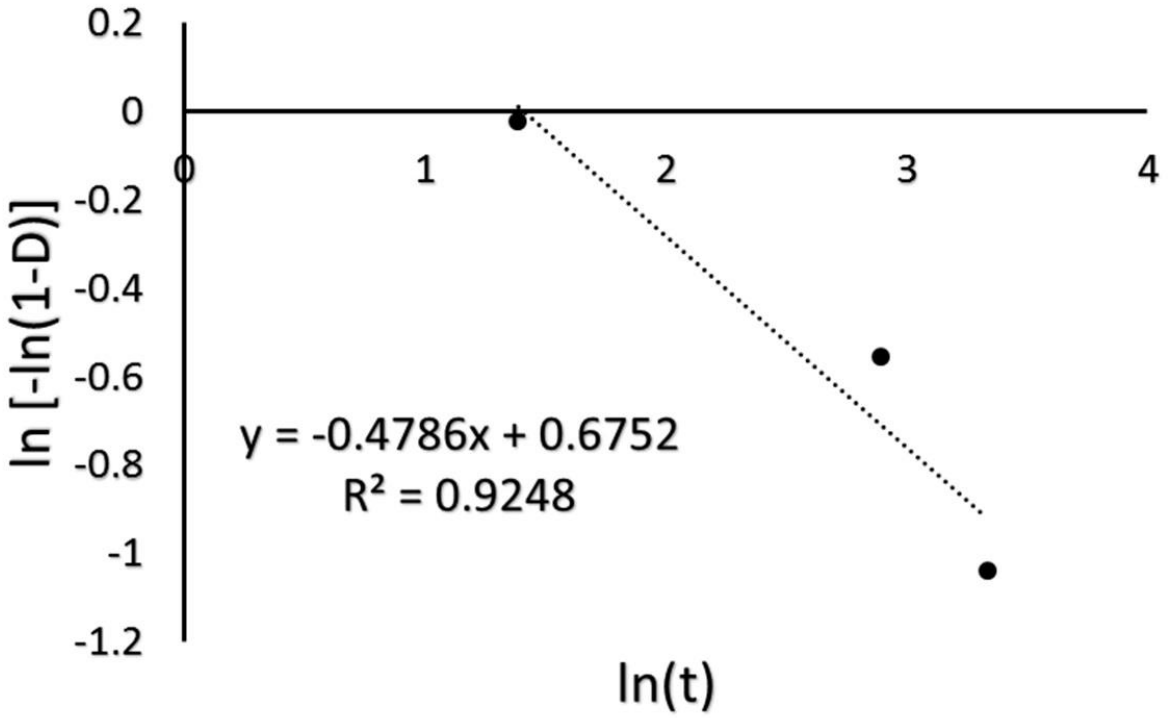

Figure 5.14. Calculation of critical parameters for degradation function (D) of PCL/in situ HAPclay scaffolds seeded with hOB cells.

The mechanical behavior of the scaffold evolves due to accelerated degradation and interactions with hOB cells. To obtain the time-dependent response of the critical bone defect implant model using integrative FE model, the following approach was used: 1) we introduced the stress-strain response of the predicted FE model of PCL/in situ HAPclay scaffolds as the "materials response" of critical defect intact scaffold model material and 2) to model the time-dependent response, the intact "material response" was modified using equation 5.7. with equation 5.6. used for accelerated degradation simulations and with equation 5.8. for hOB cell seeded samples. The results from multiscale integrative simulations of accelerated degradation and hOB cells seeded implant scaffold in critical size bone defects are presented in Fig 5.17 and Fig 5.19., respectively.

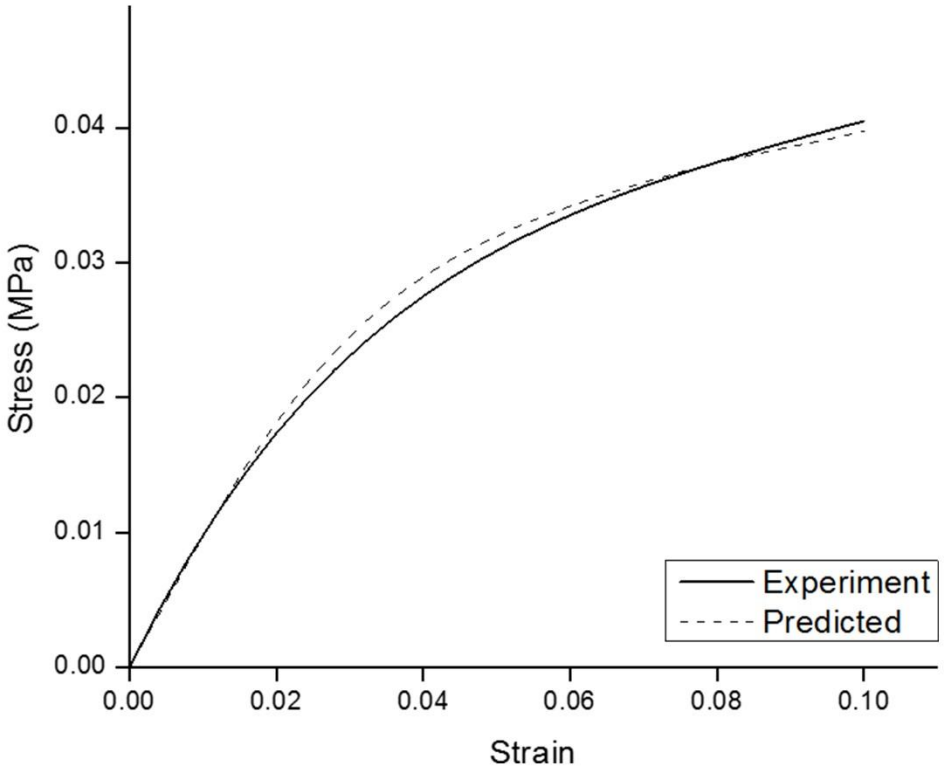

Figure 5.15. Model verification: Experimental compressive stress–strain curve of PCL/in situ HAPclay scaffolds seeded with hOB cells at 7 days and compared to the model predicted compressive stress-strain curve.

Table 5.2. Verification of Degradation function (D). Comparison of strain energy between predicted and experiment data at 7 days.

Strain	Strain Energy (exp) (Pa)	Strain Energy (predicted) (Pa)	Difference
5%	939.29	979.85	4.14%
10%	2850.54	2805.55	1.58%

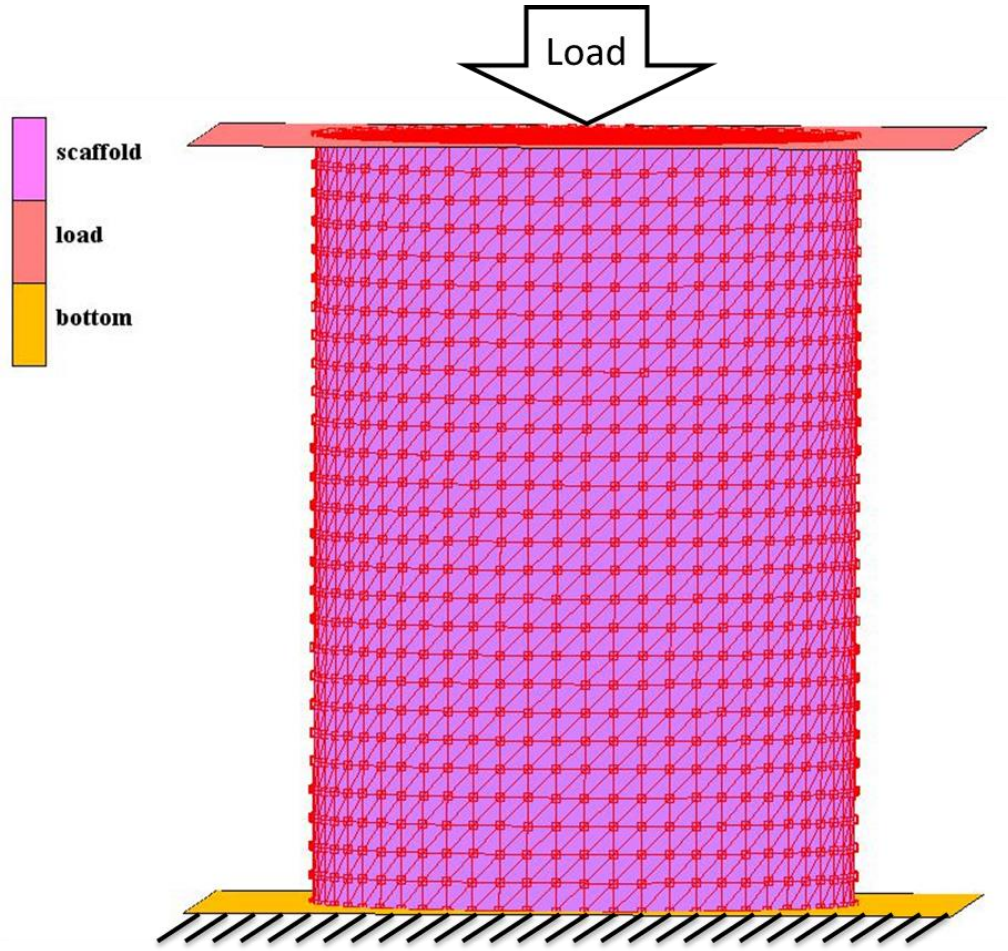

Figure 5.16. Finite element model of PCL/in situ HAPclay implant scaffold in critical size bone defects.

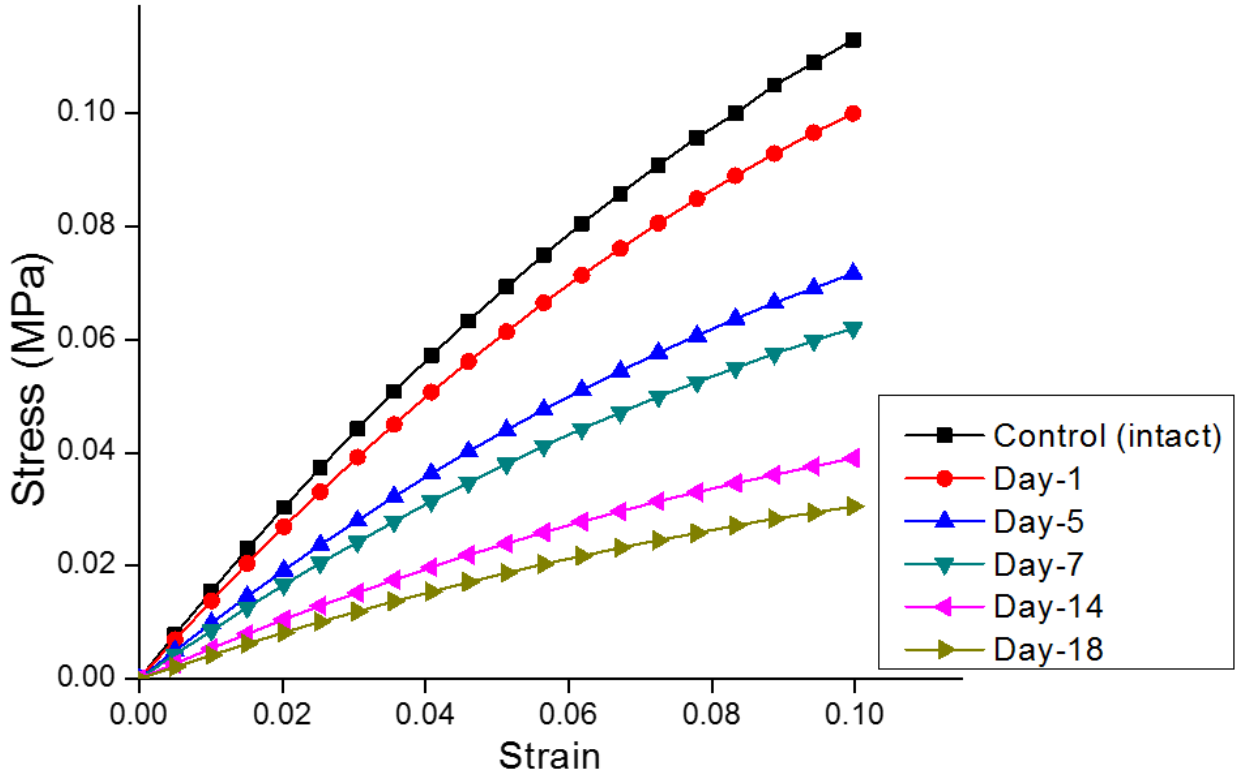

Figure 5.17. Mechanical behavior evolution of integrative finite element analysis of PCL/in situ HAPclay implant scaffold in critical size bone defects for undegraded (control) and degraded (day 1, 5, 7, 14 and 18) in alkaline condition (0.1M NaOH).

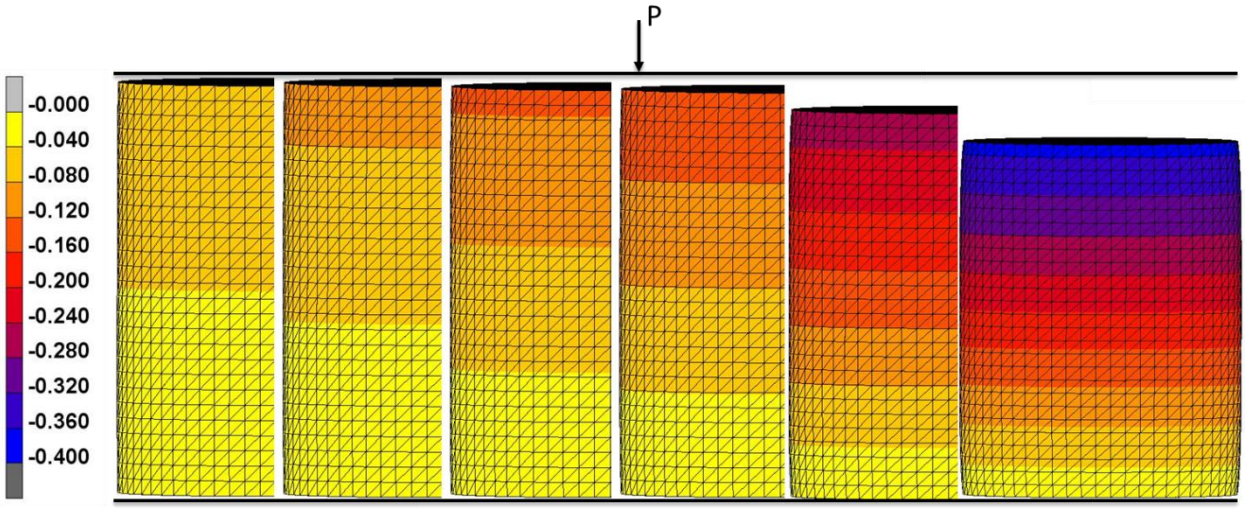

Day	Control	1	5	7	14	18
Strain	2.02%	2.4%	3.43%	3.95%	6.98%	10%

Figure 5.18. Time-dependent deformation profiles of integrative FE model of PCL/in situ HAPclay implant scaffold in alkaline condition (0.1M NaOH).

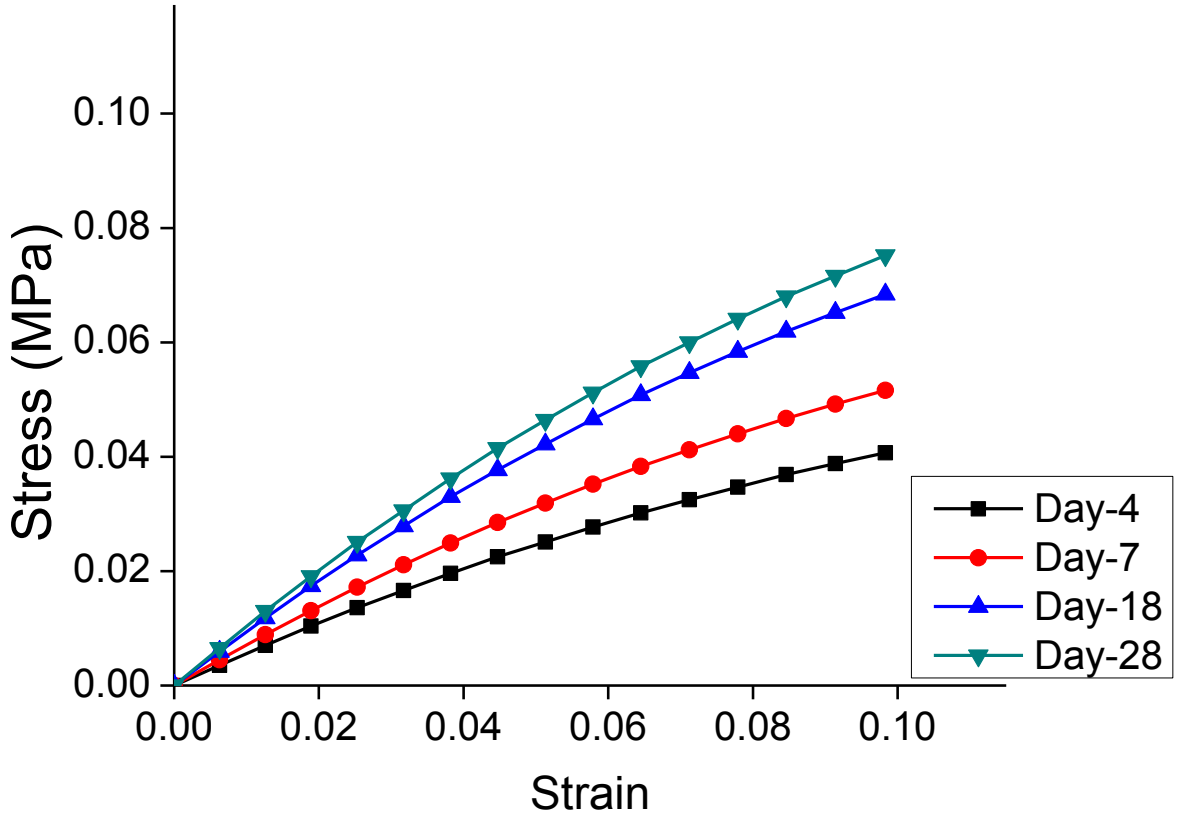

Figure 5.19. Mechanical behavior evolution of integrative finite element analysis of PCL/in situ HAPclay implant scaffold in critical size bone defects for hOB cells seeded (day 4, 7, 18 and 28).

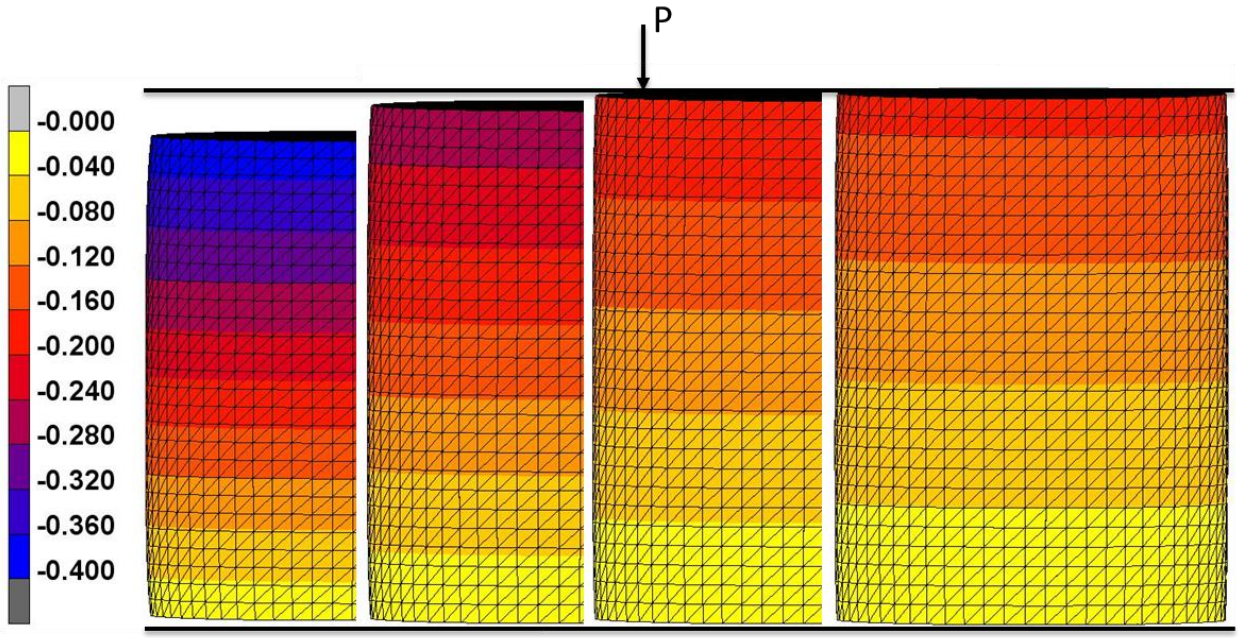

Day	4	7	18	28
Strain	10%	7.12%	5.13%	4.47%

Figure 5.20. Time-dependent deformation profiles of integrative FE model of hOB cells seeded (day 4, 7, 18 and 28) PCL/in situ HAPclay implant scaffolds.

Fig 5.17. shows stress-strain response obtained from FE simulations for the critical bone defect implant model at various days of soaking at accelerated degradation conditions. Fig 5.17. shows that the stress-strain response degrades with time as expected and as observed in our experimental work. Fig 5.19. shows stress-strain response obtained from the FE simulations on hOB seeded critical bone defect implant model with time. The mechanical properties of the cell-tissue-scaffold implant improve with time. Once again, we have observed such behavior in experiments as described in section 5.3.4. Figs 5.18. and 5.20 show the time-dependent deformation profiles of FE model in different degradation conditions. Same axial stress was applied to compare these deformation profiles.

5.4. Discussion

A simulations based materials and scaffold design, along with the ability to fabricate geometrically accurate implantable scaffolds would allow for personalizing tissue engineering for patients. In the current study, we have demonstrated the computational multiscale mechanics approach that bridges the molecular scale and microstructure of scaffold to the macroscale response. The introduction of a new degradation mechanics modeling framework allows for accurately predicting the mechanical response of scaffold over time. Potentially, this approach can be used reverse engineer the microstructure and the nanocomposite material to achieve desired macroscale response.

Our prior and current work shows that the PCL/in situ HAPclay nanocomposite material is suitable for bone tissue engineering application. SEM micrographs of PCL/in situ HAPclay scaffold (Figs 5.2. and 5.3.) show a highly porous and interconnected microstructure. It is widely reported that the macropores of 100-300 μm size support cell migration, proliferation and bone formation, whereas the micropores of <10 μm size enhance the apatite formation and protein adsorption. Our prior study also suggested that such porous and interconnected microstructure is suitable for hMSCs differentiation, proliferation and bone formation [38].

5.4.1. Finite Element Analysis of PCL/*In situ* HAPclay Scaffolds

Due to the highly complex, hierarchically organized nature of biological materials, standard protocols of using specific mechanical properties of materials such as Youngs modulus into mechanics models, are not fully capable of capturing their mechanical behavior evolution [11]. A truly computational multiscale approach is demonstrated here to predict the mechanical property evolution in biomaterials. Here, the entire stress-strain material response is used rather than just the elastic modulus traditionally used in the literature. We previously developed a

representative molecular model of PCL/in situ HAPclay composite and evaluated the molecular interactions between constituents in the nanocomposite. MD simulations revealed the strong non-bonded interactions between HAP, PCL and modified MMTclay, indicating their influence on this complex nanocomposite system. SMD simulations were conducted on the molecular model of the nanocomposite material to obtain the mechanical response of the material. The stress-strain response showed two distinct regions in terms of the slope; a stiffer behavior at lower strain and a significantly less stiff behavior at the higher strain. Similar behavior was also observed in nanoindentation experiments on the nanocomposite.

We constructed a representative FE model of PCL/in situ HAPclay scaffold, by accurately incorporating the real microstructure from a representative volume of the scaffold cylinder using high-resolution μCT and transforming the 3D image to FE models using the μCT-FE technique. The stress-strain response obtained from our steered molecular dynamics (SMD) simulations [44] was used to provide the material parameter in the FE analysis of PCL/in situ HAPclay representative scaffold models. The 3D reconstructed FE model (Fig 5.1c.) contains the high porosity and pore interconnectivity in PCL/in situ HAPclay observed in the μCT images. A significant portion of the pores is in the size range of (100-300 μm). However, the micropores in the scaffold walls (10-30 μm or less) could not be identified due to the limitation of our μCT resolution. Thus, the tetrahedral element mesh obtained from the μCT does not contain the micropores in the scaffold walls observed in SEM images. The absence of the scaffold wall porosity in the FE analysis leads to the overestimation of the stress-strain responses predicted from the FE simulations. The effect of wall porosity on the mechanical response of the scaffold is incorporated by introducing a reduction factor, K. The reduction factor considers the wall porosity and is calculated from the SEM imaging of scaffolds. The FE model of the PCL/in situ HAPclay

scaffold developed in this study was validated by comparing the results between the stress-strain responses of scaffolds as calculated with the compression test experiments on the scaffolds and FE simulation. The FE simulation results (that incorporate nanocomposite mechanical properties obtained from SMD simulations) compare well with experimentally observed response as seen in Fig 5.5.

5.4.2. Effect of Accelerated Degradation on PCL/*In situ* HAPclay Scaffolds

The PCL polymer is known for its slow degradation rate (3-4 years) [59, 73]. Thus, often alkaline conditions are used as a catalytic substance to accelerate the hydrolytic degradation of PCL to study degradation mechanism in a short period of time. Fig 5.6. shows stress–strain curves obtained from compression tests of PCL/in situ HAPclay scaffolds degraded in accelerated condition (0.1M NaOH). As seen, the mechanical properties of the PCL/in situ HAPclay scaffolds decrease gradually for first 5 days and then a higher rate of change was observed until 18 days. It has been reported that the inclusion of organomodified nanoclay particles disrupts the crystallinity of polymer nanocomposites [36, 74] and the presence of calcium phosphate based nanoparticles affect the arrangement of polymer chains [59], and the presence of nanoclay and HAP could potentially impact degradation rates.

5.4.3. Effect of Human Osteoblast Cells on PCL/*In situ* HAPclay Scaffolds

SEM micrographs of the PCL/in situ HAPclay scaffolds containing proliferating hOB cells at 28 days are shown in Fig 5.11. As seen, the hOB cells show good adhesion to the PCL/in situ HAPclay scaffolds and appear to have flat and rounded morphology. It was also observed that the attached hOB cells support the formation of mineralized ECM on the seeded scaffolds at 28 days. The hOB cells proliferation on PCL/in situ HAPclay scaffolds were evaluated at 4, 7, 18 and 28 days of *in vitro* cell culture. As seen in Fig 5.10., the number of live hOB cells have increased over

a period of 28 days. The results revealed that the proliferation of hOB cells significantly increased at 28 days compared to 4 days. The increase of hOB cells proliferation on PCL/in situ HAPclay scaffolds with the time indicated their ability to support the mineralization and formation of bone nodules. The SEM images and proliferation study results revealed that the hOB cells can thrive and proliferate on the PCL/in situ HAPclay scaffolds. Similarly, our previous studies of in situ HAPclay containing polymer composite scaffolds also showed enhanced cell adhesion and proliferation when seeded with hOB cells and hMSCs [42] [68]. The increase in mechanical properties of seeded scaffolds corresponds to the increase in cell proliferation on the scaffolds.

5.4.4. Analytical Modeling of PCl/*In situ* HAPclay Scaffolds Degradation

The polymer scaffolds can be designed to mimic the bone hierarchy with appropriate porous microenvironment and adequate mechanical properties for cell adherence, proliferation, and subsequently tissue formation. However, the prediction of the time-dependent mechanical behavior of polymer nanocomposite scaffolds during degradation and tissue regeneration is still a major challenge in bone tissue regeneration. Several material-degradation models are available to predict the degradation of polymers. We have developed damage mechanics based degradation models of PCL/in situ HAPclay scaffolds to predict the mechanical behavior of during accelerated degradation and with hOB cells over time. We have used change in strain energy to calculate experiment degradation (D) values. The strain energy calculations allow us to capture the complete mechanical response of scaffolds to predetermined strain. As seen in their respective stress-strain profiles (Figs 5.6. and 5.12.), the D values increased with time for accelerated degradation and decreased with time when hOB cells were introduced in the scaffolds. The parameters A and z were calculated from experiments and used in analytical models. Both analytical models were validated using experimental data that were not used in the calculation of degradation functions.

The validation of an analytical model for degradation studies is presented in Fig 5.9. and for hOB cell culture studies is presented in Fig 5.15. It appeared that in both cases, the stress-strain response from model and experiments have good correlation. Similarly, it is evident from Tables 5.1. and 5.2., that the strain energy comparison between model and experiments show good agreement. The parameters of such analytical models are relatively easy to obtain.

5.4.5. Finite Element Modeling of Implant scale PCL/*In situ* HAPclay Scaffold in Critical Size Bone Defects

We have developed an integrative multiscale model to predict the time-dependent mechanical behavior in implant scale PCL/in situ HAPclay scaffold for critical size bone defects. A solid cylindrical FE model in Fig 5.16. was considered as a representative of an implanted scaffold. The microstructure and time-dependent material properties of the PCL/ insitu HAPclay scaffold were captured in this model by introducing the mechanical response from FE model of PCL/in situ HAPclay representative scaffolds (Fig 5.5.) and mechanical degradation function values, D (equations 5.6. and 5.8.) in equation 5.7. The materials properties of the representative scaffolds are obtained from steered molecular dynamics simulations of the nanocomposite. From the simulations results in Figs 5.17 and 5.19., we observed that the time dependence of mechanical properties during the accelerated degradation and hOB cells culture studies were similar to that exhibit by the experimental compression tests results. This indicates that the multiscale mechanics approach presented in the current work can be applied to predict the mechanical behavior of implant scaffolds in critical size bone defects.

5.5. Conclusions

In this work, a new computational multiscale mechanics approach was developed to allow prediction of the evolution of mechanical properties of PCL/in situ HAPclay scaffolds during

degradation and during the growth and proliferation of hOB and ECM formation. This approach allows for the selection of constituents in the nanocomposite using MD simulations. The mechanical response of nanocomposite is obtained using SMD simulations. Representative FE models of scaffolds are constructed, and the material properties from SMD are introduced to obtain the mechanical response of the representative scaffold structure. A new reduction factor that takes into account wall porosities (obtained from SEM images) that have sizes below μCT imaging resolution is developed and successfully implemented. A damage mechanics based modeling approach based on the use of strain energy to calculate mechanical degradation is developed that successfully allows for accurate prediction of mechanical response of scaffolds with time. This approach allows for capturing both scaffold degradation during accelerated degradation as well as improved mechanical properties or healing of cell-seeded scaffolds. The mechanical response obtained from the multiscale modeling of representative scaffold along with the degradation model can be introduced into implant scale FE model of the scaffold at great computational cost savings because the mechanical properties introduced in the FE model include both microstructural and molecular scale information without introducing the complex microstructure in the FE model of critical size implant. This approach can be used to reverse engineer the scaffold microstructure and the nanocomposite constituents to achieve desired properties at the implant scale of the scaffold.

The multiscale mechanics study presented in this paper demonstrates a unique *in silico* approach towards the design of biodegradable, biocompatible polymer nanocomposite scaffolds with predictable time-dependent mechanical behavior for bone tissue regeneration applications. Furthermore, due to its computational advantages this approach, may also be used for the patient-specific optimization of bone tissue regeneration applications.

5.6. References

[1] F.T. Wu, M.O. Stefanini, F. Mac Gabhann, C.D. Kontos, B.H. Annex, A.S. Popel, American Journal of Physiology-Heart and Circulatory Physiology 298 (2010) H2174-H2191.

[2] R. Murugan, S. Ramakrishna, Composites Science and Technology 65 (2005) 2385-2406.

[3] D.H. Kim, R. Rhim, L. Li, J. Martha, B.H. Swaim, R.J. Banco, L.G. Jenis, S.G. Tromanhauser, The Spine Journal 9 (2009) 886-892.

[4] L.T. Kurz, S.R. GARFIN, R.E. BOOTH Jr, Spine 14 (1989) 1324-1331.

[5] J.C. Fernyhough, J.J. Schimandle, M.C. Weigel, C.C. Edwards, A.M. Levine, Spine 17 (1992) 1474-1480.

[6] J.S. Cartmell, M.G. Dunn, Tissue engineering 10 (2004) 1065-1075.

[7] J. Keating, A. Simpson, C. Robinson, Journal of Bone & Joint Surgery, British Volume 87 (2005) 142-150.

[8] D. Raabe, B. Sander, M. Friák, D. Ma, J. Neugebauer, Acta Materialia 55 (2007) 4475-4487.

[9] X. Sun, Y. Kang, J. Bao, Y. Zhang, Y. Yang, X. Zhou, Biomaterials 34 (2013) 4971-4981.

[10] D.R. Katti, A. Sharma, A.H. Ambre, K.S. Katti, Materials science & engineering. C, Materials for biological applications 46 (2015) 207-217.

[11] C. Hellmich, D. Katti, Mrs Bulletin 40 (2015) 309-316.

[12] C. Hellmich, A. Dejaco, S. Scheiner, Journal of Tissue Engineering and Regenerative Medicine 6 (2012) 389-389.

[13] S.V. Shim, C.J. Cornish, L.D. Llyod, H.P. Hunter, Journal of Tissue Engineering and Regenerative Medicine 6 (2012) 51-51.

[14] H. Wang, Y. Li, Y. Zuo, J. Li, S. Ma, L. Cheng, Biomaterials 28 (2007) 3338-3348.

[15] X. Li, L. Wang, Y. Fan, Q. Feng, F.Z. Cui, F. Watari, Journal of Biomedical Materials Research Part A 101 (2013) 2424-2435.

[16] R. Khanna, K.S. Katti, D.R. Katti, Acta Biomaterialia 7 (2011) 1173-1183.

[17] R.K. Roeder, G.L. Converse, R.J. Kane, W. Yue, Jom 60 (2008) 38-45.

[18] F.G. Lyons, J.P. Gleeson, S. Partap, K. Coghlan, F.J. O'Brien, Clinical Orthopaedics and Related Research® 472 (2014) 1318-1328.

[19] M.A. Woodruff, D.W. Hutmacher, Progress in Polymer Science 35 (2010) 1217-1256.

[20] L.S. Nair, C.T. Laurencin, Progress in Polymer Science 32 (2007) 762-798.

[21] M. Okada, Progress in Polymer Science 27 (2002) 87-133.

[22] T.K. Dash, V.B. Konkimalla, Journal of Controlled Release 158 (2012) 15-33.

[23] A. Kumari, S.K. Yadav, S.C. Yadav, Colloids and Surfaces B: Biointerfaces 75 (2010) 1-18.

[24] V.P. Torchilin, Journal of controlled release 73 (2001) 137-172.

[25] L. Shor, S. Guceri, X.J. Wen, M. Gandhi, W. Sun, Biomaterials 28 (2007) 5291-5297.

[26] S.J. Hollister, Nature Materials 4 (2005) 518-524.

[27] H. Yoshimoto, Y.M. Shin, H. Terai, J.P. Vacanti, Biomaterials 24 (2003) 2077-2082.

[28] D. Verma, K. Katti, D. Katti, Journal of Biomedical Materials Research Part A 77A (2006) 59-66.

[29] K.S. Katti, D. Sikdar, D.R. Katti, P. Ghosh, D. Verma, Polymer 47 (2006) 403-414.

[30] D. Verma, K. Katti, D. Katti, Journal of Biomedical Materials Research Part A 77 (2006) 59-66.

[31] R. Bhowmik, K.S. Katti, D.R. Katti, International Journal of Nanotechnology 6 (2009) 511-529.

[32] D. Verma, K.S. Katti, D.R. Katti, Philosophical Transactions of the Royal Society a-Mathematical Physical and Engineering Sciences 368 (2010) 2083-2097.

[33] A. Okada, M. Kawasumi, A. Usuki, Y. Kojima, T. Kurauchi, O. Kamigaito, D. Schaefer, J. Mark, Polymer based molecular composites, MRS symposium proceedings, vol 171, 1990, p. 45.

[34] E. Picard, A. Vermogen, J.F. Gérard, E. Espuche, Journal of Membrane Science 292 (2007) 133-144.

[35] K.S. Katti, D.R. Katti, R. Dash, Biomedical Materials 3 (2008) 034122.

[36] D. Sikdar, D.R. Katti, K.S. Katti, Journal of applied polymer science 107 (2008) 3137-3148.

[37] D. Sikdar, S.M. Pradhan, D.R. Katti, K.S. Katti, B. Mohanty, Langmuir 24 (2008) 5599-5607.

[38] A.H. Ambre, D.R. Katti, K.S. Katti, Journal of Biomedical Materials Research Part A 103 (2015) 2077-2101.

[39] D.R. Katti, P. Ghosh, S. Schmidt, K.S. Katti, Biomacromolecules 6 (2005) 3276-3282.

[40] K.S. Katti, A.H. Ambre, N. Peterka, D.R. Katti, Philosophical Transactions of the Royal Society a-Mathematical Physical and Engineering Sciences 368 (2010) 1963-1980.

[41] A. Ambre, K.S. Katti, D.R. Katti, Materials Science & Engineering C-Materials for Biological Applications 31 (2011) 1017-1029.

[42] A. Ambre, K.S. Katti, D.R. Katti, Materials Science and Engineering: C 31 (2011) 1017-1029.

[43] D.R. Katti, A. Sharma, A.H. Ambre, K.S. Katti, Materials Science and Engineering: C 46 (2015) 207-217.

[44] A. Sharma, S. Payne, K.S. Katti, D.R. Katti, JOM 67 (2015) 733-743.

[45] S. Lohfeld, S. Cahill, V. Barron, P. McHugh, L. Dürselen, L. Kreja, C. Bausewein, A. Ignatius, Acta biomaterialia 8 (2012) 3446-3456.

[46] C. Sandino, J. Planell, D. Lacroix, Journal of biomechanics 41 (2008) 1005-1014.

[47] D. Lacroix, A. Chateau, M.-P. Ginebra, J.A. Planell, Biomaterials 27 (2006) 5326-5334.

[48] S. Jaecques, H. Van Oosterwyck, L. Muraru, T. Van Cleynenbreugel, E. De Smet, M. Wevers, I. Naert, J. Vander Sloten, Biomaterials 25 (2004) 1683-1696.

[49] R. Singh, P.D. Lee, T.C. Lindley, C. Kohlhauser, C. Hellmich, M. Bram, T. Imwinkelried, R.J. Dashwood, Acta Biomaterialia 6 (2010) 2342-2351.

[50] J.R. Jones, P.D. Lee, L.L. Hench, Philosophical Transactions of the Royal Society of London A: Mathematical, Physical and Engineering Sciences 364 (2006) 263-281.

[51] M. Saadatfar, C.H. Arns, M.A. Knackstedt, T. Senden, Colloids and Surfaces A: Physicochemical and Engineering Aspects 263 (2005) 284-289.

[52] R. Müller, P. Rüegsegger, Medical engineering & physics 17 (1995) 126-133.

[53] E. Verhulp, B. Van Rietbergen, R. Müller, R. Huiskes, Computer methods in biomechanics and biomedical engineering 11 (2008) 389-395.

[54] A. Alberich-Bayarri, D. Moratal, J.L.E. Ivirico, J.C.R. Hernández, A. Vallés-Lluch, L. Martí-Bonmatí, J.M. Estellés, J.F. Mano, M.M. Pradas, J.L.G. Ribelles, M. Salmerón-

Sánchez, Journal of Biomedical Materials Research Part B: Applied Biomaterials 91B (2009) 191-202.

[55] D. Lacroix, J.A. Planell, P.J. Prendergast, Philosophical Transactions of the Royal Society A: Mathematical, 				Physical and Engineering Sciences 367 (2009) 1993-2009.

[56] C. Petit, S. Meille, E. Maire, Journal of Materials Research 28 (2013) 2191-2201.

[57] L.-M. Ren, T. Arahira, M. Todo, H. Yoshikawa, A. Myoui, Journal of Materials Science: Materials in Medicine 23 (2012) 463-472.

[58] S. Lohfeld, S. Cahill, H. Doyle, P. McHugh, Journal of Materials Science: Materials in Medicine 26 (2015) 1-12.

[59] C.X. Lam, M.M. Savalani, S.-H. Teoh, D.W. Hutmacher, Biomedical materials 3 (2008) 034108.

[60] C.X. Lam, D.W. Hutmacher, J.T. Schantz, M.A. Woodruff, S.H. Teoh, Journal of biomedical materials research Part A 90 (2009) 906-919.

[61] E. Díaz, I. Sandonis, M.B. Valle, Journal of Nanomaterials 2014 (2014).

[62] J.K. Perron, H.E. Naguib, J. Daka, A. Chawla, R. Wilkins, Journal of Biomedical Materials Research Part B: Applied Biomaterials 91B (2009) 876-886.

[63] S.N. Rothstein, W.J. Federspiel, S.R. Little, Biomaterials 30 (2009) 1657-1664.

[64] N. Bawolin, M. Li, X. Chen, W. Zhang, Journal of biomechanical engineering 132 (2010) 111001.

[65] M.K. Heljak, W. Swieszkowski, K.J. Kurzydlowski, Journal of Applied Polymer Science 131 (2014).

[66] A. Yeo, B. Rai, E. Sju, J. Cheong, S. Teoh, Journal of Biomedical Materials Research Part A 84 (2008) 208-218.

[67] E. Pektok, B. Nottelet, J.-C. Tille, R. Gurny, A. Kalangos, M. Moeller, B.H. Walpoth, Circulation 118 (2008) 2563-2570.

[68] K.S. Katti, A.H. Ambre, S. Payne, D.R. Katti, Materials Research Express 2 (2015) 045401.

[69] C. Desai, A consistent finite element technique for work-softening behavior, Proc., Int. Conf. on Computational Methods in Nonlinear Mechanics, University of Texas, Austin, 1974.

[70] C. Kwak, I. Park, J. Park, Soils and Foundations 53 (2013) 720-734.

[71] C. Kwak, I. Park, J. Park, Asian Journal of Chemistry 26 (2014).

[72] D.R. Katti, C.S. Desai, Journal of engineering mechanics 121 (1995) 648-658.

[73] P.A. Gunatillake, R. Adhikari, Eur Cell Mater 5 (2003) 1-16.

[74] D. Sikdar, D. Katti, K. Katti, B. Mohanty, Journal of applied polymer science 105 (2007) 790-802.

CHAPTER 6. CARBON NANOTUBE PROXIMITY INFLUENCES RICE DNA[5]

This chapter presents the changes in rice plant DNA conformation due to the presence of single walled carbon nanotube. The contents of this chapter have been published in D.R. Katti, A. Sharma, S. Pradhan, K.S. Katti; "Carbon nanotube proximity influences rice DNA", J. Chem. Phys. 455, 17 (2015).

6.1. Introduction

According to the Food and Agriculture Organization of the United Nations (Food Outlook – Biannual report on global food market, June 2013), the 2012/13 world rice production is about 490 million tones with per capita world rice consumption estimated at about 57 kg/year. Thus, rice is an important food source globally. Interactions of plants with nanomaterials are of increased interest recently because of potential for uptake of nanoparticles by plants due to accidental release of nanoparticles into the environment during manufacture and end of lifecycle of products containing nanoparticles. Consequently, the potential impact on plant health and crop output due to nanoparticles update in plants is of concern. Single walled carbon nanotubes (SWCNTs) have been widely studied for a variety of applications due to their excellent mechanical and electronic properties and cellular penetration ability. Strong adsorption of SWCNTs with the DNA enables them to be used for biosensor, biomedical, drug delivery and plant science applications [1-6]. Molecular dynamics (MD) simulations technique is widely used to evaluate the molecular

[5] The material in this chapter was co-authored by Anurag Sharma and Dinesh Katti. Anurag Sharma had primary responsibility for collecting samples in the field and for interviewing users of the test system. Anurag Sharma was the primary developer of the conclusions that are advanced here. Anurag Sharma also drafted and revised all versions of this chapter. Dinesh Katti served as proof reader and checked the math in the statistical analysis conducted by Anurag Sharma.

interaction mechanisms of composite system [7-10]. Further, molecular proximity of charged species have shown to impact biomolecule structure and mechanics in various composite systems such as bone [11], seashells [12] and also polymer-clay nanocomposites [7]. Gao et al.[13] showed using MD simulations that strong van der Waals (vdW) interactions play a dominant role in the insertion of the short ssDNA oligonucleotide into carbon nanotubes. Experimental and simulation studies of ssDNA-SWCNTs hybrid have revealed that binding interaction between ssDNA and SWCNTs is DNA sequence dependent and all ssDNA form stable helically wrapped structure around the SWCNTs [14-16]. It has also been reported that helical wrapping of DNA around the SWCNTs is significantly affected by vdW (or π–π stacking) interactions between DNA and SWCNT. Computer simulations have shown that hydrophobic nucleobases of DNA make π–π stacking with SWCNTs in the water and create a stable SWCNT-DNA hybrid structure. Therefore, binding energy and conformations of the hybrid structure were influenced by the DNA nucleobases [17]. It was observed that intra hydrogen bonding between nucleobases affect the helical conformation of ssDNA on SWCNT [18]. Kim et al. [19] have used salmon genomic DNA to sort SWCNTs of different chiralities by applying AMBER99 force field in CNT-DNA hybrid model. They observed that after 50ns equilibration, the B-form genomic DNA completely shifts to a near A-form. Similar structural changes were also observed in their circular dichroism spectra experiments. Further, vdW energy calculations between genomic DNA and SWCNT showed selective enrichment. The genomic DNA selectively enriched the CNT as compared to single stranded d(GT)20 DNA and enhanced its electronic applications. Long genomic ssDNA tightly wrapped around the SWCNT in a helical shape and thus, effectively dispersed CNT in the water [20]. A similar molecular interaction study revealed that (6,5) SWCNT- semiconducting SWCNTs adsorption energy significantly decreases in the presence of salmon genomic DNA while

adsorption energy between (6,5) SWCNT- metallic SWCNTs remains comparable. These results indicate that the metallicity of SWCNT significantly influences the enrichment capabilities of genomic DNA [21]. Skandani et al. [22] have used MD simulation method to show the translocation of SWCNTs into a lipid bilayered cell membrane. Their study showed that at a very early stage, a sufficiently long SWCNT penetrates into the membrane and as simulation time progresses, endocytosis starts. However, translocation of DNA into CNT requires threshold diameter of CNTs and external driving force to overcome its translocation energy barriers [23-25].

The commercial uses of CNTs in coatings, water filters, batteries, yarns and sheets have begun to emerge in recent years [26]. However, due to insufficient knowledge of the effect of nanoparticles on human beings, animals and plants, it is difficult to have effective regulations, from manufacture to the end of life cycle. CNTs can be released in a variety of ways into the environment that include washing of nanotubes during manufacture and purification, during application process such as manufacturing of coatings, displays, sensors, circuits etc. and end of life of the product. During these events, CNTs may be released into the waste water and end up in sewage sludge. The sludge is then spread on the farmland as fertilizer, where, they may be taken up by plants along with other nutrients in water. In recent years, researchers are investigating the use of CNTs as potential delivery systems for pesticides and to improve production. CNTs have been investigated to control accumulation of pesticides [27] in the plants and as a fertilizer to increase crop production [28]. Giraldo et al. have enhanced photosynthetic activity in the Arabidopsis thaliana plants by passively transporting SWCNTs into the leaves [29]. Recently, Lahiani et al. [30] have reported that germination and plant growth of valuable crops such as barley, soybean, and corn can be significantly regulated by multiwalled carbon nanotubes (MWCNTs). The MWCNTs penetrate into the seed coating and regulate the water channels of the

crops. Raman, photothermal and photoacoustic analysis were performed to understand the interactions between carbon nanotubes and tomato plants. Carbon nanotubes were found in roots, leaves and fruits of tomato plants and had penetrated into the cell walls. Genomic analysis of different parts of tomato plants exposed to carbon nanotubes showed significant alteration in the gene expressions compared to unexposed tomato plants. In leaves from exposed plants, gene expressions of mitogen activated proteins, which are known for their positive role in the plant cell growth and division, were found to be significantly higher. The tomato water channels (aquaporins) gene expressions were also activated in exposed plants, and this enhanced the germination and growth of tomato seedlings. Exposures of carbon nanotubes positively activate genes related to transport, cellular, stress responses, metabolic and biosynthesis processes in the tomato plants [5]. Study of the effect of carbon nanotubes on tobacco plants has shown that at molecular level plants cells recognize the presence of nanoparticles. Carbon nanotubes activate aquaporins and regulate the germination and growth of plants. It has been suggested that carbon nanotubes enter into the tobacco cells and with cell division, carbon nanotubes move to the leaves and fruits of the plants. Carbon nanotubes affect water channel genes of the plant and enhance the water uptake, cell reproduction and photosynthesis [31].

Nair et al. [32] have investigated the effects of carbon nanotubes on the growth and germination of rice plants. They reported that germination of rice seeds increases in the SWCNT enriched medium compared to the germination in the normal/control medium. Thermogravimetric analysis of seeds germinated under SWCNT enriched medium showed a higher amount of moisture content. The increase in the water uptake in SWCNT enriched medium can be a possible reason for the enhancement of the germination. They further observed that SWCNTs were able to penetrate into the rice seed coat. These SWCNTs in the medium enhanced water uptake and

consequently increased the germination. Rice root system and shoot system have shown increased average length when treated with SWCNT enriched medium. SEM and phase contrast images showed the presence of CNTs on the rice root surfaces. These results indicate that CNT's also enhance the seedling growth. However, some other published studies on the phytotoxicity of CNTs have shown that their interactions with plants are more complex and can retard the plant growth by activating hypersensitive response in the plant cells [33, 34]. Conformational changes can cause non Watson-Crick nucleobase pairings in the DNA, which can lead to spontaneous point mutations [35-38]. These changes create potential sites for permanent changes to DNA that could affect the overall health and output of plants. Hence, it is important to study the carbon nanotubes with plant DNA at molecular level to understand their interaction mechanisms. Recently, Kim et al. [21] have performed molecular dynamics simulation of genomic SaDNA for selective enrichment of SWCNTs. Although, they used genomic SaDNA for disaggregation of semiconducting SWCNTs by wrapping, our studies has investigated the influence of SWCNT on specific rice plant DNA via change in conformation and its hydrogen bonding network, to provide input for food safety and nanotoxicity applications. In this study, we have performed MD simulations of rice plant DNA in the absence and presence of SWCNT in the water. The DNA conformation, hydrogen bonding in the nucleobases and interaction energies was calculated to understand the role of SWCNT on the rice plant DNA.

6.2. Computational Methods

6.2.1. Model Construction

Effect of SWCNT on the rice DNA was simulated by molecular dynamics using the NAMD 2.9 software [39]. The genome of oryza sativa rice specie consists of 12 chromosomes. We have selected chromosome-2 of japonica subspecies of oryza sativa for our modeling study.

The DNA structure of this chromosome was build using a DNA sequence builder [40]. The obtained double stranded DNA structure was 969 base pairs long. In order to achieve computational efficiency, we chose 48 base pairs from this DNA structure. Base pair sequence of rice DNA used in our studies is:

d[TGCGGCATCAGCATTGTGCCAACCCTTTGTGCACGGAGGGATCTCCAT]

Fig 6.1a. shows the initial double stranded rice DNA structure. A single-walled carbon nanotube (SWCNT) structure was obtained using carbon nanotube builder in VMD 1.9.1 [41] software. The designed semi-conducting SWCNT (10,5) was ~1 nm in diameter and of the same length as the 48 base pair long DNA. The initial carbon nanotube (CNT) structure with rice DNA is shown in Fig 6.2a. Further, both SWCNT and rice DNA were equilibrated individually. We built two models to study the effect of CNT on DNA, first for the case of the DNA in the absence of CNT (model-1) and the other in the presence of CNT (model-2). DNA was placed parallel to the CNT at a distance of 6 Å as shown in Fig 6.2a. Fig 6.1a. shows the initial model of solvated DNA without CNT. Each model was solvated in water. The TIP3P model of water [42] was used in both the solvated models. Force field parameters used in both models were obtained from the library of CHARMm27 [43, 44]. The total number of water atoms in the model-1 and in model-2 were 166,020 and 166,017, respectively. Simulation box sizes were 87.93Å x 87.46Å x 230.25Å and 95.18Å x 85.45Å x 221.79Å for model-1 and model-2, respectively.

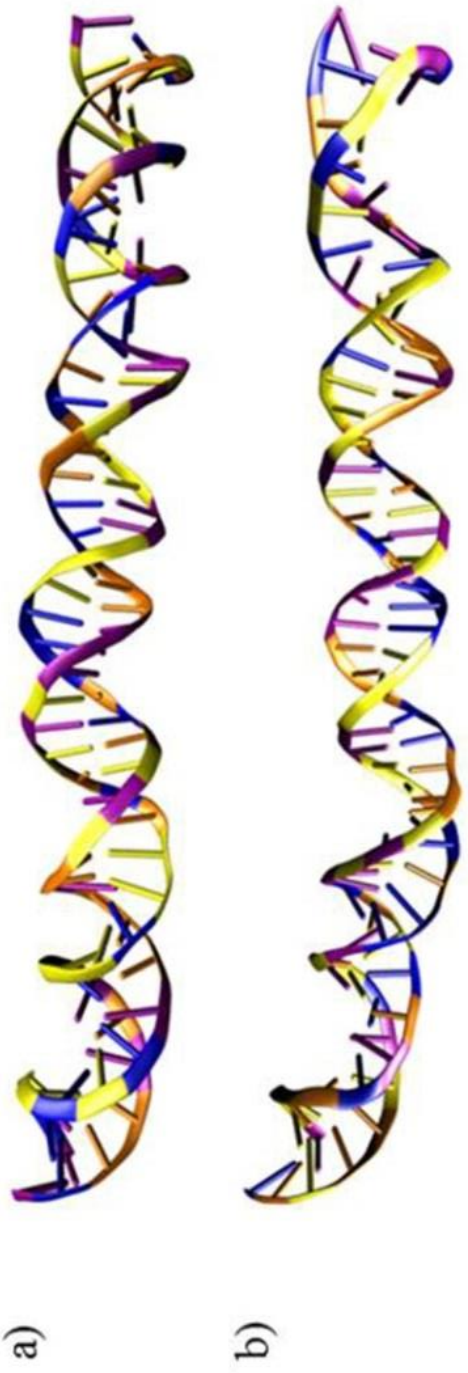

Figure 6.1. (a) Initial conformation of rice DNA, (b) final conformation of rice DNA after 10ns in model-1 shows no changes in base pairing.

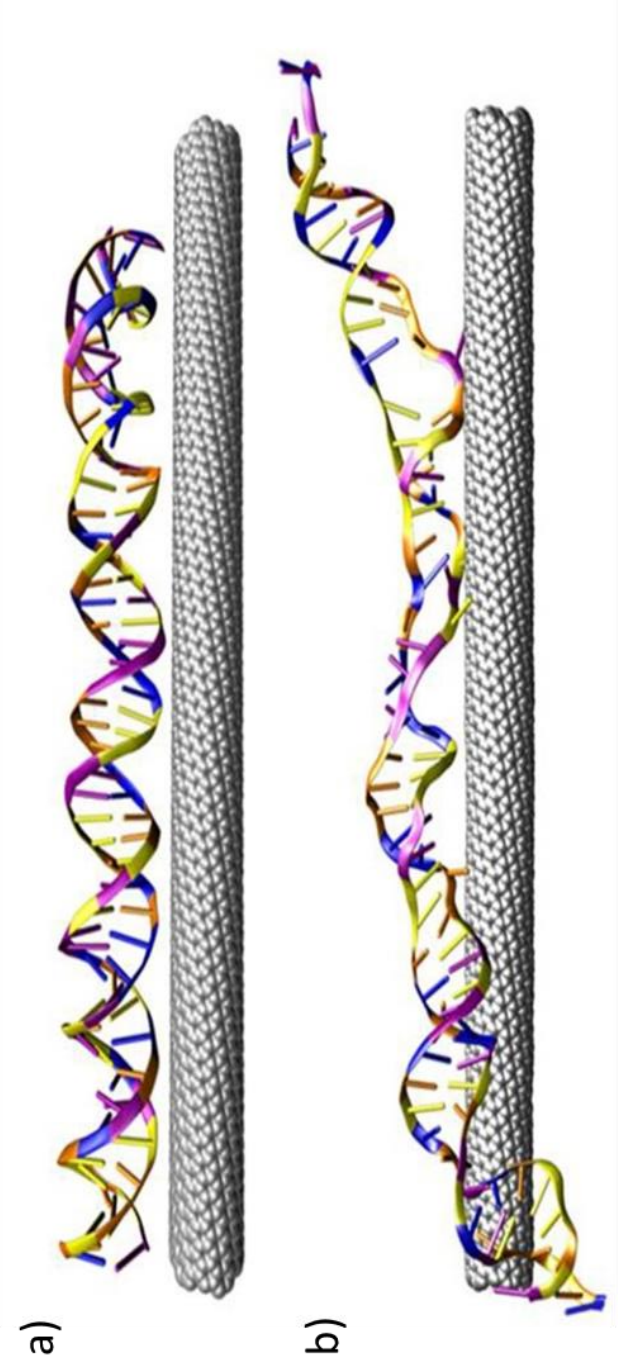

Figure 6.2. (a) initial conformation of rice DNA-SWCNT and (b) final conformation of rice DNA-SWCNT after 10ns in model-2. More number of Gua (yellow) and Cyt (orange) Watson-Crick (WC) nucleobases are unzipped and have moved towards the SWCNT (grey) compared to Ade (blue) and Thy (purple) nucleobases. Few nucleobases have changed their conformation and formed non-WC pairing. As compared to model-1, DNA conformation is significantly altered. Backbone of rice DNA is shown in ribbon shape and

nucleobases are in stick rendering. Water molecules were removed from the snapshot for visual clarity.

6.2.2. Simulation Details

All Molecular Dynamics (MD) simulations in this work were carried out using NAMD 2.9 [39] software and the molecular visualizations and analysis of the results were carried out using VMD 1.9.1 [41]. Nose-Hoover piston and Langevin dynamics methods were used to control pressure and temperature. The temperature and pressure of the molecule were raised to 300 K and 1.01 bar in three small steps of 100 K and four small steps of 0.25 bar, respectively. Each simulation was run for 200ps with time step of 0.5fs. The models were further run for 10 ns at room temperature and pressure, and the results were used for final analysis. A cutoff distance of 30 Å was used for all non-bonded energy calculations. All calculations have been performed under the condition that the tautomeric status of the DNA remains unchanged. The simulations were performed at the Center for Computationally Assisted Science and Technology (CCAST), NDSU. We have used 6 nodes, 8 processors/node (total processors = 48). Wall-time for each simulation was about 84-90 hours.

6.3. Results and Discussion

Molecular dynamics simulations were performed on a double stranded rice plant DNA in the absence and presence of single walled carbon nanotube. Figs 6.1b. and 6.2b. show the conformation of DNA in model-1 and model-2 after 10ns of simulation. The presence of SWCNT strongly influenced and altered the conformation of DNA in model-2. The conformational changes in DNA were observed within few ps of simulation; however, wrapping of DNA onto the SWCNT started after 1ns. Figs 6.3a., 6.3b. and 6.3c. show the wrapping of DNA onto SWCNT at the time period of 1ns, 5ns and 10ns, respectively. As seen in these figures, DNA wrapping onto the SWCNT begins from the one end and moves towards the other end. It was observed that the

fourteen base pairs in solvated DNA-SWCNT model have unzipped after 10ns. Fig 6.4. shows that the unzipping mechanism of the DNA base pairs is more prevalent closer to the SWCNT. The unzipping mechanism and wrapping of dsDNA onto the SWCNTs have been reported in the literature [45-48]. Small interfering ribonucleic acid (siRNA) molecules are an important part of RNA induced silencing complex, which effects cell functionality and specific gene expressions [49]. Effective binding of SWCNTs to siRNA have made them efficient delivery carriers for siRNA to transport into human T cells and primary cells [50-52].

Recently, Santosh et al. [47] have demonstrated the unzipping and wrapping of siRNA and dsDNA (same sequences) on the surface of single walled carbon nanotubes. It was suggested that the vdW interactions between hydrophobic DNA bases and hydrophobic SWCNT initiate and drive the unzipping of base pairs in DNA. Investigation of DNA conformation in our DNA-SWCNT model revealed that at 1ns few Gua-Cyt base pairs were unzipped near the SWCNT surface. Further, these base pairs initiated DNA binding onto the SWCNT. Large numbers of Gua and Cyt bases were found in the proximity of SWCNT compared to the Ade and Thy bases after 10ns of simulation. These results indicate that Gua and Cyt bases played a dominant role in binding of DNA and SWCNT. Hydrogen bonding plays an important role in the determination of DNA conformation [53-55] and wrapping onto SWCNT [56, 57]. The evolution of hydrogen bonds during simulations was studied using a combination of geometric criteria (i.e., donor-hydrogen distance $\leq$ 3.0 Å and donor-hydrogen-acceptor angle $\leq$ 120°). The h-bonds reported here were calculated as an average over the last 1ns of simulation.

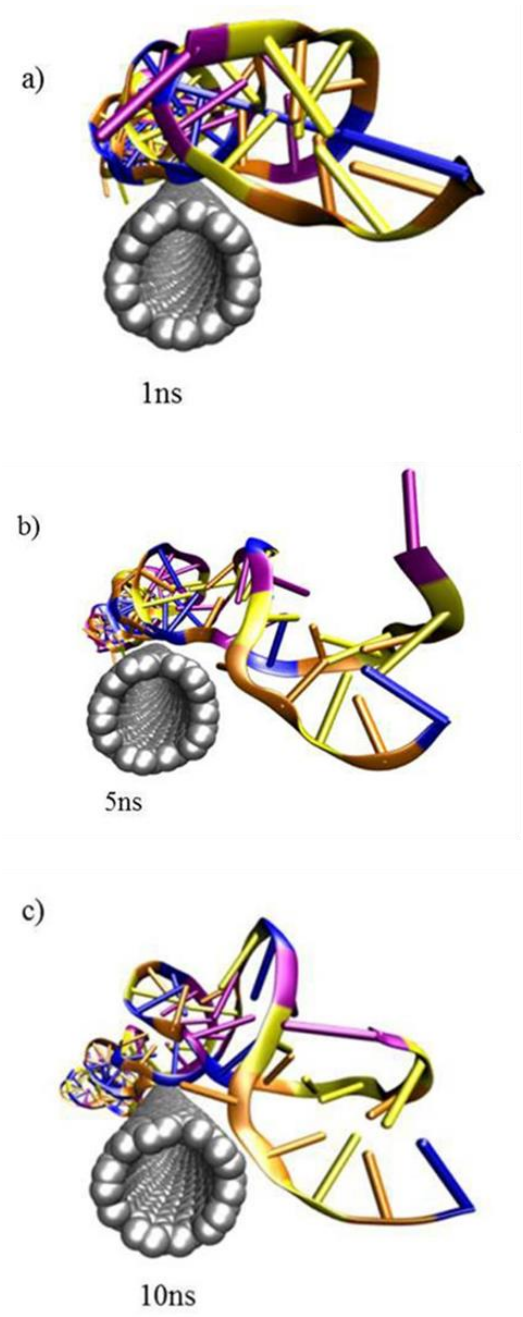

Figure 6.3. Snapshots of rice DNA-SWCNT at different simulation times (a) DNA wrapping onto SWCNT starts at 1ns, (b) more number of the WC bases pairs have unzipped at 5ns and (c) wrapping process of DNA onto SWCNT appears more visible at 10ns in model-2. Wrapping indicates the adsorption of DNA with SWCNT. Water molecules were supressed in the snapshots for ease of viewing.

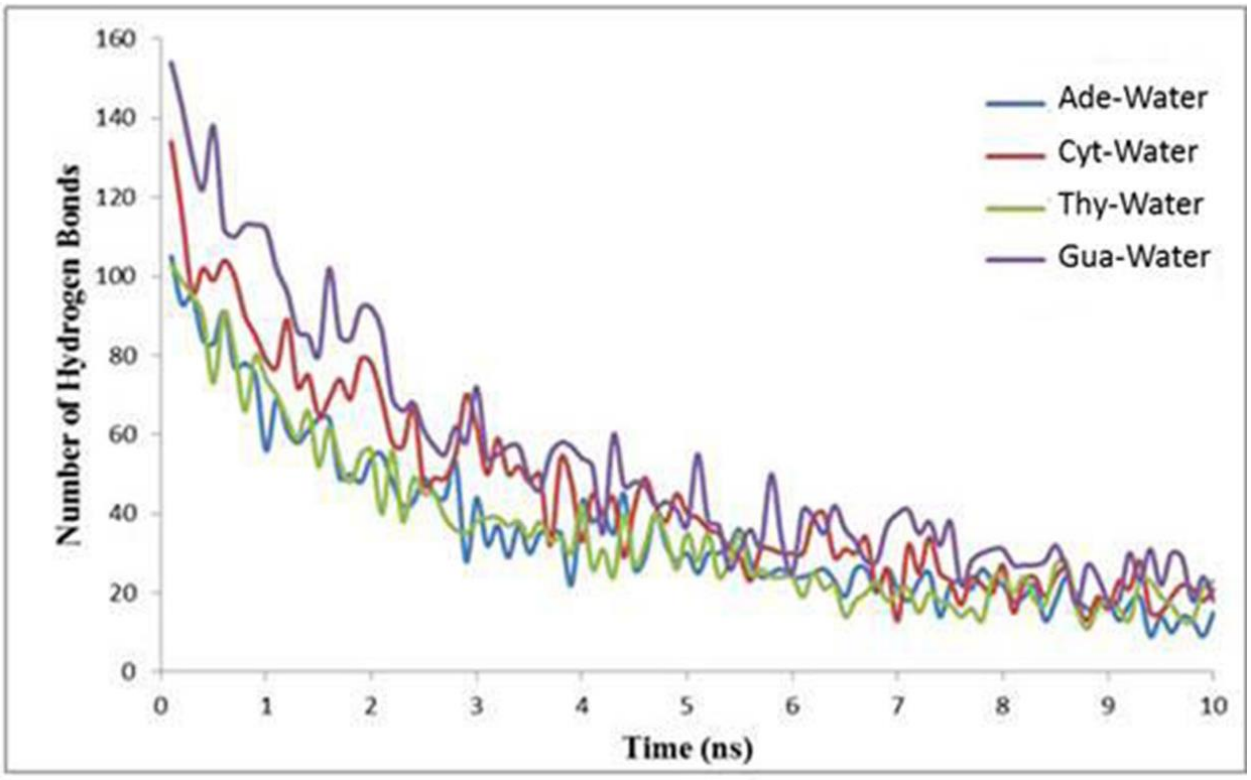

Figure 6.4. Hydrogen bonding between water molecules and different nucleobases of DNA in model-2. The hydrogen bonding between water molecules and DNA bases is dramatically decreased in first 5ns.

Fig 6.4. shows the hydrogen bonding between water molecules and different nucleobases of DNA in model-2. We observed a decreasing trend in hydrogen bonding between all nucleobases and water with time. This observation can be attributed to the wrapping of DNA onto SWCNT, which reduces the available water in the proximity of DNA. Water molecules formed larger number of hydrogen bonds with Gua and Cyt as compared to Ade and Thy. This is because Gua and Cyt expose the most number of hydrogen bonding sites among these four nucleobases.

Table 6.1. Number of hydrogen bonds between DNA Watson-Crick base pairs

Hydrogen bonding between	Number of Hydrogen Bonds	
	Model-1 (without CNT)	**Model-2 (with CNT)**
Ade=Thy	25	19
GuaΞCyt	65	30

To account for the effect of SWCNT on DNA, the number of hydrogen bonds was calculated between Watson-Crick (WC) base pairs adenine-thymine (Ade-Thy) and guanine-cytosine (Gua-Cyt) in the model-1 and 2. Table 6.1. shows the number of hydrogen bonds between DNA WC base pairs in the model-1 (without CNT) and model-2 (with CNT) calculated after 10ns of simulation. The hydrogen bonding in the Gua-Cyt base pairs decreases significantly by 35 as compared to only 6 in the Ade-Thy base pairs. As seen in Fig 6.2b., this is attributed to more unzipping of Gus-Cyt base pairs in the proximity of SWCNT than Ade-Thy base pairs in model-2. It was observed that backbone oxygen atoms of the DNA also contribute in the hydrogen bonding. This hydrogen bonding was found in all four nucleobases. This is unlike the observations reported in the literature [58] where it was reported that significantly higher backbone-base hydrogen bonding in the Gua-Cyt bases oligomer exists as compared to negligible amounts in the Ade-Thy bases oligomer. It was also seen that in our DNA-SWCNT model, more numbers of Gua and Cyt base pairs were unzipped and moved towards the SWCNT. Though, Ade-Thy DNA base pairs also stabilized by three H-bonds [59-61], the fewer number of unzipped Ade-Thy base pairs may be due to their smaller numbers compared to Gua-Cyt base pairs in our DNA sequence. These changes in conformation of DNA prevent the hydrogen atoms of nucleobases to make hydrogen bonding with oxygen atoms of the backbone. Further, the hydrogen bond occupancy analysis was

conducted to calculate the presence of hydrogen bonds during the simulation with respect to time. We observed that hydrogen bonds were breaking and forming continuously during the simulation. The hydrogen bond occupancy of base pairs that are in the proximity of SWCNT was found to be significantly lower (<10%) than the other base pairs in the DNA. This observation is in line with the observations of conformational changes reported in Fig 6.3., which indicated the influence of SWCNT on the DNA base pairs.

Table 6. 2. Non-bonded interaction energies between different bases of DNA and water.

Non-bonded interactions between	**Non-bonded Interaction Energy (kcal/mol)**					
	Model-1 (without CNT)			**Model-2 (with CNT)**		
	E_{ele}	E_{vdW}	$E_{total}=(E_{ele}+E_{vdW})$	E_{ele}	E_{vdW}	$E_{total}=(E_{ele}+E_{vdW})$
Water and DNA	-3671	-101	-3772	-3313	-88	-3401
Water and Ade	-807	-20	-827	-672	-22	-694
Water and Cyt	-1001	-32	-1033	-872	-26	-898
Water and Thy	-778	-28	-806	-797	-16	-813
Water and Guq	-1086	-23	-1109	-971	-26	-997

E_{ele} is the electrostatic interaction energy

E_{vdW} is the van der Waals interaction energy

E_{total} is the total interaction energy

The non-bonded interaction energies between different bases of DNA and water in model-1 and model-2 were calculated after 10ns of simulation. As shown in Table 6.2., strong attractive interactions exist between all the bases and water molecules. The negative values indicate

attractive interaction energies. These interactions were largely electrostatic in nature. High interaction energy between DNA and water in model-1 (-3772 kcal/mol) were reduced due to the presence of CNT in model-2 (-3401 kcal/mol). This may have resulted from a decrease in the number of water atoms near DNA, which were replaced by CNT in the model-2.

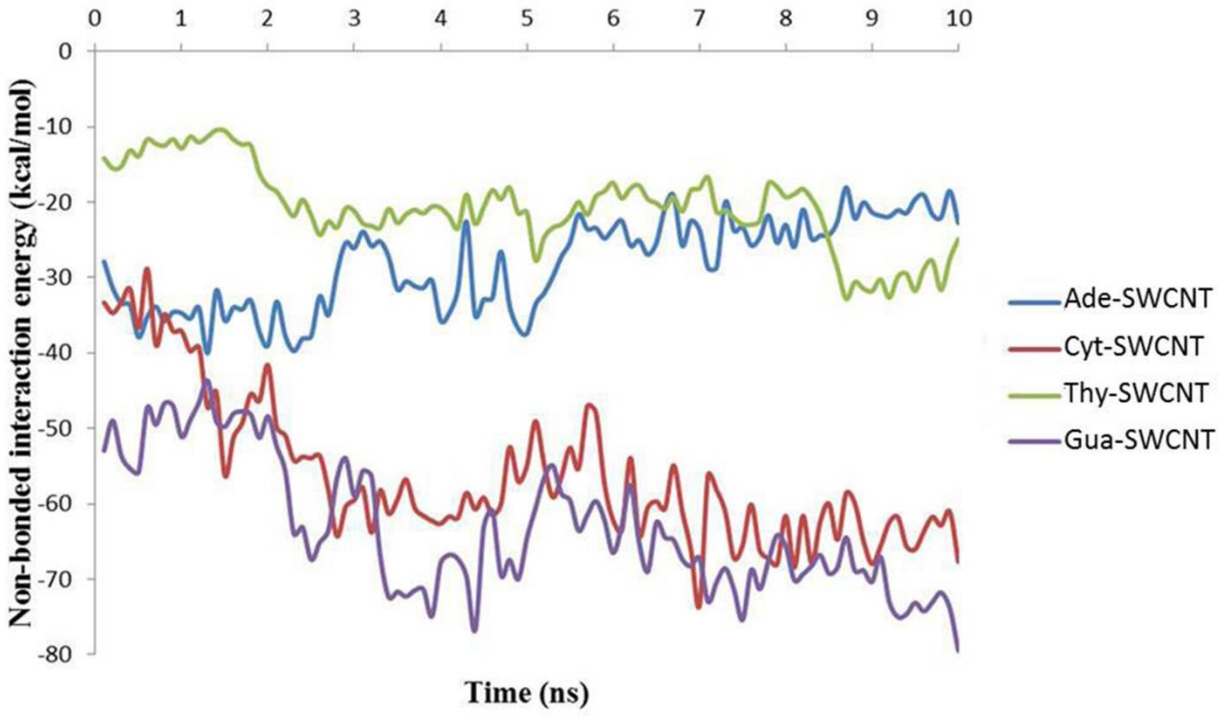

Figure 6. 5. Non-bonded interaction energies plot between different bases of DNA and CNT in model-2. Interactions (π-π stacking) increase with time in all nucleobases barring Ade bases. Increase of π-π stacking energy in Gua and Cyt bases is due to their proximity to the SWCNT.

Fig 6.5. shows interaction energies between different bases of DNA and SWCNT with time in model-2. Fig 6.5. shows that the interactions between DNA and SWCNT have increased with simulation time. The non-bonded interaction energies calculated after 10ns are -22,-67, -26 and -78 kcal/mol between CNT and Ade, Cyt, Thy and Gua, respectively. All four DNA nucleobases are strongly interacting via vdW attraction, i.e. π-π stacking with SWCNT. The highest interactions

were observed between Gua base pairs and SWCNT, followed by Cyt base pairs and SWCNT. The interaction energy increased because more number of Gua and Cyt base pairs unzipped and moved towards the SWCNT as seen in Fig 6.2b. The smallest interaction energy between Ade base pairs and SWCNT can be the result of fewer number of Ade base pairs unzipped among all four bases, and thus hindering the Ade base pairs interaction with SWCNT.

It is widely known that different stress signaling in plants affects its growth rate and morphology. Khodakovskaya et al. have demonstrated that the presence of carbon nanotubes activate the stress related genes in tomato plants. CNTs significantly changed the gene expression in the roots and leaves of tomato plants that controls the particular biological processes in the plant [5]. In another experimental study, MWCNTs have increased the reactive oxygen species (ROS) generation and oxidative stress in rice plants. It was suggested in the study that physical wrapping of proteins of rice cells on MWCNTs may have caused the induction of ROS [34]. To understand this process, we calculated hydrogen bonding between the non-WC base pairs in rice DNA. The importance of hydrogen bonds between non-WC base pairs in determination of secondary biological structure of molecules is well known [62-67]. Non-WC base pairs provide additional sites for hydration, metal binding and protein interactions [68-70]. Further, these non-Watson-Crick base pairs distort the confirmation and have essential significance for the spontaneous point mutation in the DNA [35-38]. It was observed during our simulation that some of the bases were unzipped to their complementary bases and then zipped to the non-complementary bases (mismatch pairing). Significant numbers of hydrogen bonds between non-WC base pairs were observed during the simulation of DNA-SWCNT model. The hydrogen bond occupancy showed that some of these non-WC hydrogen bonds retained their positions for more than 30% of simulation time and appeared only in a certain part of DNA. We observed three Cyt, two Ade, two

Thy and one Gua bases have formed stable non-Watson-Crick base pairs in the rice DNA. These results indicate that SWCNTs have changed the secondary structure of rice DNA by breaking of WC base pairs and forming of non-WC base pairs, and this may result in a change in gene expression. Molecular dynamics simulations conducted in this work will be helpful in understanding the possible impact of SWCNTs on the growth of rice plant DNA.

6.4. Conclusions

- For the first time, molecular dynamics simulations are performed to evaluate the impact of SWCNT on rice DNA for food safety and nanotoxicity applications.
- Interaction between SWCNT and rice DNA significantly changes the conformation of DNA. We observed unzipping of WC nucleobase pairs and wrapping of rice DNA with time onto SWCNT. Unzipping of rice DNA significantly decreases the number of WC hydrogen bonding, mainly near the SWCNT.
- The number of Gua-Cyt WC hydrogen bonds has decreased six times more compared to Ade-Thy WC hydrogen bonds. This implies that Gua and Cyt bases play a dominant role in rice DNA-SWCNT interactions.
- Breaking of WC base pairs has created sites for non-WC hydrogen bonding. High hydrogen bond occupancy of non-WC hydrogen bonds indicates the stable configuration of these non-WC bases. Formation of non-WC base pairs may cause change in gene expression in rice DNA. The findings of the present work qualitatively explain the influence of SWCNT on the rice plant DNA.
- Molecular dynamics simulations of plant DNA and nanoparticles could provide an insight into changes observed in plant health and output.

6.5. References

[1] J. Wang, Electroanalysis 17 (2005) 7-14.

[2] L. Lacerda, A. Bianco, M. Prato, K. Kostarelos, Advanced drug delivery reviews 58 (2006) 1460-1470.

[3] A. Bianco, K. Kostarelos, M. Prato, Current opinion in chemical biology 9 (2005) 674-679.

[4] N. Sinha, J.-W. Yeow, NanoBioscience, IEEE Transactions on 4 (2005) 180-195.

[5] M.V. Khodakovskaya, K. de Silva, D.A. Nedosekin, E. Dervishi, A.S. Biris, E.V. Shashkov, E.I. Galanzha, V.P. Zharov, Proceedings of the National Academy of Sciences 108 (2011) 1028-1033.

[6] Q. Liu, B. Chen, Q. Wang, X. Shi, Z. Xiao, J. Lin, X. Fang, Nano letters 9 (2009) 1007-1010.

[7] D. Sikdar, S.M. Pradhan, D.R. Katti, K.S. Katti, B. Mohanty, Langmuir 24 (2008) 5599-5607.

[8] R. Bhowmik, K.S. Katti, D. Katti, Polymer 48 (2007) 664-674.

[9] D.R. Katti, S.M. Pradhan, K.S. Katti, Journal of Biomechanics 43 (2010) 1723-1730.

[10] S. Pradhan, D. Katti, K. Katti, Journal of Nanomechanics and Micromechanics 1 (2011) 104-110.

[11] R. Bhowmik, K.S. Katti, D.R. Katti, Journal of Materials Science 42 (2007) 8795-8803.

[12] P. Ghosh, D.R. Katti, K.S. Katti, Biomacromolecules 8 (2007) 851-856.

[13] H. Gao, Y. Kong, D. Cui, C.S. Ozkan, Nano Letters 3 (2003) 471-473.

[14] M.L. Mayo, Z.Q. Chen, S.V. Kilina, The Journal of Physical Chemistry Letters 3 (2012) 2790-2797.

[15] D. Roxbury, J. Mittal, A. Jagota, Nano letters 12 (2012) 1464-1469.

[16] R.R. Johnson, A. Kohlmeyer, A.C. Johnson, M.L. Klein, Nano letters 9 (2009) 537-541.

[17] M.V. Karachevtsev, G.O. Gladchenko, A.M. Plokhotnichenko, V.S. Leontiev, V.A. Karachevtsev, The Journal of Physical Chemistry B 117 (2013) 2636-2644.

[18] S. Neihsial, G. Periyasamy, P.K. Samanta, S.K. Pati, The Journal of Physical Chemistry B 116 (2012) 14754-14759.

[19] S.N. Kim, Z. Kuang, J.G. Grote, B.L. Farmer, R.R. Naik, Nano Letters 8 (2008) 4415-4420.

[20] B. Gigliotti, B. Sakizzie, D.S. Bethune, R.M. Shelby, J.N. Cha, Nano Letters 6 (2006) 159-164.

[21] S.S. Kim, C.L. Hisey, Z. Kuang, D.A. Comfort, B.L. Farmer, R.R. Naik, Nanoscale 5 (2013) 4931-4936.

[22] A.A. Skandani, R. Zeineldin, M. Al-Haik, Langmuir 28 (2012) 7872-7879.

[23] Q. Pei, C. Lim, Y. Cheng, H. Gao, The Journal of chemical physics 129 (2008) 125101.

[24] Y. Xie, Y. Kong, A. Soh, H. Gao, The Journal of chemical physics 127 (2007) 225101.

[25] F.J. Cruz, J.J. de Pablo, J.P. Mota, The Journal of Chemical Physics 140 (2014) 225103.

[26] M.F.L. De Volder, S.H. Tawfick, R.H. Baughman, A.J. Hart, Science 339 (2013) 535-539.

[27] R. De La Torre-Roche, J. Hawthorne, Y. Deng, B. Xing, W. Cai, L.A. Newman, Q. Wang, X. Ma, H. Hamdi, J.C. White, Environmental science & technology 47 (2013) 12539-12547.

[28] A. Husen, K. Siddiqi, Journal of Nanobiotechnology 12 (2014) 1-10.

[29] J.P. Giraldo, M.P. Landry, S.M. Faltermeier, T.P. McNicholas, N.M. Iverson, A.A. Boghossian, N.F. Reuel, A.J. Hilmer, F. Sen, J.A. Brew, M.S. Strano, Nat Mater 13 (2014) 400-408.

[30] M.H. Lahiani, E. Dervishi, J. Chen, Z. Nima, A. Gaume, A.S. Biris, M.V. Khodakovskaya, ACS Applied Materials & Interfaces 5 (2013) 7965-7973.

[31] M.V. Khodakovskaya, K. de Silva, A.S. Biris, E. Dervishi, H. Villagarcia, ACS Nano 6 (2012) 2128-2135.

[32] R. Nair, M.S. Mohamed, W. Gao, T. Maekawa, Y. Yoshida, P.M. Ajayan, D.S. Kumar, Journal of Nanoscience and Nanotechnology 12 (2012) 2212-2220.

[33] F. Aslani, S. Bagheri, N. Muhd Julkapli, A.S. Juraimi, F.S.G. Hashemi, A. Baghdadi, The Scientific World Journal 2014 (2014).

[34] X.-m. Tan, C. Lin, B. Fugetsu, Carbon 47 (2009) 3479-3487.

[35] O.h.O. Brovarets, D.M. Hovorun, Physical chemistry chemical physics: PCCP 16 (2014) 15886-15899.

[36] O.h.O. Brovarets, D.M. Hovorun, Physical chemistry chemical physics: PCCP 16 (2014) 9074-9085.

[37] O.h.O. Brovarets, R.O. Zhurakivsky, D.M. Hovorun, Physical chemistry chemical physics: PCCP 16 (2014) 3715-3725.

[38] O.h.O. Brovarets', R.O. Zhurakivsky, D.M. Hovorun, Journal of Biomolecular Structure and Dynamics 33 (2015) 674-689.

[39] J. Phillips, R. Braun, W. Wang, J. Gumbart, E. Tajkhorshid, E. Villa, C. Chipot, R. Skeel, L. Kalé, K. Schulten, Journal of Computational Chemistry 26 (2005) 1781-1802.

[40] http://dna.ccs.tulane.edu/freedna/freedna.php.

[41] W. Humphrey, A. Dalke, K. Schulten, Journal of Molecular Graphics 14 (1996) 33-38.

[42] W.L. Jorgensen, J. Chandrasekhar, J.D. Madura, R.W. Impey, M.L. Klein, Journal of Chemical Physics 79 (1983) 926-935.

[43] N. Foloppe, A.D. MacKerell Jr, Journal of Computational Chemistry 21 (2000) 86-104.

[44] A.D. MacKerell, N.K. Banavali, Journal of Computational Chemistry 21 (2000) 105-120.

[45] H. Cathcart, V. Nicolosi, J.M. Hughes, W.J. Blau, J.M. Kelly, S.J. Quinn, J.N. Coleman, Journal of the American Chemical Society 130 (2008) 12734-12744.

[46] H. Cathcart, S. Quinn, V. Nicolosi, J.M. Kelly, W.J. Blau, J.N. Coleman, The Journal of Physical Chemistry C 111 (2007) 66-74.

[47] M. Santosh, S. Panigrahi, D. Bhattacharyya, A. Sood, P.K. Maiti, The Journal of chemical physics 136 (2012) 065106.

[48] B. Nandy, M. Santosh, P.K. Maiti, Journal of biosciences 37 (2012) 457-474.

[49] A. Fire, S. Xu, M.K. Montgomery, S.A. Kostas, S.E. Driver, C.C. Mello, Nature 391 (1998) 806-811.

[50] Z. Liu, M. Winters, M. Holodniy, H. Dai, Angewandte Chemie International Edition 46 (2007) 2023-2027.

[51] N.W.S. Kam, Z. Liu, H. Dai, Angewandte Chemie International Edition 45 (2006) 577-581.

[52] Z. Zhang, X. Yang, Y. Zhang, B. Zeng, S. Wang, T. Zhu, R.B.S. Roden, Y. Chen, R. Yang, Clinical Cancer Research 12 (2006) 4933-4939.

[53] Y.P. Yurenko, R.O. Zhurakivsky, S.P. Samijlenko, M. Ghomi, D.M. Hovorun, Chemical Physics Letters 447 (2007) 140-146.

[54] Y.P. Yurenko, R.O. Zhurakivsky, S.P. Samijlenko, D.M. Hovorun, Journal of Biomolecular Structure and Dynamics 29 (2011) 51-65.

[55] T.Y. Nikolaienko, L.A. Bulavin, D.M. Hovorun, Physical Chemistry Chemical Physics 14 (2012) 7441-7447.

[56] E.T. Kool, Annual Review of Biophysics and Biomolecular Structure 30 (2001) 1-22.

[57] R.R. Johnson, A.T.C. Johnson, M.L. Klein, Nano Letters 8 (2007) 69-75.

[58] D. Roxbury, A. Jagota, J. Mittal, The Journal of Physical Chemistry B 117 (2012) 132-140.

[59] O.h.O. Brovarets', Y.P. Yurenko, D.M. Hovorun, Journal of Biomolecular Structure and Dynamics 32 (2014) 993-1022.

[60] O.h.O. Brovarets, D.M. Hovorun, Journal of Biomolecular Structure and Dynamics 32 (2014) 127-154.

[61] O.h.O. Brovarets', Y.P. Yurenko, I.Y. Dubey, D.M. Hovorun, Journal of Biomolecular Structure and Dynamics 29 (2012) 1101-1109.

[62] O.B. Ol'ha, R.O. Zhurakivsky, D.M. Hovorun, Journal of molecular modeling 19 (2013) 4223-4237.

[63] O.B. Ol'ha, D.M. Hovorun, Physical Chemistry Chemical Physics 15 (2013) 20091-20104.

[64] O.h.O. Brovarets, D.M. Hovorun, Journal of computational chemistry 34 (2013) 2577-2590.

[65] O.h.O. Brovarets', D.M. Hovorun, Journal of Biomolecular Structure and Dynamics 33 (2014) 925-945.

[66] O.h.O. Brovarets', D.M. Hovorun, Journal of Biomolecular Structure and Dynamics 33 (2015) 28-55.

[67] O.h.O. Brovarets', Y.P. Yurenko, D.M. Hovorun, Journal of Biomolecular Structure and Dynamics (2014) 1-29.

[68] K. Csaszar, N. Špačková, R. Štefl, J. Šponer, N.B. Leontis, Journal of molecular biology 313 (2001) 1073-1091.

[69] K.J. Baeyens, H.L. De Bondt, A. Pardi, S.R. Holbrook, Proceedings of the National Academy of Sciences 93 (1996) 12851-12855.

[70] T. Hermann, E. Westhof, Chemistry & Biology 6 (1999) R335-R343.

CHAPTER 7. SUMMARY AND CONCLUSIONS

The biomaterials selection and design, structural integrity and mechanical properties evolution during degradation and tissue regeneration play a critical role in the successful design of nanocomposite polymeric scaffolds for bone tissue regeneration. A new multiscale mechanics based *in silico* approach is developed in my Ph.D. research which provide a robust predictive methodology to understand the role of these factors in the polymer scaffolds. In addition, the role of single walled carbon nanotube in the proximity of rice DNA was investigated using molecular modeling to provide an insight into changes observed in plant health and output. The summary and key conclusions of my Ph.D. research work are as follows:

A novel molecular dynamics based design of biomaterial nanocomposite system was developed in this study. The nanocomposite system involved MMT nanoclay (MMTclay), aminovaleric acid, hydroxyapatite (HAP) and polycaprolactone (PCL) polymer. MMTclay was modified using protonated aminovaleric acid (OMMT) to mineralize HAP. Further, PCL/in situ HAPclay nanocomposite scaffold system was synthesized by adding 10% of mineralized HAP into PCL (OMMT-HAP-PCL). The representative molecular models of OMMT, OMMT with HAP (OMMT-HAP) and OMMT-HAP-PCL were systematically developed to investigate the underlying interaction mechanism of nanocomposite system. The OMMT model was constructed by replacing Na^+ ions of 6x3 Na-MMT model with 9 protonated aminovaleric molecules (modifiers). The final OMMT representative model was validated using XRD results (d-spacing), balanced charge system and minimum energy conformation in the system. The MD simulations revealed that the molecular interactions between modifier and MMTclay are attractive in nature. The results showed parallel and flat orientation of modifiers to the MMTclay surface in final OMMT representative model.

The TEM analysis of biomineralized HAP indicated that the MMTclay sheets were in perpendicular and parallel to the mineralized HAP surfaces. Therefore, two representative OMMT-HAP models were constructed by placing OMMT model in perpendicular and parallel orientation to the HAP (001) surface. OMMT-HAP models were validated using the XRD results, chelate formation between calcium ions of HAP and carbonyl oxygen atoms of modifiers and minimum energy conformation of the models. The molecular interactions energy calculations between modifiers, HAP and MMTclay, showed strong attractive interactions with each other and found to be largely electrostatic in nature.

The aminoacid modifiers of OMMT were found to be moved out from MMTclay interlayer towards the HAP surface in the OMMT-HAP models, indicating that the HAP surface interacts with MMTclay mainly via modifiers. The change in backbone conformation of modifiers in OMMT-HAP compared to OMMT was attributed to the new interactions between HAP and backbone. The strong attractive and repulsive interactions between PO_4 and Ca groups with different constituents of modifiers and MMTclay in OMMT-HAP and change in the high attractive interaction between functional H atoms of modifiers and MMTclay surface oxygen atoms in OMMT-HAP compared to OMMT indicated the influence of HAP in the OMMT-HAP system. The attractive interactions between Ca atoms of HAP and C=O group of aminovaleric acid were attributed to chelate formation in OMMT-HAP. The molecular interaction results of OMMT-HAP models were compared to the FTIR results of experimentally mineralized in situ HAPclay. The comparison study showed good synergy between experiments and modeling results, validating that these models are the representative models of OMMT-HAP.

The XRD and TEM analysis of the nanocomposite showed that MMTclay sheets were well dispersed in the PCL polymer. Therefore, nine modifiers and one MMTClay sheet were placed

perpendicular to the HAP surface (001) to design an exfoliated system. Following the weight percentage of PCL polymer used in PCL/in situ HAPclay synthesis, the total of 261 PCL chains (90 wt.%) were added. The final OMMT-HAP-PCL representative model was validated by comparing the material system density obtained from simulation and experiment, the formation of chelation indicating the mineralization of in situ HAPclay and minimum energy conformation of the model. Similar to OMMT-HAP models, modifiers in the OMMT-HAP-PCL model were also shifted towards the surface calcium atoms at the HAP surface and formed chelation. The non-bonded interactions energy calculations showed strong interactions between MMTclay, modifiers, HAP and PCL.

The detailed analysis of complex molecular interactions energies map showed that the high interactions between MMTclay and different constituents of modifiers and HAP were mainly electrostatic in nature. These interactions resulted in the shift of the MMTclay sheet towards the HAP surface. The interaction energy calculations between MMTclay and PCL chains revealed the significant contribution of the van der Waals interactions. The high partial atomic charges of Ca and PO_4 constituents significantly contributed in the large repulsive and attractive molecular interactions between the constituents of HAP and PCL chains. The high repulsive interactions between modifier backbone and PCL backbone as well as NH3+ and PCL backbone resulted in the total repulsive interactions between PCL and modifiers in the OMMT-HAP-PCL system. The overall strong molecular interactions of PCL chains with HAP, modifiers and MMTclay indicated the significant role of PCL polymer in the PCL/in situ HAPclay nanocomposite system.

The mechanical properties of the OMMT-HAP-PCL nanocomposite scaffold were evaluated using constant-force steered molecular dynamics (F-SMD) simulations. The PCL chain atoms of bottom surface were fixed in all directions and different compressive point load was

applied on each upper surface atoms of OMMT-HAP-PCL model. The deformation in the model corresponding to every compressive point load was determined. The mechanical response of molecular model showed two distinct regions in the stress-strain plot, high modulus (6.03 GPa) at lower strain (1.8%>) and a significantly low modulus (0.98 GPa) at higher strain (>1.8%). This two phase nanomechanical behavior of the nanocomposite scaffold was incorporated in the multiscale modeling of polymer scaffold.

A multiscale model of PCL/in situ HAPclay scaffold was developed using μCT-FE modeling technique. The μCT images of highly porous PCL/in situ HAPclay scaffold geometry were acquired and reconstructed into 3D volume. The representative cylindrical shape (1.5 mm x 1.5 mm) model was extracted from the complete 3D volume scaffold and meshed into a 3D tetrahedral mesh to simulate the mechanical behavior of the scaffold under the compression loading conditions. The stress-strain response of the nanocomposite scaffold obtained from the F-SMD simulations was used as the material parameters in the μCT-FE modeling simulations. A new reduction factor, K was introduced to include the wall porosity effect on the mechanical behavior prediction of the scaffold. The predicted stress values obtained from the multiscale modeling simulations were multiplied by the reduction factor to incorporate the effect of wall porosity. The stress-strain behavior obtained from the multiscale simulations (after wall porosity correction) and compression test experiments were compared to validate the representative multiscale model of the PCL/in situ HAPclay scaffold. The experimentally calculated and simulations predicted results showed good agreement with each other. Overall, the proposed multiscale model integrates and quantitatively predicts the molecular interactions, mechanical properties at the molecular and structural level and mechanical behavior evolution in the polymer scaffold.

The time-dependent mechanical behavior of PCL/in situ HAPclay scaffolds during the accelerated degradation (0.1 M NaOH, alkaline conditions) and human osteoblast cells culture were analyzed. The effect of accelerated degradation were studied for 1, 5, 7, 14 and 18 days. The results showed a gradual decrease in mechanical properties of scaffolds for first 5 days and then a rapid drop up to 18 days. The hOB cell culture study on PCL/in situ HAPclay scaffolds were performed for 4, 7, 18 and 28 days. The SEM results after 28 days exhibited cells attachment and proliferation on the scaffolds. The cell proliferation study demonstrated a significant increase in the number of live hOB cells on the scaffolds. Furthermore, the hOB cells seeded scaffolds revealed an increase in mechanical properties over the cell culture time period. The increase in mechanical properties and cell proliferation with time indicated that the scaffolds provide a favorable environment for the bone regeneration.

A damage mechanics based modeling technique was developed using strain energy calculations that effectively captures the mechanical properties evolution with time. This technique successfully predicts the improved mechanical properties or healing of cell-seeded scaffolds as well as scaffold degradation during accelerated degradation. The predictive mechanical degradation function, D was proposed for PCL/in situ HAPclay scaffolds under alkaline conditions. The degradation values were calculated for 1, 5, 7 and 18 days using the stress-strain response of the PCL/in situ HAPclay scaffolds in 0.1 M NaOH and found to be increased with time (due to degrading mechanical properties). The predictive mechanical degradation function was validated by the comparison of the stress-strain response of the degraded PCL/in situ HAPclay scaffold (14 days) obtained from the predicted model and experimental compression tests. The results showed a good agreement with each other. The strain energy values of the degraded PCL/in situ HAPclay scaffold (14 days) at 5% and 10% strains were also calculated from the predicted

model and compared with the compression test results. The comparison of the strain energy values showed satisfactory agreement.

A similar predictive mechanical degradation function, D was proposed for the PCL/in situ HAPclay scaffolds seeded with hOB cells. In this case, the degradation values were calculated for 4, 18 and 28 days using the stress-strain response of the PCL/in situ HAPclay scaffolds seeded with hOB cells and found to be decreasing with time (due to improving mechanical properties). The predictive mechanical degradation function for the PCL/in situ HAPclay scaffolds seeded with hOB cells was validated by the comparison of the stress-strain response and strain energy values of the PCL/in situ HAPclay scaffolds seeded with hOB cells (7 days) obtained from the predicted model and experimental compression tests showed a good agreement with each other.

Finally, an integrative implant scale FE model of PCL/in situ HAPclay scaffold was developed for critical size bone defects. The predicted stress-strain responses in the integrative FE model of scaffold were found to be similar to the mechanical properties obtained from the experimental accelerated degradation and hOB cells culture studies of PCl/in situ HAPclay scaffolds. This suggests that the integrative FE model effectively captures the microstructural and molecular scale information of PCL/in situ HAPclay scaffolds and can be applied as a representative model of implant scale scaffolds in critical size bone defects.

Molecular dynamics simulations were performed to evaluate the impact of single walled carbon nanotube (SWCNT) on rice DNA for food safety and nanotoxicity applications. The molecular models of rice DNA and SWCNT were constructed and changes in rice DNA were studied. The modeling results showed that the DNA wrapped around the SWCNT, indicating the adsorption of DNA onto SWCNT. It was found that the DNA wrapping process started from the one end and moved towards the other end of the SWCNT. The hydrogen bonding between water

molecules and different DNA bases showed a significant decrease in first 5 ns due to the presence of SWCNT. During the simulation, few Watson-crick nucleobase pairs in the rice DNA showed unzipping and zipping. Some of the bases were unzipped to their complementary bases and then zipped to the non-complementary bases. Thus, forming the non-Watson-Crick nucleobase pairs in the DNA.

The simulations results revealed that the SWCNT have the ability to dramatically change the conformation of rice DNA. It was observed that intra DNA hydrogen bonds were breaking and forming due to the unzipping of Watson-Crick (WC) nucleobase pairs and wrapping onto SWCNT. A higher number of guanine-cytosine (Gua-Cyt) WC hydrogen bonds break as compared to adenine-thymine (Ade-Thy), suggesting that the Gua and Cyt bases play a dominant role in DNA-SWCNT interactions. It was also observed that the changes to non-WC nucleobase pairs and van der Waals attractive interactions between WC nucleobase pairs and SWCNT cause significant changes in the conformation of the DNA.

The major contributions from the studies are as follows:

1. First *in silico* based design of biomaterial nanocomposites and scaffolds for bone tissue engineering applications was developed. These models allow for understanding mechanisms that influence the mechanics of the nanocomposite scaffolds and provide a computational test bed for design of scaffolds with predictive mechanical properties.
2. It has been shown that the molecular interaction have significant influence on final orientation of modifiers in all the representative nanocomposite models. The energy maps between different constituents have aided in understanding mechanisms of OMMT-HAP and OMMT-

HAP-PCL. Validation of models have shown a good agreement between experimental and simulation results.

3. First multiscale models for polymer clay nanocomposite scaffolds that bridge molecular scale and macroscale mechanics have been developed.
4. A new damage mechanics based modeling technique is developed that predicts the mechanical properties evolution with time under different degradation conditions.
5. The multiscale mechanics study demonstrated a unique approach to design a biodegradable, biocompatible and multiscale polymer scaffolds with time-dependent mechanical behavior for bone tissue regeneration applications.
6. The *in silico* modeling can provide solutions for patient specific problems in tissue engineering and has tremendous potential to replace *in vitro* techniques by reducing the laboratory testing cost and time, reducing animal testing, and enable further improvement of biological substitutions for regenerative medicine.
7. The molecular dynamics simulation of plant DNA and nanoparticles provides an insight into changes observed in plant health and can help in formulating new regulations and environmental laws for sustainable nanotechnology.

CHAPTER 8. FUTURE WORKS

A novel multiscale *in silico* method was developed in this study to desing polymer nanocomposite scaffolds for bone tissue engineering. The studies presented in this dissertation have provided unique insight into the molecular interaction mechanism and multiscale mechanics of the material. Based on the results and understanding from this study following suggestions can be applicable to further improvement in biological substitutions for bone graft patients and nanoparticles in plants:

1. The *in silico* approach developed in this study provides detailed insight into different properties of polymer nanocomposite scaffolds. Therefore, this method can be used to further optimize these properties and scaffolds can be built using 3D printing methods according to patient specific requirements.
2. This multiscale model developed in this study can be further implement to other biomaterial systems that are FDA approved for patient specific uses as this method have shown great computational cost saving.
3. Dynamic mechanical tests can be carried out to gain more information about the scaffolds performance under the different loading conditions. The multiscale models can be further developed by introducing biaxial, tensile and dynamic mechanical tests results.
4. Polycaprolactone polymer has slow degradation rate (3-4 years). In this study alkaline conditions were used as a catalytic substance to accelerate its hydrolytic degradation. Therefore, this study can be further expanded to understand the polymer composite degradation mechanism and mechanical degradation evolution for a long period of time.

5. It can be useful to carry out molecular dynamics simulations for long period of time (50-100ns). Also, different plants DNA can be useful as a step towards better understanding of carbon nanotubes in plants.